



# Programme and Proceedings

## DYMAT Winter School 2020

February 9-14, 2020, Les Houches (France)



*Organized by  
Pr Pascal Forquin*





# DYMAT Winter School 2020 - February 9-14<sup>th</sup> 2020

## Experimental testing and modelling of materials at high-strain rates

As chairman of this 1<sup>st</sup> DYMAT Winter-School, it is my great pleasure to welcome you to Les Houches School of Physics, a place that has held, for the 50<sup>th</sup>, so famous researchers, some of whom awarded Nobel prizes for physics, as well as so many young colleagues and PhD students starting their careers.

On behalf of the Scientific Committee and DYMAT Governing Board, I want to express my deep gratitude to the Scientific council of Les Houches School of Physics who gave us this opportunity, and especially to Pr. Christophe Salomon, General Director of the School, Pr. Philippe Peyla, Mrs Anny Glomot, Mrs Murielle Gardette and Mrs Isabel Lelièvre, without forgetting Pr. Alain Nemoz, former President of Joseph-Fourier University who passed away on last October and who strongly supported my application to organize the DYMAT winter school at Les Houches.

I am also grateful to our invited lecturers:

- *Dr. Egil Fagerholt, Norwegian University of Science and Technology,*
- *Dr. Daniel Eakins, University of Oxford,*
- *Pr. Dirk Mohr, ETH Zürich,*
- *Dr. Jérémie Girardot, Arts et Métiers Institute of Technology,*

As well as to my PhD students sharing the last lecture with me:

- *M. Blasone, M. Dargaud, D. Georges.*

I want to express my deep thanks to our 3 sponsors for supporting this event:

- *Hadland Imaging, Scandiflash, Shimadzu companies.*

I also want to express my special thanks to all the staff involved in the local organization (ExperDYN team, 3SR) and especially to Dr. Dominique Saletti for his tremendous help. I am also grateful to all the people that contributed to this event, in particular to Mrs Laure Cavailles and Mr Matteo Carrera from Insight-Outside, and to the numerous reviewers of papers.

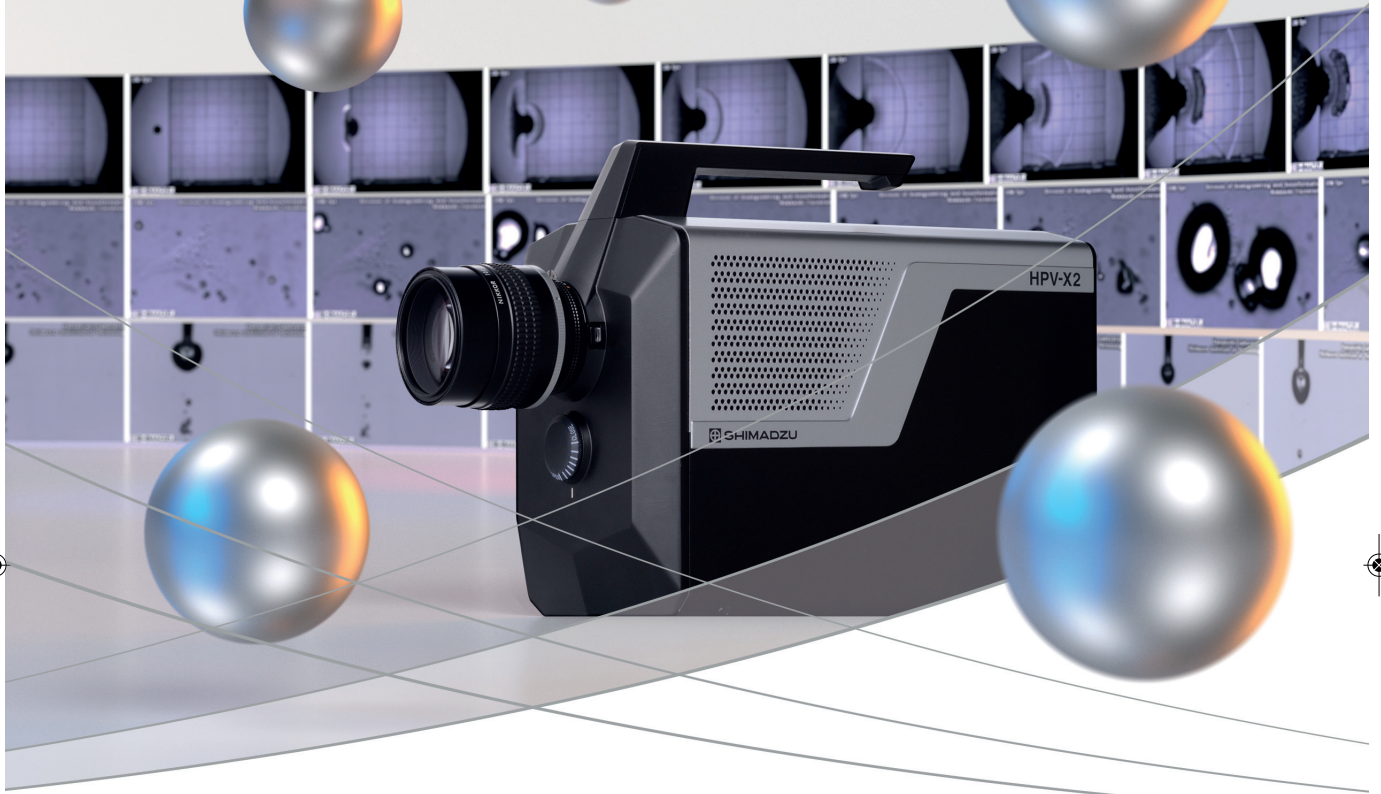
We hope you will enjoy this Winter School. This event is a great opportunity, especially for PhD students, to discover emerging approaches, to exchange with young and senior researchers and to glimpse opportunities for the rest of their career.

We are looking forward to welcoming you in Les Houches!

Yours sincerely,

Pascal Forquin, Professor at Univ. Grenoble Alpes





# Cyberspeed reality X2

The ultra-high-speed video camera HPV-X2

With its improved blooming-free FTCMOS2 sensor, the ultra-high-speed video camera HPV-X2 gives insights into phenomena which have been invisible to the human eye before now. The HPV-X2 enables extreme applications, e.g. in aerospace, explosion and shockwave visualization, cavitation, electrical discharge, advanced medical such as microbubbles, material testing of CFRPs and more.

**Cyberspeed recording**  
of up to 10 million frames per second

**Extreme sensitivity**  
over 10 times higher than other cameras in its class

**Longer recording times**  
through extended frame capacity

**3D perspectives**  
based on synchronized recording using two cameras simultaneously from different angles

# 10 MILLION FRAMES PER SECOND CAN'T BE WRONG



**BETTER GEAR.  
BETTER RESULTS.**  
We've got the gear you need to get the job done right.

EXCLUSIVE REPRESENTATIVE OF SHIMADZU HYPER VISION HPV-X2 ULTRA HIGH-SPEED VIDEO CAMERA

**HS & UHS VISIBLE & IR CAMERAS • 2D/3D DIC • MATERIAL TESTING MACHINES  
FLASH X-RAY • SPLIT HOPKINSON PRESSURE BAR/KOLSKY BAR SYSTEMS & MORE**

## HADLAND<sup>®</sup> IMAGING

CAMERAS • SYSTEMS • ACCESSORIES

 SHIMADZU



The World's Sixth Sense<sup>®</sup>



Scandiflash

1-888-43HADLAND (1-888-434-2352) | [www.hadlandimaging.com](http://www.hadlandimaging.com) | [sales@hadlandimaging.com](mailto:sales@hadlandimaging.com)

# Scandiflash

WORLDWIDE LEADING SUPPLIER OF FLASH X-RAY SOLUTIONS



## Flash X-ray Systems

SEE THROUGH THE TOUGHEST OF CONDITIONS IN THE LAB & IN THE FIELD

**Flash X-ray solutions for ballistics, hypervelocity impact testing, detonics (ordnance velocity & explosives research) and more.**

**Scandiflash AB**

Palmladsgatan 1A • SE-754 50 Uppsala • Sweden • tel: +46 18 557510 • mailbox@scandiflash.se • www.scandiflash.com



## DYMAT-WS-2020 Program – Les Houches School of Physics, February 9th-14th

### Sunday, February 9<sup>th</sup>

15:00 Opening of Les Houches centre, 18:00 Opening of the WS desk, 19:30 Dinner

### Monday, February 10<sup>th</sup>

Time	TITLE	SPEAKER	INSTITUTIONS
<u>8:20</u>	<b>Monday morning – Welcome</b> <b>Pascal FORQUIN</b> , Univ. Grenoble Alpes, Laboratoire sols, solides, structures - risques (France)		
<b>Monday morning – Lecture 1</b> <b>Chairmen: Dr. Eric Buzaud &amp; Pr. Pascal Forquin</b>			
8:30	Lecture 1: Experimental methods and measurement technics at high strain-rates	Fagerholt Egil	Dep. of Structural Engineering, Norwegian University of Science and Technology (Norway)
10:00	<b>Coffee break</b>		
<b>Monday morning, session 1 – Dynamic testing of materials</b> <b>Chairmen: Dr. Eric Buzaud &amp; Pr. Pascal Forquin</b>			
<u>10:20</u>	Compressive response of a very low density polyurethane foam using Split Hopkinson Pressure Bars and high speed imaging	Hanus Jean-Luc	Laboratoire de Mécanique Gabriel Lamé (France)
10:50	Experimental and Numerical Analysis of the Effects of Strain Rate and Adiabatic Heating on the Impact Response of Advanced Fiber-Reinforced Polymers	Pournoori Nazanin	Materials Science and Environmental Engineering, Faculty of Engineering and Natural Sciences, Tampere University (Finland)
11:20	Analyzing the Thermomechanical Behaviour of Materials with Digital Image Correlation and Infrared Imaging	Corréa Soares Guilherme	Tampere University (Finland)
11:50	Dynamic testing, Terminal Ballistics, Plate impact, numerical simulations	Castres Magali, Tartière Jérémie	ENSTA Bretagne (France), Airbus Operations SAS (France)
<u>12:20</u>	<b>End</b>		
12:30	<b>Lunch</b>		
13:30	<b>DYMAT GB</b>		
<b>Monday afternoon, session 2 – Modelling and numerical methods</b> <b>Chairmen: Pr. Francisco Galvez &amp; Dr. Teresa Fras</b>			
<u>17:20</u>	Numerically-based evaluation of the dynamic behaviour of typical triply periodic minimal surface additively-manufactured structures	Carassus Hugo	Laboratoire d'automatique et de mécanique industrielles et humaines (France)
17:50	Shear Characterization of Thin Sheet material using Rectangular Specimen on Torsion Hopkinson bar	Ramagiri Bhaskar	PhD Program (India)
18:20	Analysis of 3D Metallic Auxetic Structures at High Rates of Strain using Finite Element DIC	Trippel Antonina	Albert-Ludwig University of Freiburg, Department of Sustainable Systems Engineering (INATECH) (Germany)
<u>18:50</u>	<b>End</b>		
19:00	<b>Appetizer</b>		
19:30	<b>Dinner</b>		

**DYMAT-WS-2020 Program – Les Houches School of Physics, February 9th-14th**

**Tuesday, February 11<sup>th</sup>**

Time	TITLE	SPEAKER	INSTITUTIONS
<b>Tuesday morning – Lecture 2</b> <b>Chairmen: Pr. Dirk Mohr &amp; Dr. Georg Ganzenmueller</b>			
<u>8:30</u>	Lecture 2: Impact and shock physics	Eakins Daniel	Dep. of Engineering Science, University of Oxford, Impact Laboratory (United Kingdom)
10:00	<b>Coffee break and Poster Session</b>		
<b>Tuesday morning, session 3 – Dynamic testing of materials</b> <b>Chairmen: Pr. Dirk Mohr &amp; Dr. Georg Ganzenmueller</b>			
<u>10:20</u>	Influence of Biaxial Confinement on Dynamic Strength and Fracture Behaviours of Ordinary Concrete at High Strain Rates	Wang Huachuan	Monash University (Australia)
10:50	Effects of specimen geometry, temperature, and strain history on the effective strain rate in ductile titanium alloys: Experiments and Modelling.	Gour Govind	Department of Engineering Science (United Kingdom)
11:20	High-speed sheet metal forming	Corallo Luca	Department of materials science and engineering [Gent] (Belgium)
11:50	Highways and byways in the history of high rate mechanical testing	Walley Stephen	Cavendish Laboratory (United Kingdom)
<u>12:20</u>	<b>End</b>		
12:30	<b>Lunch</b>		
<b>Tuesday afternoon, session 4 –Modelling and numerical methods</b> <b>Chairmen: Dr. Daniel Eakins &amp; Dr. Magali Castres</b>			
<u>17:50</u>	Numerical investigations on the impact behaviour of a 7.62x39 mm projectile	Seidl Marina	French-German Research Institute of Saint-Louis (France)
18:20	Modeling and Behavior of Reinforced Concrete Panels Subjected to Blast Load	Cankaya M. Alper	Department of Civil Engineering, İzmir Katip Çelebi University, Çiğli-İzmir (Turkey)
18:50	Comparison of Two Processing Techniques to Characterise the Dynamic Crack Velocity in Armour Ceramic Based on Digital Image Correlation	Duplan Yannick	Univ. Grenoble Alpes, Laboratoire sols, solides, structures - risques (France)
<u>19:20</u>	<b>End</b>		
19:30	<b>Dinner</b>		
<u>20:30</u>	<b>Poster session</b>		

**DYMAT-WS-2020 Program – Les Houches School of Physics, February 9th-14th**

Wednesday, February 12<sup>th</sup>

Time	TITLE	SPEAKER	INSTITUTIONS
<b>Wednesday morning – Lecture 3</b> <b>Chairmen: Pr. Mikko Hokka &amp; Dr. Jean-Luc Zinszner</b>			
<u>8:30</u>	Lecture 3: Plasticity and failure in ductile materials	Mohr Dirk	Dep. of Mechanical and Process Eng., ETH Zürich (Switzerland)
10:00	<b>Coffee break and Poster Session</b>		
<b>Wednesday morning, session 3 – Damage and failure at high strain-rates</b> <b>Pr. Mikko Hokka &amp; Dr. Jean-Luc Zinszner</b>			
<u>10:20</u>	High-speed imaging for ballistic impact damage assessment of composites	Ramakrishnan Karthik Ram	Department of Engineering Science (United Kingdom)
10:50	In-Situ Flash X-ray Tomography of Low-Strength Mortar Concrete Subjected to Low Velocity Impact	Paulson Shane	School of Aeronautics and Astronautics, Purdue University (United States)
11:20	Dynamic Stress Evaluation during Hypervelocity Impact using Nanosecond Mechanical Raman Spectroscopy	Tomar Vikas	Purdue University West Lafayette (United States)
11:50	Modelling of behavior of aluminum 7020-T651 under dynamic loadings	Teresa Fras	French-German Research Institute of Saint-Louis (ISL) (France)
<u>12:20</u>	<b>End</b>		
12:30	<b>Lunch (takeaway lunch for participants to the social event)</b>		
<u>12:50</u>	<b>Social event: Montenvers train, Departure from Les Houches centre at 12:50</b>		
<b>Wednesday afternoon, session 4 – Applications</b> <b>Chairmen: Dr. Antonio Cosculluela &amp; Dr. Magali Arlery</b>			
<u>17:50</u>	Split Hopkinson bar testing at non-ambient temperatures	Walley Stephen	Cavendish Laboratory (United Kingdom)
18:20	The Brittle's CODEX chair	Forquin Pascal	Univ. Grenoble Alpes, Laboratoire Sols, Solides, Structures - Risques [Grenoble] (France)
18:50	Crashworthiness assessment considering the dynamic damage and failure of a dual phase automotive steel	Chandran Sarath	MST-DyMa Lab, Department of Electromechanical Systems and Materials, Universiteit Gent [Ghent] (Belgium)
<u>19:20</u>	<b>End</b>		
19:30	<b>Dinner</b>		
19:30	<b>Poster session</b>		

**DYMAT-WS-2020 Program – Les Houches School of Physics, February 9th-14th**

**Thursday, February 13<sup>th</sup>**

Time	TITLE	SPEAKER	INSTITUTIONS
<b>Thursday morning – Lecture 4</b> <b>Chairmen: Pr. Philippe Viot &amp; Dr. Jean-Luc Hanus</b>			
<u>8:30</u>	Lecture 4: Discrete numerical methods for damage and fracture simulation in dynamic	Girardot Jérémie	Arts et Métiers Institute of Technology, I2M Bordeaux (France)
10:00	<b>Coffee break and Poster Session</b>		
<b>Thursday morning, session 5 – Modelling and numerical methods</b> <b>Chairmen: Pr. Philippe Viot &amp; Dr. Jean-Luc Hanus</b>			
<u>10:20</u>	Validation of a discrete element model for concrete structures under impact by simulation of reference tests	Daudeville Laurent	Univ. Grenoble Alpes, Laboratoire sols, solides, structures - risques [Grenoble] (France)
10:50	Optimization of geometrical parameters under dynamic compression of auxetic re-entrant honeycomb structure	Bahi Slim	Laboratoire d'étude des microstructures et de mécanique des matériaux [Metz] (France)
11:20	On the energy absorption capability of lattice structures: a numerical study	Riot Alexandre	Arts et Métiers ParisTech. I2M CNRS UMR 5295 (France)
11:50	Modeling the dynamic strength of tantalum	Kositski Roman	Department of Mechanical Engineering [Haifa] (Israel)
<u>12:20</u>	<b>End</b>		
12:30	<b>Lunch</b>		
<b>Thursday afternoon, session 6 – Damage and failure at high strain-rates</b> <b>Chairmen: Dr. Stephen Walley &amp; Dr. Dominique Saletti</b>			
<u>17:50</u>	Polycrystal plasticity approach of the sheet necking problem	Dequiedt Jean-Lin	CEA, DAM, DIF (France)
18:20	Effect of porosity on the failure mechanisms induced in SiC brittle materials upon dynamic impact	Dargaud Marielle	Univ. Grenoble Alpes, Laboratoire Sols, Solides, Structures - Risques [Grenoble] (France)
18:50	Porosity influence on the dynamic tensile strength of polycrystalline ice	Georges David	Univ. Grenoble Alpes, Laboratoire Sols, Solides, Structures - Risques, Institut des Géosciences de l'Environnement [Grenoble] (France)
<u>19:20</u>	<b>End</b>		
19:20	<b>Dinner</b>		

**DYMAT-WS-2020 Program – Les Houches School of Physics, February 9th-14th**

**Friday, February 14<sup>th</sup>**

Time	TITLE	SPEAKER	INSTITUTIONS
<b>Friday morning – Lecture 5</b> <b>Chairmen: Pr. Wayne Chen &amp; Dr. Bratislav Lukic</b>			
<u>8:30</u>	Lecture 5: Dynamic fragmentation in brittle solids: experimental approaches and modelling	P. Forquin, M. Blasone, M. Dargaud, D. Georges	Univ. Grenoble Alpes, Laboratoire Sols, Solides, Structures - Risques [Grenoble] (France)
10:00	<b>Coffee break and Poster Session</b>		
<b>Friday morning, session 7 – Dynamic testing of materials</b> <b>Chairmen: Pr. Wayne Chen &amp; Dr. Bratislav Lukic</b>			
<u>10:20</u>	Drop weight impact resistance of advanced high strength steels (AHSSs)	Xia Peikang	IMDEA Materials Institute (Spain)
10:50	Cohesive shear strength of concrete-rock joints : a preliminary study in quasi-static and dynamic loadings	Dominique Saletti	Univ. Grenoble Alpes, Laboratoire Sols, Solides, Structures - Risques [Grenoble] (France)
11:20	Numerical Design of Plate-Impact Testing method to Determine the Spall strength of an Ultra-High Performance Concrete	Maria Celeste Blasone	Univ. Grenoble Alpes, Laboratoire sols, Solides, Structures - Risques [Grenoble] (France)
11:50	Dynamic behaviour of UD Basalt-Fibre Composites	Janzenmueller Georg	Albert-Ludwig University of Freiburg, Department of Sustainable Systems Engineering (INATECH) (Germany)
12:20	<b>Conclusion</b>		
<u>12:25</u>	<b>End</b>		
12:30	<b>Lunch</b>		
13:30	<b>Departure</b>		



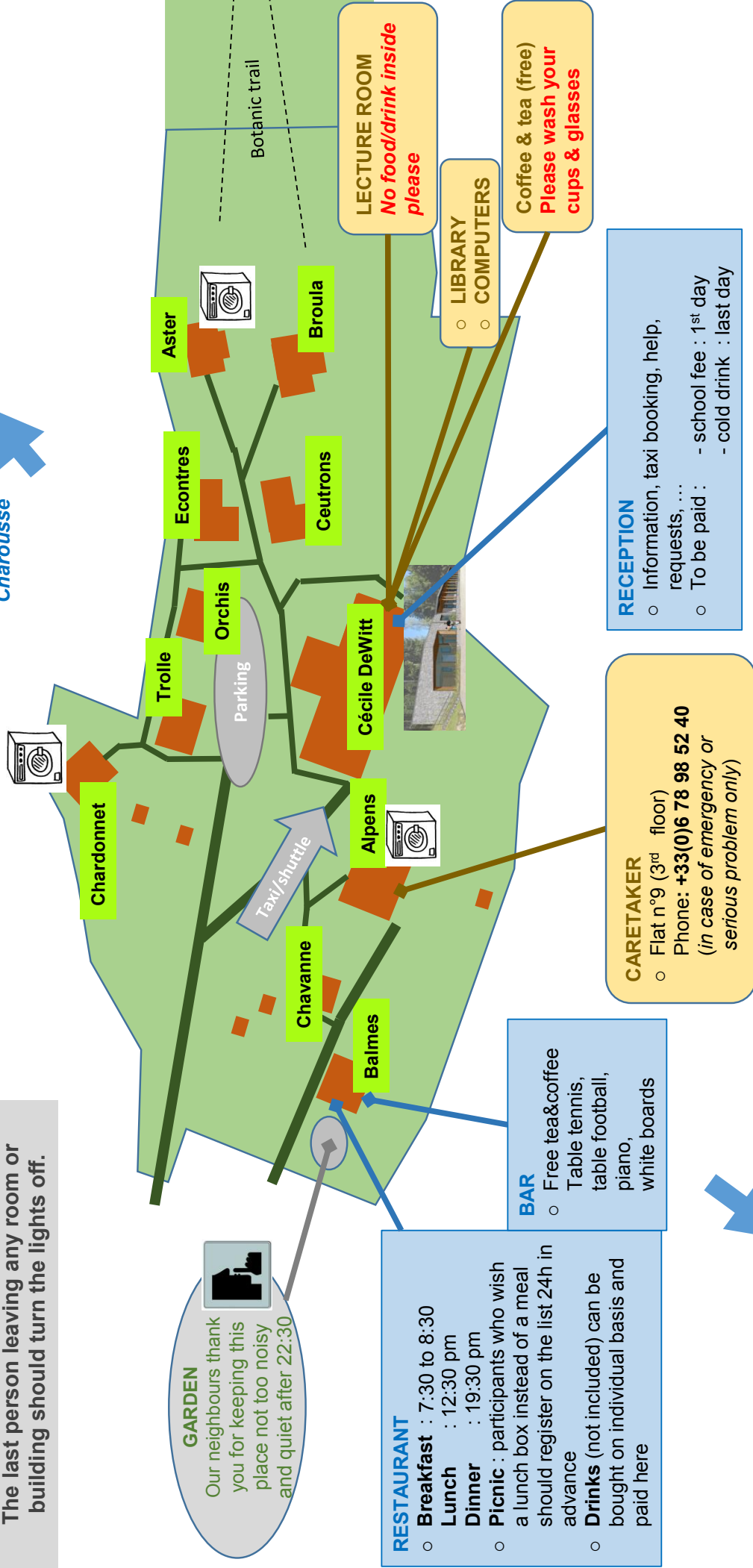


Charousse

## PRACTICAL INFORMATION

The school property is at your disposal for the session; please respect it and if possible improve it.

The last person leaving any room or building should turn the lights off.



Direction of Mont Blanc



## Mountain activities are at your own risk

Before any hike or climb, please put a note on the special book provided and include the name of the participants, approximate itinerary, schedule and phone number. We draw your attention to the fact we only hold a collective insurance for accidents occurring on the school campus.



Washing Machines  
& dryers  
Free use  
& washing powder

## Montenvers - Mer de Glace

Departure from Les Houches School of physics by bus at 12:50 on Wednesday, feb 12<sup>th</sup>.



The famous rack and pinion railway brings you to the Montenvers site at 1913 m. An imposing panorama of the Mer de Glace glacier, the Drus and the Grands Jorasses.



### ICE CAVE

The tour of the “Grotte de glace” (Ice Cave) takes visitors into the very heart of the glacier. Re-sculpted every year, it describes the life of mountain people in the early 19th century. It can be entered either by a walk of around 20 minutes on a footpath, or by gondola lift. NB: There are about 480 steps from the arrival of the gondola lift to the entrance to the cave.



## Lectures

### **Lecture 1: *Experimental methods and measurement technics at high strain-rates***

Dr. Egil Fagerholt, *Dep. of Structural Engineering, Norwegian University of Science and Technology*

The lecture will focus on measurement techniques for kinematic measurements in mechanical testing, with emphasis on high strain-rate applications. Both conventional and state-of-the art techniques will be covered, with a focus on camera-based measurement techniques, such as Digital Image Correlation. The Limitations and advantages of the different techniques in the scope of high strain-rate applications will be addressed. Inverse modeling techniques, such as the Virtual Fields Method will be briefly discussed in terms of the different measurement techniques.



### **Lecture 2: *Impact and shock physics***

Dr. Daniel Eakins, *Dep. of Engineering Science, University of Oxford*

This 2-part lecture will provide an introduction to the behaviour of materials under shock compression and release. Part 1 will present an overview of the thermodynamics of shock loading, wave propagation and interaction, strength effects, and failure mechanisms, with emphasis on the weak-shock regime. The second part will focus on current and emergent diagnostic techniques for studying different aspects of material response under extreme conditions



### **Lecture 3: *Plasticity and failure in ductile materials***

Pr. Dirk Mohr, *Dep. of Mechanical and Process Eng., ETH Zürich*

The first part of the lecture "Plasticity and failure in ductile materials" provides an overview on basic plasticity models that are suitable for describing the deformation response of polymers and metals under normal and extreme loading conditions (large strains, high strain rates and high temperatures). The identification of the model parameters based on static and dynamic experiments is discussed. Subsequently, recent developments are discussed, in particular the potential of machine learning in the context of plasticity model. The second part of this lecture is concerned with ductile failure. Here, micromechanics-based void growth models will be introduced as well as purely phenomenological damage indicator models. The hybrid experimental-numerical characterization of the stress-state (triaxiality and Lode parameter), strain rate and temperature dependent fracture response of metals is discussed. Towards the end of this lecture, examples of finite element simulations are shown involving large deformation and plasticity during impact loading.



### **Lecture 4: *Discrete numerical methods for damage and fracture simulation in dynamic***

Dr. Jérémie Girardot, *Arts et Métiers Institute of Technology, I2M Bordeaux*

This lecture will deal with a specific numerical approach which is more and more used in the field of dynamic simulation. The first part will consist on presenting basics of the Discrete Element Method (DEM) regarding the classical continuum mechanics and how it can be a good choice for dynamic problems. The second part will explore numerical techniques within the DEM that can be set in order to simulate damage, fracture, fragmentation under



dynamic loadings and will present the most used models in the litterature. It will be seen also that the discrete paradigm can be very convenient to take into account variabilities like material heterogeneities or porosities. Finally, several illustration cases will be examined in order to conclude on the usefulness of this approach. Some comparisons with continuous simulation will be analyzed and discussed and recent works on different kind of material will also be presented.

**Lecture 5: *Dynamic fragmentation in brittle solids: experimental approaches and modelling***

Pr. P. Forquin, PhD students M. Blasone, M. Dargaud, D. Georges, *3SR Lab., Univ. Grenoble Alpes*

This lecture will be dedicated to the experimental analysis and numerical modelling of dynamic fragmentation in brittle solids. In particular, the first part will be dedicated to the basis of single and multiple fragmentation modelling (critical defects, crack triggering, crack propagation) and the main related predictions in terms of cracking density, influence of loading rate, distribution of fragments. The second part will focus on the use of X-ray tomography analysis to develop a continuous or discrete modelling of the fragmentation process. A particular attention will be given to the relationship between microstructure, fragmentation properties and macroscopic behaviour of the brittle solids.



# Table of contents

<b>Dynamic testing of materials</b>	<b>3</b>
Compressive response of a very low density polyurethane foam using Split Hopkinson Pressure Bars and high speed imaging, Hanus Jean-Luc [et al.] . . . . .	3
Dynamic testing, Terminal Ballistics, Plate impact, numerical simulations, Castres Magali [et al.] . . . . .	10
Influence of Biaxial Confinement on Dynamic Strength and Fracture Behaviours of Ordinary Concrete at High Strain Rates, Wang Huachuan [et al.] . . . . .	16
Effects of strain history and temperature on the effective strain rate in titanium alloys, Gour Govind [et al.] . . . . .	23
High-speed sheet metal forming: Numerical study of high speed Nakajima testing, Corallo Luca . . . . .	29
Highways and byways in the history of high rate mechanical testing, Walley Stephen	35
Cohesive shear strength of concrete-rock joints : a preliminary study in quasi-static and dynamic loadings, De Lucia Daniela [et al.] . . . . .	41
Numerical Design of Plate-Impact Testing method to Determine the Spall strength of an Ultra-High Performance Concrete, Maria Celeste Blasone [et al.] . . . . .	45
Dynamic behaviour of UD Basalt-Fibre Composites, Ganzenmueller Georg . . . . .	50
X-ray diffraction study of the solid-solid phase transition of tin under shock loading, Palma De Barros David [et al.] . . . . .	56
Visualization of impact damage in Sapphire using high-speed photography and Edge-On impact technique, Lukic Bratislav [et al.] . . . . .	62

<b>Modelling and numerical methods</b>	<b>68</b>
Numerically-based evaluation of the dynamic behaviour of typical triply periodic minimal surface additively-manufactured structures, Carassus Hugo [et al.] . . . .	68
Shear Characterization of Thin Sheet material using Rectangular Specimen on Torsion Hopkinson bar, Ramagiri Bhaskar [et al.] . . . . .	74
Analysis of 3D Metallic Auxetic Structures at High Rates of Strain using Finite Element DIC, Trippel Antonina [et al.] . . . . .	80
Numerical investigations on the impact behaviour of a 7.62x39 mm projectile, Seidl Marina . . . . .	86
Modeling and Behavior of Reinforced Concrete Panels Subjected to Blast Load, Çankaya M. Alper . . . . .	92
Comparison of Two Processing Techniques to Characterise the Dynamic Crack Velocity in Armour Ceramic Based on Digital Image Correlation, Duplan Yannick [et al.] . . . . .	98
Optimization of geometrical parameters under dynamic compression of auxetic re-entrant honeycomb structure, Delcuse Laura [et al.] . . . . .	106
On the energy absorption capability of lattice structures: a numerical study, Riot Alexandre [et al.] . . . . .	112
Modeling the dynamic strength of tantalum, Kositski Roman . . . . .	119
Mesoscopic Modelling of a Polymeric Foam under Dynamic Loading, Pradel Pierre [et al.] . . . . .	123
<b>Damage and failure at high strain-rates</b>	<b>128</b>
High-speed imaging for ballistic impact damage assessment of composites, Ramakrishnan Karthik Ram [et al.] . . . . .	128
In-Situ Flash X-ray Tomography of Low-Strength Mortar Concrete Subjected to Low Velocity Impact, Paulson Shane [et al.] . . . . .	134
Dynamic Stress Evaluation due to Hypervelocity Impact using Time Gated Raman Spectroscopy, Tomar Vikas [et al.] . . . . .	140
Modelling of behavior of aluminum 7020-T651 under dynamic loadings, Fras Teresa	146



Polycrystal plasticity approach of the sheet necking problem, Dequiedt Jean-Lin [et al.] . . . . .	156
Effect of porosity on the failure mechanisms induced in SiC brittle materials upon dynamic impact, Dargaud Marielle [et al.] . . . . .	161
Porosity influence on the dynamic tensile strength of polycrystalline ice, Georges David [et al.] . . . . .	168
<b>Applications</b>	<b>174</b>
Split Hopkinson bar testing at non-ambient temperatures, Walley Stephen . . . .	174
The Brittle's CODEX chair, Forquin Pascal [et al.] . . . . .	180
Crashworthiness assessment considering the dynamic damage and failure of a dual phase automotive steel, Chandran Sarath [et al.] . . . . .	186
<b>List of Participants</b>	<b>192</b>

## Compressive response of a very low density polyurethane foam using Split Hopkinson Pressure Bars and high speed imaging

Hamza El Yamani<sup>1</sup>, Jean-Luc Hanus<sup>1\*</sup>, Huabin Zeng<sup>1</sup>, Patrice Bailly<sup>1</sup>, Gaëtan Prod'Homme<sup>2</sup>, and Benjamin Le-Roux<sup>2</sup>

<sup>1</sup>INSA Centre Val de Loire, Univ. Orléans, Univ. Tours, LaMé EA7494, 18000 Bourges, France, <sup>2</sup>INERIS, Parc Technologique ALATA, 60550 Verneuil-en-Halatte, France

**Keywords:** Blast mitigation, Polymeric foam, Mechanical characterization, Split Hopkinson Pressure Bar (SHPB), Digital Image Correlation

---

**Abstract:** To mitigate the disastrous effects of a blast wave, the use of layered claddings with thermal insulating materials could be a very economical solution. The present paper focuses on the study of the mechanical behaviour of a very low density insulating polyurethane foam ( $30 \text{ kg.m}^{-3}$ ) under compressive loading. Static compressive tests are conducted with a press and nylon Split Hopkinson Pressure Bars (SHPB) are used to investigate the dynamic behaviour over a wide range of engineering strain rates from  $10^{-5}$  to  $10^3 \text{ s}^{-1}$ . In addition to traditional displacement and strain measurements, the Digital Image Correlation (DIC) technique is used to observe the inhomogeneous strain fields. To better represent the mechanical state in the foam due to blast loadings, oedometric compression tests are also conducted. The foam response, showing a linear elastic stage, followed by a plastic plateau and a densification is shown to be transversely isotropic, heterogeneous and strain rate sensitive.

### 1. Introduction

Preventing the disastrous effects of an explosion is one of the key challenge in the field of industrial risk. One solution to protect buildings is to use structures that have the ability to mitigate blast load. Thanks to their dissipative properties due to their compaction behaviour, low density cellular materials are very often used in lightweight sacrificial claddings, protective equipment or to package products against impact damage during transportation [1]. An economical solution, combining protection and energy efficiency, could be to use as cellular materials, those intended for thermal insulation. In order to optimize the design of these structures to mitigate blast loads, established analytical or numerical models for use in finite element analyses can be applied. Reliable experimental results must be produced to feed these models.

The quasi-static compressive tests can be performed using a universal testing machine in accordance with EN 826 and ASTM D695. The uniaxial compressive stress-strain response, in the foam rise direction, is divided in three distinct stages: a small linear elastic response, a large relatively constant stress plateau governed by the crushing of cell walls and the compression of the trapped gases in case of closed-cell foams and a densification associated with a compaction of the crushed cell walls and a steepening increase in stress approaching asymptotically the elastic behaviour of the homogeneous solid [1,2] (see figure 1). Different experimental techniques, such as drop weight tower, Split Hopkinson Pressure Bars (SHPB), and shock tubes can be used to characterize the high strain rate response. Due to their low density, which in turn lead to a low acoustic impedance, the dynamic characterization of polymeric foams remains challenging even with the use of polymeric SHPB [2-4].

Furthermore, even at low strain rate, the specimen deformation may not be uniform due to a progressive collapse of cells [5]. The use of photography and post-processing techniques such as Digital Image Correlation (DIC) appears to be essential to evaluate the uniformity of strain in specimen, even at low strain rates [6].

\*Author for correspondence: [jean-luc.hanus@insa-cvl.fr](mailto:jean-luc.hanus@insa-cvl.fr)  
Orcid Id 0000-0001-7325-2178

## 2. Materials and methods

Among the various available thermal insulation materials, attention is restricted, in this paper to a polyisocyanurate (PIR) foam used in commercial rigid insulation panels. From a morphological point of view, this foam is rigid with closed cells and a very low relative density of 0.025 ( $\rho=30 \text{ kg.m}^{-3}$ ). Static unconfined and confined compression experiments were realised with a universal testing machine (MTS) with cylindrical and prismatic samples. A high-resolution static camera (Prosilica GX) was used to take pictures of the specimen during experiments in order to get full-field measurements from DIC. Dynamic unconfined and confined compression experiments were realised using nylon SHPB and cylindrical specimen. Transport and viscoelastic dispersion correction are performed with DAVID software [7,8]. A high-speed dynamic camera (Photron SA5) was used to take pictures of the experiments in order to obtain full-field measurements from DIC. In static and dynamic experiments specimen faces were lubricated to reduce friction and confinement is performed with transparent acrylic glass cylinders.

## 3. Results and discussion

### a. Quasi-static compression tests

In addition to elastic moduli, the main parameters identified during unconfined static experiments at 10% per minute ((EN 826 standard) are reported in Table 1. Prismatic samples were used to facilitate the identification of Poisson's ratios identification from full-field measurements [9]. The differences of the behaviour between the direction of the rise and the two in plane directions reveal a transverse isotropic behaviour (Figure 1).

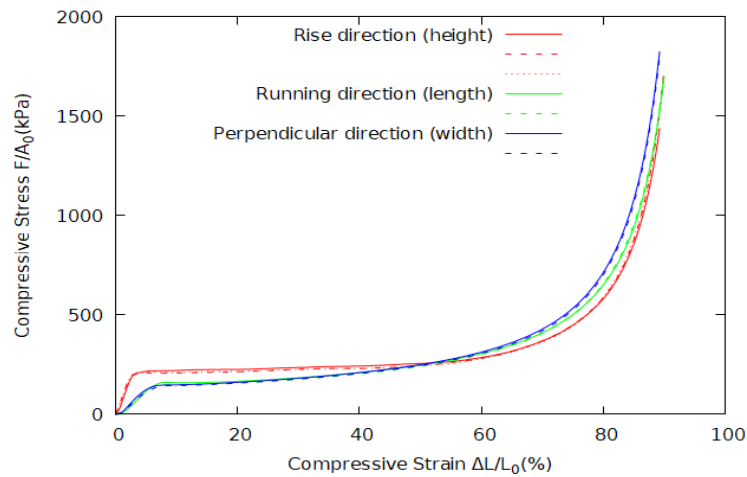


Figure 1: Static compression stress-strain curves

Table 1: PIR foam static properties (L for longitudinal and T for transverse)

Linear response	$E^L$ (MPa)		$E^T$ (MPa)		$\nu^{LT}$		$\nu^{TT}$		$G^{LT}$ (MPa)	
	11		4,2		0,14		0,17		2,8	
Non linear response	Yield stress (kPa)		Plateau stress (kPa)		Densification strain (%)		Apparent Poisson ratio		Energy absorption ( $\text{kJ.m}^{-3}$ )	
	$\sigma_y^L=190$	$\sigma_y^T=140$	$\sigma_p^L=230$	$\sigma_p^T=170$	$\epsilon_d^L=62$	$\epsilon_d^T=62$	$\nu_p^{LT}=0$	$\nu_p^{TT}=0$	$W^L=140$	$W^T=110$

In the table 1, the densification strain  $\varepsilon_d$  is defined as the strain corresponding to the maximum energy absorption efficiency:

$$\eta(\varepsilon) = \frac{\int_{\varepsilon_y}^{\varepsilon} \sigma(\varepsilon) d\varepsilon}{\sigma(\varepsilon)} \quad (1)$$

The plateau stress is defined as the mean stress during the plateau phase:

$$\sigma_p = \frac{\int_{\varepsilon_y}^{\varepsilon_d} \sigma(\varepsilon) d\varepsilon}{\varepsilon_d - \varepsilon_y} \quad (2)$$

And then the energy absorption per unit volume is defined as the strain energy at the onset of densification:

$$W = \int_0^{\varepsilon_d} \sigma(\varepsilon) d\varepsilon \quad (3)$$

These direction-dependent static results, highly repeatable, are consistent with optical micrographs showing a microstructural anisotropy: elongated cells in the foam rise direction (Figure 2).

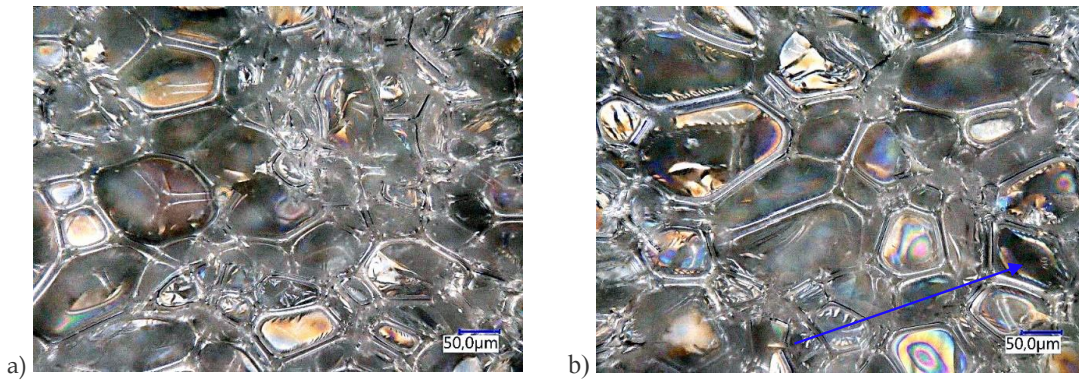


Figure 2: Optical micrographs of PIR foam a) transverse and b) foam rise direction →

The confinement, which limits the global buckling, produces only a slight increase in the plateau stress. This is explained by the apparent null plastic Poisson ratio. Such a little effect of confinement on the compressive stress-strain response of PVC closed cell foams had already been noticed by Walter et al. [11]. The analysis of the digital pictures reveal an inhomogeneous deformation state with a more or less diffused deformation pattern. As previously highlighted by Song et al. [5], one or several compaction fronts propagating in the direction of loading are observed. The main consequence is that in accordance with EN 826 and ASTM D695 standards, only an average stress-strain relation is obtained.

#### b. Dynamic compression tests

Dynamics experiments are performed at low strain rate of 100% and 1000% per minute with the MTS press and at high strain rate with the SHPB device. Performing dynamic experiments with very low density materials remains challenging. Even with the use of polymeric bars, there is an important difference in acoustic impedance between bars ( $Z_b = 2 \times 10^6 \text{ Kg.m}^{-2}.\text{s}^{-1}$ ) and specimen ( $Z_s = 2 \times 10^4 \text{ Kg.m}^{-2}.\text{s}^{-1}$ ) generating a low signal to noise ratio. Furthermore, due to the low wave celerity in the foam ( $C_s = 6 \times 10^2 \text{ m.s}^{-1}$ ) there is a transient period, observed to be equal to three to four round-trips in the specimen, before which the forces at specimen front and back faces equilibrate (Figure 3) and an almost constant engineering strain rate is obtained. Another consequence is that the mean stress during the plateau stress cannot be evaluated between  $\varepsilon_y$  and  $\varepsilon_d$  so that, to enable comparison with quasi-static experiments, the plateau stress  $\sigma_p$  is defined at a nominal strain of 20%.

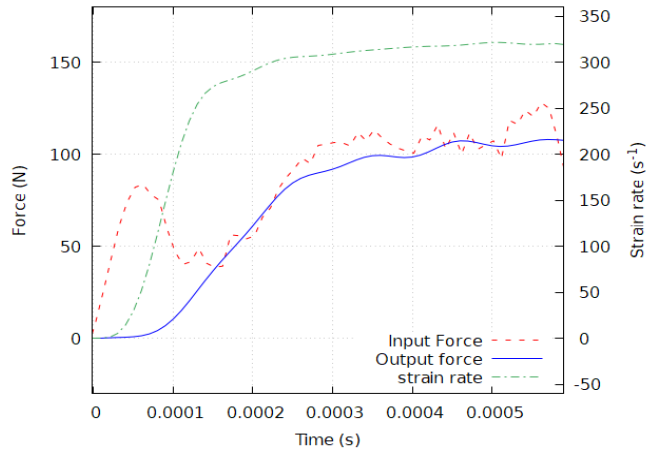


Figure 3: Forces and strain rate history of a PIR foam specimen dynamically loaded with  $V_{striker}=7.4 \text{ ms}^{-1}$

Dynamic experiments show that the collapse stress  $\sigma_p$  is sensitive to strain rate. The strain rate sensitivity can usually be explained either by inertia effects, the solid polyurethane viscous behaviour and the flow of gas initially trapped in cells [2,3]. The comparison of the confined and unconfined compression tests provides arguments to the strengthened by internal gas (Figure 4).

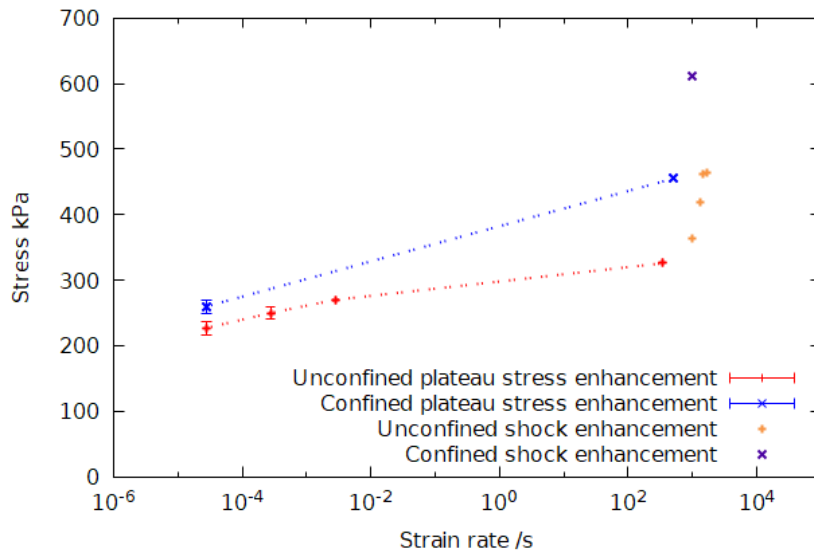


Figure 4: Stress enhancement in rise direction

c. Discussion

Due to a concave stress-strain relationship associated with densification, it is well known that, when the loading speed is sufficiently high, a compaction shock occurs during compression of most of cellular materials. The very strong apparent stress enhancement observed cannot be directly associated with the constitutive stress-strain curve. In this situation neither stress equilibrium nor strain homogeneity are satisfied. The one-dimensional Rankine-Hugoniot jump conditions through the shock front associated with the assumption of a Rigid Plastic

Perfect Locking (RPPL) idealisation of the foam stress-strain curve [11] leads to the classical formula to calculate the stress enhancement:

$$\sigma - \sigma_y = \frac{\rho_0 V^2}{\epsilon_d} \quad (4)$$

where V denotes the impact velocity and  $\rho_0$  the foam density at rest.

It is reported in the literature that there exists a critical velocity under which the strength enhancement is not significant [12]. Our SHPB experiments clearly show a difference between “low” and “high” striker velocities. For “low” impact velocities, the compaction process appears to be quite similar to that observed during quasi-static experiments and after a transient time equilibrium is established (blue and red connected dots in figure 4). For “high” impact velocities, the crush front is sharper and equilibrium is not satisfied (orange and purple dots in figure 4).

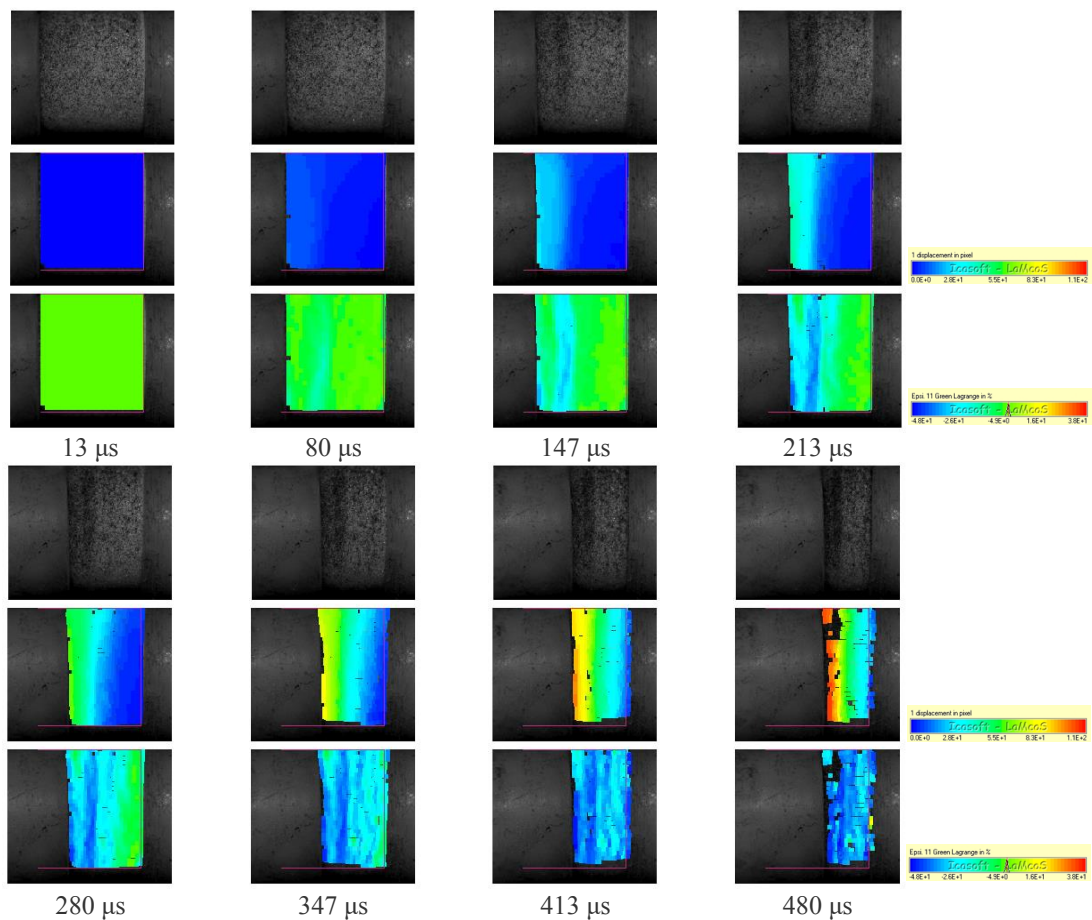


Figure 5: Gray level images, full-field axial displacement and full-field engineering strain at different times for  $V_{striker}=33 \text{ ms}^{-1}$

Figure 5 illustrates the deformation response of the foam for a high impact velocity captured and analysed with DIC. The contour maps of the axial displacement and engineering strain field, plotted in the deformed

configuration, show that two high strained zones are formed at the incident face and inside the specimen near the incident face, which coalesce between  $t=0 \mu\text{s}$  to  $t = 180 \mu\text{s}$  and propagate at a constant velocity toward the distal end from  $t=180 \mu\text{s}$  to  $t = 350 \mu\text{s}$ .

#### 4. Conclusion

Quasi-static and dynamic compression tests have been performed on a very low-density polyisocyanurate foam using a press and nylon SHPB device. The classical static and dynamic post-processing were completed by photography and DIC to access full-fields measurement at the specimen surface. The key observations of the experimental results are:

- The plateau stress is rate sensitive and this rate sensitivity is amplified by confinement.
- At high impact velocities a shock strength enhancement is observed.
- Even when a stress equilibrium state is reached, the assumption of homogeneous strain fields required to identify macroscopic constitutive laws is not fully satisfied, even in static experiments.

#### References

1. Gibson L.J., M.F. Ashby M.F., 1997, Cellular Solids: Structure and Properties, second ed., Oxford, 1997.
2. Zhao H., 1997, Testing of Polymeric Foams at High and Medium Strain Rates, Polymer Testing, Vol. 16, pp. 507-516, DOI: 10.1016/S0142-9418(97)00012
3. Bouix R., Viot P., Lataillade J.L., 2009, Polypropylene foam behaviour under dynamic loadings: Strain rate, density and microstructure effects, Int J Impact Eng, Vol. 36 (2), pp. 329-342, DOI: 10.1016/j.ijimpeng.2007.11.007
4. Chen W.W. and Song B., 2011, Kolsky Compression Bar Experiments on Soft Materials. In: Split Hopkinson (Kolsky) Bar. Mechanical Engineering Series. Springer, Boston, MA
5. Song B., Forrestal M. J., Chen W., 2006, Dynamic and quasi-static propagation of compaction waves in a low-density epoxy foam, Exp Mech, Vol. 46, pp. 127–136, DOI: 10.1007/s11340-006-5871-4
6. Liu J., Saletti D., Pattofatto S., Zhao H., 2014, Impact testing of polymeric foam using Hopkinson bars and digital image analysis, Polym Test, Vol. 36, pp. 101-109, doi.org/10.1016/j.polymertesting.2014.03.0144
7. H. Zhao H., Gary G., Klepaczko J.R., 1997, On the use of a viscoelastic split Hopkinson pressure bar, Int J Impact Eng, Vol. 19 (4), pp. 319-330, DOI: 10.1016/S0734-743X(96)00038-3
8. David : SHPB tests analysis software [Online ; accessed nov-2019]  
<https://www.sites.google.com/site/hopkinsonbars/home/david>
9. Pierron F., 2010, Identification of Poisson's ratios of standard and auxetic low density polymeric foams from full-field measurements, J Strain Anal Eng Des, Vol. 45(4), pp. 233–25, DOI: 10.1243/03093247JSA613
10. Walter T. R., Richards A. W., Andrew W., Subhash G., 2001, A unified phenomenological model for tensile and compressive response of polymeric foams, J. Eng. Mater. T. ASME, Vol. 131 (1), pp. 1-6, DOI: 10.1115/1.3026556
11. Reid S.R., Peng C., 1997, Dynamic uniaxial crushing of wood, Int J Impact Eng, Vol. 19, pp. 531–70, DOI: 10.1016/S0734-743X(97)00016
12. Tan P. , Reid S., Harrigan J., 2012, On the dynamic mechanical properties of open-cell metal foams—a re-assessment of the 'simple-shock theory', Int. J. Solids Struct, Vol. 49, pp. 2744–2753 DOI: 10.1016/j.ijsolstr.2012.03.026

## Dynamic testing of metals and composites materials for terminal ballistics applications correlated with numerical simulations

M. Castres<sup>(a)</sup>, J. Tartière<sup>(a,b)</sup> and M. Arrigoni<sup>(a)</sup>

<sup>(a)</sup>ENSTA Bretagne, IRDL, 2 rue François Verny, 29806 Brest, France

<sup>(b)</sup>Airbus Operations SAS, 18 rue Marius Terce, 31300 Toulouse, France

**Keywords:** Dynamic testing, Terminal Ballistics, Plate impact, numerical simulations

---

**Abstract:** Terminal ballistic study requires the dynamic characterization of materials. Indeed, the mechanical behaviour of ballistic protections has to be known in order to avoid the testing of such expensive devices. Depending on the strain rate field of the material, the experimental methods of characterization are not the same. In a low-speed case, there are numerous standards, but not for high-speed range. The proposed method is to use Taylor's gun to perform a plate to plate impact and measure the velocity of the back face of the targeted plate, using Visar or Heterodyne Velocimeter. Plates are made of Ultra High Molecular Weight Poly-Ethylen composite material or aluminium. The objective is to determine the shock equation of state of the material. Experiments and numerical simulation shown the non-negligible influence of the incident angle. A small angle leads to a huge decrease in free surface velocity. The experimental campaign is actually in progress. To go further in the process, the next step is to perform laser shock study to validate plate to plate impact experiment and determine other parameters such as spalling, peeling or delimitation threshold.

### 1 Introduction

The testing to determine the mechanical behaviour of materials for terminal ballistic applications are very expensive. To reduce the cost of development of ballistic protection while assuring the protection of persons using this ballistic protection there is a need to predict the mechanical behaviour of materials used. In order to predict the behaviour of material used and simulate it, it is important to characterize their mechanical behaviour on the whole conditions that the material has face. The tests performed for this characterization depend on the strain rate field studied, as shown in Figure 1. There are four different mechanical field. For creep and quasi-static loading, the experimental set up to perform the characterization are widely known equally to metals or composites materials. This experimental tests are object to numerous standards [1, 3, 8–10, 17]. For dynamic solicitation, there is no standard. The obtained results depend on the conditions and the laboratory which performed the tests. For low speed, some studies proposed methodology to perform representative and reproducible tests on hydraulic jack [4, 5]. To the other testing facilities mentioned in the Figure 1, to the author knowledge there is no standard or methodology proposed in the literature to ensure that the tests are predictive and reproducible.

In this works, the development of a methodology to perform predictive and reproducible tests to the dynamic characterization of materials has been studied. An experimental method have been considered: plate to plate impact. The plate impact test is a method currently used to determine the equation of state of a material under shock.

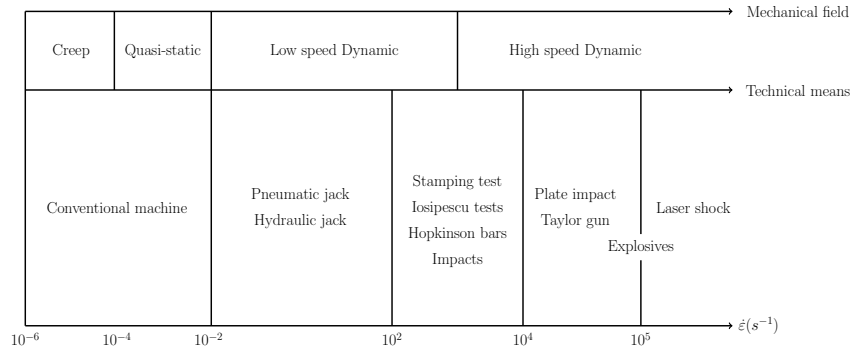


Figure 1: Example of different experimental methods used according to the mechanical field

To develop and validate the experimental methodology two different materials were selected: an aluminium for which mechanical properties are known and a composite uni-directional (UD) material ultra high molecular weight poly-ethylen (UHMWPE) for which mechanical properties are more unknown particularly for high strain rates. This materials are introduced in the second part of this article. The two experimental facilities used in this works are presented in the third section. For each method, the experimental set up are described as well as the influence of the experimental conditions on the obtained results. Lastly, the experimental results are compared with numerical simulation. Finally, a discuss about the results of this works is proposed in the fourth section of this article.

## 2 Materials studied

### 2.1 Aluminium

The AA5754 is a cheap and corrosion resistant aluminium alloy. It is composed of aluminium, few percents of magnesium, and less than one percent of manganese, iron, silicon, chromium, zinc, titanium and copper. Pressure vessels, ships and welded structures in general are commonly made of AA5754 due to its good weldability and machinability. AA5754 has already been characterized in the litterature, using mainly Hopkinson bars to evaluate strain rate sensitivity [2, 15, 16]. In the past decade, few experiments using laser shock were also performed at ENSTA Bretagne, to get higher strain rates. In addition to those works, in correlation with numerical simulation, Johnson-Cook plastic parameters were obtained, those values are summarised in Table 1.

$\rho$ (g.mm <sup>-3</sup> )	E (MPa)	$\nu$	A (MPa)	B (MPa)	n	C	m	$T_{melt}$ (K)	$T_0$ (K)
0.0027	71000	0.33	120	300	0.33	0.1	1	916	300

Table 1: AA5754 Johnson-Cook parameters established at ENSTA Bretagne, with A and Belasto-plasric coefficient, n the plastic strain exponent, C the strain rate coefficient, m the temperature exponent,  $T_{melt}$  the melting temperature and  $T_0$  ambient temperature

### 2.2 Ultra High Molecular Weight Poly-Ethylen (UHMWPE)

The UHMWPE is a thermoplastic polymer which consist of long molecular chain of poly-ethylen. The material studied in this works is a unidirectional laminate of UHMWPE [0°/90°]. The laminate includes

forty plies. The thickness of a ply is about  $60\mu\text{m}$ . This assembly is heated and pressurised to obtain the laminate. In their works Lässig et al. [13] have highlighted the influence of the manufacturing process on the mechanical behaviour of UHMWPE laminates. In the case presented a  $[0^\circ/90^\circ]_{20}$  laminate.

In the literature, some studies discuss about the characterization of UHMWPE laminate for quasi-static loading [6, 7, 12, 14, 18–20]. The mechanical behaviour of UD  $[0/90]$  UHMWPE is visco-plastic. It is composed of a first reversible behaviour followed by a second irreversible behaviour [11]. According to this studies, the elastic behaviour of UHMWPE laminate for quasi-static loading can be described thanks to a transverse isotropic behaviour law. Therefore, the properties in 11 directions are equivalent to properties in 22 direction. The properties obtained in the works of Lässig et al. [12] are summarized in the Table 2.

$\rho$ (g.mm <sup>-3</sup> )	$E_{11}$ (MPa)	$E_{33}$ (MPa)	$\nu_{23}$	$\nu_{13}$	$G_{12}$ (MPa)	$G_{23}$	$\sigma_{11}^{fail}$ (MPa)	$\sigma_{12}^{fail}$ (MPa)
0.00098	26900	3620	0.5	0.1	42.3	30.7	753	32.5

Table 2: Mechanical properties of UHMWPE laminate, from the works of Lässig et al. 2015 [12]

Some studies discuss about the influence of strain rate for low speed loading on the mechanical behaviour of UHMWPE [20]. According to these authors, the strain rates have an important influence on the mechanical behaviour of the studied material. When the strain rate increase, the Young modulus increase. When the strain rate increase the behaviour is closed to a linear behaviour.

With the regard to the high speed dynamic characterization of UHMWPE, the works performed by Lässig et al. have been considered [12] in a first approach. In this works, the parameters of Mie Grüneisen equation have been proposed and used in the presented study to the numerical simulation. To determine accurately the parameters of equation of state of the material studied an experimental campaign has been proposed.

### 3 Methods

To perform these experimental campaign a technical mean have been considered: the plate to plate impact.

#### 3.1 Plate Impact

An experimental method currently used to determine the equation of state parameters, in a first approach, is the plate / plate impact. In this works, this approach has been studied.

##### 3.1.1 Methodology of plate impact

The principle of the plate impact is summarized in the Figure 2. The experimental campaign is performed on a Taylor's gun. A specimen plate, in the case presented aluminium or UHMWPE plate, is placed in a sabot inside the Taylor's gun. The assembly sabot and impactor plate is sent over the target plate (aluminium or UHMWPE plate). During the tests, the velocity of the impactor is measured thanks to a photo-diode and the velocity of particle of specimen thanks to a Heterodyne Velocimeter or Visar placed at the back face of specimen. Thanks to the obtained results, the empirical relation between the shock velocity and the particle velocity can be determined. A currently relation used to express the link between this two velocities is the Mie Grüneisen equation:

$$U_s = C + S * U_p \quad (1)$$

$U_s$  is the shock velocity, C the sound velocity, S the shock material parameter and  $U_p$  the material velocity.

To achieve properly these experimental campaign, it is important to ensure a sufficient planarity during the impact. In default of ensuring a perfect planarity, it is proposed to accurately measured the deviation

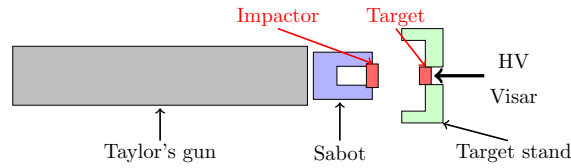


Figure 2: Representation of the plate impact experimental assembly

to the planarity. In this work, a new experimental assembly is proposed to answer to these two points. In this assembly, three different methods are proposed to measure accurately the deviation to the planarity: radial electrical pins, tangential pins and photodiode. To ensure a sufficient planarity the free flight distance is reduced to the minimum and the manufacturing tolerances are imposed at a minimum. To validate the experimental approach, a first campaign is performed on aluminium plate which the parameters are known. After that, UHMWPE plate will be tested. The experimental campaign is actually in progress.

### 3.1.2 Numerical simulations

At the same time, a numerical simulation campaign is performed to study the influence of different parameters on obtained results and to validate the equation of state obtained. The conditions imposed in the simulations are equivalent to the experimental campaign. Two experimental parameters are studied: the influence of the angle at the impact between the two plates and the decentring of the Heterodyne Velocimeter. The numerical simulations are performed for aluminium plate and UHMWPE plate. The numerical campaign is actually in progress, but the exploratory results showed a small influence of the Heterodyne Velocimeter centring and an important influence of the impact angle between the plates as shown in the Figure 3. A 3

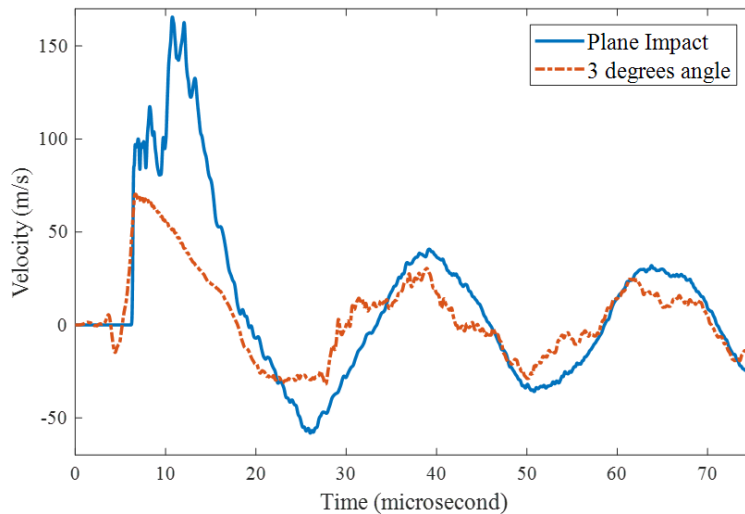


Figure 3: Free surface velocity behind AA5754 target impacted by an AA5754 impactor at 100m/s

degree angle is enough to divide by twice the highest free surface velocity value. Since it is not negligible,

the experimental setting will have to be accurate enough to ensure both planarity and angle of incidence measurement of the impactor. A laser shock study could be complementary to the plate to plate impact experiment in order to validate the equation of state.

## 4 Conclusions

The literature about the characterization of material for dynamic solicitation is sparse. There are few works about these domains. In this works, a first experimental approach is proposed to determine the parameter of equation of state. This approach is available for different materials, metals or composites. The experimental approach consists of performing plate to plate impact. This approach is correlated and supplemented by numerical simulations, this last one shown the huge influence of the angle of incidence on back face velocity and has to be taken into account during experimental campaign.

Laser shock would be suitable to validate and complement the plate to plate study, and lead to further characterizations by the analysis of spalling, peeling and delamination threshold.

Thus, knowing all those parameters, stress level and material resilience to bullet impact or explosion can be determined assuming hydrodynamic effects will have the most influence, based on shock polar theory. Moreover shock equation of state parameters is available in many dynamic codes and sometimes mandatory to model terminal ballistic impact.

## Acknowledgements

The authors would like to thank the DGA (French Armament Procurement Directorate).

## References

- [1] A. 2016. *Standard Test Methods for Tension Testing of Metallic Materials*. ASTM international.
- [2] E.-Y. K. S.-H. C. T. G.-H. Amit Pandeya, Akhtar S. Khan. Experimental and numerical investigations of yield surface, texture, and deformation mechanisms in aa5754 over low to high temperatures and strain rates. *International Journal of Plasticity*, 41:p. 165–188, 2013.
- [3] ASTM D3518/D3518M-94(Reapproved 2001). *Standard test method for in-plane shear response of polymer matrix composite materials by tensile test of a +/- 45 laminate*. ASTM international.
- [4] J. Berthe. *Comportement thermo-visco-élastique des composites CMO - De la statique à la dynamique grande vitesse*. PhD thesis, ONERA/Laboratoire Mécanique de Lille/ EDSPI 072, 2013.
- [5] E. Deletombe, J. Berthe, D. Delsart, J. Fabis, B. Langrand, and G. Portemont. Experimental and Numerical Simulation Strategies for the Prediction of the Macroscopic Behavior and Rupture of Structural Materials under Fast Dynamic Loadings. *AerospaceLab*, (9):p. 1–12, Aug. 2015.
- [6] L. Iannucci and D. Pope. High velocity impact and armour design. *Express Polymer Letters*, 5(3), 2011.
- [7] L. Iannucci, D. Pope, M. Dalzell, P. D. Dstl, and W. Salisbury. A constitutive model for dyneema ud composites. In *17th International Conference on Composite Materials*, pages 27–31, 2009.
- [8] ISO 527-1:2012. *Plastics-Determination of tensile properties-Part 1: General principles*. International Standard Organisation.

- [9] ISO 527-5:1997. *Plastics - Determination of tensile properties-Part 5: Test conditions for unidirectional fibre-reinforced plastic composites*. International Standard Organisation.
- [10] ISO 6892-1:2016. *Tensile Testing Metallic Materials*. International Standard Organisation.
- [11] F. Kromm, T. Lorriot, B. Coutand, R. Harry, and J. Quenisset. Tensile and creep properties of ultra high molecular weight pe fibres. *Polymer Testing*, 22(4):463 – 470, 2003.
- [12] T. Lassig, L. Nguyen, M. May, W. Riedel, U. Heisserer, H. van der Werff, and S. Hiermaier. A non-linear orthotropic hydrocode model for ultra-high molecular weight polyethylene in impact simulations. *International Journal of Impact Engineering*, 75:110–122, 2015.
- [13] T. R. Lassig, M. May, U. Heisserer, W. Riedel, F. Bagusat, H. van der Werff, and S. J. Hiermaier. Effect of consolidation pressure on the impact behavior of uhmwpe composites. *Composites Part B: Engineering*, 147:47 – 55, 2018.
- [14] A. Levi-Sasson, I. meshi, S. Mustacchi, I. Amarilio, D. Benes, V. Favorsky, R. Eliasy, J. Aboudi, and R. Haj-Ali. Experimental determination of linear and nonlinear mechanical properties of laminated soft composite material system. *Composites Part B: Engineering*, 57:96 – 104, 2014.
- [15] S. W.-M. W. M.J. Hadianfard, R. Smerd. Effects of strain rate on mechanical properties and failure mechanism of structural al-mg alloys. *Materials Science and Engineering*, 492:p. 283–292, 2008.
- [16] A. P.-D. L. S. C. M.J. Worswick, Z.T. Chen. Damage characterization and damage percolation modelling in aluminum alloy sheet. *Acta Materialia*, 49:p. 2791– 2803, 2001.
- [17] NF EN ISO 899-1:2003. *Plastiques-Détermination du comportement au fluage-Partie 1:fluage en traction*. Association Francaise de Normalisation (AFNOR).
- [18] L. H. Nguyen. *The ballistic performance of thick ultra high molecular weight polyethylene composite*. Theses, RMIT University, Dec. 2015.
- [19] L. H. Nguyen, T. R. Lassig, S. Ryan, W. Riedel, A. P. Mouritz, and A. C. Orifici. A methodology for hydrocode analysis of ultra-high molecular weight polyethylene composite under ballistic impact. *Composites Part A: Applied Science and Manufacturing*, 84:224–235, 2016.
- [20] B. Russell, K. Karthikeyan, V. Deshpande, and N. Fleck. The high strain rate response of ultra high molecular-weight polyethylene: From fibre to laminate. *International Journal of Impact Engineering*, 60:1 – 9, 2013.

# Influence of Biaxial Confinement on Dynamic Strength and Fracture Behaviours of Ordinary Concrete at High Strain Rates

Huachuan Wang, Kai Liu and Qianbing Zhang\*

*Department of Civil Engineering, Monash University, Wellington Rd, Clayton VIC 3800, Australia*

**Keywords:** Triaxial Hopkinson bar; Biaxial confinements; Dynamic strength; High strain rates; Concrete

---

**Abstract:** Concrete materials, widely used in civil engineering fields with multiaxial confinements, are likely to suffer from accidental and extreme loadings, like earthquake, impact and blast. In order to investigate the dynamic strength and fracture behaviours (e.g. crack initiation, crack propagation and post-failure fractures) of ordinary concrete under biaxial confinements and high strain rates, triaxial Hopkinson bar, high-speed camera, three-dimensional digital image correlation (3D-DIC) and synchrotron X-ray computed tomography (CT) techniques were adopted. Results show that axial pre-stress  $\sigma_1$  reduces dynamic strength and promotes fracture development, but lateral pre-stress  $\sigma_2$  enhances dynamic strength and restricts the development of fractures. By capturing the surface crack process using high-speed camera and 3D-DIC, it is found that crack initiates from interface and matrix of concrete at around 100 $\mu$ s, and mainly propagates along tensile strain localisation areas.

## 1. Introduction

Concrete materials, widely used in civil engineering fields (e.g. buildings, dams and oil wells), are vulnerably subjected to accidental and extreme loadings, like earthquake, impact and blasting [1]. At the same time, their stress states change from uniaxial to triaxial related to pre-stress, self-weight, water pressure, etc. Under these complex conditions, concrete materials are more likely to suffer from deterioration and failure, which will cause extensive damage to the infrastructures and great loss of human lives. One important reason is the momentary generation and development of cracks resulted from extreme loadings.

To consider the confinement effect of concrete under dynamic loadings, some experiments have been carried out and produced many significant outputs. Lateral pre-stress was first applied into the drop weight test, from uniaxial to biaxial pre-stress realized by compression device [2-4]. However, the dynamic strength can hardly be obtained due to the stress disequilibrium during the impact. In order to realize the confinement under high strain rates, active confinements and passive confinements are mainly considered into the split Hopkinson pressure bar (SHPB) system. For instance, brass strip and steel sleeve are often used jacketing the cylindrical surface of the specimen to produce passive confinement by boundary limitation [5-7]. Various fluids like water or oil are placed inside the pressure chamber to produce hydrostatic pressure [8-9]. Besides, in order to measure the deformation of specimens, resistance wire extensometers/strain gauges are often mounted on the jackets of specimen [10]. An obvious shortcoming of the SHPB combined with the active or passive confinement is that the confinement is isotropic due to the lack of stress difference of hydrostatic pressure. However, the actual stress states are very complex, maybe biaxial or triaxial loading conditions.

Therefore, to better understand the dynamic responses of concrete materials under coupled static and dynamic loads, it is required to apply different stress states (e.g. uniaxial, biaxial and triaxial), and followed by dynamic loading over a wide range of strain rates from 10 to 10<sup>3</sup> s<sup>-1</sup>. A triaxial Hopkinson bar was developed [11], which allows for precise determination of dynamic behaviours of concrete materials under different confinement conditions at high strain rates.

\*Author for correspondence (qianbing.zhang@monash.edu).

†Present address: Dept. of Civil Engineering, Monash Univ., Clayton, VIC 3800, Australia

## 2. Material preparation

Ordinary Portland cement (OPC), a general purpose cement produced in Australia, was used in the production of concrete specimens. All of the specimens adopted the same water–cement ratio 0.6 with tap water provided in laboratory as fresh water. Ordinary concrete was mixed in the proportion of 0.6:1:2:3 (water: cement: sand: coarse aggregate) by weight. River sand was used in this research with maximum size of 1.12mm. Coarse aggregate is basalt with maximum size of 7mm.

The specimens were firstly cast in steel molds with dimensions of 50mm×50mm×50mm, more than three times the maximum size of coarse aggregates, satisfying the requirement of ASTM C192 [12]. After that, the specimens were covered with plastic film to prevent moisture loss from evaporating and de-moulded after 24 h, then moist-cured in a special curing chamber at  $21 \pm 2$  °C. After curing for 28 days, the specimens were milled for good parallelism and smoothness (i.e. 0.02mm roughness). The uniaxial compressive strength (UCS) of concrete is 38MPa.

## 3. Methodology

### 3.1 Triaxial Hopkinson bar system

The dynamic compression tests of concretes under biaxial confinements were conducted on the Triaxial Hopkinson Bar apparatus (Figure 1.a). It consists of a servo-controlled hydraulic loading system to apply the quasi-static multiaxial confining pressures and a dynamic loading system to apply an additional dynamic loading on the specimen. Details of the design, operation and calibration of the triaxial Hopkinson bar system are given in the literature [11, 13]. The experimental setup for dynamic biaxial compression is depicted in the Figure 1.b.

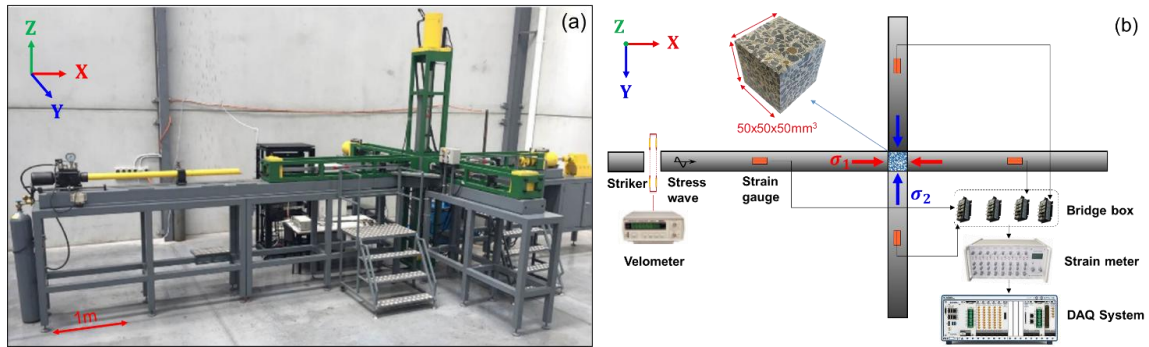


Figure 1: Triaxial Hopkinson bar apparatus (a) and dynamic biaxial compression setup (b)

The specimen is initially subjected to a desired biaxial pre-stress state ( $\sigma_{1\text{-static}}$ ,  $\sigma_{2\text{-static}}$ ), achieved independently by hydraulic cylinders installed at the end of steel square bars in X and Y loading directions, respectively. Dynamic loads are applied by launching a striker in the gas gun which generates an incident elastic compressive wave towards the specimen. Strain gauges are mounted on the input and output bars to record the signals. Then signals are transferred to the DAQ system by bridge box and strain meter. Finally, based on elastic one-dimensional (1D) stress wave propagation theory, the dynamic strength of concrete samples under coupled static and dynamic loadings is determined.

### 3.2 3D-DIC system

3D-Digital Image Correlation (3D-DIC) system was applied to study the surface crack initiation and propagation, by quantification of surface full-field strain fields. 3D-DIC setup and schematic are shown in figure 2. The resolution was set as 256×256 pixels with frame rate 200,000 fps. LED lights were used for

exposure compensation. Details of operation, calibration and correlation algorithm could refer to the literature [14, 15].

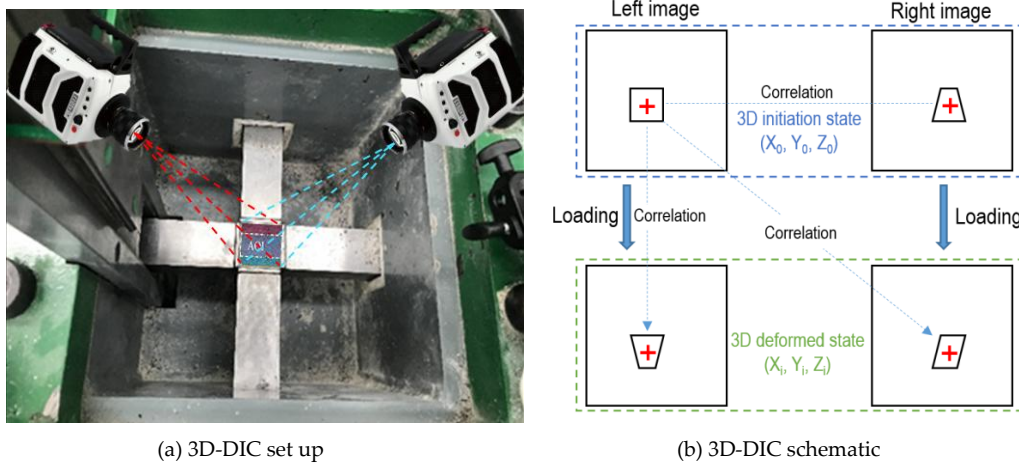


Figure 2: 3D-DIC setup and schematic

### 3.3 Synchrotron X-ray CT system

X-ray computed tomography (CT) system at the Australian Synchrotron is shown in Figure 3, which is adopted to obtain internal fractures of post-failure specimens. X-ray is emitted from X-ray source and passes through the specimen to the detector. Based on the difference of densities inside the concrete specimen, post-failure fractures can be reconstructed. Scanning parameters are set below, X-ray energy 80 keV, pixel size 17.8 $\mu$ m, exposure time 0.75s, and acquisition time 1.5h, which could distinguish the concrete structures and fractures clearly. Schematic and operation process of synchrotron X-ray CT system could refer to literature [16].



Figure 3: X-ray CT system at Australian Synchrotron

## 4. Dynamic strength and fracture characteristics

Typical experimental results (including stress waves in X and Y directions, stress equilibrium and stress-strain curves) are obtained by existed methods [11, 13, 17], as shown in Figure 4. Figure 4(a) shows the curves of incident, reflected and transmitted waves. Stress equilibrium could be satisfied before peak stress, which proves the dynamic stress equilibrium between both ends of specimen before failure. Figure 4(b) gives the results of stress-strain history of axial and lateral stress during dynamic loadings.

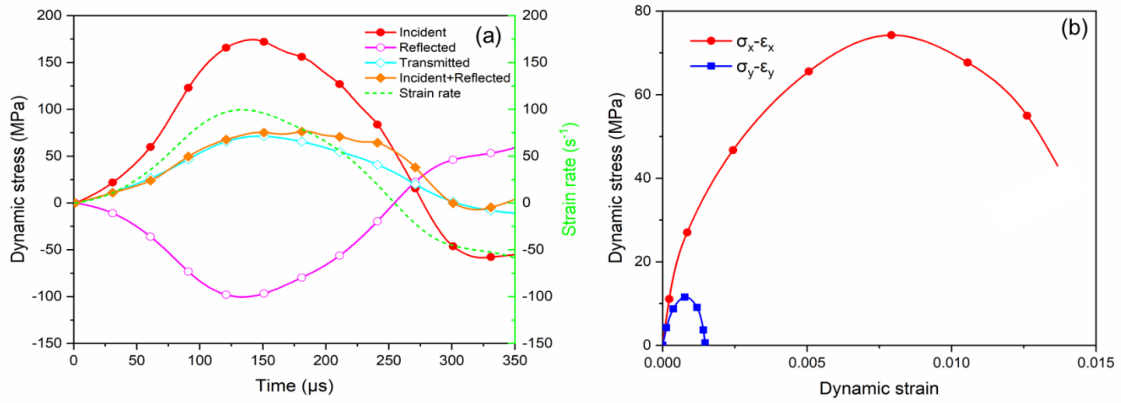


Figure 4: Typical experimental results under impact velocity 16m/s ( $\dot{\epsilon} = 100 \text{ s}^{-1}$ ) and pre-stress (20, 10) MPa: (a) Dynamic stress equilibrium and (b) Stress-strain curves

The effect of confinements on dynamic strength and peak strain of concrete is shown in Figure 5. The dynamic stress decreases with the increasing axial pre-stress  $\sigma_1$  along impact direction, but enhances with the increase of lateral pre-stresses  $\sigma_2$ . Besides, the peak strain shows similar law as the peak stress, which indicates that the specimen with lower dynamic strength reaches its peak stress with less strain. The reason is that microcracks inside specimens are reactivated by pre-stress  $\sigma_1$ , and thus a damaged state is induced. However, the dilatancy for crack growth in the  $\sigma_2$  direction is suppressed by the lateral confining pre-stress.

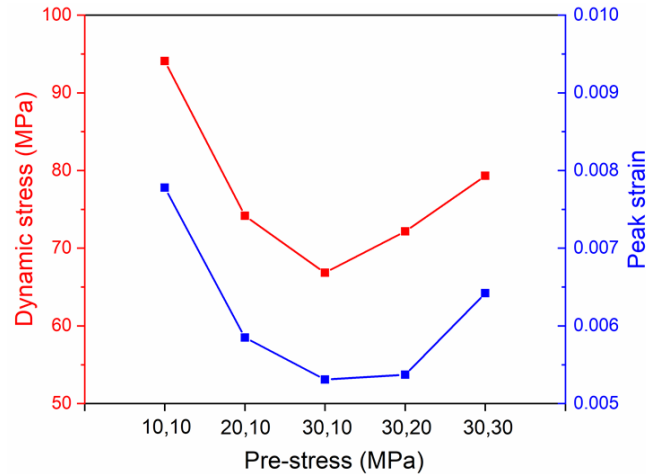


Figure 5: Effect of confinement on dynamic stress and peak strain under impact velocity 16 m/s ( $\dot{\epsilon} = 80\text{-}110 \text{ s}^{-1}$ )

The surface fracture evolution captured by high-speed camera is shown in Figure 6. The result shows in the first 50μs, there is no obvious crack on the specimen surface. Then at 100μs, interfacial cracks and matrix cracks appear near the edges of the specimen. When the peak stress reaches at 150μs, more matrix cracks appear and propagate towards the centre part of specimen. After the peak stress, transgranular cracks appear around 200μs, which indicates aggregate seems to play limited role on peak stress, which is also mentioned in literature [7].

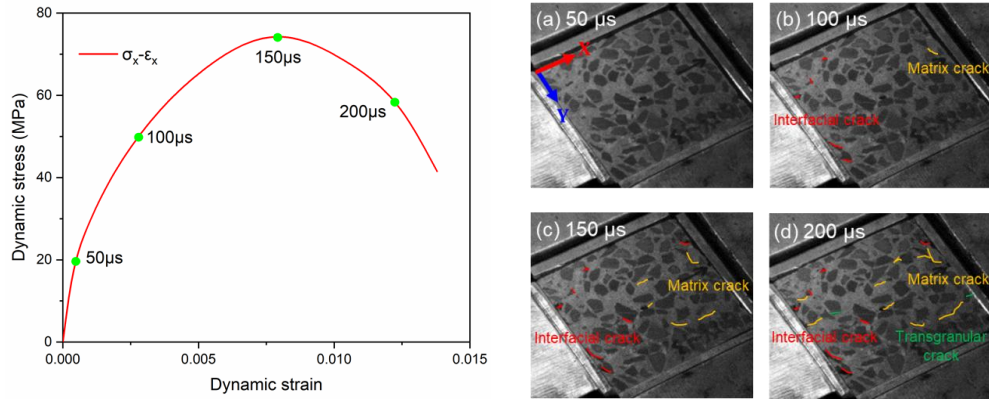


Figure 6: Fracture evolution of concrete under biaxial pre-stress (20, 10) MPa and impact velocity 16 m/s ( $\dot{\epsilon} = 100 \text{ s}^{-1}$ )

Surface fracture evolution is further explained by strain fields with 3D-DIC technique, as shown in Figure 7. At 100 $\mu\text{s}$ , axial strain ( $e_{xx}$ ) localisation can be observed, caused by inhomogeneous deformation around aggregates, which seems to be the cause of interfacial cracks. Lateral strain ( $e_{yy}$ ) localisation also appears at 100 $\mu\text{s}$ , indicating that matrix cracks are induced by lateral tensile strain localisation, which is verified by the results in literature [15]. Then at 150 $\mu\text{s}$ , tensile strain localisation expands along the loading direction, which is consistent with the matrix crack propagation observed in Fig.6(c). At 200 $\mu\text{s}$ , tensile strain localisation further develops.

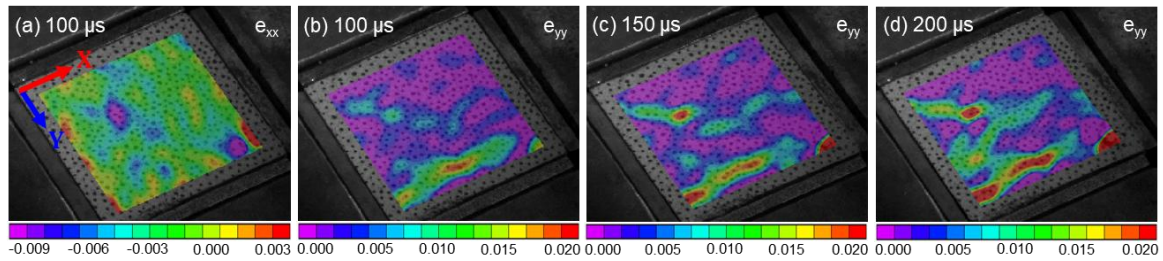


Figure 7: Strain fields of concrete under biaxial pre-stress (20, 10) MPa and impact velocity 16 m/s ( $\dot{\epsilon} = 100 \text{ s}^{-1}$ )

Post-failure fractures obtained by synchrotron X-ray CT technique are shown in Figure 8. It can be seen that fractures concentrate on top and bottom parts of each specimen since deformation develops towards free faces. Fracture area is aggravated with axial pre-stress  $\sigma_1$  but restrained by lateral confinement  $\sigma_2$  since axial pre-stress  $\sigma_1$  reactivates the microcracks which could induce crack propagation more easily, but lateral confinement  $\sigma_2$  limits the reactivation of microcracks. This phenomena is similar to the trend observed with sandstone in literature [11].

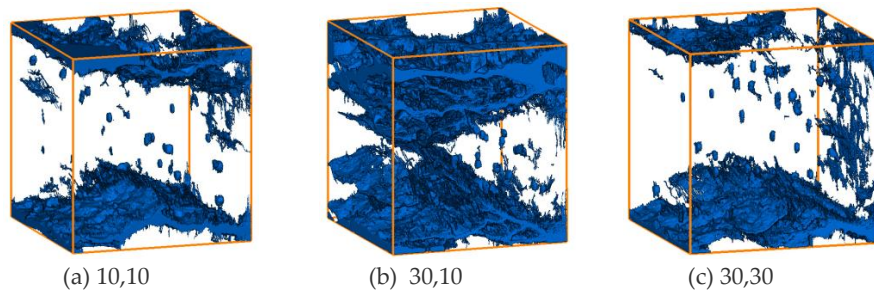


Figure 8: Effect of confinement on fracture of concrete specimen under impact velocity 16 m/s ( $\dot{\epsilon} = 80\sim 110 \text{ s}^{-1}$ )

## 5. Conclusions

The dynamic strength and fracture properties of ordinary concrete under biaxial confinements have been studied by triaxial Hopkinson bar, high-speed camera, 3D-DIC and X-ray CT system. The results show that dynamic strength of concrete is dependent on confinements, and it decreases with axial pre-stress  $\sigma_1$  but increases with lateral pre-stress  $\sigma_2$ . At the stage of pre-failure, interfacial cracks and matrix cracks appear at around 100 $\mu$ s due to axial and lateral strain localisation. Then, matrix cracks propagate mainly along tensile strain localisation areas. At the stage of post failure, fracture area concentrates on top and bottom parts of each specimen due to lateral confinements, and it is aggravated by axial pre-stress  $\sigma_1$  but restrained by lateral pre-stress  $\sigma_2$ .

### Acknowledgments

This work was supported financially by the Australian Research Council (LE150100058). The author would also appreciate the availability of Australian Synchrotron beamtime provided by Australia's Nuclear Science and Technology Organization (ANSTO) grant (NO: AS192/IMBL/14709). The first author is supported by the China Scholarship Council-Monash University (CSC-Monash) project (NO: 201807090100).

### References

1. Zhang QB, Zhao J (2014). A review of dynamic experimental techniques and mechanical behaviour of rock materials. *Rock Mech. Rock Eng.* **47(4)**, 1411-78. (doi: 10.1007/s00603-013-0463-y)
2. Weerheijm, J., and H. W. Reinhardt (1988). Biaxial loading device for dynamic concrete response. *J. Phys. Colloq.* **49(C3)**, 733-738. (doi: 10.1051/jphyscol:19883104)
3. Rieder, K. A., & Mindess, S. (1998). New test method to evaluate the impact behaviour of biaxially confined concrete. *Mater Struct*, **31(10)**, 669-675. (doi: 10.1007/bf02480443)
4. Sukontasukkul, P., Mindess, S. and Banthia, N. (2005). Properties of confined fibre-reinforced concrete under uniaxial compressive impact. *Cement Concrete Res*, **35(1)**, 11-18. (doi: 10.1016/j.cemconres.2004.05.011)
5. Forquin, P., Gary, G., & Gatuingt, F. (2008). A testing technique for concrete under confinement at high rates of strain. *Int J Impact Eng*, **35(6)**, 425-446. (doi: 10.1016/j.ijimpeng.2007.04.007)
6. Forquin, P., Safa, K., & Gary, G. (2010). Influence of free water on the quasi-static and dynamic strength of concrete in confined compression tests. *Cement Concrete Res*, **40(2)**, 321-333. (doi: 10.1016/j.cemconres.2009.09.024)
7. Piotrowska, E., Forquin, P., & Malecot, Y. (2016). Experimental study of static and dynamic behaviour of concrete under high confinement: Effect of coarse aggregate strength. *Mech Mater*, **92**, 164-174. (doi: 10.1016/j.mechmat.2015.09.005)
8. Gary, G., & Bailly, P. (1998). Behaviour of quasi-brittle material at high strain rate. Experiment and modelling. *Eur J Mech A-Solid*, **17(3)**, 403-420. (doi: 10.1016/s0997-7538(98)80052-1)
9. Schmidt, M. J., & Cazacu, O. (2006). Behaviour of cementitious materials for high-strain rate conditions. *J Phys IV*, **134**, 1119-1124. (doi: 10.1051/jp4:2006134171)
10. Forquin, P., Arias, A., & Zaera, R. (2007). An experimental method of measuring the confined compression strength of geomaterials. *Int J Solids Struct*, **44(13)**, 4291-4317. (doi: 10.1016/j.ijsolstr.2006.11.022)
11. Liu, K., Zhang, Q.B., Wu, G. et al. (2019). Dynamic mechanical and fracture behaviour of sandstone under multiaxial loads using a triaxial Hopkinson bar. *Rock Mech. Rock Eng.* **52(7)**, 2175-95. (doi: 10.1007/s00603-018-1691-y)
12. ASTM C192, C. (2018). Standard practice for making and curing concrete test specimens in the laboratory. ASTM International, West Conshohocken.
13. Liu, K., & Zhang, Q. (2019). Dynamic behaviours of sandstone under true triaxial confinements: triaxial Hopkinson bar tests. In *53rd US Rock Mechanics/Geomechanics Symposium*. American Rock Mechanics Association.
14. Xing HZ, Zhang QB, Zhao J (2018). Stress thresholds of crack development and Poisson's ratio of rock material at high strain rate. *Rock Mech. Rock Eng.* **51(3)**, 945-51. (doi: 10.1007/s00603-017-1377-x)
15. Xing, HZ. et al. (2018). Full-field measurement and fracture characterisations of rocks under dynamic loads using high-speed three-dimensional digital image correlation. *Int J Impact Eng*, **113**, 61-72. (doi: 10.1016/j.ijimpeng.2017.11.011)

16. Zhang, G., Ranjith, P. G., Wu, B. et al. (2019). Synchrotron X-ray tomographic characterization of microstructural evolution in coal due to supercritical CO<sub>2</sub> injection at in-situ conditions. *Fuel*, **255**, 115696. (doi: [10.1016/j.fuel.2019.115696](https://doi.org/10.1016/j.fuel.2019.115696))
17. Hokka, M. et al. (2016). Effects of strain rate and confining pressure on the compressive behaviour of Kuru Granite. *Int J Impact Eng*, **91**, 183-193. (doi: [10.1016/j.ijimpeng.2016.01.010](https://doi.org/10.1016/j.ijimpeng.2016.01.010))

# Effects of strain history and temperature on the effective strain rate in titanium alloys

Govind Gour, Longhui Zhang, Nik Petrinic, Antonio Pellegrino\*

*Department of Engineering Science, University of Oxford, Oxfordshire, Parks Road, OX1 3PJ, United Kingdom*

**Keywords:** Dynamic Testing, Pure Titanium, Hopkinson Bar, necking

---

**Abstract:** The determination of the mechanical response of engineering materials subjected to impact loading plays a vital role in determining their application. The high strain rate tensile response of metals is usually investigated by means of the Split Hopkinson Tension Bar (SHTB) apparatus. The interpretation of the obtained results is, however, subjected to the analogous stress and strain uniformity challenges present during quasi static tensile tests. Beyond the onset of necking, strains cease to be uniform along the gauge length and localise around the necking zone. Consequently, the nominal strain rate underestimates the effective strain rate experienced by the material. The analysis of the effective strain rate and stress state beyond the onset of necking has received considerable attention in literature. Several research efforts have focused on the optimisation of the geometry of specimens to be employed for the characterisation of the dynamic tensile response using the SHTB. The current work investigates, systematically, strain history on effective strain rate and thermal softening during dynamic tensile loading. A series of monotonic and strain rate jump tests were conducted and analysed.

## 1. Introduction

The mechanical behaviour of engineering materials is, in general, dependent on the rate of deformation to which there are deformed. Consequently, the employment of metal alloys in transportation and defence requires the dynamic characterisation of their mechanical response to predict deformation and failure during impact loading scenarios such as bird strikes, blade release, crashworthiness analysis and many more.

Titanium and its alloys have been popular in the aviation sector due to their high strength to density ratio coupled with superior corrosion resistance and durability. The response of this class of materials is, in general, dependent on their surface texture, grain size, manufacturing process and subsequent anisotropic properties [1, 2]. The mechanical response in the range of  $10^2 \text{ s}^{-1}$  to  $10^4 \text{ s}^{-1}$  is usually measured by means of Split-Hopkinson Bar apparatuses (SHB) in which the specimen is sandwiched between two bars namely, input and output bars. During SHB experiments, a striker, accelerated by a compressed air piston system, collides with the input bar, thereby generating a stress wave that propagates until reaching the sample. Due to the impedance mismatch between the specimen and the bar, the incident pulse is partially reflected back and partially transmitted through the output bar. The displacements and forces on the specimen can be determined from the recorded strain gauge signals using one dimensional wave analysis and used to calculate nominal stresses and strains within the specimen.

The dynamic tensile experiments on ductile alloys, however, introduce additional technical difficulties. Beyond necking, deformations cease to be uniform along the gauge length. Consequently, the computation of stresses and strains using their nominal or logarithmic form poorly approximates the true stress and true strain in the necked region of the specimen [3, 4]. In fact, after necking initiates, strain localises around the minimum cross section and cannot be related anymore to the gauge length. The calculation of the true stress and true strain in the post-necking phase is possible only if the diameter evolution of the cross section is accurately measured for example using high-speed imaging. Additionally, as the specimen undergoes necking the gradual increase in stress triaxiality requires the measured true stresses to be transformed to equivalent stresses.

Moreover, high-speed machining of titanium alloys faces many challenges owing to their low thermal conductivity and high chemical reactivity with the cutting tool. Its low thermal conductivity increases the temperature at the cutting edge of the tool leading to rapid wear [5]. In the experimental investigation [6] commercial Ti-6Al-4V was investigated from room temperature to  $1000^\circ\text{C}$  at the average strain rate of the  $1800 \text{ s}^{-1}$  and the result indicated strong thermal softening

..

\*Author for correspondence Dr Antonio Pellegrino (antonio.pellegrino@eng.ox.ac.uk).

†Present address: Department of Engineering Science, University of Oxford, Oxfordshire, Park Road, OX1 3PJ, United Kingdom

with allotropic transformation from initial hcp/bcc to full bcc ( $\beta$ ) structure. It was confirmed with microstructural analysis formation. Experimental investigations exploring the temperature effect on the strain localisation, are however, scarce in the literature. Hence, the current research work will also explore external temperature effect on necking experimentally. The present research work investigates, systematically, the effects of strain history on the effective strain rate and thermal softening during the dynamic tensile loading. A series of monotonic, and strain rate jump tests are conducted and analysed. The evolution of the nominal and effective strain rate (True strain rate) was measured using digital image correlation and compared. Moreover, the effect of the temperature on the Ti-6Al-4V under high strain rate is explored experimentally.

## 2. Experimental setup and result

This section illustrates the experimental techniques used to pre-strain cylindrical samples, conduct high strain rate tests using a Split Hopkinson Tensile Bar (SHTB) and control the temperature of the samples.

### 2.1 Experimental technique apparatus

The experimental investigation on Ti-6Al-4V samples was performed on standard cylindrical specimens illustrated in Figure 1. In the first experimental set, a batch of specimens were prestrained (10%) using a screw driven Zwick mechanical test machine equipped with a 20kN load cell. A speckle pattern on the specimen was created using a white background and applying black dots randomly. The prestrained measurements were taken using high definition cameras equipped with low distortion lenses to acquire high-resolution images. Later, the acquired images were analysed using the commercial software GOM Aramis<sup>†</sup> focusing in the gauge section of the specimens. The specimens were strained until 10% before testing at high strain rate.

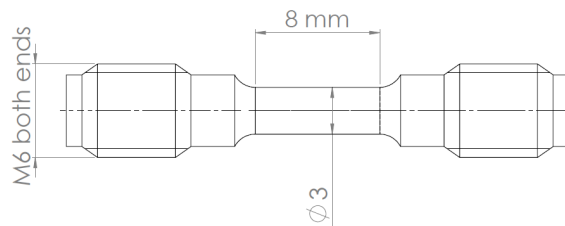


Figure 1: Geometrical description of the used specimens of Ti-6Al-4V.

High rate tensile experiments were carried out using the Hopkinson Bar apparatus described in [7] and schematically is shown in Figure 2. The input and output bars of the SHTB were made of titanium, with solid cross section of the diameter 10 mm with length of 2.7 m. The experimental setup comprised also of a high-speed camera typically used at 400~500 kfps to capture the deformation history and strain localisation. With classical split Hopkinson bar analysis, stress-strain histories can be calculated using the procedure detailed by Gray [8].

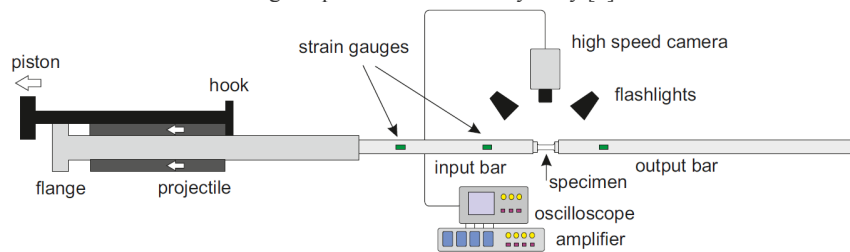


Figure 2: Schematic of split Hopkinson pressure tensile bar.

During plastic deformation, beyond necking, the deformation ceases to be uniform along the gauge length and the computation of the true stresses and strains obtained using their logarithmic form constitutes an inaccurate approximation of the real material behaviour, especially in the localized region of the specimen. Moreover, beyond the onset of necking, strain becomes localised around the minimum cross section and it cannot be related to the gauge length. A complete

<sup>†</sup><https://www.gom.com/metrology-systems/aramis.html>

evaluation of true stress-strain curve can only be obtained if the cross section radius is measured accurately and the following equation must be used:

$$\epsilon_{true} = 2 \ln\left(\frac{r_0}{r}\right) \tag{1}$$

$$\sigma_{true} = \frac{F}{\pi r^2} \tag{2}$$

$$\dot{\epsilon}_{true} = \frac{d}{dt} \left[ 2 \ln\left(\frac{\phi_0}{\phi}\right) \right] \tag{3}$$

The nominal strain rate underestimates the effective strain rate experienced by the materials after the strain localisation. This is particularly evident in the ductile metal alloys. The effective strain rate can be estimated by differentiating true strain with respect to the time interval. Generally, the effective strain rate can be much higher in magnitude than nominal strain rate. Furthermore, for temperature effect, the specimens were heated up to high temperatures using a feedback controlled induction heating system. In order to guarantee a uniform heating, the specimens were heated imposing a temperature rate of approximately 30 Celsius degrees per second, monitored by means of type K thermocouples.

### 2.2 Pre-strain Effect on dynamic strain localisation of Ti-6Al-4V

The Ti-6Al-4V specimens were prestrained (10%) in quasi-static conditions ( $1 \cdot 10^{-3} \text{ s}^{-1}$ ) using a Zwick mechanical test machine. Later, these prestrained samples were tested at high strain rate ( $\sim 3000 \text{ s}^{-1}$ ) using the SHTB. Figure 3 (a) compares the diameter reduction against engineering strain of pre-strained (initially prestrained and later tested using SHTB) and monotonically (directly tested using SHTB) dynamically loaded specimens. Figure 3 indicates that prestrained specimen have higher elongation to failure. Under monotonic condition, the specimens failed at engineering strains included between 14% and 17% whereas the prestrained samples failed at nominal strains included between 19% and 21%. It is also clear that, in the case of monotonic tests the rate of reduction of the diameter at engineering strains in the proximity of failure is higher than in in the case of pre-strained specimens. As stated earlier [5] that the Ti-6Al-4V possess low thermal conductivity which restrain the dissipation of heat (heat generated during the plastic deformation) rapidly to the environment. It is, therefore, reasonable to believe that the temperature increment caused by adiabatic heating in the material increases its ductility, exacerbating the rate of reduction of the diameter in the necking area, particularly at relatively large nominal strains. This effect appears to be mitigated for pre-strained specimens. Figure 3 (b) compares the effective (true strain rate) and nominal strain rates measured during monotonic high rate tension tests on Ti6Al4V samples. Although, the deformation rate varies slightly for different experiments it is evident that, as the necking begins, the true strain rate history diverges sharply from the corresponding nominal strain rate history.

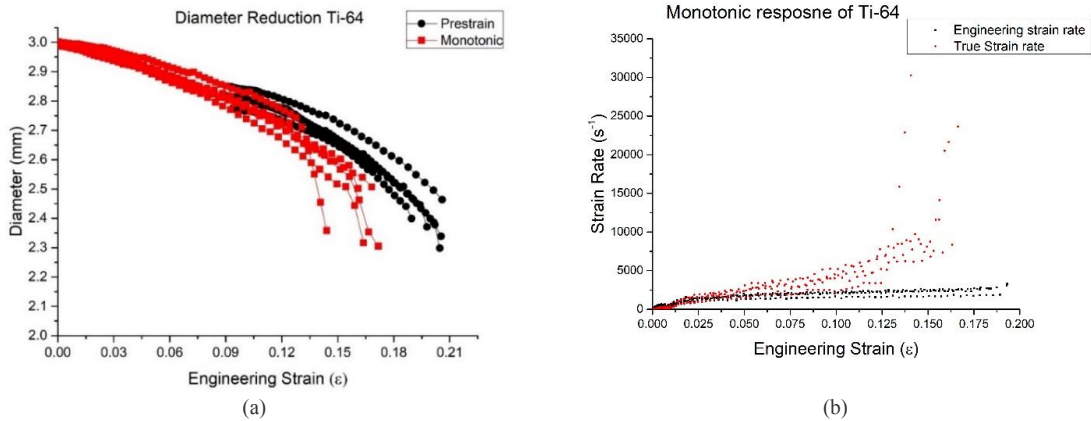


Figure 3: (a) Diameter reduction for the prestrain-monotonic Ti-6Al-4V, (b) comparison between nominal and effective strain rate.

The dependence of the Taylor-Quinney coefficient on the dynamic loading mode and on the investigated material was examined in [9] using a high-speed infrared radiation detector to measure the temperature evolution on the tested

specimens. The concurrent effects of dynamic strain localisation and adiabatic heating were recently assessed in [10]. An extensive series of quasi-static pre-strain experiments followed by high strain rate tensile deformation constitute the experimental baseline to determine the temperature history in necked area of the specimen. The Taylor-Quinney coefficient could then be determined using material models which are able to represent accurately strain localisation in ductile alloys [11] and reverse engineering procedures.

### 2.3 Effect of temperature on the dynamic behaviour and strain localisation of Ti-6Al-4V

This section reports the effect of the temperature (200°C, 300°C, and 400°C) on the mechanical performance and strain localisation of Ti-6Al-4V samples tested at high strain rate. The rise in temperature increases the ductility of the alloy, increasing the engineering strain to failure to 20% at 200°C, and 24% at 400°C). Figure 4 (a) shows the engineering stress-strain curves obtained under high deformation rate at various temperatures. It is evident that the temperature rise in the specimen influences the behaviour, reducing the flow stress of Ti-6Al-4V. It is also clear that the ductility increases at higher temperatures. The average strain rate measured during the high temperature experiments was in the order of 1500 s<sup>-1</sup>. The yield stress reduces progressively from 950 MPa at 200°C to approximately 775 MPa at 300°C degrees and 625 MPa at 400°C. Figure 4 (b) comprises the diameter reductions at room temperature to elevated temperature (up to 400°C). It is evident that at the elevated temperature, the cross section reduces (increment in the strain localisation) with increment in the elongation.

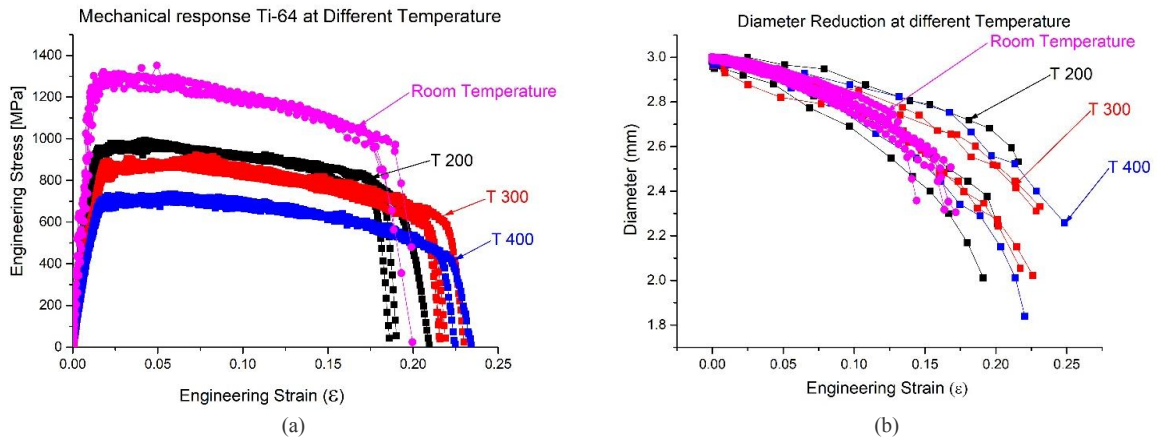
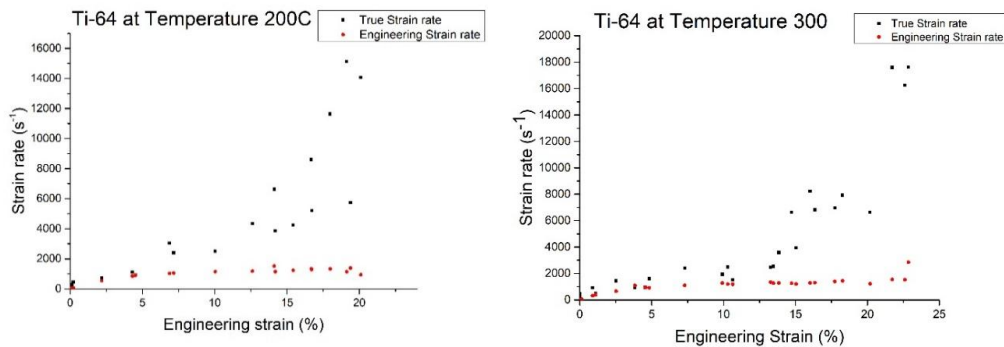


Figure 4: Mechanical response of the Ti-6Al-4V at different temperatures, (b) radial reduction against engineering strain.

Figure 5 shows an initial comparison between engineering and true strain rate rates of Ti-6Al-4V specimens tested at various temperatures. Similarly, to what observed at room temperature, it is clear that beyond necking the true strain rate diverges from the nominal strain rate reaching values up to one order of magnitude higher than the latter at strains in the proximity of failure.



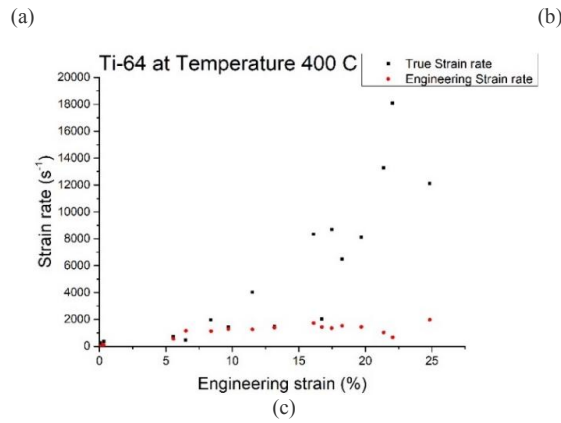


Figure 5: Comparison of nominal and true strain rate of the Ti-6Al-4V at various temperature.

Figure 6 summarises the overall influence of the various testing conditions on dynamic strain localisation plotting the average values of the final necking diameter for all experiments conducted in this study. It is clear that both pre-strain and temperature conditions affect the final minimum diameter in the necking cross section.

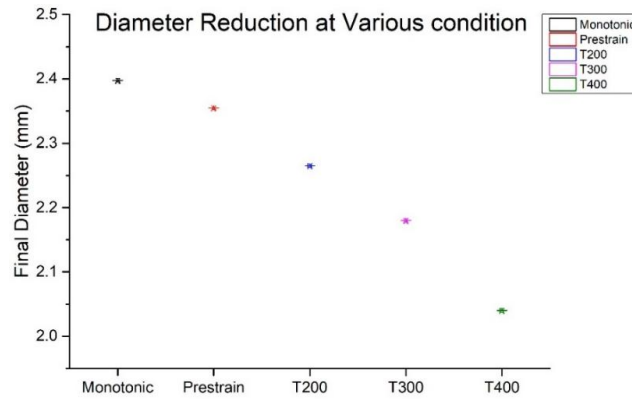


Figure 6: Diameter reduction of the cylindrical Ti-6Al-4V under various conditions.

### Conclusions and future work

- The initial experimental result on the prestrained specimens indicate an increment in the engineering strain to failure and an effect on the dynamic strain localization history and final necking diameter reduction at failure. The effect of the pre-strain on different materials will be explored with additional experiments at several pre-strain conditions. These experiments will constitute the experimental baseline to estimate via reverse engineering the temperature evolution in the necked area of the specimen.
- The effect of temperature on ductility and dynamic necking was assessed. The ductility of Ti-6Al-4V is found to be increasing with temperature, while the flow stress drops significantly from room temperature to 400 Celsius degrees.
- Future numerical modelling will aim at understanding the effects of stress triaxiality and adiabatic heating on the localized deformation and failure. Microstructural micrographs will complement the experimental results and provide insights on the failure mechanisms.

## Acknowledgement

The authors would like to thank Mr Stuart Carter and Mr Jeffrey Fullerton for manufacturing the specimens and Dr David Townsend for helpful suggestions about the writing.

## References

1. Tuninetti, V. and A.M. Habraken, *Impact of anisotropy and viscosity to model the mechanical behavior of Ti–6Al–4V alloy*. Materials Science and Engineering: A, 2014. **605**: p. 39-50.
2. Gilles, G., et al., *Experimental characterization and elasto-plastic modeling of the quasi-static mechanical response of TA-6V at room temperature*. International Journal of Solids and Structures, 2011. **48**(9): p. 1277-1289.
3. Mirone, G., *The dynamic effect of necking in Hopkinson bar tension tests*. Mechanics of Materials, 2013. **58**: p. 84-96.
4. Mirone, G., D. Corallo, and R. Barbagallo, *Experimental issues in tensile Hopkinson bar testing and a model of dynamic hardening*. International Journal of Impact Engineering, 2017. **103**: p. 180-194.
5. Che-Haron, C.H. and A. Jawaid, *The effect of machining on surface integrity of titanium alloy Ti–6% Al–4% V*. Journal of Materials Processing Technology, 2005. **166**(2): p. 188-192.
6. Gangireddy, S. and S.P. Mates, *High Temperature Dynamic Response of a Ti-6Al-4V Alloy: A Modified Constitutive Model for Gradual Phase Transformation*. Journal of Dynamic Behavior of Materials, 2017. **3**(4): p. 557-574.
7. Gerlach, R., C. Kettenbeil, and N. Petrinic, *A new split Hopkinson tensile bar design*. International Journal of Impact Engineering, 2012. **50**: p. 63-67.
8. GRAY III, G.T., *Classic split Hopkinson pressure bar testing*. 2000(In: Kuhn H, Medlin D (eds) ASM Handbook Vol 8: mechanical testing and evaluation. Materials Park, OH, ASM International): p. 462-476.
9. Rittel, D., L. Zhang, and S. Osovski, *The dependence of the Taylor–Quinney coefficient on the dynamic loading mode*. Journal of the Mechanics and Physics of Solids, 2017. **107**: p. 96-114.
10. Mirone, G., R. Barbagallo, and F. Giudice, *Locking of the strain rate effect in Hopkinson bar testing of a mild steel*. International Journal of Impact Engineering, 2019. **130**: p. 97-112.
11. Zhang, L., et al., *Rate dependent behaviour and dynamic strain localisation of three novel impact resilient titanium alloys: Experiments and modelling*. Materials Science and Engineering: A, 2020. **771**: p. 138552.

# High-speed sheet metal forming: Numerical study of high speed Nakajima testing

Luca Corallo, Patricia Verleysen

*“Department of Electromechanical, Systems and Metal Engineering,  
Technologiepark Zwijnaarde 46, Gent, 9052 Zwijnaarde, Belgium, 0000-0003-2471-5177”*

**Keywords:** Forming, high strain rates, material characterization

---

## Abstract

In recent years, the forming community has shown an increased interest in the effect of strain rate on the formability of sheet metals. The assessment of sheet metal formability in dynamic deformation conditions requires the development of experimental techniques which allow to decouple the material response from the test related parameters. In this paper, results of numerical finite element simulations of dynamic Nakajima experiments on a dog bone sample are presented. The simulations are performed in order to verify the reliability of the technique under different frictional contact conditions and punch velocities. The necking locus, strain path linearity and stress state evolution are extracted and investigated in-depth. The numerical study highlighted several drawbacks which led to the conclusion that dynamic Nakajima tests might not be the most appropriate way to investigate sheet metal formability at high strain rates.

## 1. Introduction

Sheet metal forming is commonly used in industry to produce metal components for different applications. The formability of a metal sheet is generally quantified by tests which impose different strain paths to material samples. The sheet metal forming community often adopts the forming limit diagram (FLD) developed by Keeler et al. and Goodwin [1, 2]. The shape and location of the FLD in the principal strain space define the boundary between strain states that are always free of necks, i.e. below the FLD, from those prone to necking and splitting. Several studies showed that the formability of sheet metals can significantly be improved by increasing the deformation rate. Balanethiram et al. [3] observed that the formability in biaxial stretching conditions can increase with a factor of almost three when the material is tested at high strain rates. Wood [4] found that the forming limit can improve by a factor of two or more when performing experiments in dynamic loading conditions. In quasi-static loading conditions, formability is experimentally assessed by means of techniques described in the ISO 12004-2:2008 standard, such as Nakajima and Marciniak tests. However, the techniques still have no well-defined dynamic counterparts. The strain rate effect at the right-hand side of the FLDs is investigated by electro-magnetic, electro-hydraulic and explosive forming. A few researchers introduced new approaches which combine Hopkinson bar experiments with existing standard techniques. Sasso et al. [5] developed a testing device combining the split Hopkinson pressure bar (SHPB) with a Nakajima test, Gilat et al. [6] modified a SHPB to perform dynamic punch tests, Grolleau et al. [7] proposed an adaptation of the SHPB apparatus to perform dynamic bulge tests. However, all these approaches still have limitations in terms of linearity and variety of imposed strain paths. Deviations from the ideal linear strain path are often caused by experimental factors such as contact conditions, friction, lubrication, clamping system, and many more [8]. Indeed, the linearity of the strain path is one of the most important requirements for the determination of FLDs. This paper investigates the reliability of dynamic Nakajima tests using dog bone material samples to characterize sheet metal formability in dynamic loading conditions. Numerical finite element simulations in Abaqus/Standard are performed considering different frictional contact conditions and punch velocities. Necking onset, strain path linearity and evolution of the stress components are carefully examined. The reliability of dynamic Nakajima tests as experimental technique to characterise sheet metal formability in dynamic loading conditions is broadly discussed based on the numerical results.

Luca Corallo (Luca.Corallo@UGent.be)  
Department of Electromechanical, Systems and Metal Engineering,  
Technologiepark 46, Gent, 9052 Zwijnaarde, Belgium,

2. Methods

Numerical simulations of Nakajima tests are performed using the commercial finite element program Abaqus/Standard. The simulations aim at reproducing actual Nakajima experiments in which a hemispherical rigid punch penetrates a sheet metal fixed to a rigid die. Boundary conditions are imposed to replicate the actual experimental conditions. Due to limitations in deformation capacity typical for dynamic tests, the dimensions of the components, shown in Figure 1, are reduced compared to the guidelines of ISO 12004-2:2008. The sample material is Ti-6Al-4V, which has been studied in-depth at the DyMaLab research group of Ghent University [9]. Associative J2-plasticity with isotropic hardening is adopted to describe the material behaviour. The strain rate and temperature dependent hardening is modelled by the Johnson-Cook hardening law, the parameters are reported in Table 1.

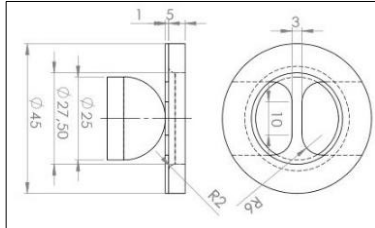


Figure 1: Dimensions components Dynamic Nakajima simulations

Table 1: Mechanical properties Ti-6Al-4V [9].

E	v	$\rho$	A	B	n	m	Melting temperature	Room Temperature
MPa	-	Ton/mm <sup>3</sup>	MPa	MPa	-	-	°C	°C
117000	0.3	4.4E-9	951	892	0.7	0.71	1630	20

A recent approach proposed by Martinez-Donaire et al. [10] is used to detect the time at which necking occurs. As shown in Figure 2, the onset of necking is detected by monitoring the strain rate evolution at a point B external to the necking region. The time at which the strain rate in B reaches its maximum value is used as criterion to identify the time at necking during the simulation; hence to extract the strain and strain rate values at the necking section. The methodology is local and does not take into account experimental conditions such as sample geometry, punch shape, contact and friction. Different friction coefficients and punch velocities, are adopted in order to establish their influence on the mechanical response of the sheet metal. Three simulations with fixed punch velocity of 5m/s and different friction coefficients: 0, 0.04 and 0.3, are executed to investigate how friction affects the necking position, the strain path linearity, the principal in plane stress components and the strain rate level. Strain path linearity is estimated by fitting major and minor in plane strain components using a linear fitting function, characterized by a correlation coefficient R, which gives an indication of the linearity. The analysis is repeated for three elements placed at the necking section through the sheet thickness: at the external surface, at the internal surface in contact with the punch and, finally, at the middle section of the sheet. The study on the stress components is reduced to the elements at the external surface and at the middle section of the sheet. Furthermore, the effect of the test velocity is studied by repeating the simulation for three different punch-velocities: 5,10 and 15m/s, while the friction coefficient is kept constant at 0.04.

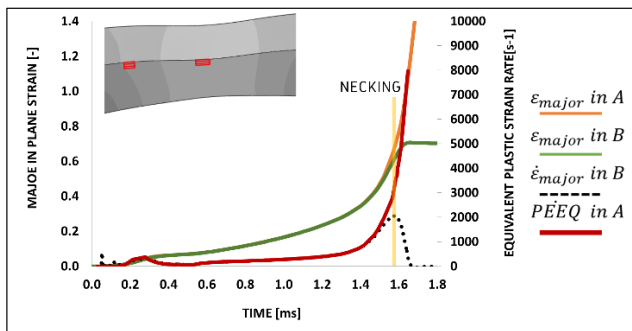


Figure 2: Martinez-Donaire approach to detect the time at onset of necking for a punch velocity of 5m/s without friction

Table 2: Summarizing table: results simulations punch velocity 5m/s

Friction coefficient	Time at necking Martinez-Donaire approach [ms]	Major in plane strain at necking in A [-]	Equivalent plastic strain rate at necking in A [s <sup>-1</sup> ]
-	1,58	0,70	3300
0,04	1,71	0,68	2050
0,3	1,44	0,61	1550

### 3. Results

#### 3.1 Necking detection

The use of the Martinez-Donaire criterion is illustrated in Figure 2 which shows the major in plane strain and strain rate at a point B close to the neck, and the plastic equivalent strain (PEEQ) and major strain in the neck. All values are taken at the external surface of the sheet. The time, strain and strain rate at the onset of necking are summarized in Table 2 for different friction conditions and a punch velocity equal to 5m/s. The position of the necking section is post-mortem detected. The effect of the friction on the strain localization is further investigated by plotting the initial position of the nodes A,B,C and D which delimit the necking as showed in Figure 3a. In Figure 3b, an increment of the friction coefficient makes the necking locus shift from the centre of the specimen to the shoulders of the sample.

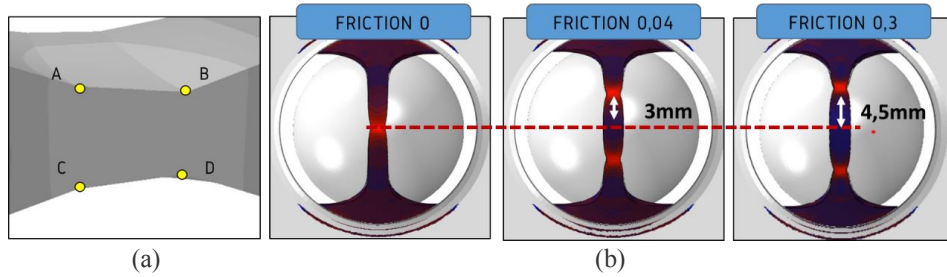


Figure 3: (a)Nodes delimiting the necking, (b) Necking locus shift

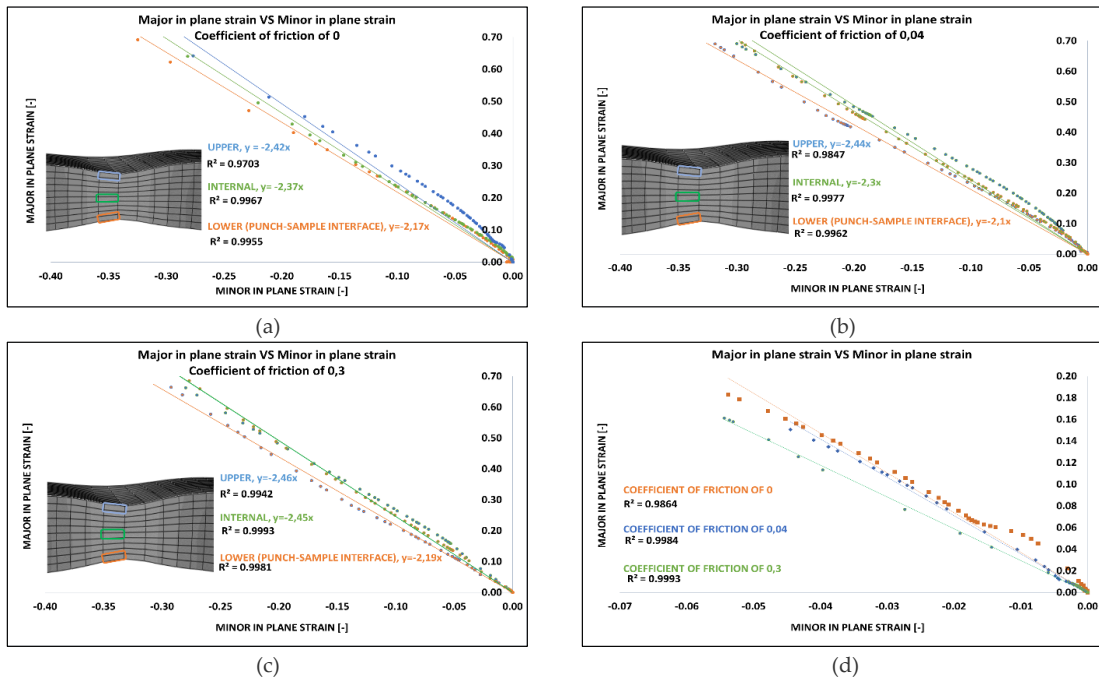


Figure 4: Study of the strain path for different friction coefficients 0(a),0.04(b),0.3(c). Strain path analysis in small strain regime(d)

#### 3.2 Strain path linearity and stress components evolution

In Figure 4 the major versus minor in plane strains in the neck section are presented till the onset of necking together with a linear fit. Results are presented for the three friction conditions in three different elements through the sheet thickness. The most pronounced mismatch with the linear fit is observed for the element

placed at the upper surface of the sheet metal, for which R is around 0.97. Only slight deviations of the slope, about 3 degrees, are observed comparing the linear paths for the elements through the sheet thickness. The evolution of the stress components at the upper surface (circular dot) and internal section (uniform line) in the neck are reported in Figure 5a, b and c. All the curves in Figure 5 show a peak corresponding to the instant at which the contact between the punch and sheet metal starts. The peak value depends on the combination of different factors: contact forces, punch curvature, and friction coefficient. In addition, the stress component at the external surface of the specimen is zero, while moving towards the punch-sample interface, it becomes more and more influent.

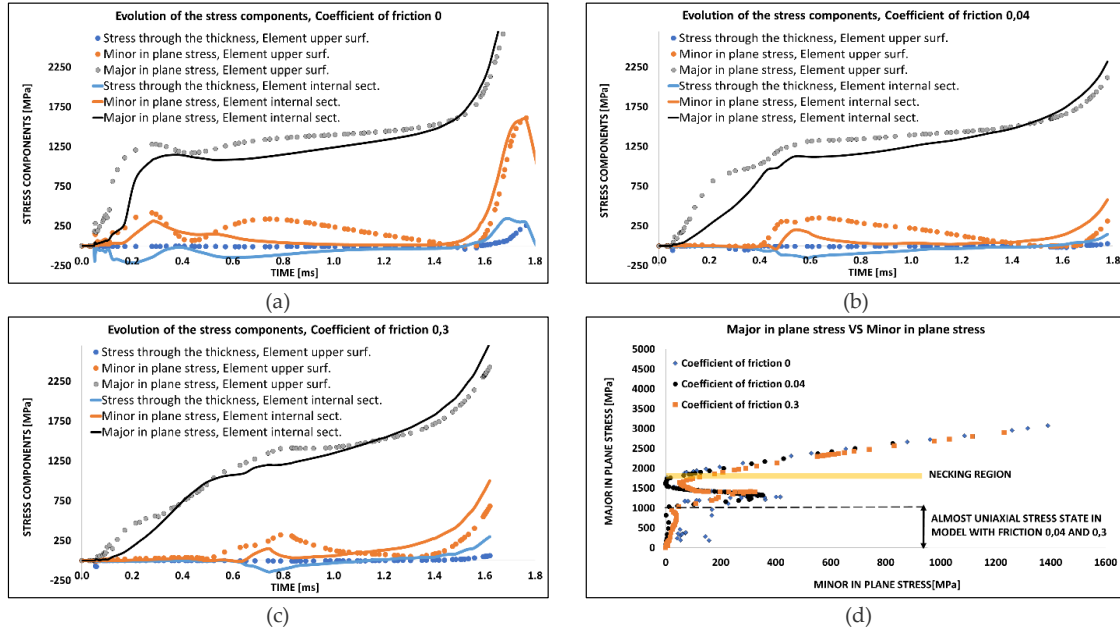


Figure 5: Stress components evolution at the upper surface (circular dot) and internal section (uniform line) in the neck for different friction coefficients : 0 (a), 0.04(b), 0.3(c). Figure 5d: stress path element at the upper surface of the neck for different friction coefficients.

### 3.3 Effect of the punch velocity

The comparison of the punch force–displacement curves in Figure 6 shows just a small amplification of the force level due to the increase of the punch velocity. Since the force-displacement curves take into account the global response of the specimen, the curves cannot be used to characterise the mechanical response of the metal sheet. The Martinez-Donaire criterion is applied to determine the major in plane strain and equivalent plastic strain rate at the necking onset for each punch velocity. The results of the simulations are summarized in Table 3.

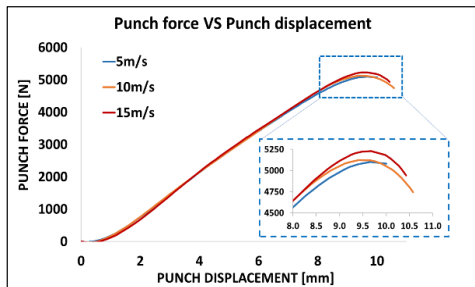


Figure 6: Punch force-displacement for initial punch velocities of 5, 10 and 15 m/s

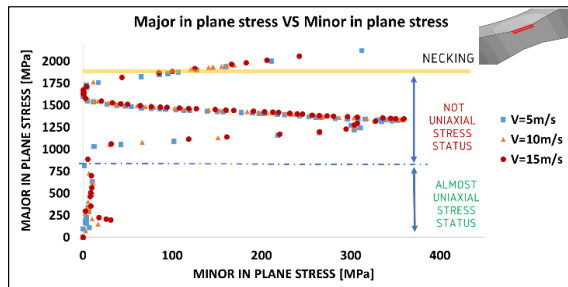


Figure 7: Major in plane stress versus minor in plane stress for initial punch velocities of 5, 10 and 15 m/s

**Table 3: Summarizing table: results simulations for three different punch velocities 5,10,15 m/s**

Punch velocity [m/s]	Max. Punch Force [N]	Time at the Max. punch force [ms]	Time at necking Martinez-Donaire approach [ms]	Major in plane strain at necking [-]	Equivalent plastic strain rate at necking [ $s^{-1}$ ]
5	5120	1,93	1,71	0,68	2000
10	5180	0,96	0,85	0,7	4050
15	5215	0,64	0,57	0,7	6350

## 4. Discussion

### 4.1 Necking detection

From an experimental point of view, the necessity of controlling and monitoring the friction coefficient introduces huge limitations, especially in dynamic loading conditions. Indeed, it is known that friction is highly dependent on the relative slipping velocity between the surfaces involved in the contact. Comparing the results for the frictionless contact conditions with the results for higher friction coefficients, a small reduction of the major in plane strain is observed, whereas the equivalent plastic strain rate is almost halved. The introduction of a friction coefficient as low as 0.04 results in a reduction of the equivalent plastic strain rate from  $3300s^{-1}$  to  $2050s^{-1}$ . A value of 0.04 is considered to be an achievable technological lower limit for friction in forming experiments. In a Nakajima test, the friction between punch and sheet sample is different in every point and it changes during the test. Even for the friction coefficient of 0.04, the necking section already shifts away from the centre. As shown in the results section, friction conditions along the sample gage length cannot be neglected.

### 4.2 Strain path linearity and stress components evolution

The strain path at the necking section, on the sample surface and through the thickness, is almost linear: the discrepancies between the linear fit functions are negligible. However, restricting the study to the small strain domain ( $\epsilon_{major} < 0.15$ ,  $\epsilon_{minor} < -0.05$ ), see Figure 4d, for the element at the upper surface, the slopes of the strain paths deviate from the slopes obtained when the strains till necking are considered, see Figure 4a,b and c. The deviations are even more pronounced during the initial stage of the simulations at which the punch starts deforming the specimen. Friction has a double effect on the stress components evolution. On one hand, the resulting tangential forces modify the stress state at the centre of the sample, on the other hand, friction results in a stress concentration away from the centre, and therefore the shift of the neck to a location with a different loading history. Moreover, the non-uniform stress distribution through the sheet thickness and the changing triaxiality constitute two other important model outcomes. The stress through the thickness, which is zero for the element at the external surface, becomes more and more relevant moving towards the sample-punch interface. In addition, as shown in Figure 5d, the principal in plane stress components evolve in a non-proportional way and the uniaxial loading condition is never reached, see . The stress components study reveals other shortcomings of the Nakajima test. First, the stress state is not uniform along the gage length of the sample, and even not through the sheet metal thickness. Second, the components of the stress evolve non-proportional. Last, the friction and related tangential forces drastically affect the stress in the entire sample.

### 4.3 Effect of the punch velocity

The punch velocity does not influence the major in plane strain which is almost the same for all the simulations. Consequently, since the time to necking is proportional with the punch velocity, also the equivalent plastic strain rate in the neck increases proportionally with the punch velocity. The determination of the necking locus reveals that for all the simulations the neck appears at the same position: the punch velocity does not play any role on the strain localization. The strain and stress path analysis does not show any influence of the punch velocity: in Figure 7 the stress paths perfectly coincide. Thus, it can be concluded that the punch velocity in a Nakajima experiment only affects the obtained strain rate, and that the variables previously considered, i.e. necking locus, strain path and stress components, are not significantly changed.

## 5. Conclusions

The numerical study reveals that the characterization of sheet metal formability in dynamic loading conditions, by means of Nakajima experiments on dog bone samples, has serious shortcomings. Indeed, based on the analysis of the numerical simulation results, the following can be concluded:

- Friction affects the necking localization together with the strain rate amplitude. Indeed, even when an extremely low friction coefficient of 0.04 is adopted, the strain distribution and its evolution in the sample drastically deviate from those obtained assuming frictionless contact between punch and sample. The influence of friction on the location of the neck can clearly not be ignored. Additionally, also the FLD value, experimentally determined at the onset of necking, is dependent on the friction. Moreover, the strain path is not perfectly linear, certainly not in the early stages of the deformation.
- To assess the formability, the forming community very often exclusively focuses on the in plane strain components. The numerical investigation shows that, even if good results are obtained in the strain space in terms of linearity of the principal strain components, a totally different image is obtained in the stress space. Indeed, the stress components evolve non-proportionally. Moreover, the stress varies along the sample gage length and through the specimen thickness.
- The punch velocity does not play any role in the localization of the strain, as well as in the strain path linearity and the evolution of the stress components. On the other hand, the increment of the punch velocity leads to a proportional increase of the local strain rate at the neck. In real tests, however, the friction coefficient depends on the relative velocity between the punch and the sample. Therefore, full understanding of the test outcome requires experimental campaigns to determine the evolution of the friction in order to calibrate a contact model within the FE software.

As a general conclusion, it can be stated that the numerical study on dynamic Nakajima tests shows that the test outcome is dominated by test conditions rather than by the material behaviour. As such, the material response aimed at is masked by test conditions. Moreover, friction which is difficult, yet impossible, to control has a significant influence on the sample response, including the strain state in the neck.

## Acknowledgments and funding statement

This research is supported by the Research Foundation Flanders-FWO, application number 1SC5619N.

## References

1. S. P. Keeler and W. A. Backhofen. 1963. "Plastic Instability and Fracture in Sheet Stretched over Rigid Punches" *ASM Transactions Quarterly*, Vol. 56, No. 11, pp. 25-48.
2. G. M. Goodwin. 1968. "Application of Strain Analysis to Sheet Metal Forming in the Press Shop" *SAE Paper*.
3. Balanethiram VS, Daehn GS (1992) Enhanced formability of interstitial free iron at high strain rates. *SCRIPTA METALL MATER* 27:1783–1788. ([https://doi.org/10.1016/0956-716X\(92\)90019-B](https://doi.org/10.1016/0956-716X(92)90019-B))
4. Wood WW (1967) *Experimental mechanics at velocity extremes —Very high strain rates: Study covers tensile and compression specimens, spherical bulging and cylindrical bulging for a wide variety of materials*. *EXP MECH* 7:441–446. (<https://doi.org/10.1007/BF02326303>)
5. Sasso M, Mancini E, Chiappini G, et al (2018) Adapted Nakajima test to evaluate dynamic effect on strain distribution and dome height in balanced biaxial stretching condition. *INT J MECH SCI* 148:50–63. (<https://doi.org/10.1016/j.ijmecsci.2018.08.024>)
6. Gilat A, Seidt JD, Hammer JT, Liutkus TJ Development of Dynamic Punch test with DIC for Verification of Simulations with MAT224. 5
7. Grolleau V, Gary G, Mohr D (2008) Biaxial Testing of Sheet Materials at High Strain Rates Using Viscoelastic Bars. *EXP MECH* 48:293–306. (<https://doi.org/10.1007/s11340-007-9073-5>)
8. Zhang L, Min J, Carsley JE, et al (2017) Experimental and theoretical investigation on the role of friction in Nakajima testing. *INT J MECH SCI* 133:217–226. (<https://doi.org/10.1016/j.ijmecsci.2017.08.020>)
9. Verleysen P, Peirs J (2017) Quasi-static and high strain rate fracture behaviour of Ti6Al4V. *INT J IMPACT ENG* 108:370–388. (<https://doi.org/10.1016/j.ijimpeng.2017.03.001>)
10. Martínez-Donaire AJ, García-Lomas FJ, Vallellano C (2014) New approaches to detect the onset of localised necking in sheets under through-thickness strain gradients. *MATER DESIGN* 57:135–145. (<https://doi.org/10.1016/j.matdes.2014.01.012>)

## Highways and byways in the history of high rate mechanical testing

Stephen M. Walley\*

SMF Fracture and Shock Physics Group, Cavendish Laboratory, J.J. Thomson Avenue, Cambridge CB3 0HE,  
United Kingdom ORCID ID 0000-0002-5399-6185

**Keywords:** Hopkinson pressure bar, Taylor impact, high strain rate testing

**Abstract:** Two exhaustive studies of the history of the mechanical testing of materials have been published in book form. The first entitled *The Experimental Foundations of Solid Mechanics* was written by J.F. Bell in 1973. Bell's book is mostly about low rate testing, but it also surveys the development of high rate tests from the 17<sup>th</sup> century onwards. The second (*History of Shock Waves, Explosions and Impact*) by Krehl (2009) is concerned solely with the shock-loading of materials. Although indebted to these books, I do not seek in this paper to summarise their scholarship, but rather to take an idiosyncratic ramble through about a century of the mechanical testing literature from around 1850 to about 1950 in order to outline the background to where we are today.

**Note on Imperial units of measurement:** Some quotes in this article are taken from British and American sources where Imperial Units of length and weight were used. For those unfamiliar with these units, the (approximate) conversion factors to the metric system are as follows: 1 inch is 25 mm; 1 pound (abbreviation lb.) is 0.45 kg).

### 1. Introduction: Why study the history of high rate testing?

“[History] serves as a guide to the investigator in what has been done, and what ought to be done. In this latter respect the individualism of modern science has not infrequently led to a great waste of power; the same bit of work has been repeated in different countries at different times...As it is, the would-be researcher either wastes much time in learning the history of his subject, or else works away regardless of earlier investigations. The latter course has been singularly prevalent with even some first-class British and French mathematicians” [1].

There was increasing concern around the middle of the 19<sup>th</sup> century about the novel use of iron in railways and bridges since the dynamic fracture properties of this material were unknown. This may be seen in the following quote dating from 1849: “There is no subject in practical science which has been more elaborately investigated than the theory of the statical transverse strength of beams. ... But the DYNAMICAL strength of beams, or their capability of sustaining weights moving rapidly over them, has never been satisfactorily discussed” [2]. Although Hodgkinson had published in the 1830s the results of some studies he had performed into the dynamic properties of various materials [3, 4] (see also figure 1), it was not until 1865 that a *quantitative* difference was reported between the dynamic and static tensile strengths of the iron that cannon were made from: “...the dynamic tensile strength of an iron cannon burst using gunpowder was 75,684 lbs per square inch whereas its strength measured using a ‘testing machine’ was only 26,866 lbs per square inch” [5, p. 300].

\*Author for correspondence (smw14@cam.ac.uk).

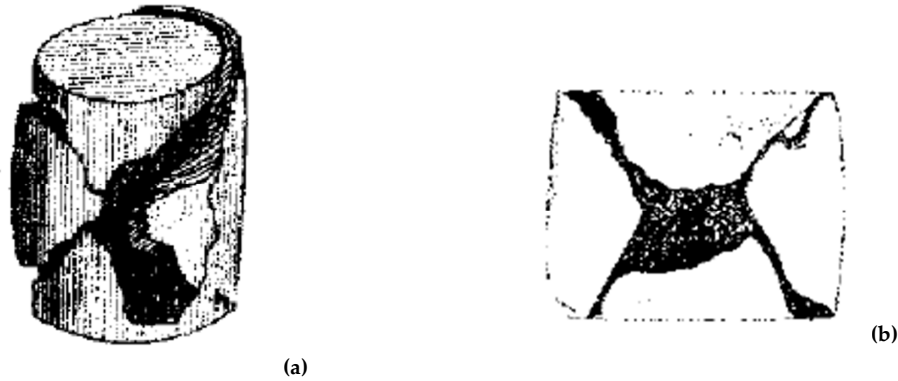


Figure 1. Engraving from the first known published report of the response of metal cylinders (cast iron) to compression. From [6].

2. What dynamic mechanical experiments was it possible to perform in the 19<sup>th</sup> century?

The matter of the dynamic strength of iron became important in the 1860s due to the recently developed practice of armouring wooden naval ships with iron plates [7]. Watts *et al.* [8] stated: “Owing to the imperfect state of our experimental knowledge, there does not yet exist any complete and exact theory of the laws of the dynamic resistance of plates to shot”. Despite the thousands of terminal ballistics experiments that were performed during the 19th century in various countries (principally the United Kingdom, France, Prussia, Italy, Belgium, the United States, and Russia), men were aware of their lack of understanding as can be seen from the following quote from Holley (an American) in 1865: “The great problem remains unsolved. Indeed, engineers are looking for its solution in diverse or opposite directions. Seeing that the results of experiments, and especially of warfare, in testing guns against armor are developing new features of strength and weakness every day; that these results are still somewhat uncertain, and that time enough has not elapsed to enable the profession at large to collect and digest what facts there are, few if any *first principles* are universally recognized” [5, pp. 133-134].

Holley did, however, make some prescient observations about the reasons for difference between low and high velocity impact on plates. For example, he made the first mention that I know of concerning shock wave effects: “if the plate is 100 times heavier than the shot, and the shot has a velocity of 1000 feet per second, the plate will be moved bodily at the rate of 10 feet per second. But before this occurs, the whole force of the shot will have been communicated through the mass from one layer to the other, by a wave moving at about the velocity of sound.” [5, pp. 280-281]. He also published the first drawing (figure 2) of what later became known as ‘Hertzian fracture’ after the German scientist who first analysed the elastic stress field under an indenter and showed qualitatively that the lines of maximum shear stress form a cone [9, 10]. Figure 2 is typical of its time, for in the absence of sufficiently fast methods of recording force and deformation, all the investigators could do was describe, draw and later photograph the damage done to a target. There are many thousands of such descriptions in the military literature of the second half of the 19<sup>th</sup> century [7]. Although it would be some decades after the invention of photography before it became possible to trigger a flash accurately enough to capture the moment of impact [11, 12], people quickly understood the potential of photography to obtain information about ballistic events [13-15].

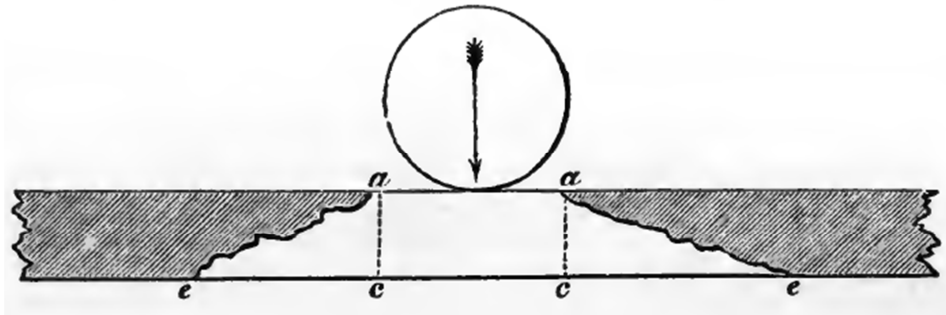


Figure 2. Engraving of a cross-section through an impact site produced by the impact of shot on a solid iron plate. The impact can clearly be seen to produce a cone-shaped spall. From [5].

Towards the end of the 19<sup>th</sup> century. Garrison reviewed the progress that had been made in iron and steel armour during the previous 100 years [16, 17]. He wrote the following about cast iron: “Chilled cast iron is one of the hardest substances known in the arts, but what iron gains in hardness when in this form it loses in other qualities such as elasticity, ductility, etc. In order to possess a maximum of ballistic resistance an armor-plate must be not only very hard, but also elastic and ductile; these fundamental conditions have been thoroughly demonstrated by several trials of chilled cast-iron armor.” This had been summarized in a remarkable graph (figure 3) published by Holley in 1865.

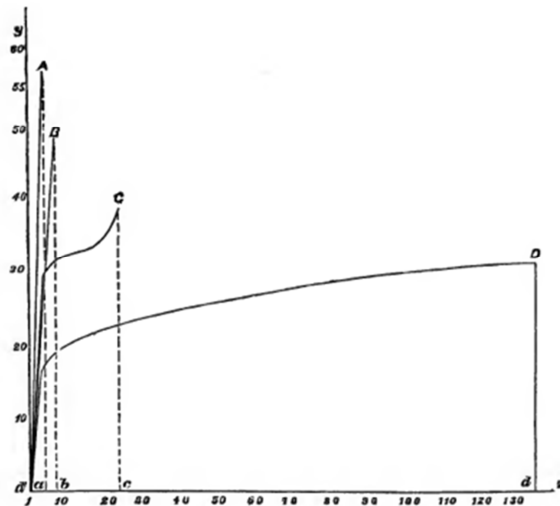


Figure 3. First known published comparison of load-extension curves for various types of iron and steel. From [5].

Ingenious electromechanical devices for measuring dynamic events with an accuracy of around 100  $\mu$ s were invented in the 1890s [18], but it took another 20 years or so for optical and electronic methods of measuring time to that accuracy to be developed [19, 20].

An understanding of the effects of explosive loading of iron plates was first provided in 1912 in a lecture by Bertram Hopkinson to the North-East Coast Institute of Engineers and Shipbuilders when he used elastic wave theory to explain why scabs of metal are thrown off the inside of a metal plate at high speed by the detonation of an explosive charge on the outside (figure 4) [21], a phenomenon later called ‘Hopkinson fracture’ by Kolsky in 1958 [22]. This had almost immediate implications for battleships and tanks in the Great War.

Very few soldiers in the Great War were given body armour. However, the German army did make some provision, particularly for their shock troops. However, as can be seen from the following quote (published in English in 1922), it wasn’t very well-designed and in addition some accused the suppliers of this armour of war-profiteering: “Why were, in 1915, movable firing screens supplied by thousands and in 1918 breast plates by the hundred thousand? The home people were astonished by seeing pictures of ‘knights without fear and

without reproach' in armor. The procurement of breast plates involved an enormous useless expense and waste of material, because they were worn only when the superior officer was in sight, or possibly by a Landswehrsman who had left wife and children and home and was oppressed with anxiety on their account; one could neither shoot not go about while wearing this thing. The front reported at once that they were impractical: we were supplied with new ones. Again we reported for the second and third time, but they continued to arrive. We had the impression that war material contractors had a good piece of business" [23].

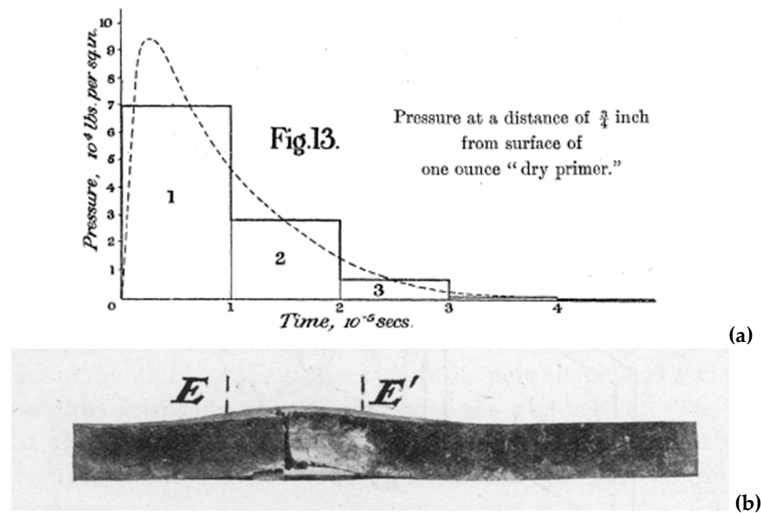


Figure 4. (a) Data obtained by Bertram Hopkinson on the approximate shape of the shock pulse produced by the explosion of a small explosive charge at one end of a steel rod. From [24]. (b) Photograph of the spall produced in a steel plate by the explosion of a explosive charge. From [21]. The shape of the graph shown in (a) allowed Hopkinson to explain the phenomenon shown in (b) [25].

From that time onwards, researchers had both the theoretical and experimental tools to understand, measure and explain the phenomena that their predecessors had observed but struggled to explain [26]. No longer would it be adequate simply to fire a gun at a target and describe what happened. However, it was not until the Second World War that Hopkinson's pressure bar began to find a new use in the measurement of the dynamic mechanical properties of materials in studies performed in secret by G.I. Taylor and co-workers [27-30] (see also figure 5).

In dynamics, G.I. Taylor is more famous for developing the so-called 'Taylor test' in which a cylinder of the material of interest is fired against a massive rigid anvil [31]. Simple measurements of the change of the dimensions of the cylinder give an estimate of the dynamic yield stress of the material. What is less well-known is that in 1942 he and R.M. Davies developed a hybrid Taylor-Hopkinson method for the measurement of the dynamic stress-strain curves of explosives (figure 6). This research was not published until 1958 [31].

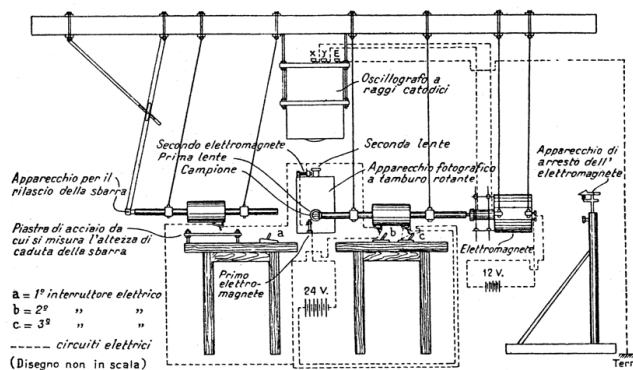


Figure 5. Enrico Volterra's split Hopkinson pressure bar apparatus for measuring the dynamic properties of soft materials (secondary explosives and polyethylene) [27, 28].

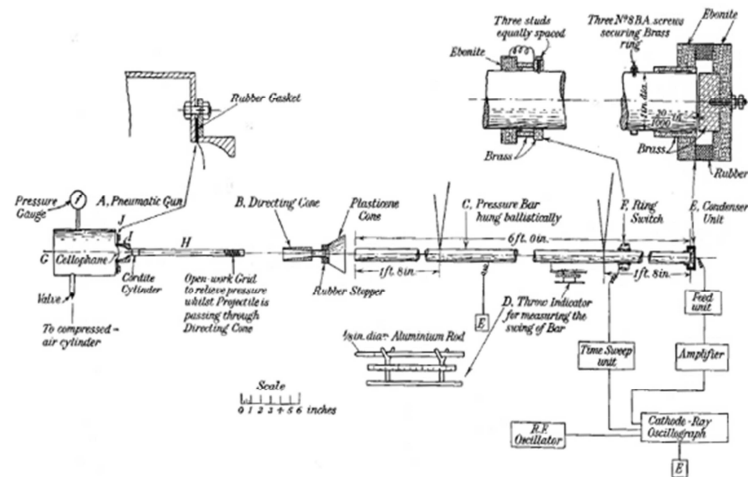


Figure 6. Schematic diagram of G.I. Taylor's 1942 design for a direct impact Hopkinson bar for measuring the dynamic properties of a secondary explosive (cordite). From [30].

Taylor was not the first to report the result of firing right circular cylinders against anvils [32, 33]. However, he was the first to publish a mathematical analysis of the problem (albeit approximate) as de Maupeou simply reported what he (or his subordinates) observed: “Lorsqu’un cylindre métallique lancé avec une vitesse suffisante (plus de 30 m/s pour l’acier) rencontre un obstacle rigide, la partie avant s’écrase en forme de champignon, se déchire si l’élargissement est trop considérable, et finie même par se détacher...” He also reported that the front end of the cylinders became hot during impact whereas the rear end did not. Despite not publishing an analysis, de Maupeou appears to have had great physical insight into the deceleration process: “Pendant que la face avant du cylindre s’écrase, la face arrière subit une série de ralentissements, qui se succèdent à des intervalles de temps très rapprochés. La partie arrière du cylindre se ralentit donc progressivement, ce qui explique qu’elle ne se déforme pas comme l’avant.”

### 3. Conclusions

I have been struck while going through this early literature by two apparently contradictory things: (i) how long ago some measurements were made, but on the other hand (ii) how recent other measurements were reported, despite people being aware that the information would be useful. In dynamics, what held people back was the lack of instrumentation with the necessary (microsecond) time resolution.

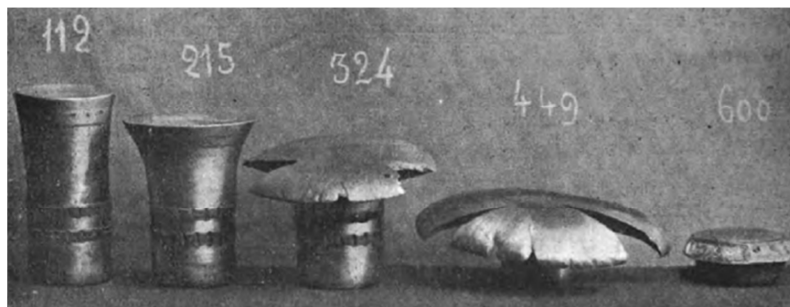


Figure 7. First known report (1902) of rod-on-anvil experiments for steel. From [32].

### References :

1. Pearson K. 1886. Preface to A History of the Strength of Materials From Galilei to the Present Time 1: Galilei to Saint-Venant. Todhunter I, Pearson K (eds). Cambridge: Cambridge University Press. p. xi
2. Cox H. 1849. *J Franklin Inst* **47** 73-84, 145-153
3. Hodgkinson E. 1834. *Rep Brit Assoc Adv Sci* **4** 534-543
4. Hodgkinson E. 1836. *Rep Brit Assoc Adv Sci* **5** 93-116
5. Holley AL. 1865. A Treatise on Ordnance and Armor. New York: van Nostrand

7. Walley SM. 2018. The beginnings of the use of iron and steel in heavy armour. In: Kaufman B, Briant CL (eds) *Metallurgical Design and Industry: Prehistory to the Space Age*. New York: Springer. pp. 71-153
8. Watts I, Rankine WJM, Barnes FK, Napier JR. 1866. Shipbuilding for purposes of war. In: *Shipbuilding: Theoretical and Practical*. London: William Mackenzie. pp. 293-297
9. Hertz H. 1896. On the contact of elastic solids. In: Jones DE, Schott GA (eds) *Miscellaneous Papers by Heinrich Hertz*. London: Macmillan. pp. 146-162
10. Hertz H. 1896. On the contact of rigid elastic solids and on hardness. In: Jones DE, Schott GA (eds) *Miscellaneous Papers by Heinrich Hertz*. London: Macmillan. pp. 163-183
11. Cranz C, Schardin H. 1929. *Z Phys* **56** 147-183
12. Edgerton HE, Killian JR. 1939. *Flash! Seeing the Unseen by Ultra-High Speed Photography*. Boston: Hale, Cushman and Flint
13. Anon. 1866. *Brit J Photography* **13** 328-329
14. McKinley P. 1866. *Min Proc Royal Artillery Inst* **5** 113-115
15. Boys CV. 1893. *J Royal United Services Inst* **37** 855-873
16. Garrison FL. 1892. *J Franklin Inst* **133** 337-356, 421-453
17. Garrison FL. 1892. *J Franklin Inst* **134** 20-42
18. Griffith M. 1897. *J Military Service Institution United States* **20** 180-191
19. Guyau A. 1914. *J Phys Théor Appliq (Sér 5)* **4** 195-206
20. Dufour A. 1920. *J Phys Radium (Sér 6)* **1** 147-160, plate I
21. Hopkinson B. 1914. *Trans North-East Coast Inst Engineers Shipbuilders* **30** 199-217
22. Kolsky H, Shi YY. 1958. *Proc Phys Soc Lond* **72** 447-453
23. Hesse K, Merz H, Ruhlen G. 1922. *J United States Artillery* **56** 346-356
24. Hopkinson B. 1914. *Phil Trans R Soc Lond A* **213** 437-456
25. Hopkinson B. 1921. The effects of the detonation of gun cotton. In: Ewing JA, Larmor J (eds) *The Collected Scientific Papers of Bertram Hopkinson*. Cambridge: Cambridge University Press. pp. 461-474
26. Landon JW, Quinney H. 1923. *Proc R Soc Lond A* **103** 622-643
27. Taylor GI. 1946. *J Inst Civil Engrs* **26** 486-519
28. Volterra E. 1948. *Rivista Nuovo Cimento* **4** 1-28
29. Kolsky H. 1949. *Proc Phys Soc Lond B* **62** 676-700
30. Taylor GI, Davies RM. 1958. The mechanical properties of cordite during impact stressing (this was originally written for the Ministry of Supply of the UK Government in 1942). In: Batchelor GK (ed) *The Scientific Papers of Sir Geoffrey Ingram Taylor Vol 1: Mechanics of Solids*. Cambridge: Cambridge University Press. pp. 480-495
31. Taylor GI. 1948. *Proc R Soc Lond A* **194** 289-299
32. de Maupeou M. 1902. *Bull Assoc Technique Maritime* **13** LVIII-LIX, 271-365
33. Régnault P. 1927. *Rev Métall Mémoires* **24** 509-515

# **Cohesive shear strength of concrete-rock joints : a preliminary study in quasi-static and dynamic loadings**

**Daniela De Lucia, Dominique Saletti\*, Matthieu Briffaut, Pascal Forquin**

*Univ. Grenoble Alpes, CNRS, Grenoble INP\*\*, 3SR, 38000 Grenoble, France*

**Keywords:** concrete-rock joint; dynamic shear strength; confined shear test.

---

**Abstract:** This study is focused on the cohesive shear strength of concrete-rock joints in quasi-static and dynamic conditions. While the quasi-static behaviour in static conditions of unbonded and bonded joints was deeply investigated in previous studies, there is still a lack of knowledge for dynamic loading ranges. This knowledge would be fundamental for better predicting the mechanical response of these joints to seismic loadings applied to a structure (*e.g.* dams). This study represents a first attempt to reach that goal. To do so, an experimental set-up initially developed for the study of the quasi-static and dynamic shear behaviour of concrete under confined conditions has been adapted and carried out on concrete-rock joints. The results were compared with the one obtained with a classic quasi-static set-up (BCR3D). It is shown that the shear strength is dependent of the confined pressure and the applied strain-rate. These first results have to be confirmed with additional data but are already encouraging.

## 1. Introduction

The general context of this study is to contribute to the assessment of the seismic safety of a concrete gravity dam for which the main mode of failure is the sliding. If the structure is subjected to horizontal forces bigger than the frictional resistance between body of dam and foundation, the failure that occurs is called sliding failure. The safety against sliding could be checked only for friction (for low dams), but in order to respect precise economical design, it is necessary to consider the shear strength of joints (for high dams). The interest is to evaluate the shear strength of the rock-concrete joints considering the pressure applied by the concrete dam on the interface. The shear strength of joints depends on several factors that the Mohr-Coulomb criteria does not take into account, such as: the roughness of the surfaces, the shear displacement rates, the compressive/tensile strength of the materials in contact but in particular the initial cohesion between the materials. In fact, rock and concrete are characterized by an initial cohesion due to the chemical bond between the two materials. The unbounded behaviour was studied with an extensive research; in fact, the main literature criteria are based on joints without initial cohesion. In addition, the influence of the roughness was deeply investigated on surfaces with artificial and controlled shape or natural ones. Recently, the research has moved towards understanding how an interface behaves if it presents an initial cohesion (bonded joint) [1] but only in quasi-static conditions, with testing rock-concrete joints at different levels of normal stress and with different types of surface's geometries.

The objective of this work is to increase the strain-rate loading of the shearing test on concrete-rock joints. In order to perform this kind of test, an experimental technique is used: the Punch-Through Shear (PTS) test. The concept of this test is pre-stressing the sample with a dynamometric ring prior applying a shear loading. Previously, this kind of experimental technique was designed and used to test only concrete [2]. With a view to investigate joints in dynamic conditions, the present work considers the precedent experimental technique but with a sample formed by a central part in rock and two lateral sides in concrete. Thus, the new sample is characterized by the presence of two rock-concrete discontinuities. The surface, which is tested under shear, has a dimension of 30x30 mm<sup>2</sup>. Quasi-static and dynamic tests were carried out respectively with a hydraulic press and a Split-Hopkinson Bar apparatus.

\*Author for correspondence (dominique.saletti@univ-grenoble-alpes.fr).

\*\* Institute of Engineering Univ. Grenoble Alpes

## 2. Material and method

The concrete used for the PTS test and the BCR3D test is the R30A7 (Table 1), widely tested in the 3SR Laboratory. It is characterized by a compressive strength of 30 MPa and slump of 7cm at 28 days. The chosen typology of rock is granite. This rock is the most common type of rock found at the level of dam-foundation in France. The granite is a mechanically strong rock with characteristics of very low permeability and insolubility, except in the fault zones. Exposed masses of granite will formed excellent dam sites. The sample geometry is detailed in Figure 1.

**Table 1. R30A7 ordinary concrete composition**

Component	Quantity (kg/m <sup>3</sup> )
Siliceous gravel D0.5/8mm	1008
Sand Dmax 1.8mm	838
Cement CEM I 52.5 N PM ES	263
Water	169

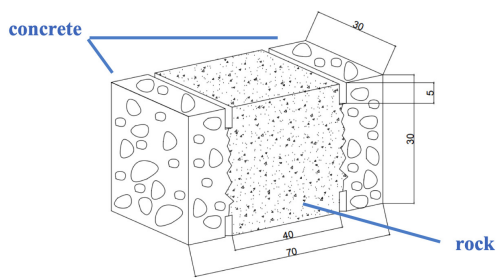


Figure 1. Sample dimensions (in mm).

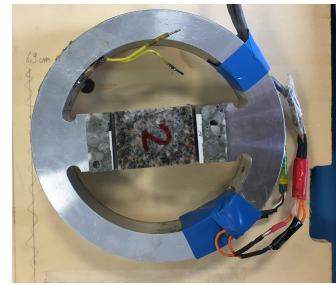


Figure 2: Sample inserted in the confining ring.

The confinement pressure on the sample is applied by a pre-stressed ring in aluminium, instrumented with gages in quarter-bridge configuration, on its inner and outer surfaces in order to evaluate the pressure acting on the interfaces between the two materials. The pre-stressed cell is useful to obtain that the two surfaces slide on each other and the crack displacement is in the crack plane, perpendicular to the crack front (crack mode II, sliding). The confinement is applied on the sample before testing it with the shear test by pre-deforming the cell and inserting the sample between the two confining place (Figure 2).

The quasi-static tests were performed with a hydraulic press. A steel cylinder was put between the rock surface and the upper plate and two steel parts were put between the two concrete surfaces and the lower platen (Figure 3). Regarding the dynamic test, a Hopkinson bar apparatus was used. This apparatus consists into a cylindrical projectile of 45 mm in diameter and 480 mm in length, made of high strength aluminium alloy as well as the 45-mm diameter aluminium bar positioned on the rock surface. The output bars, positioned on the concrete surfaces are 20 mm in diameter and made of high strength steel.



Figure 3. Quasi-static PTS test.



Figure 4. Dynamic PTS test. View of the sample with the input bar and the two output bars.

### 3. First results

The first results indicate clearly that the strain-rate and the confinement influence the level of shear strength of the joint. Figure 5 shows a comparison of the shear strength obtained for the test in quasi-static conducted at  $4.3 \cdot 10^{-4}$  /s and the one obtained with a dynamic test conducted at 16 /s.

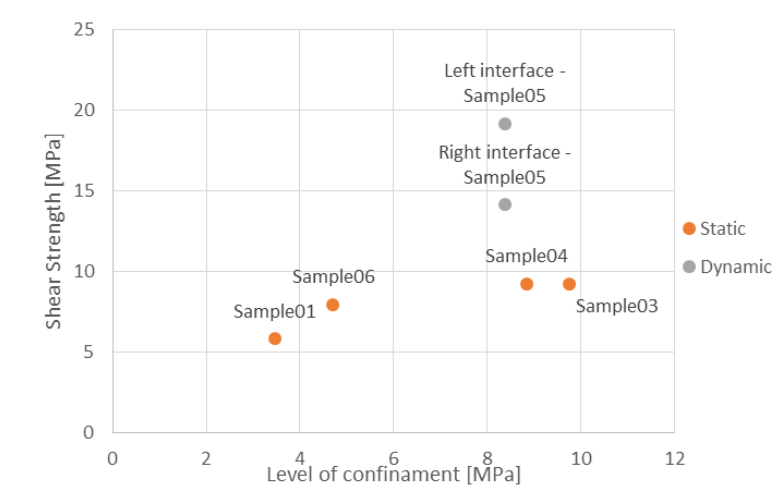


Figure 5. Comparison of the shear strength obtained for the test in QS and Dynamic conditions.

For sample 05, it was possible to keep in one piece the sample at the end of the test. In these conditions, the investigators had the opportunity to observe the plane of fracture of the sample in different cross-section views, using micro-tomography scans (Figure 6)

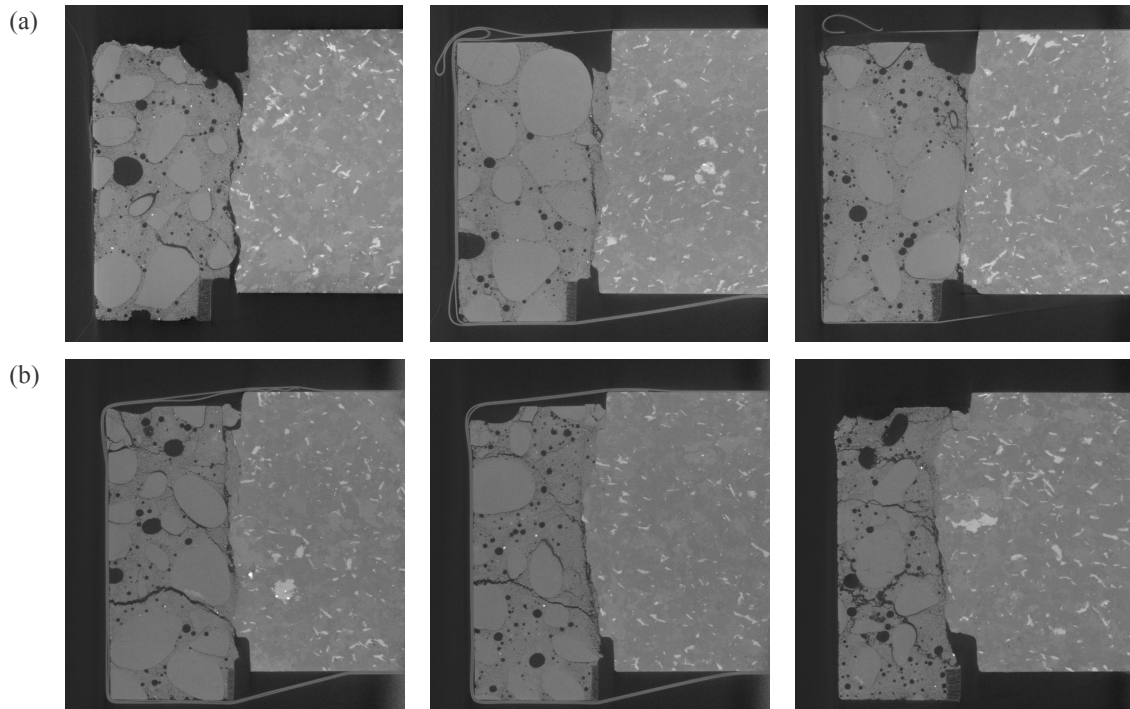


Figure 6. Rays scans. Initial, central and final section of plane fracture: (a) Left interface (b) Right interface

The cross sections in the direction perpendicular to the shear (initial, central and final section) for both the interfaces show that: for the first joint, as well as the right one, the fracture follows the joints or develops in the concrete, depending on the slope of the granite. This is evident in the middle part of the left surface, where the fracture starts in the interface but goes in the concrete due to the relative minimum depth on the granite surface in this area. Moreover, the right concrete's part presents more fracture perpendicular to the shear plane. The shear strength of this interface is lower; thus this could be due to the smaller thickness of the right concrete part due to the roughness of the granite that is more convex in the concrete.

#### 4. Conclusion

These results are encouraging and allow the author thinking that PTS test may be an experimental set-up to characterize the shear behaviour of concrete-rock joints. Additional parameters, which are not presented here, have to be taken into account such as the roughness of the interface, the size of the specimen, its representativeness with real dam cases and will be presented in further studies.

#### Acknowledgments

The laboratory 3SR is part of the LabEx Tec 21 (Investissements d'Avenir - grant agreement n°ANR-11-LABX-0030)

#### References

1. El Merabi. 2018. Mechanical behavior of cohesive concrete-rock joints at the dam-foundation interface: geometrical and mechanical influence of asperities. *Phd dissertation. Université Grenoble Alpes.*
2. Abdul Rahman et al. 2018. Experimental Investigation of the Confined Behavior of Concrete under Shear Loading at High Strain Rates. *The 18<sup>th</sup> International Conference of Experimental Mechanics* (doi:10.3390/ICEM1805408)

# Numerical Design of Plate-Impact Testing method to Determine the Spall strength of an Ultra-High Performance Concrete

M. Blasone, P. Forquin

*Univ. Grenoble Alpes, CNRS, Grenoble INP, Laboratoire 3SR, BP53, 38041 Grenoble Cedex 9*

**Keywords:** Plate-Impact, High Strain-rate sensitivity, Pulse-shaper, Ultra-High Performance Concrete

---

**Abstract:** The plate-impact spalling testing technique constitutes one of the few available experimental methods to observe the dynamic tensile response of mortars and concretes, in uniaxial strain condition, at very high strain-rate (about  $10^4$ - $10^5$  1/s). However, the technique suffers from a strong limitation: strain-rates are difficult to measure. Indeed, the level of strain rate within a target subjected to plate-impact testing with traditional flyer plate is not constant during the experiment. Finally, to characterize the behaviour of concrete and other rock-like materials as function of strain-rate remains difficult. The present work aims to numerically design a strain-rate adjusted Plate-Impact experiment to be applied to an Ultra-High Performance Concrete (UHPC) based on “toothed” and/or “wavy” machined flyer-plate and buffer. It has been observed that the “wavy-shape” of the buffer provides a smooth loading allowing to control the rising time whereas the “toothed-shape” of the rear surface of flyer plate provides a smooth unloading allowing to control the descending time.

## 1. Introduction

Ultra-High Performance Concretes (UHPC) are cementitious materials having a compressive strength between 150 MPa and 250 MPa [1]. This surprising property makes UHPC ideal for protective solutions against ballistic and explosion threats. A main prerequisite that may lead to improve the use of UHPC in engineering solutions is a better understanding of UHPC behaviour over a wide range of strain-rates and loading conditions.

Spall is a phenomenon whereby materials fail in dynamic tension due to the superposition of rarefaction waves. Favourable conditions for spall can be produced by plate-impacts [2] [3]. Figure 1 (a) shows a typical time-distance diagram. The sketch provides a graphical solution to the wave propagation problem keeping track of the relative position of the waves. Both released waves coming from the target and the flyer plate rear surfaces are crossing each other at time  $T_4$  leading to spalling at a distance  $d$  from the free surface of the target. In each test, a laser interferometer is pointed out on the free surface of the sample in order to record the particle velocity profile (Figure 1 (b)). The spall strength is proportional to the so-called “velocity pullback” corresponding to the difference between the maximum particle velocity and the particle velocity at the rebound [4].

In classical plate-impact test, the compressive pulse transmitted to the target has sharp rising and descending edges. As a consequence, the strain rate in the target at spalling is generally above  $10^5$  1/s and it cannot be adjusted by changing the striker speed. In fact, the striker speed is bounded by a lower limit to ensure a spall failure and by an upper limit to avoid any material damage in compression before spalling [5]. In 2017, Forquin & Zinsser [7] proposed to use machined plate to produce a smooth compression in plate-impact experiments on ceramics. By means of numerical simulations, they prove that machined contact surfaces provide an easy way to modify the rising time of the pulse generated by the impact. This publication aims to numerically design a Plate-Impact experiment configuration to be applied to an Ultra-High Performance Concrete (UHPC) in order to determine its spall strength at various strain-rates. The investigation is conducted on a commercial Ultra-High Performance Concrete powder called Ductal®.

\*Pascal Forquin ([pascal.forquin@3sr-grenoble.fr](mailto:pascal.forquin@3sr-grenoble.fr)).

†Present address: Laboratoire 3SR, BP53, 38041 Grenoble Cedex 9

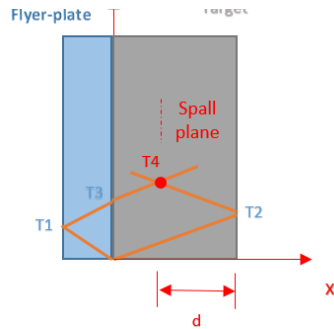


Fig. 1. (a) Time-distance diagram for a plate-impact experiments

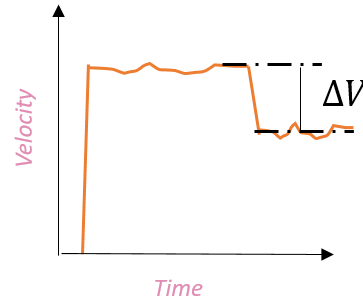


Fig. 1. (b) Particle velocity at the rear face of the specimens versus time.

1. Numerical simulation considering a 1D model

Strain-rate cannot be directly measured during a plate-impact experiment, but it can be deduced by numerical simulation considering uniaxial strain condition. The objective of this section is to quantify the strain rate at spalling. To do so, 1-D strain calculations have been conducted using the explicit transient finite-element (FE) code Abaqus/Explicit. For a standard plate impact experiment, we assumed a 5-mm-thick 6061-T6 Aluminum striker impacting a 10-mm-thick Ductal target. A linear elastic – perfectly plastic behaviour is assumed for striker whereas an elastic behaviour is used for the target. The material parameters are reported in the Table 1. Two initial axial velocities of respectively 25 and 55 m/s were set for the striker. After impact, compressive axial stress developed first and the tensile load arises second. The spalling is expected to occur almost in the middle part of the target at around 60 MPa [6].

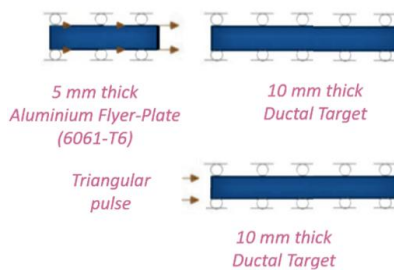


Fig. 2. (a) Numerical simulations of plate-impact in 1D strain

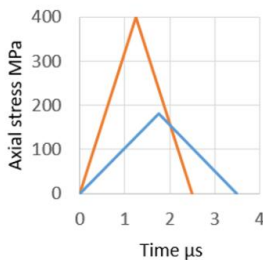


Fig. 2. (c) Ideal incident waves

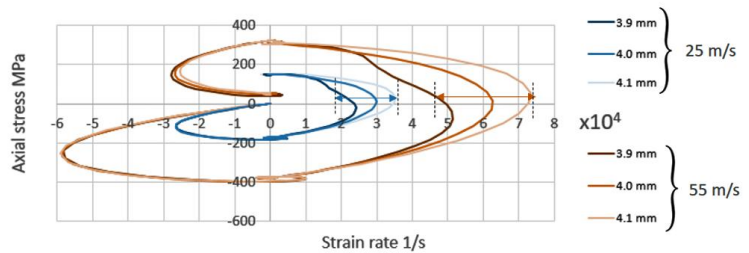


Fig. 2. (b) Axial stress Vs strain rate at the spalled plane for a classical plate-impact experiments

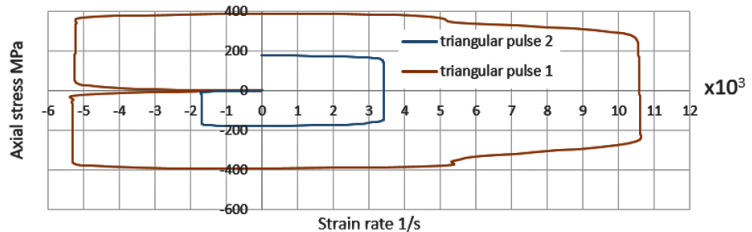


Fig. 1. (d) Axial stress Vs strain rate generated by triangular waves

The axial stress versus strain rate curves are plotted on the figure 2 (b) at different locations from the free surface. The level of strain-rate is in the order of few  $10^4 \text{ s}^{-1}$  and is observed to be heterogeneous during the tensile loading. As expected, increasing the striker speed the strain rate level increases but the strain rate heterogeneity increases too. This simple calculation underlines that classical plate impact configuration are not adapted to discuss the strain-rate effect on the spall strength. A second calculation was performed considering

1-D strain state and a pressure pulse directly applied to the target. Two triangular pulses were selected with the same peak axial stress in compression (Fig. 2c). In this second case the level of strain rate is noted to be perfectly constant during the development of the tensile stresses from 0 to 60 MPa (Fig. 2d). It demonstrates that, if they can be generated, triangular-shaped compression pulses can bring a real improvement in view of investigating the strain-rate sensitivity of concrete with the plate-impact technique.

material	Density (g/cm <sup>-3</sup> )	Elastic proprieties		Plastic yield strength	
		E (GPa)	$\nu$	$\bar{\sigma}_y$ (MPa)	$\epsilon_p$
6061-T6	2700	68.9	0.33	270	0
Ductal®	2425	55	0.19		

Table. 1. Material parameters used in the Abaqus/Explicit numerical simulation.

## 2. Numerical simulation considering a 2D model

The objective of this section is to design plate-impact experiment producing a compressive pulse approximating a triangular pulse by means of chip-forming machined plates with “toothed” and “wavy” shape surfaces. The proposed testing configuration is composed of a 5-mm-thick Aluminium flyer-plate and a 10-mm-thick ductal plate. A 5-mm-thick aluminium buffer is placed between the impactor and the target to homogenize the stress field along the transverse direction of the target. The diameter of each plate is set to 70 mm. The calculations were made in 2D by considering a single half-period of the toothed-shaped flyer plate. The normal displacement is set to zero on the top and bottom surfaces to model the corresponding symmetry planes. A frictionless surface-to-surface contact algorithm was used to describe the contact between each component of the systems. An initial axial velocity of 40 m/s was set for the strikers whereas the buffer and the target are initially in contact. Figure 3 provides the mean axial stress (axial force divided by the vertical cross-section) versus time at the buffer/sample interface for three diverse configurations: classical striker and buffer; classical striker and “wavy” buffer; and “toothed” striker and “wavy” buffer. It is shown that, the “wavy-shape” of the impacted surface of the buffer provides smooth rising and descending edges, whereas, the “toothed-shape” of the rear surface of flyer plate provides a smoother descending edge and does not affect at all the rising edge.

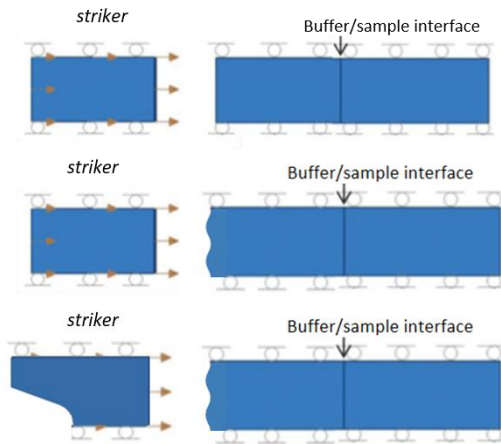


Fig. 3. (a) Description of the three configurations of plate-impact in 2D strain

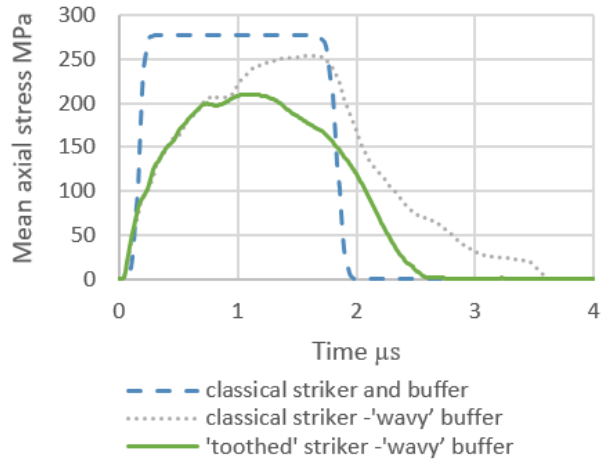


Fig. 3. (b) Mean axial stress versus time at the buffer/sample interface for the three configuration

## 3. Numerical simulation considering a 3D model

orthogonal directions) and a Ductal® target were considered. Numerical simulations were conducted with Abaqus/Explicit FE code and a 3D model made of C3D8R elements (eight-node hexahedral reduced integration elements). The out-of-plane displacement is set to zero on all the nodes of the vertical surfaces. The compression pulse at the buffer/sample interface for an impact velocity of 40 m/s is plotted in the Figure 4 (b). It is shown that a pointed contact between striker and buffer generates rising and descending edge less bended compared to a linear contact. The next figure shows the change of strain rate as function of the axial stress in the spalled section corresponding to points A and B located on the top and on the bottom of the section. The stress and strain state in the target is homogeneous along the transverse direction, so the buffer is thick enough compared with the period of the “toothed” shape.

#### 4. Conclusion

The strain rate sensitivity of spall strength in concretes still needs to be investigated. To do so, the Plate-Impact testing with adjusted strain-rate may represent a very attractive way to characterize the dynamic material response properly at strain-rate above 1000 1/s. A series of numerical simulations have been developed to shape the loading-rate applied to the sample subjected to a Plate-Impact test. An experimental campaign on an Ultra-High Performance Concrete called Ductal® is ongoing at 3SR laboratory including traditional and strain-rate adjusted Plate-Impact experiments.

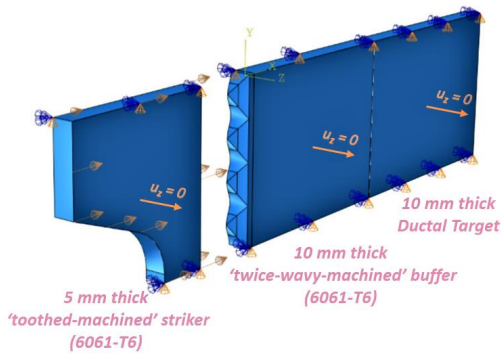


Fig. 4. (a) Numerical simulation in 3D strain

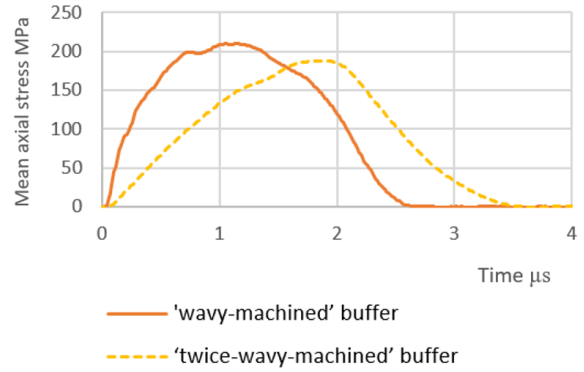


Fig. 4. (b) Mean axial stress versus time at the buffer/sample interface for a linear and pointed contact

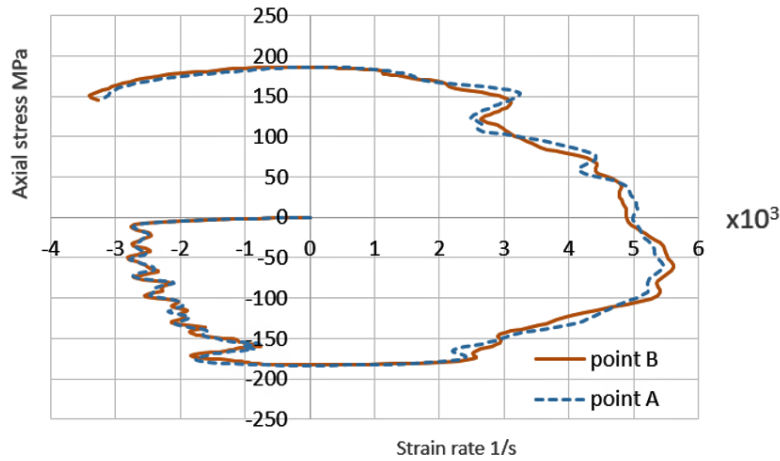


Fig. 4. (c) Stress and strain states along the transverse direction

#### Acknowledgments

This work has been performed in the framework of the Brittle's CODEX chair supported by the UGA (Univ. Grenoble Alpes) Foundation and sponsored by the Saint-Gobain and Lafarge-Holcim companies. These sponsors are gratefully acknowledged by the authors.

### References

1. Richard P., (1995). Composition of Reactive Powder Concretes. *Cement and Concrete Research*, 25, 1501- 1511.
2. Antoun T., (2003). *Spall Fracture (Shock Wave and High Pressure Phenomena)*. New York – Springer.
3. Meyers M.A. (1994). *Dynamic behavior of materials*. John Wiley & Sons, Inc.
4. Novikov S.A., Divnov I.I., and Ivanov A.G. (1966). Fracture of steel, aluminum, and copper under explosive loading, *Fiz. Met. Metalloved*, 21, No. 4, 608-615, 1966
5. Grote D. L., Park S.W., Zhou M. (2001). Experimental characterization of the dynamic failure behavior of mortar under impact loading. *J. Applied Physics*, 89(4), 2115-2123.
6. Neel, C. (2018). Compaction and Spall of UHPC Concrete Under Shock Conditions. *Journal of Dynamic Behavior of Materials*. 4. 1-24. 10.1007/s40870-018-0173-3.
7. Forquin P, Zinszner J-L. (2017). A pulse-shaping technique to investigate the behaviour of brittle materials subjected to plate-impact tests. *Phil. Trans. R. Soc. A*, 375: 20160333.

## Dynamic behaviour of UD Basalt-Fibre Composites

G.C. Ganzenmüller<sup>1,2</sup>, A. Trippel<sup>2</sup>, D. Plappert<sup>2</sup>, S. Hiermaier<sup>1,2</sup>

Albert-Ludwigs Universität Freiburg, INATECH, Freiburg i. Br., Germany

Fraunhofer Ernst-Mach-Institute for High-Speed Dynamics, EMI, Freiburg i. Br., Germany

**Keywords:** Mechanical testing, Basalt fibres, Composites, Split-Hopkinson Bar

---

**Abstract:** This paper investigates the strain rate sensitivity of laminated composites made of plies of unidirectional basalt fibres and epoxy resin. We consider laminates with quasi-isotropic  $[0^\circ, -45^\circ, 45^\circ, 90^\circ]_s$  and orthogonal  $[+45^\circ, -45^\circ]_4$  layup. A Split-Hopkinson Tension Bar is used to generate accurate stress/strain data at elevated rates of strain of  $10^2$  /s. Moderate strain rate effects are observed with strength increase of  $\approx 3.5\%$  per decade of increased loading rate for both laminate types.

### 1. Introduction

The purpose of this work is to present reasonably accurate dynamic tensile strength data for composites made of plies of endless, unidirectional basalt fibres and epoxy resin. Over the last two decades, basalt fibres have come into consideration as potential reinforcement for composite materials requiring high strength and temperature resistance. In contrast to the infamous asbestos fibre, which meets these application requirements from a mechanical point of view, basalt is not considered carcinogenic [1]. It is a mineral belonging to the group of silicates and as such similar to glass in its chemical composition but with more iron and less calcium content. While glass fibres are completely amorphous solids, basalt fibres can feature some degree of crystallinity [2]. Basalt's mechanical properties strength and stiffness are lower than those of carbon fibres, and more akin to those of S-2 glass fibres. The quasi-static properties of basalt fibres and its composites are already well known [3]. A promising field of application for basalt fibre composites are structural elements in the automotive sector, where it is important to predict the dynamic material behaviour at elevated strain rates relevant at crash, which are on the order of  $10 - 100$  /s. However, as of now, only a few studies are available on dynamic properties. This is particularly true for composites composed of plies of endless, unidirectional (UD) fibres. To our knowledge, only one, very recent study is available [4], where the authors report that the dynamic tensile strength of a pure  $0^\circ$  basalt/epoxy composite doubles its strength when strain rate is increased from  $10$  /s to  $300$  /s. This amount of strain rate sensitivity appears exceptionally high, as UD composites of carbon or glass fibres only exhibit strength increases of approximately  $1\% - 10\%$  *per order of magnitude* of increased strain rate [5]. In another study, the strain rate sensitivity of woven basalt/epoxy composites was studied, and a similarly exceptional high strain rate sensitivity was observed [6]. Is there something special about basalt fibres which makes them very strain rate sensitive? To shed some light on this issue, we investigate the strain rate dependency of the tensile failure strength and strain for quasi-isotropic  $[0^\circ, -45^\circ, 45^\circ, 90^\circ]_s$  and orthogonal  $[+45^\circ, -45^\circ]_4$  layups of unidirectional basalt fibres in a thermoset epoxy matrix within the strain rate regime  $10^{-3} - 3 \times 10^2$  /s.

### 2. Materials and Methods

Sheets of cured UD basalt fibre composites with layups  $[0^\circ, -45^\circ, 45^\circ, 90^\circ]_s$  and orthogonal  $[+45^\circ, -45^\circ]_4$  were tested. This composite is made from a prepreg of basalt fibres with filament diameter  $17 \mu\text{m}$  and a low-viscosity epoxy resin system. Laminates were cured in an autoclave process resulting in fibre volume fraction of  $60\%$ . To illustrate the mechanical properties of this material, we quote the nominal strength and stiffness of pure  $0^\circ$  specimens according to ISO-527 as  $1310 \text{ MPa}$  and  $44 \text{ GPa}$  [7]. Testing specimens were cut from the

\*Author for correspondence (Georg.Ganzenmueller@inatech.uni-freiburg.de).

† Present address: Albert-Ludwigs Universität Freiburg, INATECH, Freiburg i. Br., Germany

sheets using a diamond coated saw blade to obtain good cut surface quality. The dimensions of the quasi-isotropic (QI) specimens are  $100 \times 3 \times 1.6 \text{ mm}^3$  with a nominal gauge length of 20 mm. The dimensions of the  $\pm 45^\circ$  specimens are  $100 \times 5 \times 2.0 \text{ mm}^3$  with the same nominal gauge length. The same specimen geometry was used across all strain rates. Specimens were bonded to grooved 7075 aluminium tabs with a high-strength, thermally activated epoxy resin according to Figure 1 (left). We use split tabs as these can be easily manufactured in large quantities using a CNC router. Additionally, the split tabs provide good accessibility to the interior which makes it trivial to correctly apply the adhesive. The tabs feature holes for M4 through-bolts to affix the assembled specimen to the aluminium grips as shown in Figure 1 (right). The clamps are designed to fulfill three tasks: (i) they provide an ISO M12 $\times$ 1.5 thread to interface with either the Split-Hopkinson bars or the universal testing machine. (ii) The transition from the circular interfacing end with the testing apparatus to the rectangular shape used to attach the specimen maintains a constant cross section area. For dynamic testing, the Split-Hopkinson bars are also made of aluminium, such that constant acoustic impedance is obtained. This avoids unwanted wave reflections due to the specimen gripping device, see [8] for details. (iii) The 4.1 mm through holes allow for clamping the specimen inside the grip. To this end, lightweight M4 aluminium bolts with strength class ISO 5.6 may be used, yielding an axial force of 1.8 kN per bolt. With 4 bolts and a conservatively assumed friction coefficient  $\mu=1.0$  between the clean and unlubed aluminium surfaces, this translates into a useful upper force limit of  $\approx 14 \text{ kN}$  for this clamp. This limit exceeds the expected forces in this work by a factor of 4. We note that those parts of the through-bolts and nuts protruding from the surfaces introduce additional mass, which causes unwanted wave reflections. However, this effect is so minor that its effects cannot be observed in our data.

**Quasi-static and low strain rate testing.** For the quasi-static and low strain rates of  $10^{-3} / \text{s}$  and  $10^{-1} / \text{s}$ , we use a screw-driven universal testing machine with 100 kN capacity and a maximum testing velocity of 1500 mm/min. Specimens were attached using the gripping device described before, which itself was mounted to the testing machine using cardanic joints to prevent off-axis loading. Strain was measured locally on the specimen using Digital Image Correlation (DIC). Both force and strain time series were combined into nominal stress/strain graphs by eliminating the time information.

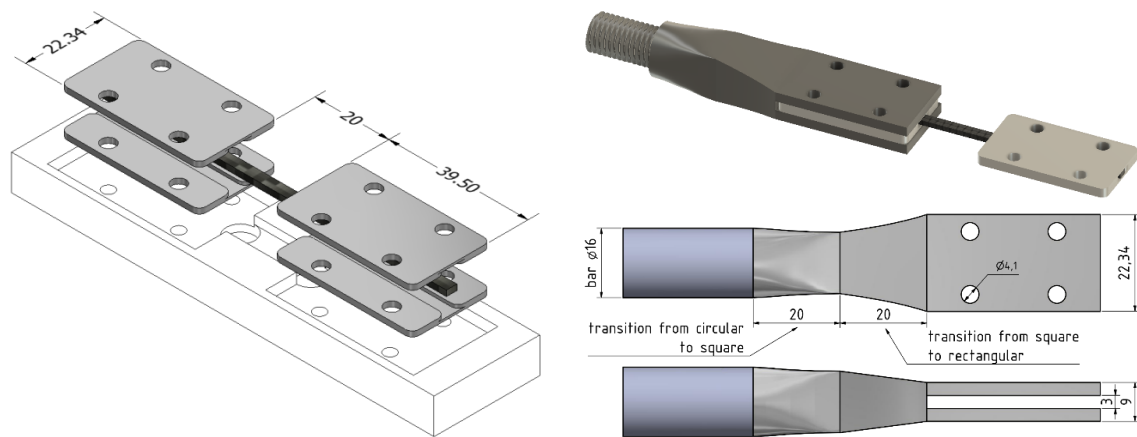
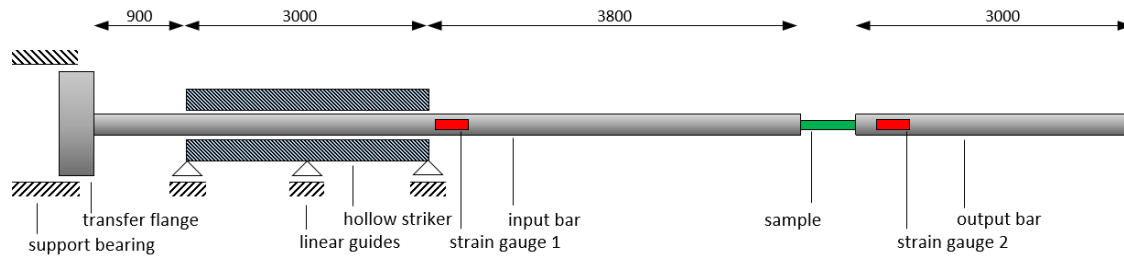


Figure 1: (left) CAD rendering of the specimen with its split aluminium tabs. Also shown is the fixture which is used to align all parts during assembly and curing of the epoxy adhesive. (right) Clamping fixture maintains cross section area and thus provides constant acoustic impedance which is required for reflection-free wave transmission.



**Figure 2: sketch of the SHTB setup employed in this work. All dimensions in mm. Input and output bars are 16 mm diameter aluminium rods. The striker is a hollow aluminium tube of 40 mm outer diameter and 20 mm inner diameter.**

**Dynamic Testing.** The Split-Hopkinson Tension Bar (SHTB) used here is sketched in Figure 2 and described in detail in [9]. Compared to other SHTBs, this setup is optimized for low velocities, low forces and a long pulse duration of 1.2 ms. Specimens were attached to the bars using the grips detailed above. Shortly before performing the experiment, white contrast marks were painted on the specimen at the edges of the gauge section using a paint marker. We have observed that it is crucial for the paint to be still compliant. If it is fully dried it will come off the specimen before actual failure occurs, thus voiding the strain measurement. For determining the strain, we employ a line-scan camera to track the displacement of the contrast marks. If only uniaxial displacement is of interest, line-scan cameras are advantageous over area cameras due to higher 1D resolution and increased light sensitivity due to larger pixel size. We employ a model with  $1 \times 4096$  pixel resolution and a line scan frequency of 200 kHz. The strain is ultimately obtained by post-processing the line-scan data using a pattern matching algorithm with sub-pixel accuracy. Force is measured via a pair of conventional strain gauges mounted on the output bar, connected diagonally in a Wheatstone bridge circuit to eliminate bending information.

The line-scan camera is triggered by the DAQ card to start recording when the incident wave created by the striker reaches strain gauge no. 1, c.f. Figure 2. In the case of the line-scan camera, a synchronization signal is fed back to the DAQ card, so precise timing information is available to correlate strain and force signals. It is important to realize that even though strain and force signals are perfectly well synchronized in this manner, these signals are measured in different locations: strain is measured on the specimen but force is inferred from the strain gages on the output bar, in our case 200 mm upstream in the transmitted elastic wave direction. The time taken by the elastic wave to travel this distance must be accounted for by shifting the force signal by  $-\Delta t = 200 \text{ mm} / 5090 \text{ mm/ms} = 0.039 \text{ ms}$ , where 5090 mm/ms is the longitudinal wave speed in aluminium.

Our SHTB experiments were set up such that the incident wave attains a force amplitude of 20 kN, corresponding to a particle velocity of 7.2 m/s. This marks the upper end of what is safely attainable with our aluminium setup due to its mechanical strength. Figure 3 shows the recording of such an experiment on a quasi-isotropic specimen. The incident wave has a pronounced rise time of  $\approx 0.2 \text{ ms}$ , which is due to the use of a pulse shaper between striker and transfer flange, a rubber disk of 1 mm thickness. This pulse shaper significantly reduces oscillations in the transmitted force signal, which would otherwise completely dominate. However, the pulse shaper also implies that the strain rate is not constant at the start of loading but instead slowly ramps up. In this case, the pulse shape is chosen such that a nearly constant strain rate is obtained before failure. The strain rate may be obtained in two different ways, either directly from the strain gauge signals via the reflected wave, or by measuring locally on the specimen using an independent method. In the present case, the specimen is glued into a holder, and the deformation of the adhesive contributes erroneously to the nominal strain measured using the reflected wave. It is therefore necessary to employ a local measurement of specimen strain.

Figure 3 compares the local specimen strain measured using the line scan camera with the strain computed from the reflected wave. The locally measured strain is 4.9% and thus approximately only 65% of the classic estimate. Additionally, the local strain rate as obtained from a linear fit to the specimen strain is  $300 \pm 20 \text{ /s}$ ,

which is half of what is estimated by the classic approach. We would like to emphasize that this difference is not due to the two-wave approximation, but instead caused by the compliance of the specimen holding fixture.

Our SHTB setup with its long pulse duration allows to reach relatively low strain rates compared to what is common in the SHTB community. In principle, we could have realized even lower strain rates for same-sized specimens: in the quasi-isotropic case, only 0.25 ms of the available pulse duration of 1.2 ms is used, and for  $\pm 45^\circ$  specimens, failure is reached at approx. 0.55 ms. However, such experiments would deliver little additional insight as strain rate effects typically depend logarithmically on the strain rate. It was therefore our aim to achieve the highest possible strain rate. The quality of our data compares well with other Split-Hopkinson studies [5, 10], and we feel confident that quantitative conclusions can be drawn from these data.

### 1. Results and Discussion

Stress/strain curves for the quasi-isotropic specimens are shown in Figure 4 (left), along with their representative average curves. We note that the results obtained with the universal testing machine show some undulations at strains  $< 1\%$ , which is due to initial movement of the cardanic joints. Nevertheless, we are confident that the average curves are reliable. The material exhibits almost linear-elastic, brittle character. Maximum stress and strain at maximum stress coincide with the failure stress and strain. Comparison among the different strain rates shows that the failure stress and increases with strain rate from approximately 428 to 524 MPa, i.e. by  $22 \pm 8\%$ .

To illustrate that the comparatively small specimen size used here allows representative results to be obtained, we note that the corresponding quasi-static strength according to ISO-527 using much larger, 25 mm wide specimens is  $436 \pm 10$  MPa [7]. Failure strain increases significantly from approximately 3.3% to 4.8%. Classic visco-elastic behaviour, i.e., increased stiffness and decreased failure strain with strain rate, behaviour is not observed. Instead, all curves are superimposed but extend to higher stress and strain as the strain rate is increased. Within the uncertainty estimate, no distinction in stiffness can be observed. The location at which failure occurred exhibited little systematic behaviour, independent of strain rate. Experiments were only considered valid, if failure occurred in the gauge region.

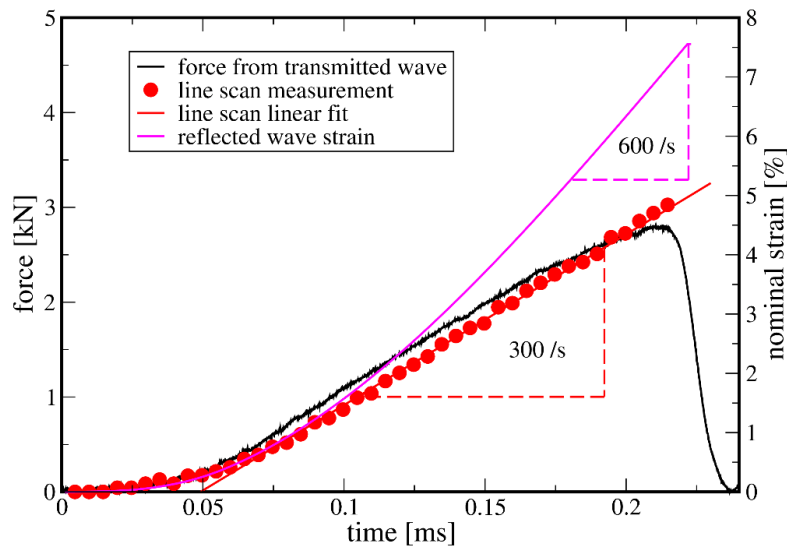
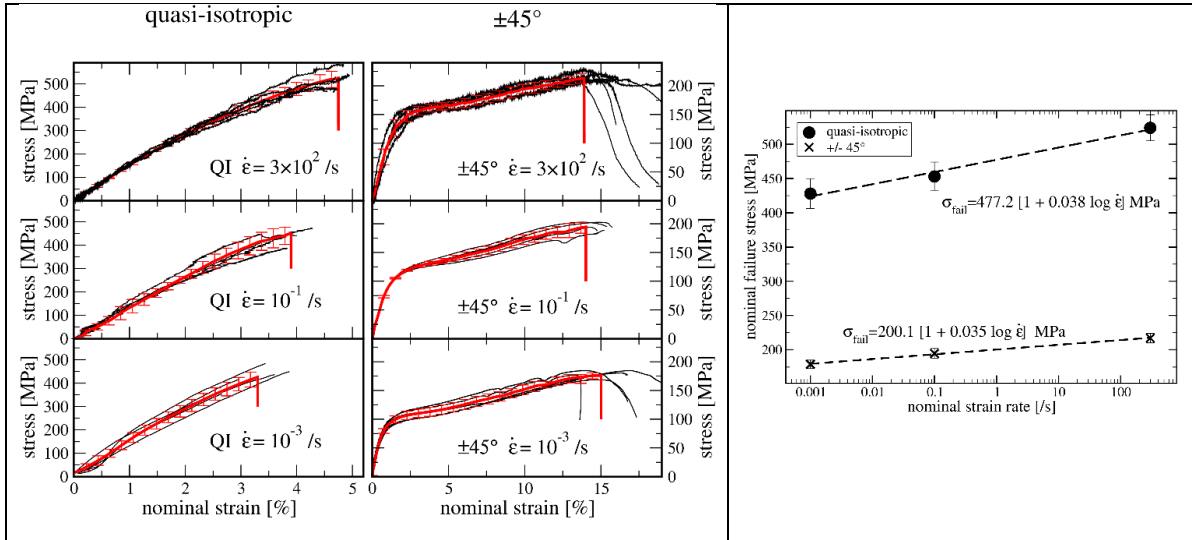


Figure 3: Force and strain time series for a single Split-Hopkinson Tension Bar experiment on a quasi-isotropic specimen at strain rate 300 /s. Force data (black solid line) is sampled at 10 MHz, local specimen strain (red circular symbols) is sampled at 200 kHz using a line scan camera. The solid red line is a linear regression to the local strain data points with slope 0.295 / ms, corresponding to the target strain rate of  $\approx 300$  /s. The classic, but erroneous, Split-Hopkinson estimate of the specimen strain as computed from the reflected wave is also shown.



**Figure 4: (left) Stress/strain curves for quasi-isotropic and  $\pm 45^\circ$  specimens at different strain rates. Black lines show individual experiments and red lines represent their averages. Error bars indicate the standard deviation of the average. An artificial steep drop in the average curves the average failure strain. (right) Strain rate sensitivity analysis of failure stress for quasi-isotropic (solid circles) and  $\pm 45^\circ$  specimens (crosses). Error bars denote one standard deviation. Straight lines are fits using a sensitivity model which is proportional to the logarithm of the strain rate, see text.**

In contrast,  $\pm 45^\circ$  specimens exhibit classic strain rate dependent pseudo-viscoplastic behaviour. Following an initial linear response, which is the same at all strain rates within the uncertainty estimate, a rounded transition to an inelastic regime with constant strain hardening is observed. The stress level of the inelastic regime increases significantly with strain rate: the maximum stress increases from approximately 179 to 217 MPa, i.e. by  $21 \pm 4\%$ . The corresponding quasi-static results for conventionally-sized specimens of 25 mm width according to DIN ISO-527 is  $203 \pm 8$  MPa [7]. This differs slightly but finite-size effects are expected especially for this specimen type as the amount of shear deformation that can be sustained is proportional to the specimen width. Failure strain (strain at maximum stress) is approximately 14% and thus much higher than in the quasi-isotropic case. The failure strain appears to decrease slightly with increased strain rate, although this observation cannot be fully justified given the uncertainty estimate.

We analyse the strain rate dependency by plotting failure stress against the decadic logarithm of strain rate, see Fig.~\ref{fig:scaling}. Both quasi-isotropic and  $\pm 45^\circ$  datasets are well described with a simple model, which is proportional to the logarithm of the strain rate, i.e.,

$$\sigma_{fail} = A \times \left[ 1 + B \log \left( \frac{\dot{\epsilon}}{\dot{\epsilon}_0} \right) \right]$$

Here,  $\dot{\epsilon}_0 = 1 /s$  is a reference strain rate which serves to render the argument of the log function dimensionless;  $A$  is the failure stress at the reference strain rate and  $B$  is the slope, i.e., the strain rate sensitivity. Fitting this function to the measured strength values using the Levenberg-Marquardt algorithm yields the parameters  $A$  and  $B$  including their uncertainty estimates. As is obvious from Figure 4 (right), the failure stress at  $\dot{\epsilon}_0$  is higher for the quasi-isotropic specimens than for the  $\pm 45^\circ$  specimens,  $A = 477.2 \pm 5.0$  MPa vs.  $A = 200.1 \pm 0.5$  MPa. More interestingly, the strain rate sensitivity is identical within the uncertainty estimate: We observe  $B = 0.038 \pm 0.005$  in the quasi-isotropic case and  $B = 0.035 \pm 0.001$  for the  $\pm 45^\circ$  specimens. This is somewhat surprising, as most of the load within the quasi-isotropic specimen is carried by the fibres of the  $0^\circ$  ply, and the strain rate sensitivity of the fibres itself is believed to be weak [11]. In contrast, in the  $\pm 45^\circ$  specimens, the epoxy matrix is loaded in shear, and it is well known that epoxy resins exhibit pronounced strain rate sensitivity [12]. However, these simple arguments may be misleading, as the composite's strength is also a

function of the fibre-matrix interface strength. To the knowledge of the authors, no published information is available about the loading rate sensitivity of interface properties in the case of basalt fibres and epoxy resins.

### Funding Statement

This work was supported by the Gips-Schüle-Stiftung and the Carl-Zeiss-Stiftung [Sonderlinie 2017/2018 Grundlagenwissenschaften mit Anwendungsbezug].

### References:

1. Kogan FM, Nikitina OV. 1994. Solubility of chrysotile asbestos and basalt fibers in relation to their fibrogenic and carcinogenic action. *Environ Health Perspect* **102** pp. 205–6.
2. Deak T, Czigany T. 2009. Chemical composition and mechanical properties of basalt and glass fibers: a Comparison. *Textil Res J* **79** pp. 645–51.
3. Liu Q, Shaw MT, Parnas RS, McDonnell A-M. 2006. Investigation of basalt fiber composite mechanical properties for applications in transportation. *Polym Compos* **27** pp. 41–8.
4. Chen W, Hao H, Jong M, Cui J, Shi Y, Chen L, Pham TM. 2017. Quasi-static and dynamic tensile properties of basalt fibre reinforced polymer. *Compos B Eng* **125** pp. 123–33.
5. Gilat A, Goldberg RK, Roberts GD. 2002. Experimental study of strain-rate-dependent behavior of carbon/epoxy composite. *Compos Sci Technol* **62** pp. 1469–76. ([https://doi.org/10.1016/S0266-3538\(02\)00100-8](https://doi.org/10.1016/S0266-3538(02)00100-8))
6. Zhang H, Yao Y, Zhu D, Mobasher B, Huang L. 2016. Tensile mechanical properties of basalt fiber reinforced polymer composite under varying strain rates and temperatures. *Polym Test* **51** pp. 29–39. (<https://doi.org/10.1016/j.polymertesting.2016.02.006>)
7. Plappert D. 2019 Quasi-static testing of basalt-fibre reinforced epoxy composites according to DIN ISO 527, Tech. rep., to be published elsewhere.
8. Ganzenmüller GC, Langhof T, Hiermaier S. 2018. A constant acoustic impedance mount for sheet-type specimens in the tensile Split-Hopkinson Bar. *EPJ Web Conf* **183** pp. 02064 (<https://doi.org/10.1051/epjconf/201818302064>)
9. Ganzenmüller GC, Blaum E, Mohrmann D, Langhof T, Plappert D, Ledford N, Paul H, Hiermaier S. 2017. A simplified design for a Split-Hopkinson Tension Bar with long pulse duration. *Procedia Eng*. **197** pp. 109–18. (<https://doi.org/10.1016/j.proeng.2017.08.087>)
10. Gomez-del Río T, Barbero E, Zaera R, Navarro C. 2005. Dynamic tensile behaviour at low temperature of CFRP using a split Hopkinson pressure bar. *Compos Sci Technol* **65** pp. 61–71 (<https://doi.org/10.1016/j.compscitech.2004.06.004>.)
11. Yazici M. 2009. Loading rate sensitivity of high strength fibers and fiber/matrix interfaces. *J Reinf Plast Compos* **28** pp. 1869–80. (<https://doi.org/10.1177/0731684408090379>)
12. Amos Gilat, Goldberg Robert K, Roberts Gary D. 2007. Strain rate sensitivity of epoxy resin in tensile and shear loading. *J Aerosp Eng* **20** pp. 75–89. ([https://doi.org/10.1061/\(ASCE\)0893-1321\(2007\)20:2\(75\)](https://doi.org/10.1061/(ASCE)0893-1321(2007)20:2(75)))

## **X-ray diffraction study of the solid-solid phase transition of tin under shock loading**

**PALMA DE BARROS David<sup>†\*</sup>, CHAUVIN Camille<sup>†</sup>**

<sup>†</sup>*CEA Gramat, Gramat, 46500, France*

**Keywords:** X-ray diffraction, shock, tin, single crystal, plate impact

---

### **Abstract:**

The modelling of materials behaviour under dynamic loading remains a great issue particularly upon phase transition. The usual measurement methods that provide only macroscopic information are not enough to fully model the materials behaviour. Towards X-ray diffraction, a microscopic analysis of materials can be implemented on shock loading. This study focuses on the tin polymorphic phase transition ( $\beta$ - $\gamma$ ) under shock loading occurring around 9 GPa. Plate impact experiments are performed on a single stage gas gun and coupled with an X-ray X-Pinch generator developed at CEA Gramat. Studied samples are tin single crystals of known orientation with a diameter of 20 mm and a thickness of 1 mm backed by a boron carbide window. The projectiles are disks of various materials according to the pressure targeted with a diameter of 30 mm. X-ray diffraction measurements are achieved with a polychromatic X-ray radiation (100 ns duration) and recorded on image plate. A system has been developed to synchronize the X-ray generator with the impact facility. Experiments are performed at pressures beneath, above and near the tin solid-solid transition. Diffraction spots of each phase are expected to be identified and a transition mechanism inferred.

### 1. Introduction

A further understanding of the mechanisms involved in shock transformations is needed to improve our current numerical models. In most cases, static compression data and macroscopic measurements under dynamic loading, such as velocimetry, are used to infer the materials properties. However, our simulations do not reproduce accurately the materials behaviour. A microscopic analysis must be used to investigate mechanisms that could be incorporated into numerical models.

The implementation of X-ray diffraction is a complementary technique that could bring a new insight for studying materials at the atomic scale on both single crystals and polycrystals. Diffraction in these conditions requires that the X-rays are emitted in a powerful burst lasting several nanoseconds. Monochromatic or polychromatic radiations are needed respectively for polycrystals and single crystals. Nowadays, several techniques exist to perform such experiments in reflection or transmission geometry. It is possible to couple a synchrotron radiation with impact facilities to perform diffraction under shock [1] [2]. High energy lasers are also suitable to generate fast X-ray bursts [3]. In this case, the radiations emitted are specific to the material illuminated by the laser. Crystal compression [4] and phase changes [1] [2] [5] can be observed in diffraction under shock loading.

A device developed at CEA Gramat is an alternative to these techniques by using the radiation emitted by an X-Pinch generator [6]. Here, the X-rays are emitted by a short-circuit current going through thin metallic wires, crossed in a “X” shape. The wires implode during the current rise and generate a plasma emitting soft X-rays (< 10keV) followed by a harder emission (>10 keV) characteristic of the material constituting the wires.

\*Author for correspondence (david.palmadebarros@cea.fr).

less reproducible and less intense than those of synchrotron or laser backlighting but it is transportable, more accessible and easy to use. It can be used to prototype setups prior to perform experiments on great facilities.

The main challenge in using X-ray diffraction during fast compression relies on synchronizing the X-ray burst with the shock wave arrival in the material. Unlike laser shock experiments, gas (or powder) guns experiments uncertainties require to implement a synchronization system activated by the shock wave itself.

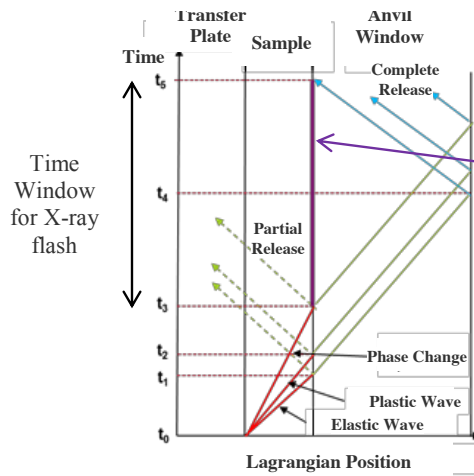
Tin is a material of great interest because it possesses a low fusion temperature and a low pressure solid-solid phase transition. It is therefore a good candidate for preliminary studies prior to investigating materials with a more complex phase diagram. In this study, the pressures of interest range from ambient pressure to approximatively 15 GPa. In this domain, tin exists in three different phases: two solid phases (beta and gamma phases) and a liquid phase. Several studies determined the crystal structure and the existence domain of each phase under static loading [7] [8] [9]. The beta phase exists at low temperature and low pressure, it possesses a double body centered tetragonal (bct) structure and transforms into the gamma phase (simple bct structure) around 10 GPa at ambient temperature and static compression. The tin phase structure has been studied over pressures ranging to 1,2 TPa [10] but it exceeds the frame of this study. The solid-solid phase transition on shock loading will be particularly investigated. Past studies have shown that an overshoot exists between the static transition pressure of this polymorphic transition and the pressures measured on shock loading. The transition pressures measured spreads between 8.5 and 10.5 GPa whereas a 7.5 GPa pressure is indicated by the static phase diagram at an equivalent temperature [11] [12] [13].

This paper describes the experiments performed at CEA Gramat coupling a single stage gas gun with an X-Pinch X-ray generator and the first results obtained. Additional experiments will be performed at CEA Gramat and in collaboration with the Dynamic Compression Sector (DCS) of the Advanced Photon Source (APS) and Sandia National Laboratories (SNL) in 2020. X-ray diffraction on shocked tin will enable to study its behaviour and compare it to static data particularly upon the phase transition where an overshoot was observed. Thanks to the results, several transformation mechanisms and kinetics could be proposed and integrated into our multiphase numerical model.

## 2. Experimental setup

The experiments are performed on a 32 mm bore single stage gas gun which can accelerate projectiles up to 750 m/s. The impactor nature is chosen relative to its impedance to reach the desired pressure in the target. The impact velocity is measured by wires in the barrel separated by a known distance and triggered by the impactor. The samples studied are tin single crystals (Goodfellow, purity 99,999%) of several orientations with a diameter of 20 mm and 1 mm thick. These samples are oriented and mounted on a copper transfer plate (Figure 2 a)). This one prevents the sample from being curved by the vacuum in the barrel and also enables to delay the shock wave arrival to let the synchronization system trigger the X-ray burst.

Since the diffraction measurements are performed in a reflection geometry at the center back of the sample, an anvil window must be used to maintain the pressure in the sample long enough to proceed the diffraction measurements. However, because of impedance mismatch, between tin and the window, only released states can be studied in tin (in the case of a lower impedance window). Boron Carbide ( $B_4C$ ) is used as anvil window. Its impedance is lower than tin but very close, this way, the pressure loss after shock wave reflection is reduced compared to other anvil windows (LiF, TPX). The  $B_4C$  windows are made of powder compressed into pellets which are 750  $\mu m$  thick and covering the whole sample (20 mm of diameter). The X-ray burst may occur during the round trip of the shock wave in the anvil (Figure 1). As a result, this one must be thick enough to enlarge the time window of observation, considering that it will arise its X-ray absorption. The polychromatic X-rays are produced by the implosion of gold wires with a diameter of 25  $\mu m$ . Past studies [6] have shown that this polychromatic beam has not a homogeneous spectrum. Its intensity is mainly governed by  $L_\alpha$  and  $L_\beta$  lines of gold.



The zone probed by the X-rays spreads over a few microns beneath the tin surface. A homogeneous state is reached in tin after the last shock wave has passed and before the arrival of the first release wave coming from the free surface. This time window is around 100 ns wide with a 750  $\mu\text{m}$  thick B<sub>4</sub>C window.

Figure 1: Wave propagation diagram during shock

The experimental setup is shown in Figure 2 b). A photodiode is used to measure the radiation power. It has been observed that the power profile is highly non reproducible from shot to shot in spite of the identical experimental configuration. This beam variation only affects the intensity of the diffraction patterns but not their shape. The beam is collimated by an adjustable tungsten slit before the interaction with the sample. The incidence angle is less than 20° and typically set to 14°. Diffraction patterns are collected on Image Plate (Fujifilm BAS-MS, 23x25 cm) and scanned (Typhoon FLA 7000). A secondary arm is used to analyze the diffraction pattern of a static sample which serves as reference. A Photon Doppler Velocimetry (PDV) system is also implemented at the back of the sample.

The X-ray burst is triggered by two diametrically opposed piezoelectric pins placed in a groove located on the transfer plate. Internal studies concluded that two pins are enough to compensate the potential impactor tilt (< 5 mrad) and trigger the X-ray burst. The trigger chain consists in several devices used to shape the signal and delay it relative to the shock wave travel. In order to set up this chain, the travel time of the shock wave between the pins and the back of the sample (probed zone) is calculated with impedance mismatch relations. As a tilt may be present during the impact, the two pin signals may be shifted in time. A Delay Generator is used to delay the trigger signal to synchronize the shock wave arrival with the X-ray flash taking into account the shifted pin signals and the internal delay of each device used in the chain.

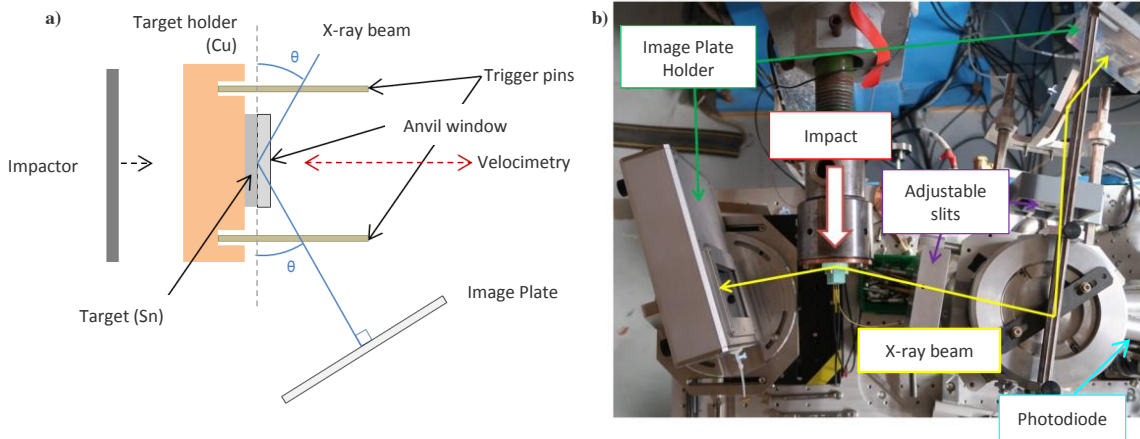


Figure 2: Target design (left) and experimental apparatus (right)

Prior to shock experiments, static diffraction patterns were obtained to determine the best experimental parameters: nature of wires, distance between detector and target, distance between source and target, slit dimensions. (110) oriented tin samples were chosen because of the numerous diffraction spots detected using gold wires with an incidence angle of 14°. The distance between the imaging plate and the sample was set to 22 cm. The slit dimensions was 3 mm high and 2 mm large, resulting in a spot size of 1,47 cm wide and 5 mm high on the sample, assuming a 400 μm diameter source [6].

Several experiments were performed on both free surface and backed surface at various impact speed. Table 1 summarizes the different shots. A static image was done before the shot to compare the results. Shots 311 and 317 were dedicated to test the synchronization system.

**Table 1: Summary of experiment parameters**

Shot number	Impactor	Impact Speed	Sn Orientation	Window	Sn shock pressure	X-Pinch wire
311	Cu	473 m/s	(110)	None	6.6 GPa	Au 25 μm
317	W	635 m/s	(110)	None	13 GPa	Au 25 μm
319	Cu	442 m/s	(110)	B <sub>4</sub> C	6.1 GPa	Au 25 μm

In the following, for each shot are showed diffraction patterns before and during shot. It is also showed velocity measurement performed by PDV and the corresponding X-ray emission during shot. The diffraction pattern of the reference sample did not show any difference between pre-shot and shot imaging. A specific tool developed at Gramat was designed to predict and index the diffraction patterns of tin single crystals. It takes into account the crystal orientation and the experimental parameters to simulate a possible diffraction pattern in a specific spectral range.

i. Shot 311

An impact velocity of 473 m/s was measured for shot 311 (450 m/s expected). The results are shown in Figure 3. The pressure target was far above the transition. By comparing the diffraction patterns (Figure 3 a) and Figure 3 b)), it is possible to see that the characteristic diffraction spots of (110) oriented tin remain under shock. However, the diffraction spots seem broader under shock indicating a possible texturation of the sample during compression [5] [14] [15]. The appearance of an arc shaped spot (red ring Figure 3 b)) is coherent with this hypothesis as it may correspond to a part of a diffraction ring of a tin polycrystal by a L<sub>α</sub> line of gold. Figure 3 c) shows that the X-ray flash was emitted during the velocity plateau reached by the tin free surface: the material was then probed after the shockwave has passed. The zone probed might not be representative of the real conditions into the material because of the vicinity of the free surface remaining at a constant atmosphere pressure. In spite of the presence of a free surface, the crystal seems to undergo crystallographic perturbations upon loading.

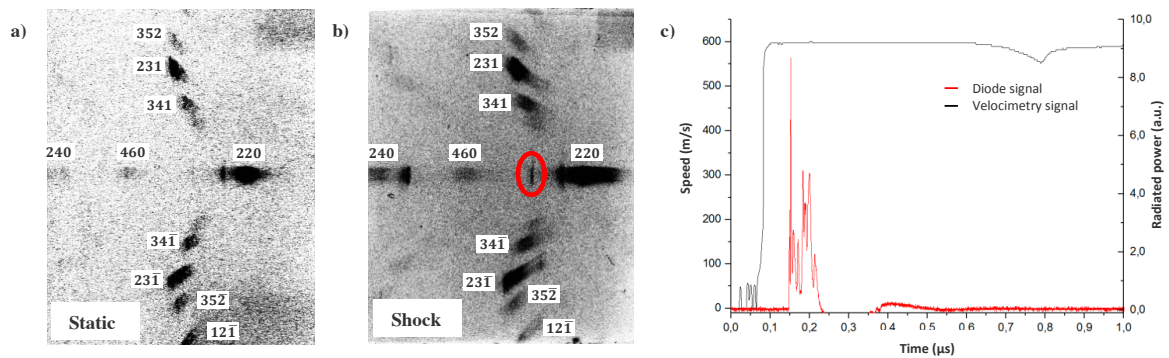


**Figure 3: Diffraction pattern in a) static, b) dynamic loading and c) velocity and X-ray signals for shot 311**

ii. Shot 317

Shot 317 was performed with an impact velocity of 635 m/s. The results are shown in Figure 4. The shock pressure was above the observed shock pressure of transition for tin of 9 GPa. This was confirmed by the presence of a shoulder during the velocity rise of free surface indicating the phase change. The presence of the diffraction spots indicate that a single (110) crystal still remain in the zone probed which is coherent with the free surface hypothesis. The spot in the red ring in Figure 4 a) indicates that the sample might possess some texture before the shot. During the shock, this spot grew and seem to be part of dim arcs with new elongated points (blue circles in Figure 4 b)). The broadening of diffraction spots is also observed. Like in shot 311, the zone probed might not be representative of the conditions in the material. However, a possible crystal deterioration may also be observed and seems to be more intense than for the shot 311.

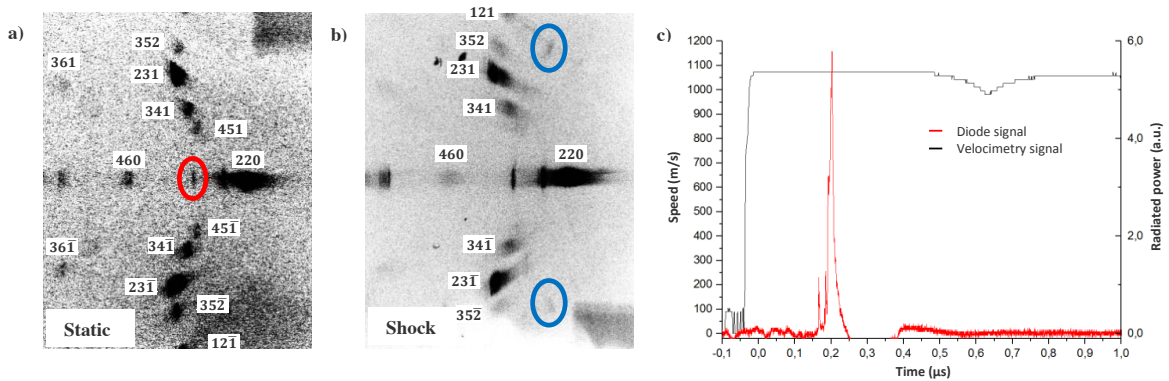


Figure 4: Diffraction pattern in a) static, b) dynamic loading and c) velocity and X-ray signals for shot 317

iii. Shot 319

A boron carbide window was used to maintain homogeneous pressure conditions under loading. Because impedance mismatch between tin and the window, a pressure of 5.7 GPa is deduced during the X-ray burst. The presence of diffraction rings in Figure 5 a) and b) shows that the X-ray emission is governed by intense monochromatic lines. An analysis of the boron carbide diffraction rings led to the conclusion that  $L\alpha$  and  $L\beta$  lines of gold wires may be responsible of the presence of the rings. These lines may also be responsible for the little arcs identified in the tin diffraction data.

A few tin diffraction spots are observed under shock loading in Figure 5 b). This can be explained by the low radiation power emitted by the source: this one is variable and has a great influence on the results. Between Figure 5 a) and b), the X-ray beam peak power during shock was almost one third of the radiated peak power for the first image (8.7 a.u. versus 3.4 a.u.). As a result, only the more intense points can be identified ((220), (231) and (341)). Unlike with a free surface, the presence of a window reduces the X-ray incoming and diffracted intensity. Tin seem to remain a single crystal with the same orientation. No evidence of texture evolution can be observed, maybe because of the lower beam intensity.

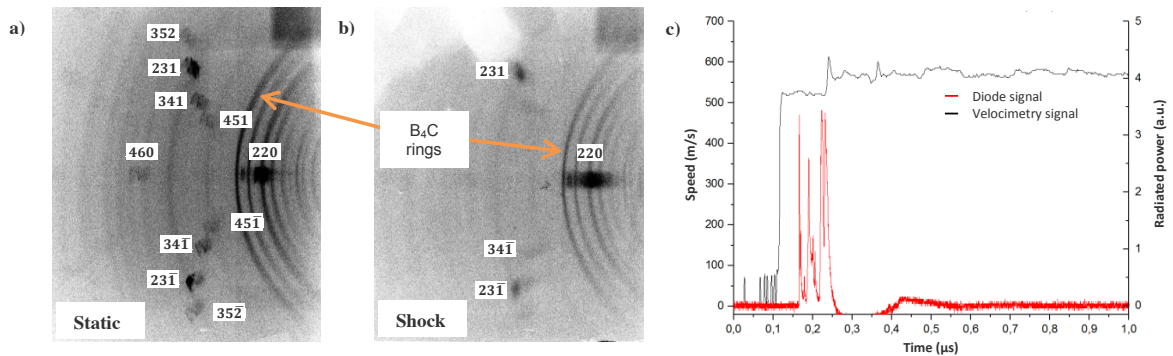


Figure 5: Diffraction pattern in a) static, b) dynamic loading and c) velocity and X-ray signals for shot 319

These first experimental results have demonstrated the possibility to use an X-Pinch source to perform X-ray diffraction. A triggering system was designed and approved to synchronize the X-ray flash with the shock wave propagation into the material. The comparison of the diffraction patterns before and during the shot gives the first clues of the tin behavior under dynamic loading. The loss of single crystalline properties seems to be more and more preponderant as the material gets closer to the transition. The transformation into a  $\gamma$  polycrystal could be proposed regarding the first results. Further experiments will be performed with anvil window of different impedance to probe several post-shock released states in order to propose a transition mechanism. The use of boron carbide windows will enable to probe states close to shock whereas lithium fluoride and PMMA windows will enable to probe states of lower pressure, near the transition border or the complete reverse transition.

### Acknowledgments

The team would like to thank Frederic Sinatti, Olivier Chaumeil, Lionel Renault, Sebastien Bergey and Ophélie Lassalle for their support in setting up plate impact experiments. The team would also like to thank Frederic Zucchini for his help on the X-Pinch generator and Thierry D'Almeida for useful discussion on X-ray diffraction.

### Funding Statement

This work was supported by the Commissariat à l'énergie atomique et aux énergies alternatives.

### References

1. Turneaure S. et al. 2016. Real-Time Examination of Atomistic Mechanisms during Shock-Induced Structural Transformation in Silicon. *Phys. Rev. Lett.* **117**, 045502. (10.1103/PhysRevLett.117.045502)
2. Kalita P. et al. 2017. Direct Observations of a Dynamically Driven Phase Transition with in situ X-Ray Diffraction in a Simple Ionic Crystal. *Phys. Rev. Lett.* **119**, 255701. (10.1103/PhysRevLett.119.255701)
3. Kalantar D.H. et al. 2005. Direct Observation of the  $\alpha$ - $\epsilon$  Transition in Shock-Compressed Iron via Nanosecond X-Ray Diffraction. *Phys. Rev. Lett.* **95**, 075502. (10.1103/PhysRevLett.95.075502)
4. D'Almeida T. et al. 2000. Real-time X-Ray Diffraction Measurements of the Phase Transition in KCl Shocked along [100]. *Phys. Rev. Lett.* **85**, 330-333.
5. Briggs R. et al. 2019. Observation of the shock-induced b-Sn to b.c.t.-Sn transition using time-resolved X-ray diffraction. *J. Synchrotron Rad.* **26**, 96-101. (10.1107/S1600577518015059)
6. Zucchini F. et al. 2015. Characteristics of a molybdenum X-pinch X-ray source as a probe source for X-ray diffraction studies. *Rev. Sci. Instrum.* **86**, 033507. (10.1063/1.4915496)
7. Liu M. et al. 1986. Compressions and phase transitions of tin to half a megabar. *High Temp.-High Press.* **18**, 79-85.
8. Plymate T.G. et al. 1988. Pressure-Volume-Temperature Behavior and Heterogeneous Equilibria of the Non-quenchable Body-centered Tetragonal Polymorph of Metallic Tin. *J. Phys. Chem. Solids* **49**, 1339-1348.
9. Cavaleri M.E. et al. 1988. A Pressure-Volume-Temperature Equation of State for b-Sn by Energy Dispersive X-Ray Diffraction in a Heated Diamond Anvil Cell. *J. Phys. Chem. Solids* **49**, 945-956.
10. Lazicki et al. 2015. X-Ray Diffraction of Solid Tin to 1.2 TPa. *Phys. Rev. Lett.* **115**, 075502. (10.1103/PhysRevLett.115.075502)
11. Anderson W.W. et al. 2000. Phase transition and spall behaviour in  $\beta$ -Tin. *AIP Conference Proceedings* **505**, 443-446. (10.1063/1.1307163)
12. Mabire C. et al. 2000. Shock Induced Polymorphic Transition and Melting of Tin. *AIP Conference Proceedings* **505**, 93-96. (10.1063/1.1303429)
13. Zhernokletov M.V. et al. 2012. Measurement of the Sound Velocities behind the Shock Wave Front in Tin. *Combustion, Explosion, and Shock Waves* **48**, **1**, 112-118. (10.1134/S0010508212010145)
14. Turneaure S. et al. 2018. Nanosecond Melting and Recrystallization in Shock-Compressed Silicon. *Phys. Rev. Lett.* **121**, 135701. (10.1103/PhysRevLett.121.135701)
15. Gorman M.G. et al. 2015. Direct Observation of Melting in Shock-Compressed Bismuth With Femtosecond X-ray Diffraction. *Phys. Rev. Lett.* **115**, 095701. (10.1103/PhysRevLett.115.095701)

# Visualization of impact damage in Sapphire using high-speed photography and Edge-On impact technique

Bratislav Lukić<sup>1</sup> and Pascal Forquin<sup>1</sup>

<sup>1</sup>Univ. Grenoble Alpes, CNRS, Grenoble INP\*, 3SR, F-38000 Grenoble, France

\*Institute of Engineering Univ. Grenoble Alpes

**Keywords:** Edge-On impact test, Sapphire, High-speed photography, Impact damage.

## Abstract

Fragmentation experiments have been carried out on a sapphire mono-crystalline using the Edge-On impact technique. Direct ultra-high speed photography, with inter-frame time down to 200 ns, was used to record the time resolved evolution of the impact damage during the first thirty microseconds from impact. The influence of the orientation of the principle c-axis with respect to impact direction was investigated as well as the condition of sample edges. Consequently, samples with both polished and unpolished edge surfaces were impacted with a steel projectile at a striking velocity of around  $260 \text{ ms}^{-1}$ . The visual inspection of the obtained image sequences is carried and the results are discussed and compared in terms of damage phenomenology and cracking patterns.

## Introduction

High-strength transparent ceramics are been used in many industrial and military situations in which structural integrity of the end product is of key importance. In such applications, that range from aerospace vision systems over optical protection covers to transparent lightweight solutions, the material gets constantly exposed to extreme scenarios in which its ability to resist impact and shock dictates its applicability and the overall design. Sapphire mono-crystalline solutions are often preferred choice in these situations, thanks to the material's high mechanical and physical properties. However, the challenges related to fabrication demand for constant optimisation. The careful design needs to be backed by faithful numerical models. These models need to be validated against experimental works which are able to reproduce corresponding extreme loading scenarios under controlled conditions. The Edge-on impact (EOI) test is one such experiment which, thanks to ultra-high speed imaging, allows to study the material fragmentation by visualising the material damage phenomenology during an impact of a projectile against the edge of a ceramic tile. This data then presents a good basis for comparing various damage modeling tools in terms of fragmentation prediction [1,2].

In this work, EOI tests are conducted on sapphire samples with different orientations of the crystalline c-axis with respect to impact direction. Additionally, two cases of edge surface treatment are considered, namely with and without edge polishing. The aim of this investigation is to contribute to the better understanding of the fragmentation processes sapphire under impact, as well as to investigate how the production processes might affect the corresponding damage morphology.

## Methods and Material

### Experimental set-up

The EOI tests were conducted with an existing experimental installation in the 3SR Laboratory. The schematic representation of the test configuration is shown on Fig 1. A gas gun is used to launch a cylindrical steel projectile ( $D=10 \text{ mm}$  and  $L=20 \text{ mm}$ ) with a polytetrafluoroethylene (PTFE) sabot ( $D=20.1 \text{ mm}$  and  $L=19.1 \text{ mm}$ ),

\*Author for correspondence (bratislav.lukic@3sr-grenoble.fr).

† Present address: Laboratoire 3SR, Université Grenoble Alpes, Grenoble, 38400, France

resulting in a total mass of around 16 g. Both spherical-cap and flat-end projectile types were used in order to alter the shape of the stress wave front generated in the samples. Three photo-diodes at 50 mm subsequent distance from the barrel exit were used to record the passage times and deduce the exit speed of the striker. The impact velocity was extrapolated from this information taking into account the striker acceleration which was compared to that obtained from the recorded image sequences. In this work the Kirana ultra-high speed camera from Specialised Imaging (S.I.) was used to film the entire fragmentation process in the sample with 5 Mfps and 100 ns exposure time, which allowed to substantially reduce the motion blur effect due to rapid crack propagation. Thanks to the camera in-situ memory storage, both images before and after the supplied trigger event can be obtained, resulting in a total 180 frames of  $924 \times 768$  px in one single sequence. A laser interferometer of 10 MHz bandwidth and 10V capacity was pointed towards the rear-end of the sapphire plates and was used to supply the trigger event to the camera. The camera was equipped with a standard 105 mm Sigma Macro lens providing an approximate  $135 \mu\text{m}$  pixel size. Due to the low exposure time a powerful illumination source proved to be necessary in order to well illuminate the scene. To this end a flash light having a maximum of 500 J (AD-500) stored charge was employed. Owing to a rising time of approximately  $160 \mu\text{s}$  until a stable illumination level, the flash needed to be triggered separately at a exact instance. The signal from the photo-diode was used with a signal generating oscilloscope (Keysight DSOS254A) to produce a trigger event. Then a signal delay generator (SI-VT-SYS) unit was used taking into account the time of flight of the projectile to finely shift the signal and trigger the flash at desired moment. A blank paper was placed in the background of the sample and the camera focus point was set to the samples middle plane. In such configuration, direct light reflection imaging was made possible despite the transparency of the sample. This allowed circumventing the challenges of using shadowgraph methods which can lead to image saturation or gluing a reflective aluminium foil on the sample surface as in [4].

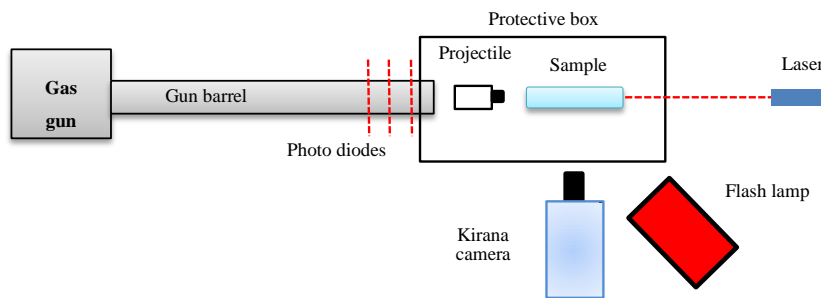


Figure 1: Schematic representation of the EOI set-up (top-view).

## Tested samples

The tests were conducted on sapphire mono-crystal ( $\text{Al}_2\text{O}_3$ ) samples of  $100 \times 100 \times 7.62$  mm supplied by Saint Gobain. This material owns its variety of application, that ranges from optical windows for ballistic protection, over aeronautical to semiconductor industry, thanks to its extremely high mechanical characteristics (Table 1). Two types of sample edge treatment were considered, namely samples with polished edge surfaces, and samples with unpolished or also referred to 'as grown'. The question arises to which extent the surface polishing can alter the sample fragmentation under extreme loading scenarios. Furthermore, the orientation of the principal c-axis was also considered by altering it with respect to impact direction for both types of samples.

## Observations

In the following a visual inspection is carried out as to provide a qualitative comparison between the tested samples. The terminology adopted to describe the damage phenomenology corresponds to the nomencla-

\*Author for correspondence (bratislav.lukic@3sr-grenoble.fr).

† Present address: Laboratoire 3SR, Université Grenoble Alpes, Grenoble, 38400, France

Density	3970 kg/m <sup>3</sup>
Young's Modulus	435 GPa
Compressive strength	2 GPa
Flexural strength	1 GPa

**Table 1:** Mechanical properties of Saint-Gobain Sapphire material [3]

ture used in [4,5,6].

### Effect of c-axis orientation

Figure 2 presents frames at specific time from the impact for the case of two EOI experiments carried out on sapphire samples with treated surface edges. The two cases correspond to different c-axis orientation, namely the orientation perpendicular (C1) and parallel (C2) to the impact direction. A spherical-cap steel projectile ( $R=100$  mm) was used to impact the edge of the samples at speed of  $260\text{ ms}^{-1}$  for C1 and  $245\text{ ms}^{-1}$  for C2. Figure 2a and 2b correspond to sample damage state  $10\text{ }\mu\text{s}$  after the impact. At this stage a characteristic cracking pattern can be observed in terms of two cone cracks for both cases. The primary fracture front driven by the compression stress wave appears to be of the same size for both cases. However, the C2 sample exhibits higher concentration of sharp cracks in the secondary crack zone above and below the characteristic cone cracks. As the compressive stress wave progresses towards the free-end, Figures 2c and 2d, it can be observed that the damage morphology between the two cases starts to deviate. In the case of C1 sample orientation, several cracks initiate in zone closer to the free-end. These cracks seem to be initiated from the volume since the possibility of them being the tip of the front propagating cracks is ruled out by tacking into account the distance at which they form and the wave propagation speed. These volume initiated cracks appear to propagate with an angle between 30 and 40 degrees with respect to c-axis orientation. In the case of the C2 sample orientation, no such cracks are observed, rather several cracks initiate directly from the sample free-end which after short propagation time tend to branch. Furthermore, several pronounced cracks can be observed just in front the primary fracture front in the C2 case. And an overall higher number of so-called fuzzy cracks can be observed in the C2 case while cracking patterns of seem more diffuse in the C1 case. Similar observations were made in C1 and C2 samples for which the edge surfaces were not treated (Figure 3a-d).

### Effect of the edge surface treatment

Damage patterns at several specific time increments regarding EOI tests conducted on sapphire samples which did not undergo edge surface treatment are presented in Figure 3. The impact velocity was around  $265\text{ ms}^{-1}$  in both cases. During the first  $10\text{ }\mu\text{s}$  from the impact the damage patters for the samples without edge surface treatment show subtle difference with respect to samples with polished edges presented in 2. For example, for the case when c-axis is perpendicular to impact direction (C1) the damage patterns are quite similar (Figure 2a and Figure 3a). In the case when the c-axis is parallel to the impact direction (C2), a crack type 2 can be noticed for the case of sample non-treated edges in Figure 3b in comparison to Figure 2b. It can be speculated that due the presence of this crack the formation of the cracks at the free-end is delayed with respect to polished sample (Figure 3d). Nevertheless, the damage phenomenology seems to follow the same sequence for the case of samples without polished edges and samples with polished edges. In case for C1 orientation, cracks initiate within the volume and in the case of C2 orientation several cracks initiate from the free-end as previously observed for samples with polished edges. This suggests that the orientation of the c-axis plays a leading role with respect to fragmentation phenomenology in sapphire tiles under impact. What is interesting is to compare is number of cracks initiated at the free-end and the spall crater size in case of C2 orientation for both types of samples, as depicted in Figure 4. It appears that a slightly higher number of cracks are initiated in case with samples with polished edges (Figure 4a and 4b) which propagate, branch and fuse together finally forming an apparently larger spall crater than in the case for samples with no edge treatment.

\*Author for correspondence (bratislav.lukic@3sr-grenoble.fr ).

† Present address: Laboratoire 3SR, Université Grenoble Alpes, Grenoble, 38400, France

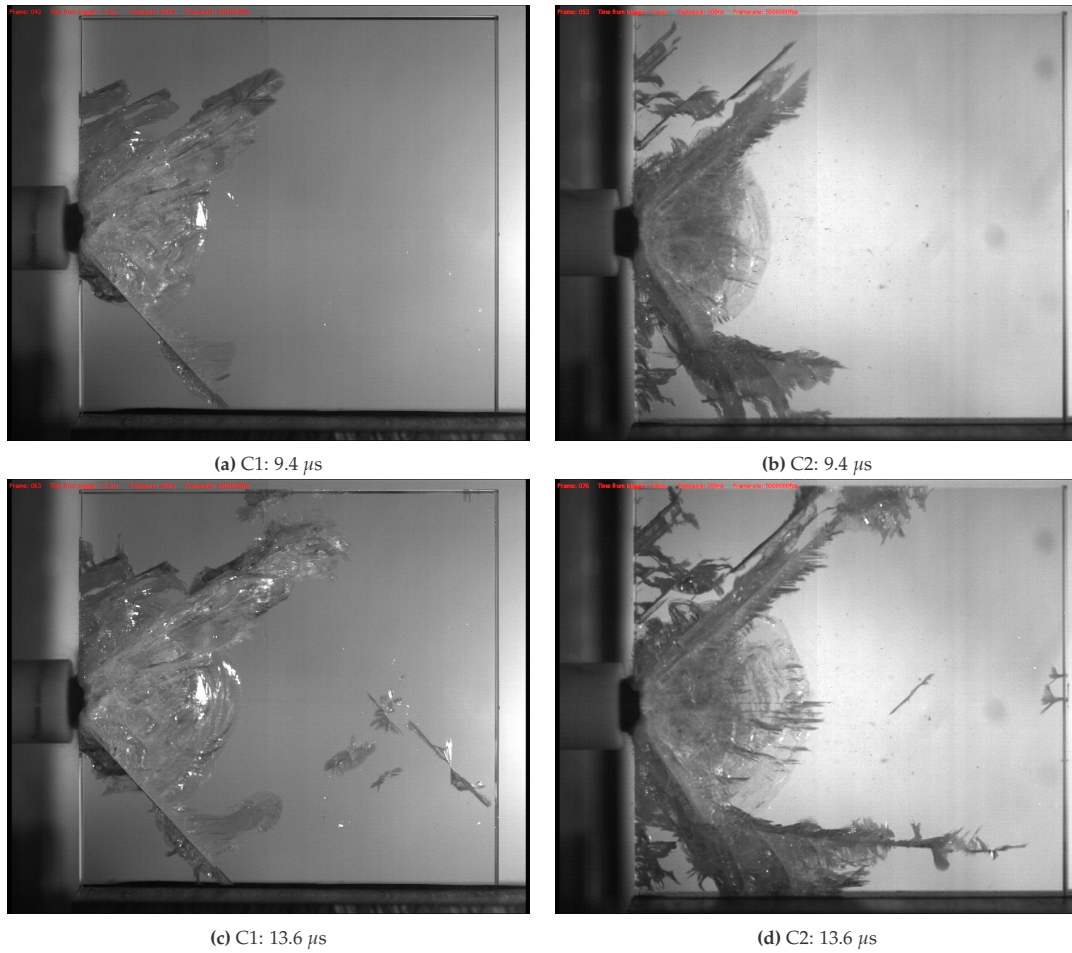


**Figure 2:** Subsequent images of two sapphire samples with polished edges (SCPCP) after impact alternating the c-axis orientation: *left* – c-axis perpendicular to impact direction (C1); *right* – c-axis parallel to impact direction (C2).

\*Author for correspondence (bratislav.lukic@3sr-grenoble.fr).

† Present address: Laboratoire 3SR, Université Grenoble Alpes, Grenoble, 38400, France

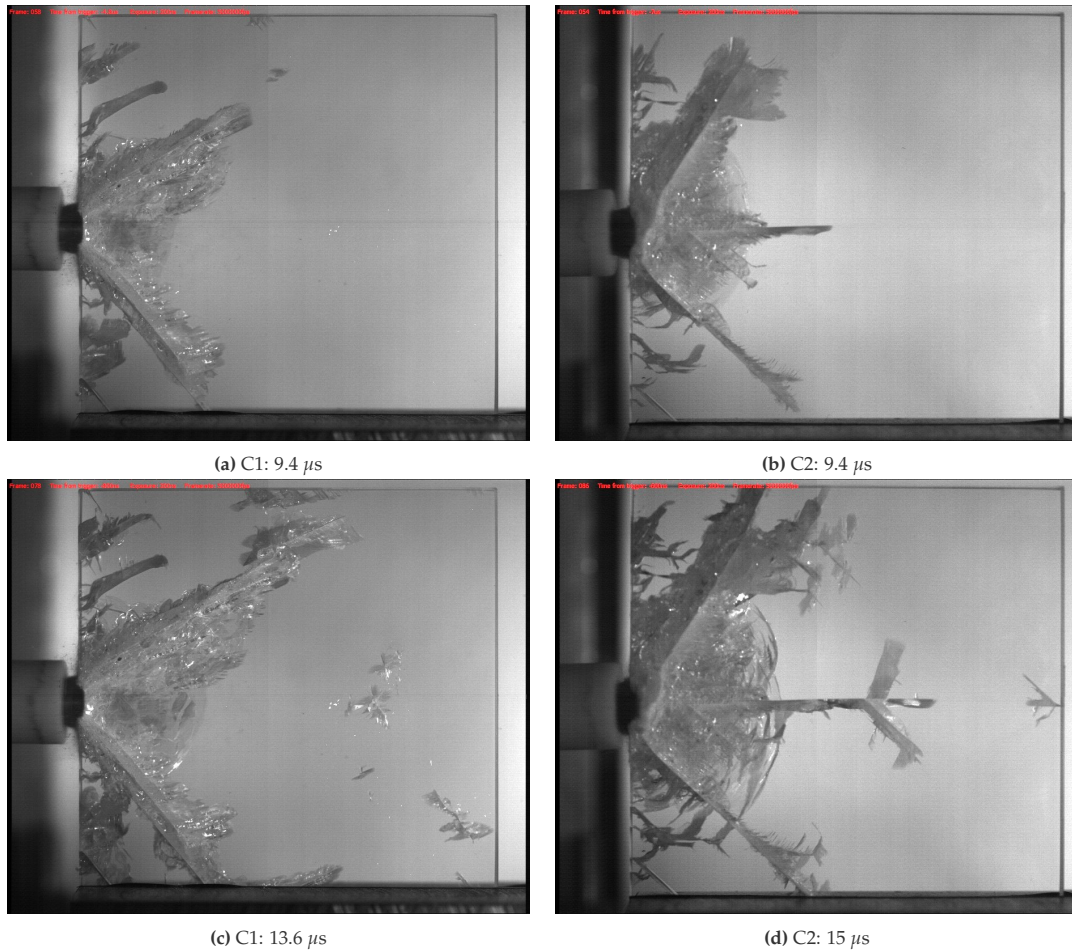


**Figure 3:** Subsequent images of two sapphire samples without edge surface treatment (SCDCD) after impact alternating the c-axis orientation: *left* – c-axis perpendicular to impact direction (C1); *right* – c-axis parallel to impact direction (C2).

\*Author for correspondence (bratislav.lukic@3sr-grenoble.fr ).

† Present address: Laboratoire 3SR, Université Grenoble Alpes, Grenoble, 38400, France

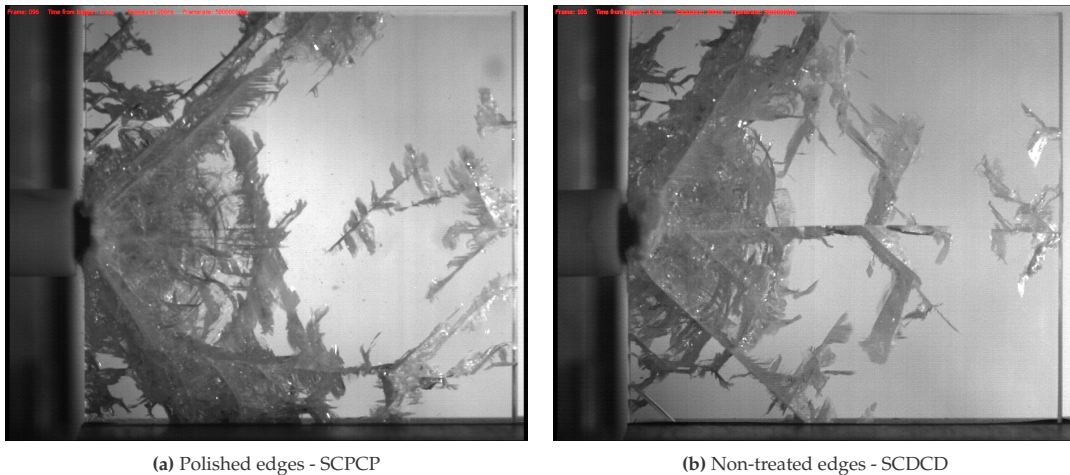


**Figure 4:** Final images of two sapphire samples with and without edge surface treatment having the c-axis orientation parallel to the impact direction. More cracks can be observed to initiate from free-end in the case of sample with polished surface edges.

## Summary

The Edge-On impact experiments were carried out on sapphire mono-crystal tiles of 100x100x7.62 mm with impact velocities around  $260 \text{ ms}^{-1}$ . An ultra-high speed imaging camera was used to film the damage phenomenology over  $30 \mu\text{s}$  from the impact with 5 Mfps and exposure time of 100 ns. Samples with and without surface edge polishing was considered as well as the orientation of the crystallographic c-axis with respect to impact. It was observed that the orientation of the c-axis plays a role in the fracture development. While in cases when the c-axis was perpendicular to the impact directions some volume fractures were observed after first  $10 \mu\text{s}$  from impact, while in the case where the c-axis was parallel to the impact direction the cracks initiated at the free surface instead. In the case of sample polishing, it was observed that the samples with polished edges exhibit somewhat larger number of fractures that initiate from free end.

## References

1. Strassburger, E. 2004. Visualization of impact damage in ceramics using the edge-on impact technique *International Journal of Applied Ceramic Technology* **3**, 235-242.
2. Forquin, P., Hild, F. 2010. A probabilistic damage model of the dynamic fragmentation process in brittle materials. *Adv. Appl. Mech.* **44**, 1-72.
3. <https://www.crystals.saint-gobain.com/products/synthetic-sapphire-materials>
4. Strassburger, E., Senf, H., Rothenhäusler, H. 1994 *Journal de Physique IV Colloque* **04**, C8-653-C8-658.
5. McCauley, J.W., Strassburger, E., Patel, P., Paliwal, P., Ramesh, K.T. 2012. Experimental Observations on Dynamic Response of Selected Transparent Armor Materials. *Exp. Mech.* **53**, 3-29. (doi)
6. Senf, H., Strassburger, E., Rothenhäusler, H. 1994 Stress Wave Induced Damage and Fracture in Impacted Glasses *Proc. 4th DYMAT conference*

# **hNumerically-based evaluation of the dynamic behaviour of typical triply periodic minimal surface additively-manufactured structures**

**H. Carassus\* \*\*, J.D. Guérin\*, H. Morvan\*, G. Haugou\*, E. Markiewicz\*, S. Guérard\*\***

*\* Univ. Polytechnique Hauts-de-France, CNRS, UMR 8201-LAMIH, F-59313 Valenciennes, France*

*\*\* Arts et Métiers ParisTech, I2M, CNRS UMR 5295, F-33405 Talence, France*

**Keywords:** Finite element modelling, Cellular materials, Gyroid, Diamond, Mechanical behaviour, Energy absorption, TPMS, Dynamic compression

---

## 1. Introduction

Cellular materials such as foams or honeycombs are widely used to design several mechanical parts of components thanks to their high specific strength, good energy absorption capabilities and acoustic insulation performances [1;2].

Additive manufacturing (AM) is more and more used to build easily and efficiently architectural materials such as lattice structures [2]. By giving access to a new level of complexity at the mesoscopic scale, AM can produce periodic structures with a unit cell sizes in the range of the millimeter and a truss diameter close to 100  $\mu\text{m}$  [3].

Numerous studies have been performed on lattice structures in order to compare the crushing behaviour of several patterns [4;5], to study the influence of the bulk material behaviour [5] or even to investigate the effect of the loading rate [6]. Due to the manufacturing process, an important limitation of these cellular materials is linked to the build angle of the truss with the possible need of support structures to achieve good results. It has been shown that a strut inclination of 0 degree is not recommended due to an oversized strut diameters and unmelted particles [5].

Triply Periodic Minimal Surfaces (TPMS) are minimal surfaces with a periodicity in the three independent directions which lead to smooth and continuous structures unlike lattice structures. A recent study on the mechanical behaviour of several 3D printed cellular materials under quasi-static compression loading has shown that sheet TPMS diamond pattern leads to better mechanical properties in terms of energy absorption performances, than most of lattice structures [7].

So far and to our knowledge, TPMS were not studied at high rate of loadings. Thus, considering the efficiency of TPMS to absorb energy, the aim of this paper is to investigate the dynamic behaviour under uniaxial compression of two kinds of promising patterns: diamond and gyroid.

As a first step, before printing 3D specimens and performing an experimental campaign, a numerical study has been performed to assess the performance of these two patterns in the two sub-families of TPMS: skeletal and sheet. The influence of density was also investigated.

\*Author for correspondence: H.Carassus (hugo.carassus@uphf.fr).

†Present address: LAMIH CISIT, UPHF, 59300 Valenciennes, France

a. TPMS design

TPMS are defined by implicit functions, namely Equation (1) for gyroid and (2) for diamond, that minimize locally the area of the surface for given boundaries. With Fourier series expansions, those equations give access to the approximated level surface.

Gyroid 
$$\cos(kx) \sin(ky) + \cos(ky) \sin(kz) + \cos(kz) \sin(kx) = t \quad (1)$$

Diamond 
$$\sin(kx) \sin(ky) \sin(kz) + \cos(kz) \cos(ky) \sin(kx) + \cos(kx) \sin(ky) \cos(kz) + \cos(kz) \cos(kx) \cos(ky) = t \quad (2)$$

where  $x, y$  and  $z$  are the Cartesian coordinates,  $k = 2\pi/l$  where  $l$  is the length of a unit cell,  $t$  is the level-set parameter ( $t \in [-1.41; 1.41]$  for gyroid and  $t \in [-0.99; 0.99]$  for diamond). Then it is possible to distinguish two types of TPMS: sheet TPMS and skeletal TPMS.

The first one is obtained by a homogeneous thickening of the isosurface, with  $t = 0$ , whereas the second one has a non-null value of the level-set parameter  $t$ , given that it is implicitly linked to the relative density, as shown on Figure 1.

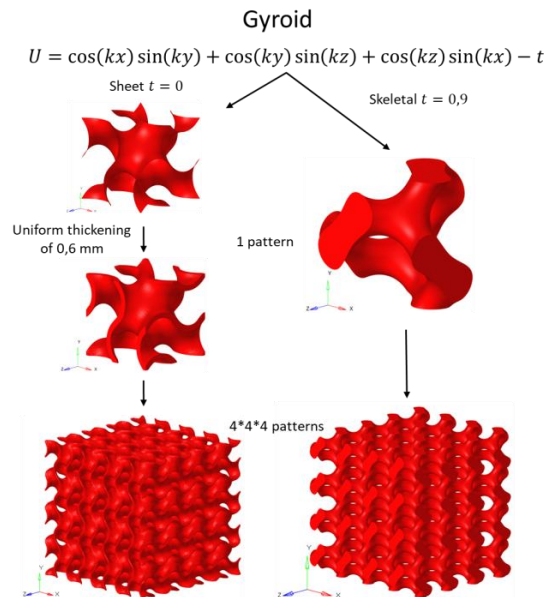


Figure 1 : Generation process of skeletal and sheet gyroid with a unit cell size of 10 mm for a 20 % relative density

Figure 2 represents the unit cell's models for sheet and skeletal TPMS : the left column displays the isosurfaces of diamond and gyroid TPMS whereas the central and right columns present four patterns studied in this work with a 20 % fixed relative density.

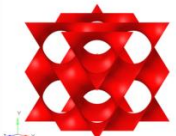
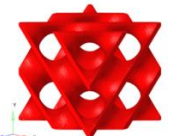
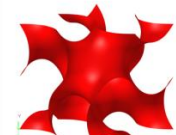
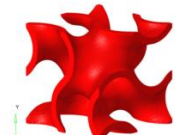
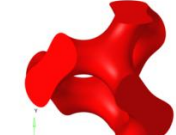
	Isosurface	Sheet TPMS	Skeletal TPMS
Diamond			
Gyroid			

Figure 2 : 10 mm unit cell's models with 20 % relative density for sheet and skeletal TPMS

fixed to  $40 * 40 * 40 \text{ mm}^3$  with a unit cell size of  $10 \text{ mm}$  to fulfil experiment capacities, 64 patterns in total with four cells in the three space directions were then created. The number of repeating cells is the minimum to have a convergence of mechanical properties [8]. Thus, eight CAD of the four patterns with two relative densities of 20 % and 30 % were used for simulations. 20 % relative density corresponds to a critical minimal thickness for additive manufacturing and 30 % corresponds to an upper boundary defining cellular structures [9].

As design methods for sheet and skeletal TPMS are not the same, sheet models are composed of pentahedron elements (triangle elements thickened) whereas skeletal models are constituted with tetrahedron elements.

A titane alloy, Ti-6Al-4V, was picked as base material because of the possible applications of this study concerning the aeronautical field. The elasto-plastic material behaviour was implemented using a Johnson-Cook model expressed by Equation (3)

$$\sigma_s = [A + B(\varepsilon_e)^n] \left[ 1 + C \ln \frac{\dot{\varepsilon}}{\dot{\varepsilon}_0} \right] \left[ 1 - \left( \frac{T - T_0}{T_m - T_0} \right)^m \right] \quad (3)$$

where  $\varepsilon_e$  is the equivalent plastic strain with  $\dot{\varepsilon}_0 = 1.0 \text{ s}^{-1}$  for a metallic alloy,  $T_m$  the melting temperature,  $T_0$  the room temperature and  $A, B, n, C$  and  $m$  are the material constants. The material data were extracted from the work of [10] which considered the properties of the bulk material used in SLM. They are expressed in Table 1.

**Table 1 : Parameters of the Johnson-Cook model**

$A \text{ (MPa)}$	$B \text{ (MPa)}$	$C$	$n$	$N$	$T_m \text{ (}^\circ\text{C)}$	$T_0 \text{ (}^\circ\text{C)}$
1567	952	0.01	0.8	0.4	1605	20

The numerical study was carried out with the software HYPERCRASH. To model the dynamic uniaxial compression, TPMS were placed between two parallel rigid bodies (as shown on Figure 3). The bottom plane remains fixed while the top plane is moved to a constant speed of  $20 \text{ m.s}^{-1}$ , with a maximal displacement of  $0,28 \text{ mm}$  (corresponding to a macroscopic strain of 7 %). Computations were not pursued furthermore because the fracture behaviour of the material is not considered in the Johnson-Cook model. Three contact interfaces master/slave were necessary here: two for each plane and the TPMS and one self-contact applied to the TPMS to avoid self-penetration.

Calculations were launched with the explicit solver RADIOSS using parallelisation on six processors.

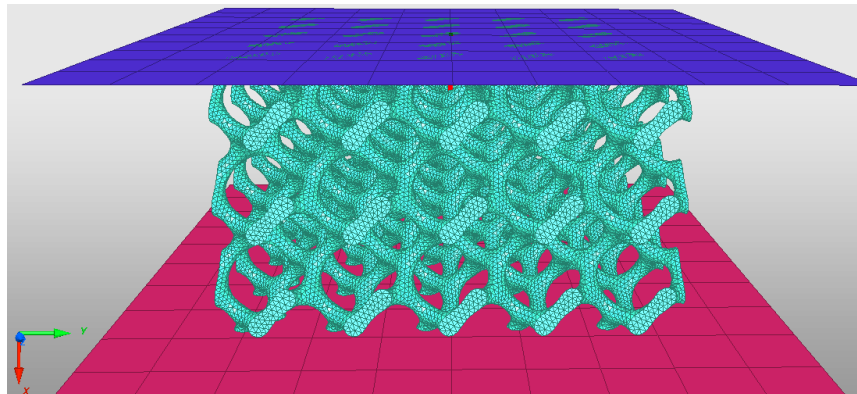


**Figure 3 : Compression's modelling of skeletal gyroid with a 20% relative density**

reaction force of the bottom plane (pink plane on the Figure 3) divided by the apparent section  $40 * 40 \text{ mm}^2$ , and the strain is the division of the top plane displacement by the height ( $40 \text{ mm}$ ). Values of absorbed energy  $\psi$ , defined as areas under stress-strain curves, and absorbed energy density  $\psi_v$  are presented in Table 2.

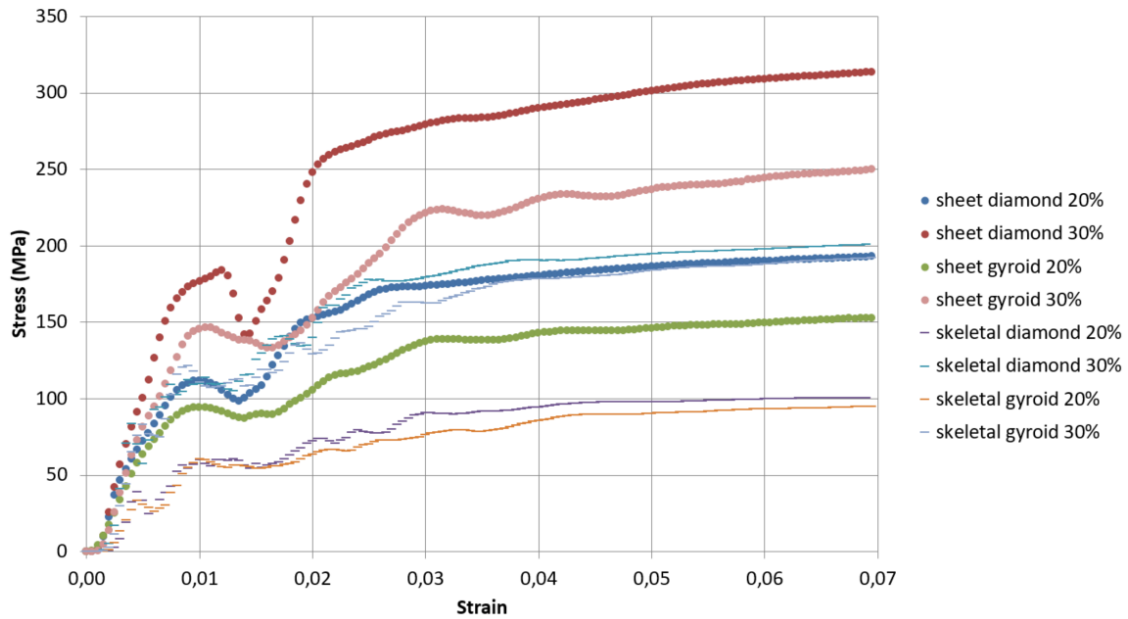


Figure 4 : Stress-strain curves of the eight models at a loading rate of 20 m/s

Table 2 : Absorbed energy and absorbed energy density extracted from stress-strain curves

	Sheet				Skeletal			
	diamond 20%	diamond 30%	gyroid 20%	gyroid 30%	diamond 20%	diamond 30%	gyroid 20%	gyroid 30%
$\psi \text{ (J)}$	10,8	17,3	8,5	13,4	5,4	11,1	5	10,5
$\psi_v \text{ (MJ/m}^3\text{)}$	0,84	0,90	0,66	0,70	0,42	0,58	0,39	0,55

Similar trends are discernible for all models on the Figure 4. At first a peak of stress can be observed followed by a stress collapse and progressively reduced oscillations leading to a slowly increase in stress. It can be interpreted that the drop and oscillations are due to reflexions of elastic's waves between the upper and lower planes. A phenomenon that is less pronounced at lower loading rate (Figure 5).

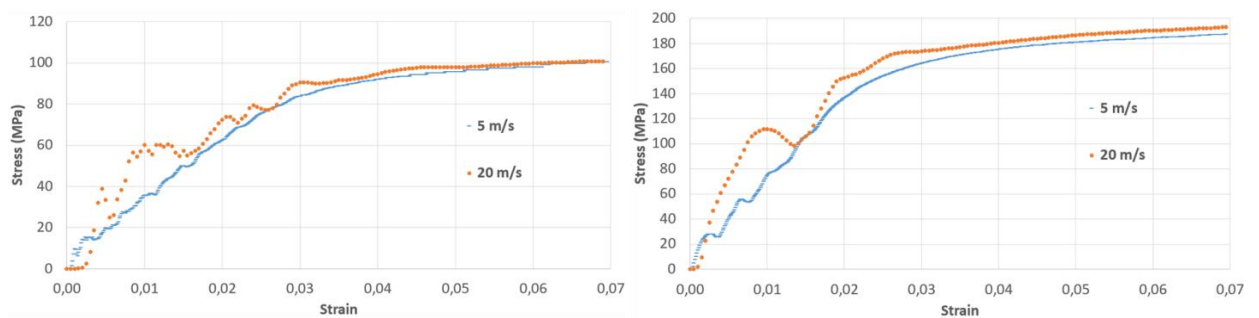


Figure 5 : Loading rate's influence on skeletal diamond on the left and sheet diamond on the right, both with a 20% relative density

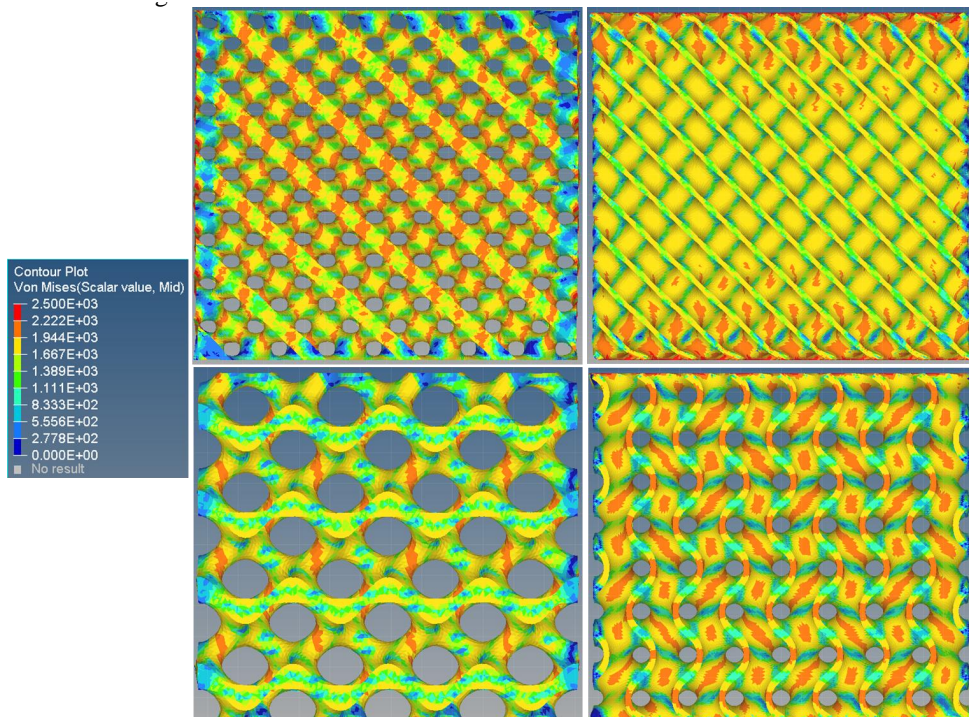


Figure 6 : Von Mises's stresses (MPa) distribution on a mid-slice of skeletal diamond on the upper left and sheet diamond on the upper right, skeletal gyroid on the lower left and skeletal gyroid on the upper right, all with 20 % relative density and deformed by a 0,28 mm compression (macroscopic strain of 7 %)

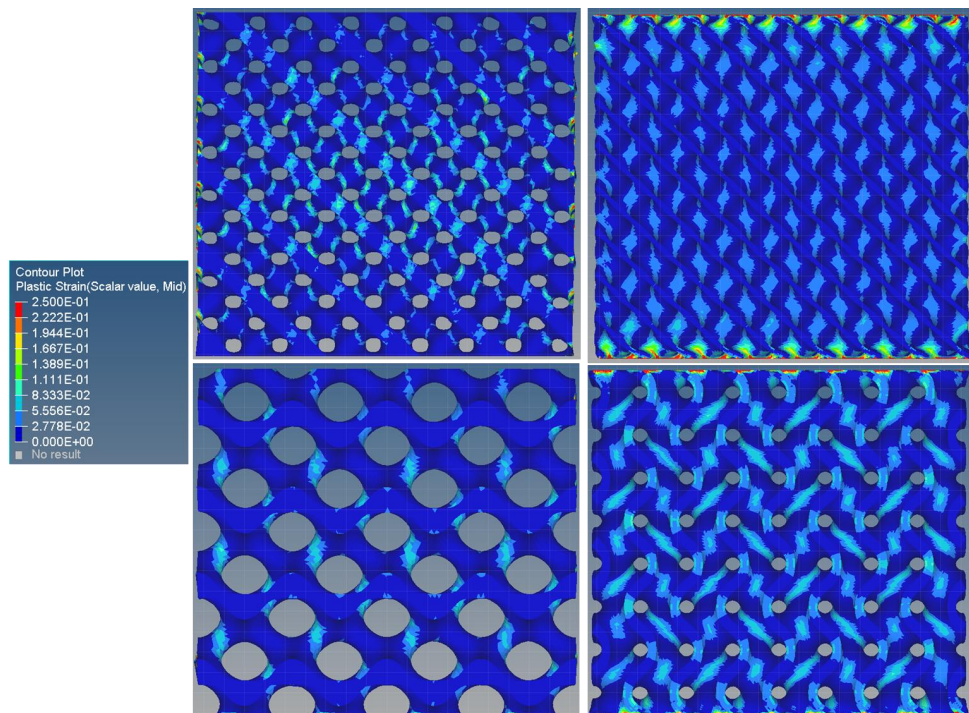


Figure 7 : Plastic strains distribution on a mid-slice of skeletal diamond on the upper left and sheet diamond on the upper right, skeletal gyroid on the lower left and skeletal gyroid on the upper right, all with 20 % relative density and deformed by a 0,28 mm compression (macroscopic strain of 7 %)

and 6 % difference's in average for sheet's.

For both 20 % and 30 % relative densities, sheet diamond is the one which is able to absorb more energy in the case of a dynamic uniaxial compression.

#### 4. Conclusions

The aim of this simulation campaign is to compare additive manufactured architected structures in terms of dynamic performances. Thus influences of the TPMS family, the relative density and the pattern have been numerically investigated on dynamic uniaxial compression. Sheet TPMS, thanks to a smoother surface and a greater surface area is more performant to absorb energy. With the two relative densities tested, the amount of energy absorbed during the compression increases as the relative density increases, even more for skeletal TPMS. Over the two patterns studied, diamond and gyroid, the first one is always ahead of the other with skeletal or sheet TPMS's.

Further works will be focusing on multi-axial loadings simulations with those eight patterns. Results will be combined with those of this work to choose the best configurations for experimental works.

#### Funding Statement

This work is supported by Institut Carnot ARTS and Haut-de-France region.

#### References:

- 1.M.F. Ashby. 2006. The properties of foams and lattices. *Phil. Trans. R. Soc. A* **364**, 15-30. (10.1098/rsta.2005.1678)
2. M.G. Rashed, Mahmud Ashraf, R.A.W.Mines, Paul J. Hazell. 2016. Metallic microlattice materials: A current state of the art on manufacturing, mechanical properties and applications. *MD* **95**, 518-533. (10.1016/j.matdes.2016.01.146)
3. T. A. Schaedler, A. J. Jacobsen, A. Torrents, A. E. Sorensen, J. Lian, et al. 2011. Ultralight Metallic Microlattices. *Science* **334**, issue 6058 p 962-965. (10.1126/science.1211649)
4. Nan Jin, Fuchi Wang, Yangwei Wang, Bowen Zhang, Huanwu Cheng, Hongmei Zhang. 2019. Failure and energy absorption characteristics of four lattice structures under dynamic loading. *Materials and Design* **169**, 107655. (10.1016/j.matdes.2019.107655)
5. M.Mazur, M.Leary, M.McMillan, S.Sun, D.Shidid, M.Brandt. 2017. Mechanical properties of Ti6Al4V and AlSi12Mg lattice structures manufactured by Selective Laser Melting (SLM). *LAM*, 119-161. (10.1016/B978-0-08-100433-3.00005-1)
6. Thomas Tancogne-Dejean, Adriaan B. Spierings, Dirk Mohr. 2016. Additively-manufactured metallic micro-lattice materials for high specific energy absorption under static and dynamic loading. *AM* **116**, 14-28. (10.1016/j.actamat.2016.05.0541359-6454)
7. Oraib Al-Ketan, Reza Rowshan, Rashid K. Abu Al-Rub. 2018. Topology-mechanical property relationship of 3D printed strut, skeletal, and sheet based periodic metallic cellular materials. *AM* **19**, 167-183. (10.1016/j.addma.2017.12.006)
8. S.J.N. Morrish, M. Pedersen, K.F.W.Wong, I.Todd, R.Goodall. 2017. Size effects in compression in Electron Beam Melted Ti6Al4V diamond structure lattices. *Materials Letters* **190**, 138-142. (doi.org/10.1016/j.matlet.2016.12.130)
9. Lorna J. Gibson, Michael F. Ashby. 1997. Cellular Solids: Structure and Properties. Second Edition. Chapter I, Introduction (10.1017/CBO9781139878326)
10. Lei Yang, Chunze Yan, Changjun Han, Peng Chen, Shoufeng Yang, Yusheng Shi. 2019. Mechanical response of a triply periodic minimal surface cellular structures manufactured by selective laser melting. *IJMS* **148**, 149-157. (10.1016/j.ijmecsci.2018.08.039)

# Shear Characterization of Thin Sheet Material using Rectangular Specimen on Torsion Hopkinson Bar

Bhaskar Ramagiri<sup>1</sup>, Chandra Sekher Yerramalli<sup>1</sup>

<sup>1</sup>Department of Aerospace Engineering, Indian Institute of Technology Bombay, Powai, Mumbai, 400076, India

**Keywords:** Torsion Hopkinson Bar, Rectangular Torsion, Dynamic Shear Response

---

**Abstract:** The conventional shear characterization by Torsional Split Hopkinson bar setup (TSHB) requires a tubular specimen with circular or hexagonal flanges. The machining of specimen out of thin sheet material to have tubular gauge section and flanges is complex. The use of rectangular cross-sectional specimen for dynamic shear characterization is explored. The theory to relate shear pulses captured on incident and transmitter bars of TSHB to the maximum shear stress that is seen on a rectangular cross-section is formulated. The tubular specimen that are used in TSHB are of small gauge lengths for specimen stress equilibrium. In rectangular torsion a sufficiently large gauge lengths are required for valid use of Saint- Venant's torsion theory. A parametric study is carried out using Finite Element Simulations to find the minimum gauge length at which the maximum stress on rectangular specimen is close to Saint- Venant's torsion theory and can fit into practical limits of dynamic TSHB shear characterization. The challenges in grip design that subject the specimen for unconstrained warping for valid use of theory is discussed.

## 1. Introduction

Torsion Hopkinson bar is most commonly used apparatus for dynamic shear characterization. Typically, thin-walled tubular specimens either with hexagonal or circular flanges are used in TSHB characterization. Tubular specimen is proven to be effective for pure shear characterization [1,2]. To use tubular specimens in TSHB requires material with sufficient thickness to machine flanges and tubular gauge length. Compression Hopkinson bar can also be used for shear characterization using hat specimen [3,4]. The section between hat and shoulders of specimen acts as shear zone under compression. The machining of hat and shoulders to have thin gauge section also requires enough thickness. Most of the composite laminates and polymers are manufactured as thin sheets of thickness below 5 mm. In such cases the machining of tubular specimen or hat specimen is not possible. Hence, the feasibility of using rectangular specimen for shear characterization is studied using FE simulations.

The rectangular torsion theory assumes a definite distribution of forces at ends to give solution. The practical application of solution is not limited to these cases. From Saint-Venant's principle, on rectangular bars at sufficient distance away from application of loads, the stresses depend on magnitude of load. Rectangular specimen when subjected to torsion has a complex stress distribution in the cross-section. The stress distribution along the length however, remains almost uniform. The maximum shear stress, which is seen in the middle of longer side in cross-section can be related to the torque applied. The twist per unit length can be related to the torque applied. The correct solution to rectangular torsion

\*Author for correspondence (chandra@aero.iitb.ac.in).

†Present address: Department of Aerospace Engineering, IIT Bombay, Mumbai, 400076

was first discussed by Saint-Venant [5]. Timoshenko and Goodier [6] discussed a mixed approach based on membrane theory and stress function in detail.

The rectangular specimen when clamped on either sides and subjected to torsion it leads to a state of warp constrained torsion. When the specimen is clamped the tension and compression that are seen in outer and inner layers of the cross-section are constrained and the torsional rigidity of the specimen increases and the stress distribution alters from theory. The holders have to be designed in such a way that the warping has to be unconstrained or correction factors have to be introduced in to the torsion equations. Study on a range of aspect ratios with thickness and width fixed to 4mm and 20mm respectively is carried out. The feasible dimensions of rectangular specimen are accessed. The challenges that are involved in shear characterization of rectangular specimen to achieve higher strain rates is discussed. The modifications that are required on regular TSHB setup to test rectangular samples is discussed.

## 2. Theory

Rectangular specimen when subject to torque as shown in Fig .1. The maximum shear stress  $\tau_{xz}$  is seen in middle of longer side of cross section. The equations for the  $\tau_{xz}$  and  $\tau_{yz}$  are given below equation [1].

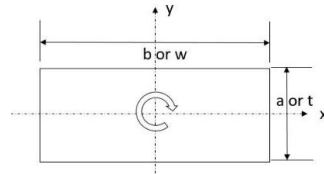


Figure 1: Rectangular cross-section in torsion

$$\begin{aligned}\tau_{xz} &= -\frac{8G\theta b}{\pi^2} \sum_{i=0}^{\infty} \frac{(-1)^i}{(2i+1)^2} \frac{\sinh\left(\frac{(2i+1)\pi y}{b}\right)}{\cosh\left(\frac{(2i+1)\pi a}{2b}\right)} \cos\left(\frac{(2i+1)\pi x}{b}\right) \\ \tau_{yz} &= 2x - \frac{8a}{\pi^2} \sum_{i=0}^{\infty} \frac{(-1)^i}{(2i+1)^2} \frac{\cosh\left(\frac{(2i+1)\pi y}{b}\right)}{\cosh\left(\frac{(2i+1)\pi a}{2b}\right)} \sin\left(\frac{(2i+1)\pi y}{b}\right)\end{aligned}\quad (1)$$

The convergence of above equation is rapid and can be reduced to two terms which is given by

$$\begin{aligned}\tau_{xz} &= -\frac{8G\theta b}{\pi^2} \sum_{i=0}^{\infty} \frac{\sinh\left(\frac{\pi y}{b}\right)}{\cosh\left(\frac{\pi a}{2b}\right)} \cos\left(\frac{\pi x}{b}\right) \\ \tau_{yz} &= \frac{8G\theta a}{\pi^2} \sum_{i=0}^{\infty} \frac{\sinh\left(\frac{\pi y}{b}\right)}{\cosh\left(\frac{\pi a}{2b}\right)} \cos\left(\frac{\pi y}{b}\right)\end{aligned}\quad (2)$$

The  $\tau_{max}$  for ( $b > a$ ) is  $\tau_{xz}$  in the middle of longer side  $b$  and can be more generalized to one given by Roark formula book [7]

$$\frac{\gamma_{max}}{\theta} = \frac{t}{l_{actual}} \left[ 1 - 0.378 \left( \frac{t}{w} \right)^2 \right] \quad (3)$$

$$\frac{\tau_{max}}{T} = \frac{\left[ 3 + 1.8 \left( \frac{t}{w} \right) \right]}{wt^2} \quad (4)$$

In TSHB, the torque and angular displacement on incident bar side and the transmitted bar side of specimen is given by shear strain pulses

$$\begin{aligned}
 T_1 &= \frac{G(\gamma_I(t) + \gamma_R(t))\pi D_b^3}{16} \\
 T_2 &= \frac{G\gamma_T(t)\pi D_b^3}{16} \\
 \theta_1 &= \frac{2C}{D_b} \int_0^t (\gamma_i - \gamma_r) dt \\
 \theta_2 &= \frac{2C}{D_b} \int_0^t (\gamma_t) dt
 \end{aligned} \tag{5}$$

The rectangular specimen maximum stress and strain can be related to strain pulses on bars by

$$\begin{aligned}
 \tau_{max} &= \frac{\left[3 + 1.8\left(\frac{t}{w}\right)\right]}{wt^2} \frac{G(\gamma_I + \gamma_R + \gamma_T)\pi D_b^3}{32} \\
 \gamma_{max} &= \frac{t}{l} \left(1 - 0.378\left(\frac{t}{w}\right)^2\right) \left(\frac{2C}{D_b} \int_0^t (\gamma_i - \gamma_r - \gamma_t) dt\right)
 \end{aligned} \tag{6}$$

### 3. Finite Element Simulation

Static FE simulations are carried out for aspect ratios in range of 1 to 20 to check the stress distribution and maximum shear stress in cross section. The static and dynamic simulations are carried out with grips having a rectangular slot. Frictionless contact definition is used between specimen and the rectangular slot on grip to allow the specimen to slide. Simulations are carried out in ANSYS 16.2 (Academic Research) using Static Structural and Transient Dynamics modules. Aluminum nonlinear material is used for both specimen and grips.

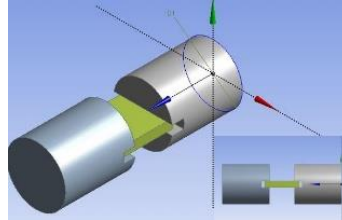


Figure 2: Geometry used for static simulation

The specimen with holder used for static simulation is shown in Fig. 2. The dry setup used for dynamic simulation is shown in Fig. 3. For static analysis, a torque of 10Nm is given to all aspect ratios and the maximum shear stress is compared with theoretical value in Table .1. For aspect ratio of one the maximum stress is not  $\tau_{xz}$  as expected, as the length of the specimen is not sufficient enough to subject the specimen to pure torsion. The theoretical maximum shear stress for the cross-section dimensions used is 105 MPa.

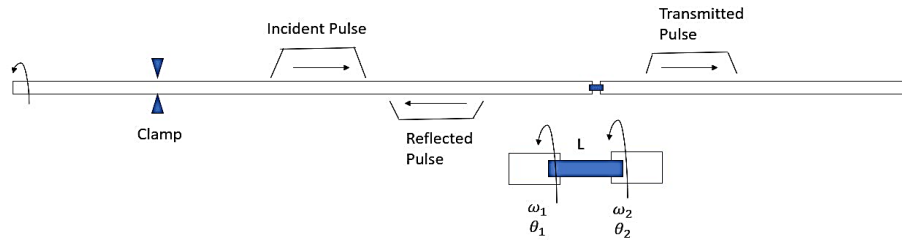


Figure 3: Dry setup used for dynamic simulation

Table 1: Comparison of Maximum shear stress

Aspect ratio	Simulation $\tau_{max}$ (MPa)	% Error
1	76.682 ( $\tau_{yz}$ )	26
5	100.94 ( $\tau_{xz}$ )	3.8
10	106.35 ( $\tau_{xz}$ )	1.28
15	106.93 ( $\tau_{xz}$ )	1.83
20	107.15 ( $\tau_{xz}$ )	2

For aspect ratio beyond 4 the maximum expected shear stress is within 4 % error. The length corresponding to aspect ratio 4 is chosen for dynamic simulation. Dynamic simulation is carried out in two steps. In first step the part of incident bar (0.3m) is clamped and the free end is subjected to angular rotation. In the second step, the clamp constraint is removed to generate torsional pulse. The shear strain pulses captured from bars is shown in Figure 4. The dynamic maximum shear stress directly from the specimen is compared to stress calculated from Incident, transmitted and reflected pulsed using TSHB formulation. The maximum shear stress on specimen over pulse duration obtained using TSHB formulation and the maximum stress taken from specimen is compared and is shown in Fig. 5.

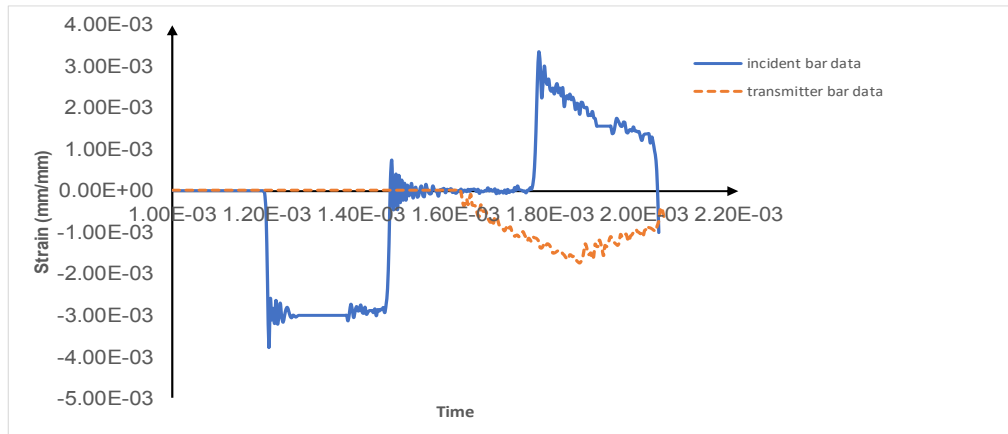


Figure 4: Shear strain pulse data from simulation

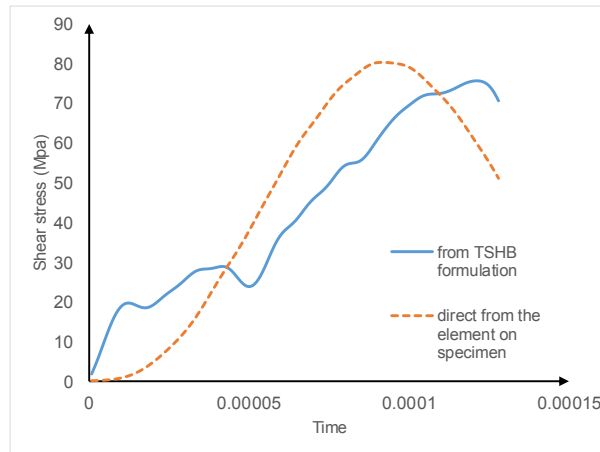


Figure 5: Maximum shear stress over pulse duration

#### 4. Stored Torque Hopkinson bar Apparatus

The experiments on Torsion Hopkinson bar is carried by first clamping the incident bar at a certain distance from loading end. This length determines the pulse duration. Once the bar is clamped, a rotary actuator is used to give rotation to the incident bar at loading end. When necessary rotation is achieved, the clamp is unconstrained by breaking the notched fracture pin. When the fracture pin breaks, two waves start traveling simultaneously, one towards the specimen (loading wave) and the other in the direction of the rotating end (unloading wave) of the incident bar. Half the stored torsion energy is responsible for a wave traveling to the specimen which is called loading wave. The remaining half of the wave moving towards the rotating actuator end of TSHB is called unloading wave. When the wave propagating towards the rotating end reaches the rotary actuator, it senses a rigid condition and reflects back unloading the clamped portion. Hence, the pulse interval is essentially the time required for the shear wave to travel double the clamped length of the incident bar. The bar lengths and position of the gauges are chosen in such a way that the reflected and incident pulses do not overlap. TSHB setup is discussed in detail by Naik [8].

#### 5. Results

The static analysis of rectangular specimen suggests to use rectangular specimen with aspect ratio above 5 for maximum shear stress to be close to Saint-Venant's theory expected value. The dynamic simulation carried out gave a maximum shear stress of 80 MPa on direct measurement on the specimen element. The maximum shear stress measured using the transmission pulse and TSHB formulation is in good agreement with directly measured maximum shear stress as shown in Fig.6. The strain rate is highly dependent on the length of specimen. The length corresponding to aspect ratio of 5 in dynamic simulation leads to small strain rates. The present dynamic simulation carried out with 16mm gauge length resulted in strain rate of  $15 \text{ s}^{-1}$ . In conventional tubular specimen the tube thickness is limited to less than 0.5mm thick. The specimen failure will be captured clearly with tubular specimen. The rectangular specimen failure is not clear as the specimen thickness is relatively large and does not the result in die out of transmission signal to show specimen failure.

## 6. Discussion

The simulations are carried out with frictionless contact definition between specimen and grips. The experiments when carried out, care has to be taken to see the rectangular slots of the grip is machined to good smoothness and lubricated for smooth motion of specimen. The roughness between specimen and grip would constrain the warping and lead to a stress distribution which is not similar to Saint-Venant's theory. The strain rate is dependent on length of the specimen and magnitude of incident moment pulse. For rectangular specimen as the length required is relatively larger when compared to conventional specimen, strain rates will be smaller compared to conventional TSHB characterization. To achieve higher strain rates, we need to subject the specimen to large amplitude torsional pulse. The magnitude of torsional pulse in TSHB setup is constrained by the shear yield strength of bars. Material with higher yield strength as bar material has to be used to achieve this. Larger incident pulse durations are required for specimen equilibrium when rectangular specimen is used. Larger pulse duration requires the larger clamped portion of Incident bar. This increases the incident bar length and there by total length of the setup. The failure stress will not be clear if rectangular specimen is used. The thickness of the rectangular specimen is considerably large compared to tubular thickness. This thickness of rectangular specimen will not die out transmission signal which makes the failure strength unclear. However, the rectangular torsion can help in understanding the rate sensitivity of material.

## 7. Conclusion

Static FE simulations are carried out to find the aspect ratio that creates a stress distribution and maximum shear stress as expected by Saint- Venant's theory. The dynamic simulation is carried out on specimen with the aspect ratio chosen based on static analysis. The Maximum shear stress on specimen directly measured taking elements on specimen and shear stress calculated by TSHB formulation using shear strain pulses measured from bars are in good agreement. The strain rate that is seen in current work is relatively small compared to conventional TSHB strain rates. The strain rate can be increased by using larger magnitude incident moment pulse and large pulse duration, which requires higher yield strength material and longer incident bar on setup.

## References:

1. White C S, 1992, Use of the Thin-Walled Torsion Specimen, U.S. Army Materials Technology Laboratory
2. Gowtham, H. L., Pothnis, J. R., Ravi Kumar, G., and Naik, N. K., 2015, Dependency of dynamic Interlaminar shear strength of composites on test technique used, *Polym Test* 42:151–159.
3. Xu, Z., Ding, X., Zhang, W., and Huang, F., 2017, A novel method in dynamic shear testing of bulk materials using the traditional SHPB technique, *Int J Impact Eng* 101:90–104.
4. Zhou, T., Wu, J., Che, J., Wang, Y., and Wang, X., 2017, Dynamic shear characteristics of titanium alloy Ti-6Al-4V at large strain rates by the split Hopkinson pressure bar test, *Int J Impact Eng* 109:167–177.
5. Saint-Venant, A. J. C. B, 1856, Mémoire sur la torsion des prismes, *Mémoires présentés par Divers savants a l'Académie des Sci.* 14, 233–560.
6. S. Timoshenko, 1951, *Strength of Materials, Part I.*
7. Roark, R. J., and W. C. Young, 1975, *Formulas for Stress and Strain*, 1st ed.
8. Naik, N. K., Gadipatri, R., Thoram, N. M., Kavala, V. R., and Ch., V., 2010, Shear properties of epoxy under high strain rate loading, *Polym Eng Sci*, vol. 50, pp. 780–788.

# Analysis of 3D Metallic Auxetic Structures at High Rates of Strain using Finite Element DIC

A. Trippel<sup>1\*</sup>, F. Gutmann<sup>1,2</sup>, G.C. Ganzenmüller<sup>1,2</sup>, and S. Hiermaier<sup>1,2</sup>

<sup>1</sup> INATECH, Albert-Ludwig University of Freiburg, Emmy-Noether-Straße 2, 79110 Freiburg, Germany

<sup>2</sup> Fraunhofer Institute for High-Speed Dynamics, Ernst-Mach-Institut, EMI, Ernst-Zermelo-Straße 4, 79104 Freiburg, Germany

**Keywords:** Hopkinson Bar, DIC, auxetic, dynamic, metallic

---

**Abstract:** At quasi-static conditions, auxetic metamaterials generally exhibit well defined negative Poisson's ratio over a wide range of strains, while at dynamic rates of strain, this is not necessarily the case. A detailed analysis of the structural response is mandatory, which is often performed using Digital Image Correlation (DIC). However, widely used local DIC applied to slender structures such as auxetic lattices often yields inaccurate measurements. An alternative approach is used, utilizing a finite element based DIC procedure combined with dynamic loading of a Symmetric Direct Impact Hopkinson Bar (SDIHB). We apply this approach to a number of different 3D auxetic metal specimens, report their structural response and compare quasi-static and dynamic rates of strain, providing an insight in the application of a finite element mesh based global DIC.

## 1. Introduction

Auxetic metamaterials are structures that exhibit a well defined negative Poisson's ratio. Poisson's ratio is defined as the negative quotient of the transversal and the longitudinal strain. When loaded, an auxetic structure reacts with element rotation. Those rotations in their entirety are responsible for the auxetic effect. 3D metallic structures with auxetic properties show interesting behaviour in comparison to conventional non-auxetic metamaterials, especially when loaded with a high rate of strain, such as higher yield strengths, higher energy absorptions [1] and possibly enhanced energy dissipation [2]. This makes the materials an interesting candidate for application in the automotive sector, especially in crash applications.

The structural response of auxetic structures is dependent on loading rate. At quasi-static conditions, auxetic structures generally exhibit well defined negative Poisson's ratio over a wide range of strains. However, at dynamic rates of strain, this is not necessarily the case: the magnitude of the rate of strain determines whether an auxetic effect occurs or the structure collapses. If the structure does not have enough time to achieve dynamic equilibrium, it experiences structural failure similar to pore collapse in foams before auxetic behaviour can occur.

To provide an in-depth understanding of a structure and collect data in order to accurately model and simulate the metamaterial, a detailed analysis of the structural response is mandatory. Our work investigates an alternative approach for obtaining accurate deformation data for auxetic structures under dynamic loading.

## 2. Structure Manufacturing

The structures were printed at Fraunhofer Institute for High-Speed Dynamics, Ernst-Mach-Institut, EMI using two different metals: Scalmalloy®, which is an aluminium alloy, and EOS MaragingSteel MS1. Specimens in

\*Corresponding author. (A.Trippel@inatech.uni-freiburg.de).

†INATECH, Albert-Ludwig University of Freiburg, Emmy-Noether-Straße 2, 79110 Freiburg, Germany

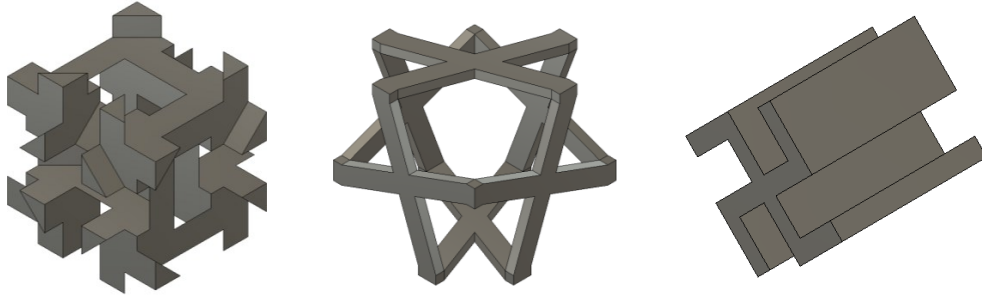


Figure 1: CAD-Models of three unit cells used to design the auxetic structures, first being an antitetrachiral unit cell, second a 3D cross chiral unit cell, third a missing rib unit cell. Each unit cell has the size of 3 mm.

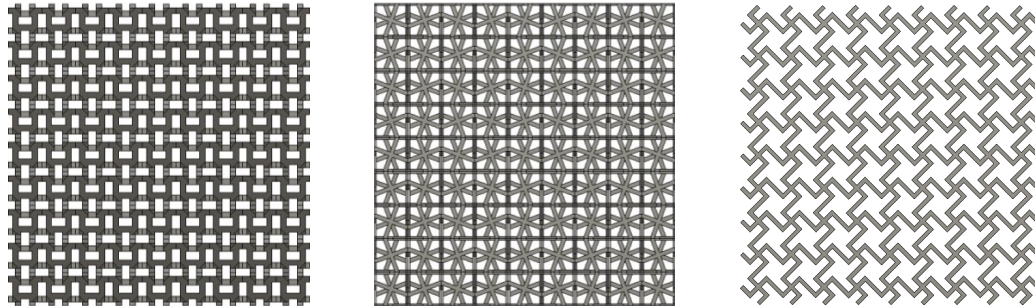


Figure 2: CAD-Models of three different auxetic structures using the unit cells shown in Figure 1. The cells are copied in three directions in space, forming a 3D structure each. Each structure has the size of 27 mm. The models are used to print the structures using Scalmalloy® and EOS MaragingSteel MS1.

Scalmalloy® were printed via selective laser melting (SLM) using EOS M400. Specimens in EOS MaragingSteel MS1 were manufactured via SLM using EOS M100. To investigate different structural responses and test the limits of the manufacturing process, three different unit cells of the size of 3 mm were designed (Figure 1). The first cell is a antitetrachiral unit cell suggested in [3]. The second cell geometry is a 3D cross chiral unit cell proposed in [4]. The third cell is the base for a missing rib structure [5]. Each unit cell was multiplied in three different directions in space forming an auxetic 3D structure with the size of 27 mm each (Figure 2).

The resulting dimensional accuracy of the 3D printed metamaterials differed based on the machine and the parameters used. Since the aluminium specimens were printed using a rougher machine, the dimensions of the specimens were bigger than designed. In comparison, the geometry of the steel specimens was close to the geometry of the CAD-model. This issue not only affects the experimental results, but the low dimensional accuracy makes the optical analysis of the specimens more challenging. Especially in case of the antitetrachiral structure the base structure is barely visible on the surface due to the significant amount of excessive material.

### 3. Experimental Setup

In order to prevent collapse of the structure and still apply a dynamic loading, we need to achieve dynamic strain rates in the order of 100 /s. This strain rate regime is relevant in automotive and aerospace crash. Accurate force measurement at dynamic rates of strain calls for a Split-Hopkinson Bar (SHB) type setup. However, testing of large samples combined with a relatively low strain rate in SHB typically requires long bars, which can be impractical due to building space constraints. Therefore, we employ a symmetric direct-impact Hopkinson bar, based on the work of Meenken [6] as well as Govender [7]. This setup maximizes the possible experiment duration for a given available bar length. Due to its symmetric design, force equilibrium is also attained earlier compared to classic SHB.

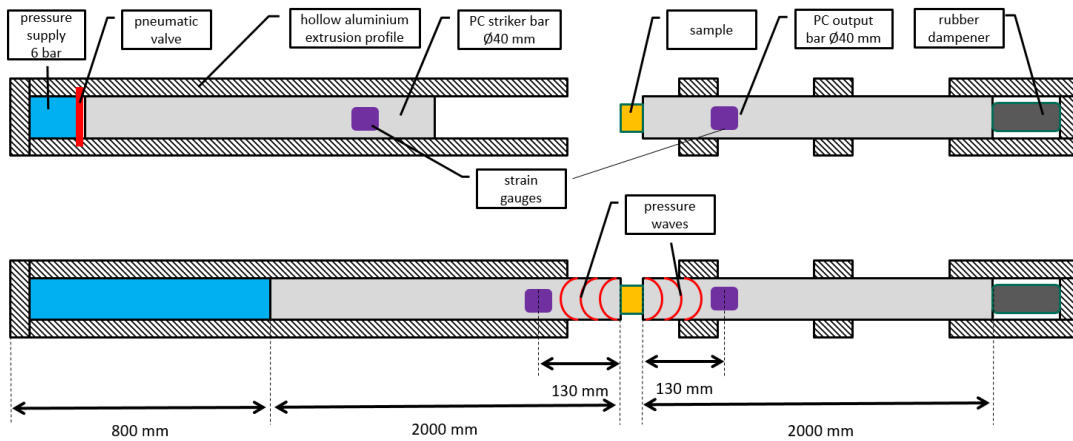


**Figure 3: Schematic setup of a Symmetric Direct Impact Hopkinson Bar (SDIHB). The striker bar is accelerated by releasing the pressure supply by opening the pneumatic valve. The bar strikes the sample and releases pressure waves. Our setup allows for impact velocities of up to 10 m/s.**

The schematic setup is shown in Figure 3. The striker bar is accelerated by releasing the pressure supply by opening the pneumatic valve. The bar strikes the sample and releases pressure waves. The result is measured via two strain gauges, one placed on the striker bar and one placed on the output bar. Since the setup is symmetric, the signals on both sides are almost identical.

Dependent on the sample the bars can be made out of either polycarbonate or aluminium. Polycarbonate elongates the testing time to 3.2 ms. The testing time is important to ensure a sufficient structure deformation. Aluminium bars reduce the testing time to 0.78 ms, but increase the possible impact forces. In case of metallic structures, polycarbonate bars showed not to be able to deform the structures sufficiently due to lower impact forces. Therefore, we used aluminium bars in our experiments.

#### 4. Experimental Results

The experimental results of the experiments using the SDIHB are shown in Figure 4. The results are the force over the experiment time for each structure and each material for an impact speed of 10 m/s, yielding a strain rate of 370 /s. The drop of each curve at the end indicates the experiment duration of 0.78 ms.

Comparing the curves of different materials in case of the second and third structure shows, that the curves are similar even though the materials exhibit different characteristics on their own. However, the assumption that the properties of the material are more reliant on the structure than the material cannot be made yet, since the aluminium specimens are influenced by a significant amount of excessive material due to the manufacturing process. These assumptions require additional parametric studies.

Out of three structure geometries, only the antitetrachiral structure showed a well defined negative Poisson's ratio. Though the other structures are also auxetic in theory, the specimens tested exhibited a strong local one directional deformation. The 3D cross chiral structure out of MS1 was the only one that collapsed.

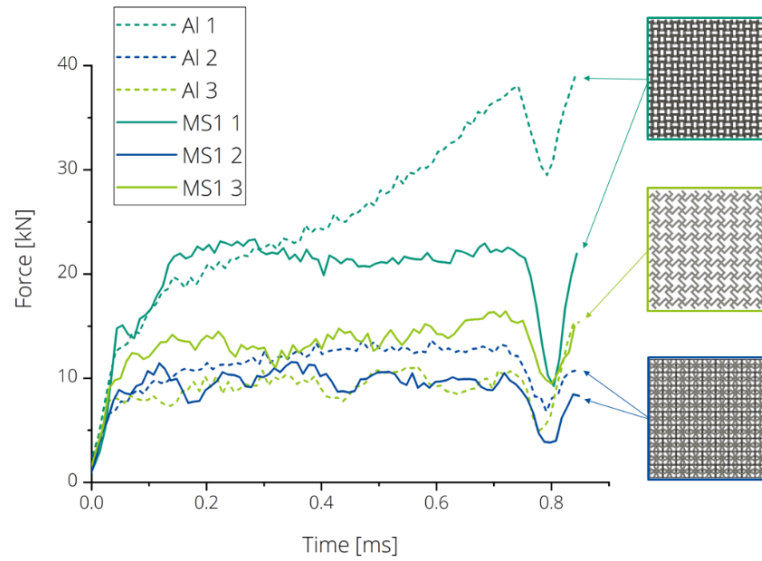


**Figure 4: Experimental results for all three structures and two materials, “AL” standing for Scalmalloy® and “MS1” for EOS Maraging Steel MS1. Structure No. 1 is the antitetrachiral structure, structure No. 2 is the 3D cross chiral structure and the third is the missing rib structure. Each structure was measured at 10 m/s, yielding a strain rate of 370 /s.**

## 5. Digital Image Correlation

To provide an in-depth understanding of a structure and collect data in order to accurately model and simulate the metamaterial, a detailed analysis of the structural response is mandatory. The analysis is performed often using Digital Image Correlation (DIC). DIC registers two or more images of the same scene and extracts a displacement field. Advanced DIC codes add additional information, such as residuals and noise sensitivity. To apply DIC, in addition to the force measurements specimens were recorded in form of grayscale images with a resolution of 640 x 432 px at 56,000 fps using a Photron SAZ High Speed Camera. These recordings are used to analyze the deformation in detail.

To calculate the displacement field, two image frames  $f$  and  $g$  at each pixel position  $x$  shot at two different instances in time are assumed. The image frames are matrices with each elementary component representing a grey level value. Assuming the displacement  $u(x)$ , the images can be related as

$$f(x) = g[x + u(x)]$$

corresponding to grey level conservation. The image is divided in smaller sub-images (or elements, facets). The displacement field  $u(x)$  is then calculated by minimizing the mean squared deviation of both images over a sub-image:

$$T(u_p) = \int_{sub-image} [f(x) - g(x + \sum u_p \psi_p(x))]^2 dx$$

approximating the displacement field using a field function  $\psi_p(x)$  and the unknown degrees of freedom  $u_p$ .

$$u(x) = \sum u_p \psi_p(x)$$

Local and global DIC are distinguished. In case of local DIC, the sub-images are not interconnected but calculated individually. This results in fast and robust calculations since it does not account for continuity. Therefore, local DIC is a popular method, which is easily commercially available. However, local DIC applied to slender structures such as auxetic lattices often yields inaccurate measurements. Since the structures include

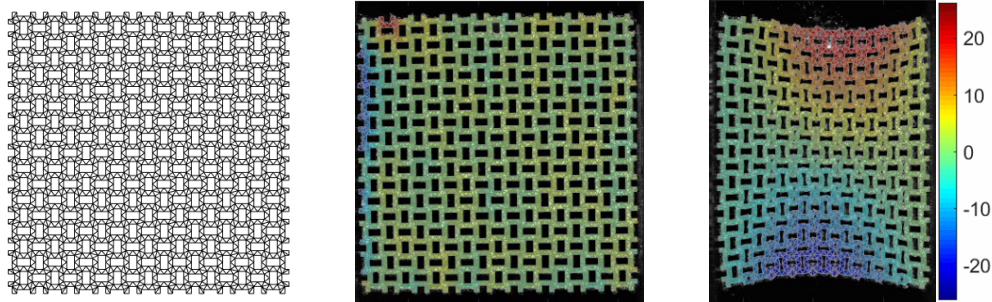


Figure 5: On the left is the FE mesh based on the CAD model of the structure. In the middle, the mesh is applied to the surface of the structure in its initial state. On the right, the structure has already been deformed using a Symmetric Direct Impact Hopkinson Bar with a strain rate of 370 s<sup>-1</sup> showing the perpendicular displacement in pixels.

empty spaces, elements placed in those areas do not experience displacements. Because the displacement field is discontinuous, it has to be excessively smoothed in space, so empty areas are also accounted for. Therefore, typical commercial tools tend to reach their limits when it comes to its application on auxetic structures.

In global DIC, however, the field functions, and therefore the sub-images, are interconnected. The displacement of adjacent elements is continuous, which results in a continuous displacement field. Since the displacement field does not have to be smoothed, it does not account for the empty areas. The downside to global DIC are the comparatively long calculation time and the user dependent result quality. On the other hand, global DIC and its continuity of elements opens the room for new calculation methods.

One of those methods is the combination of DIC with a finite element mesh. Since the pictures used in DIC already have to be divided in sub-images, it is natural to consider a structure directly comparable to FE simulations for identification and validation. The pictures are based on pixels, so it is logical to use rectangular or triangular elements to create a mesh. Since we do not want to calculate the displacement of empty areas, the mesh is created based on the CAD model of the structure, see Figure 5. This method results in a displacement field, which deforms depending on the deformation of the structure. The structure can be analyzed locally in detail. Beyond the displacement, the displacement field can be used to calculate other information such as local strains, local rotations and Poisson's ratio, which contributes to an in-depth understanding of the structure and the auxetic response. [8]

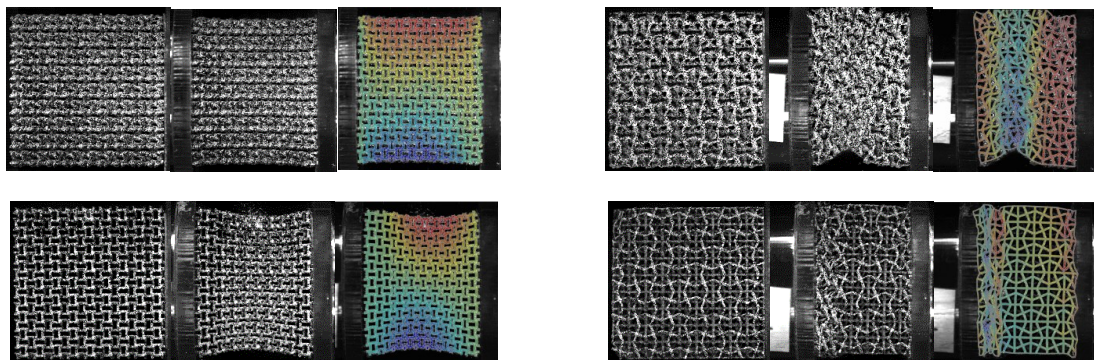


Figure 6: The rows on the left show the optical results for the antitetrahedral structure, the rows on the right show the results of the 3D cross chiral structure. On top are the structures manufactured using Scalmetalloy®, on the bottom the structures manufactured using EOS MaragingSteel MS1. Each row shows three images. On the left is the non-deformed structure prior to the experiment. In the middle, the structure has already been deformed using a Symmetric Direct Impact Hopkinson Bar with a strain rate of 370 /s. On the right, the mesh is applied to the surface of the structure showing the perpendicular displacement in pixels.

Beyond local analysis, the combination of global DIC with a finite element style mesh allows for analysis of structures affected by low dimensional accuracy (Figure 6). By overlaying the images with a finite element

mesh, the initial structure and the structural response can be revealed. In case of the antitetrachiral aluminium structure, which was affected by excessive material the most, global FE DIC is the only optimal way to optically show the structural deformation. High local deformation, as in the case of the 3D cross chiral structure, is accurately analyzed not only in case of high deformation, but also in case of a structural collapse as experienced by the MS1 structure.

## 6. Conclusion

The method of global DIC combined with a finite element mesh yields accurate results for structural deformation and information which is useful in developing new material models. In case of structures with a significant amount of excessive material and therefore low dimensional accuracy, this method allows for analysing the structure nonetheless.

The next step is the execution of parametric studies and the implementation of the results in a numerical simulation. The simulation based on this information can be used to find a critical strain rate where the structural response devolves from auxetic to collapsing. Additionally, the information obtained through the DIC can be used to find homogenized material models and therefore improve calculation times of the simulations.

### Acknowledgments

We are thankful to Francois Hild for introducing us to global DIC methods and providing us with their software "Correli".

### Funding Statement

We gratefully acknowledge the funding from Carl-Zeiss-Stiftung "Grundlagenforschung mit Anwendungsbezug".

### References

1. R.Lakes and K.Elms. 1993. Indentability of conventional and negative Poisson's ratio foams. *J. Compos. Mater.* **27(12)**, pp. 1193–1202.
2. M.Bianchi, F.Scarpa and C.Smith. 2010. Shape memory behaviour in auxetic foams: mechanical properties. *Acta Mater.* **58(3)**, pp. 858–865.
3. H.Huang, B.Wong, Y.Chou. 2016. Design and properties of 3D-printed chiral auxetic metamaterials by reconfigurable connections. *Physica Status Solidi b* **253(8)**, pp. 1557-64.
4. Z.Lu, Q.Wang, X.Li, Z.Yang. 2017. Elastic properties of two novel auxetic 3D cellular structures. *International Journal of Solids and Structures* **124**, pp. 46-56.
5. S.W.Smith, J.N.Grima and E.K.Evans. 2000. A novel mechanism for generating auxetic behaviour in reticulated foams: missing rib foam model. *Acta Mater.* **48**, pp. 4349–56.
6. S.Hiermaier and T.Meenken. 2010. Characterization of Low-Impedance Materials at Elevated Strain Rates. *J. Strain Analysis for Engineering Design* **45**, pp. 401-9.
7. R.A.Govender and R.J.Curry. 2016. The "Open" Hopkinson Pressure Bar: Towards Addressing Force Equilibrium in Specimens with Non-Uniform Deformation. *J. Dynamic Behavior of Materials* **2**. pp. 43-49.
8. F.Hild and S.Roux. 2012. Digital Image Correlation. *Optical Methods for Solid Mechanics. A Full Field Approach*, pp. 183-228.

# Numerical investigations on the impact behaviour of a 7.62x39 mm projectile

Marina Seidl\*, Marvin Becker, Matthieu Kern

*French-German research institute of Saint-Louis (ISL),  
Department of Protection Technologies, Security and Situational Awareness,  
5 rue du Général Cassagnou, BP 70034, 68300 SAINT-LOUIS - France*

**Keywords:** FEM, Cowper-Symonds, Johnson-Cook, high velocity impact, strain hardening

**Abstract:** A dismounted soldier relies on his body armour for protection against ballistic threats. A 7.62x39 mm rifle bullet is a common threat during combat. Ballistic vests protect against a direct hit, but the weight limitations of a combat helmet compromise its protection. When a rifle projectile impacts a helmet, it is most probable not perpendicular to its surface. At certain conditions, such as high impact velocities and a sufficiently large oblique angle, the projectile ricochets. The aim of this project is to enhance the likelihood of projectile ricochet off helmets and increase the survivability of the wearer. For a better understanding of the dynamics of impact, numerical simulations accompany this research. This publication focuses on the influence of different numerical descriptions of the material to projectile damage representation. A qualitative comparison of the experimental and numerical results has been provided.

## 1. Introduction

Armed forces are more likely to face 7.62x39 mm rifle threats than the handgun projectile that helmets are designed for [1]. Although there do exist helmets which withstand a perpendicular impact of a 7.62x39 mm projectile, most combat helmets are made of lightweight materials for long-time use in varied environmental conditions and thus cannot withstand such a threat. A better protection against a 7.62x39 mm bullet, without adding additional weight to the helmet, is thus being investigated. For instance, sandwich layers might increase the likelihood of the projectile ricochet – a phenomenon observed for oblique impact at a certain velocity. However, this may still not stop a direct impact of a rifle ammunition. Instead, it would increase the probability of projectile ricochet and the survivability of the wearer. The rounded surfaces enhance the likelihood of projectile ricochet [2], but make repeatable and comparable measurements challenging. Numerical simulations support the understanding of this complex scenario. Not only the material response and modelling of the composite target, but a correct representation of the projectile behaviour is important. Previous work [3] has showed that the numerical representation of the material of the projectile behaves softer, as compared to the experiment. This work discusses the influence of the strain rate hardening effect on the description of the deformation and fracture of the projectile. Therefore, an experimental study, launching a projectile against a characterised armour steel plate, was conducted. In the numerical study, the material of the rifle bullet is described with two different available material models in LS-DYNA®, the Johnson-Cook and the Cowper-Symonds material model. The numerical results are compared to those obtained from the experiments.

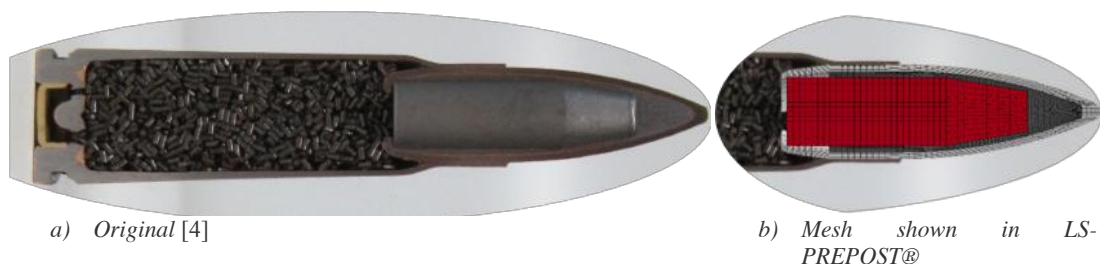


Figure 1: Section view of 7.62x39 mm M43 projectile [5]

\*Author for correspondence (marina.seidl@isl.eu).

†Present address: ISL, BP 70034, 68300 Saint-Louis, France

Experiments were conducted launching the 7.62x39mm projectile against an 8 mm thick MARS@190 plates. The projectile was launched perpendicular to the target surface, at 0 deg (NATO). The experimental set-up was chosen according to previously conducted experiments [6] [2]. **Figure 1 a)** shows the section view of the projectile in the cartridge and its mesh created CAD (Computer Aided Design) drawings (**Figure 1 b**).

Three different initial velocities  $v_i$  of 552 m/s, 580 m/s and 638 m/s were investigated. **Erreur ! Source du renvoi introuvable.** and  $v_i$  was measured with light barriers placed ~500 mm before impact position. The remainder was recovered to evaluate the deformation. Figure 2 top shows the measured projectile core length deformation  $D_l$  and radial deformation  $D_r$ , at different  $v_i$ . For the radial deformation  $D_r$  a mean value with the largest and lowest measured value is given (Table 1).

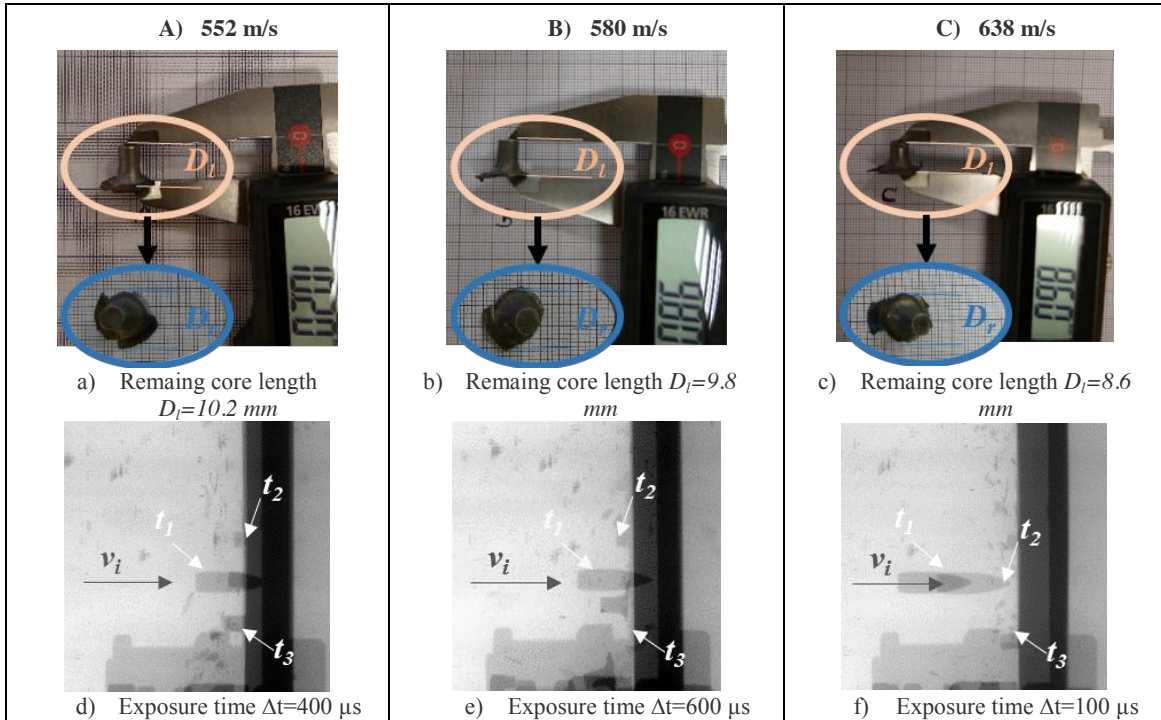


**Figure 2 M43 projectile core length deformation  $D_l$  dependent on impact velocity  $v_i$**

X-ray results are shown in Figure 2 (d-f). Three exposure were captured for each image. The exposure time  $t$  were adjusted to the  $v_i$ . They are summarised in Table 1 and it is shown that the X-ray results are the most conclusive for test B with 580 m/s where the rebound of the deformed projectile core is clearly visible (Figure 2 e). For test A and C, the exposure time  $t$  was too short in order to capture the deformed projectile core upon impact (Figure 2 d and f).

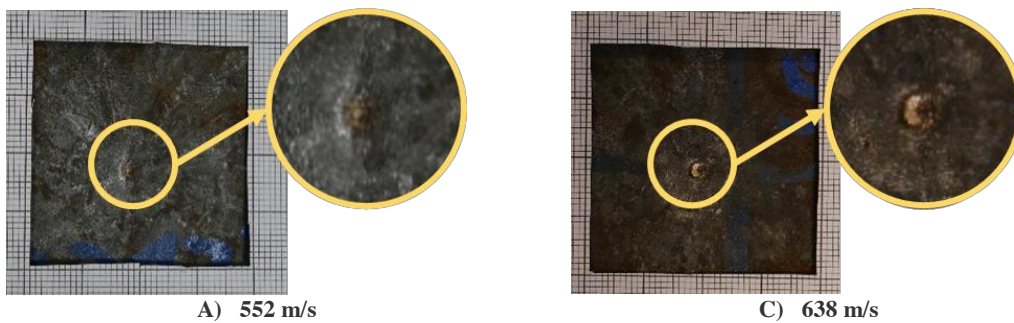


**Figure 3 Strike face damage MARS@190 8 mm target plates**

The target deformation is shown in **Erreur ! Source du renvoi introuvable.** for the lowest measured  $v_i$  of 552 m/s and the highest 638 m/s (Figure 3). A dependency on the plate damage, size of depth of the impact crater was not further investigated. The damage caused on the armour steel plates is not further discussed in this paper; based on the results it was decided to neglect it.

**Table 1 Experiment test matrix**

Test	$v_i$	$D_l$	$D_r$	X-ray exposure time t			Notes
	m/s	mm	mm	$\mu$ s	$\mu$ s	$\mu$ s	
A	552	10.2		100	500	900	exposure time longer
B	580	9.8		100	700	1300	core rebound visible
C	638	8.6		100	200	300	exposure time too short

### 3. Numerical Simulation

The explicit Lagrangian finite element solver in the commercial LS-DYNA® software has been used to solve the underlying equations of continuum mechanics [7]. A Finite Element Method (FEM) describes the high velocity scenario of the 7.62x39 mm projectile impacting on the armour steel plate. The target plate is not discussed further in this paper, and has been described in previous publications [6] [2]. Three parts describe the projectile: steel core (red), lead filler (dark grey), and brass jacket (light grey) (compare Figure 1a). All parts are modelled with hexahedral elements and interact with one another using a symmetrical erosion criterion. The mesh and boundary conditions of the model were described in previous works [8]. The material of all parts is represented by the empirical Johnson-Cook model, which describes the flow stress  $\sigma_y$  as a function of plastic strain  $\bar{\epsilon}^{p^n}$ , strain rate  $\dot{\epsilon}^*$ , and homogenised temperature  $T^*$ .

$$\sigma_y = (A + B\bar{\epsilon}^{p^n})(1 + c \cdot \ln(\dot{\epsilon}^*))(1 - T^{*m}), \quad (1)$$

where,  $A, B, c, n$ , and  $m$  are material parameters. Additionally, the Grueneisen equation of state defines the initial material state. The damage is described by a Johnson-Cook failure criterion:

$$\epsilon^f = (D_1 + D_2 e^{D_3 \sigma^*})(1 + D_4 \cdot \ln(\dot{\epsilon}^*))(1 + D_5 T^*), \quad (2)$$

which accumulates damage until the strain at fracture  $\epsilon^f$  is reached;  $D_1, D_2, D_3, D_4$ , and  $D_5$  are the material-specific damage parameters. Table 2 shows the defined material parameter set for the Johnson-Cook material model. The elastic and temperature softening parameters were taken from Adams [9]. Hardening and fracture constants were taken from Carbajal [10]. This parameter set was published [8] and is here shown with a special focus on the strain hardening parameter  $c$  in cursive.

**Table 2 Johnson-Cook constitutive model constants [10]**

	Elastic constants and density			Yield stress and strain hardening			Strain rate hardening		
	G [GPa]	$\nu$ []	$\rho$ [g/cm <sup>3</sup> ]	A [MPa]	B [MPa]	n	$\dot{\epsilon}$ [s <sup>-1</sup> ]	<i>c</i>	
Core	79.6	0.3	7.85	234.4	413.8	0.25	1	<i>0.0033</i>	
Lead	5.6	0.43	11.34	10.3	41.3	0.21	1	<i>0.0033</i>	
Jacket	40	0.43	8.96	448.2	303.4	0.15	1	<i>0.0033</i>	
Adiabatic heating and temperature softening			Fracture strain constants						
	$c_p$ [J/kgK]	$T_m$ [K]	$T_0$ [K]	m	D <sub>1</sub>	D <sub>2</sub>	D <sub>3</sub>	D <sub>4</sub>	D <sub>5</sub>
Core	4.5	1800	293	1.03	5.625	0.3	-7.2	-0.0123	0
Lead	1.29	328	293	1.03	0.25	0	0	0	0
Jacket	3.86	1356	293	1.03	2.25	0.0005	-3.6	-0.123	0

Previous studies have proposed the Cowper-Symonds relation for the strain-rate dependence at high dynamic events [11]. The Cowper-Symonds formulation takes into consideration the non-linear dependence of yield stress at high strain rates, scaling the static yield stress  $\sigma_s$  as follows:

$$\frac{\sigma_d}{\sigma_s} = 1 + \left(\frac{\dot{\epsilon}}{C}\right)^{\frac{1}{P}}, \quad (3)$$

where,  $\sigma_d$  is the dynamic yield stress, and  $C$  and  $P$  are material constants. When applying the Cowper-Symonds relation in LS-DYNA®, by defining the equivalent strain-rate term in the Johnson-Cook material model, following additional changes are applied:

Firstly, the  $c$  parameter as shown in Table 2 and defined in Equation (1) is changed to the  $C$  of the Cowper-Symonds relation (Equation 3). These two parameters only share the position in the material card and have no other

Symonds relation will not be used for the calculation. The last definition is the  $P$  value (Equation 3), which is set in the pressure cut-off (PC) flag. In order to distinguish in the implementation between the PC and P in the flag, PC is positive and  $P$  a negative value. Although, each flag is described in the literature [7], a summary of all the changes needed to apply the Cowper-Symonds relation was not found. For both relations, a Mie-Grueneisen equation of state (EOS) defines solid pressure state. The general definition is

$$P - P_H = \frac{\gamma}{\nu} (E - E_H) \quad (4)$$

with reference state H (one point on the Hugoniot) and the Grueneisen parameter  $\gamma$ . Also these parameters were taken from literature [12] and are not in focus in this paper. The strain hardening description is in focus of this study, as previous numerical tests of the projectile material parameters showed, that the literature material parameters have a softer response than the experimental results [3]. Although a through constitutive material parametric study was published [10], some missing parameters for EOS [12] and temperature softening were taken from other sources [9]. Although there may be more reasons for the difference of numerical and experimental results, the strain hardening influence is in focus.

#### 4. Results

Table 2 shows the initial parameter  $c=0.0033$  ( $=3.3e-3$ ) as taken from literature [10]. It was decided to increase the value by the factor ten (Figure 4 a). The orange line is suggested by Carbajal [10], so that the projectile does not show significant strain rate hardening. That assumption may hold true for their measurement. However, an increase of the hardening parameter showed a better agreement between the numerical simulations with the experimental data (Figure 4 b).

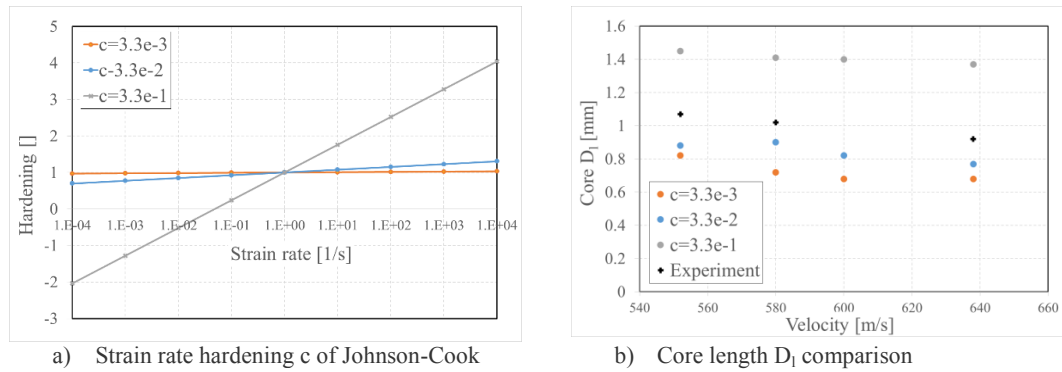


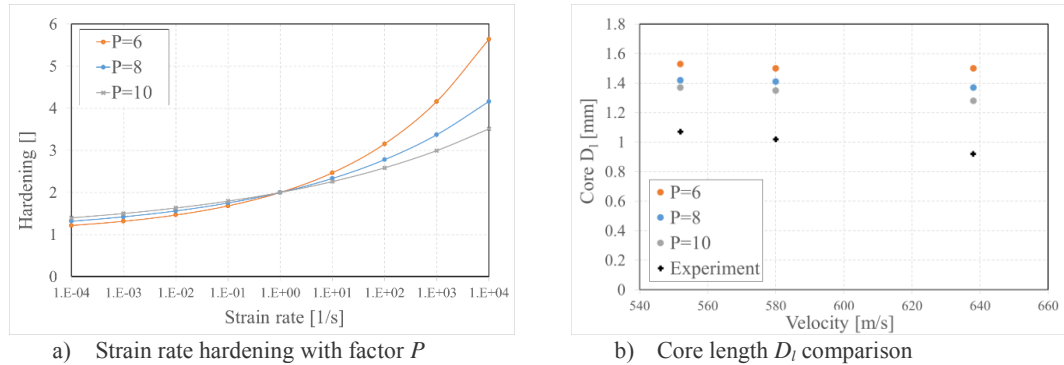
Figure 4: Johnson-Cook strain rate parameter  $c$  evaluation

Table 3 summarizes the results and shows the error between the numerical simulation and the experimental results. The original data showed an under-prediction of the core length between 23-29 %. By increasing the  $c$  parameter to  $c=0.033$  ( $=3.3e-2$ ), the error in the representation of the remaining core length was between 12-18 %. As the aim was not to achieve an especial low error and measurement inaccuracies neither of the numerical simulation, nor the experimental result are not taken into consideration, the error was sufficiently low for this investigation.

Table 3 Comparison Johnson-Cook and Cowper-Symonds strain hardening with experimental results

	Test A 552 m/s		Test B 580 m/s		600 m/s		Test C 638 m/s		
	$D_1$ in [mm]	Error [%]	$D_1$ in [mm]	Error [%]	$D_1$ in [mm]	Error [%]	$D_1$ in [mm]	Error [%]	
c	0.0033	0.82	23	0.72	29	0.68	-	0.68	26
	0.033	0.88	18	0.9	12	0.82	-	0.77	16
	0.33	1.45	-36	1.41	-38	1.4	-	1.37	-49
P	2	1.53	-43	1.5	-47	-	-	1.5	-63
	6	1.42	-33	1.41	-38	-	-	1.37	-49
	10	1.37	-28	1.35	-32	-	-	1.28	-39
Experiment	1.07		1.02		-		0.92		

For the Cowper-Symonds relation, the ratio of  $\epsilon/C=1$  (Equation 3) and the parameter  $P$  is tested. It is shown in **Table 3** that the chosen settings over-predict the core length  $D_I$ . For the  $P=2$  are the original core length of the  $1.9\text{ mm}$  is conserved. This setting shows almost rigid behaviour and perforation of the plate. Increasing the value  $P$  shows softer behaviour and an approach to the experimental values (**Figure 5**). More parameter studies are needed, in order to find the best suitable parameter set for the Cowper-Symonds relation.



**Figure 5: Cowper-Symonds strain rate parameter  $P$  evaluation**

When comparing the Johnson-Cook strain hardening of  $c=0.033$  ( $=3.3e-2$ ) and the Cowper-Symonds relation with  $P=10$ , both settings have for the strain-rates from 100-1000 1/s a hardening factor of 2.5 to 3. Both approaches show, with the similar hardening factors an over-prediction of about 30-40 % of the core length. **Figure 6** shows the numerical model for both settings. Although more parameter studies are needed, adjusting the strain hardening values improves the numerical results.

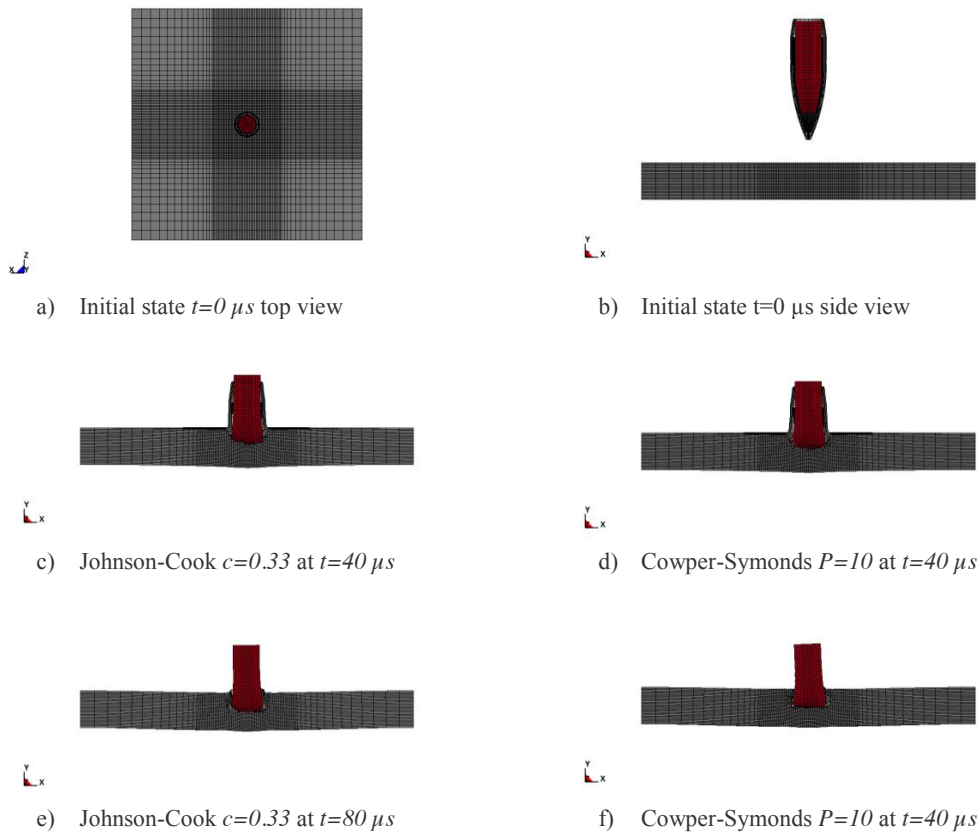


**Figure 6: Comparison of strain hardening for  $v_i=552\text{ m/s}$**

This work is part of an ongoing project and focuses specifically on the numerical representation of the 7.62x39 mm rifle projectile upon impact. The numerical approach with the Johnson-Cook and Cowper-Symonds material models, are compared with experimental results, where core deformation has been used for validation. Based on these results, the strain hardening effect is considered to be very important for this application. In future steps, the modified projectile model will be transferred from the impact upon armour steel plates to the ricochet off combat helmets.

## 6. References

- [1] S. Laville, J. Burke and A. Bogovac, *Why has the AK-47 become the jihadi terrorist weapon of choice?*, London, UK: The Guardian, 2015.
- [2] M. Seidl, T. Wolf and R. Nuesing, "Numerical investigations on ricochet of a spin-stabilised projectile on differently shaped target surfaces," in *30th ISB*, Long Beach, US, 2017.
- [3] M. Seidl, A. Ramezani and L. Linz, "Investigations on ricochet off complex targets – woven layered composite," in *Nordic LS-DYNA Conference*, Gothenburg, Sweden, 2018.
- [4] M. Seidl, "Ricochet off helmets," in *PASS*, Washington D.C., USA, 2018.
- [5] M. Seidl, T. De Vuyst and N. Djordejevic, "Numerical investigations on 7.62x39 mm projectile ricochet off aramid plates," in *LWAG*, Roubaix, France, 2019.
- [6] M. Seidl, T. Wolf and R. Nuesing, "Numerical ricochet investigation of spin-stabilized projectile on plane armor steel targets," in *LS-Dyna User Conference*, Salzburg, Austria, 2017.
- [7] J. O. Hallquist, *LS-Dyna Theory Manual*, Livermore, US: LSTC, 2015.
- [8] M. Seidl, N. Faderl and R. Nuesing, "Modelling back face deformation of woven layered composite targets under oblique impact," in *13th European LS-DYNA user conference*, Koblenz, Germany, 2019.
- [9] B. Adams, *Simulation of ballistic impacts*, Eindhoven, NL: Eindhoven University of Technology, 2003.
- [10] L. Carbajal, J. Jovicic and H. Kuhlmann, "Assault Rifle Bullet-Experimental Characterization and Computer (FE) Modeling," in *Society for Experimental Mechanics*, Uncasville, Connecticut, US, 2011.
- [11] T. De Vuyst, R. Vignjevic, J. C. Campbell, A. Klavzar and M. Seidl, "A Study of the effect of aspect ratio on fragmentation of explosively driven cylinders," in *14th Hypervelocity Impact Symposium 2017*, Canterbury, Kent, UK, 2017.
- [12] V. Favorsky, Z. Assaf, F. Aizik, E. Ran, A. Borenstein, A. Vazel, M. Ravid and N. Shapira, "Experimental-Numerical Study of Inclined Impact in Al7075-T7351 Targets by 0.3" AP Projectiles," in *26th Symposium on Ballistics*, Miami, United States, 2011.

# Modeling and Behavior of Reinforced Concrete Panels Subjected to Blast Load

M. Alper ÇANKAYA<sup>1\*</sup>

*1 Department of Civil Engineering, İzmir Katip Çelebi University, Çiğli-İzmir, TURKEY*

\*mehmetalper.cankaya@ikcu.edu.tr

**Keywords:** Reinforced Concrete, Blast Loading, Finite Element Analysis, LS-DYNA

---

**Abstract:** Objective of this study is to perform a blind simulation and investigate the behavior of reinforced concrete (RC) panels subjected to blast loading using non-linear finite element (FE) software LS-DYNA. For this purpose, an experimental study performed by Razaqpur et al. (2007) is selected from literature. One RC panel, having 1000x1000x70 mm prismatic geometry was simulated under blast load that is generated by 33.4 kg ammonium-nitrate/fuel-oil (ANFO) type explosive from three-meter standoff distance. In the model, all parts were discretized in space using eight node hexahedron solid elements except reinforcements. Beam elements were selected to discretize the bars in space. Supports were not modelled explicitly; instead, only the restraints in vertical and horizontal directions were applied. Numerous material models are available for both concrete and reinforcement in LS-DYNA. WINFRITH\_CONCRETE (MAT084) is a well-suited one for concrete material under blast/impact type of loading, and thus, was implemented in the analysis. The output obtained from the numerical analysis included peak mid-point deflection, reflected pressure and crack profile variables which are also considered to verify the experimental results.

## 1. Introduction

Civil engineering structures -specifically the RC ones- have been exposed to many military or terrorist attacks, explosions or sudden loads. Therefore, these risks should be taken into consideration when designing structures, especially the main structural members such as columns, shear walls, beams, and panels or slabs should be carefully investigated in RC buildings.

In order to understand the behavior of these type of structural members, generally; complex, time consuming and economically expensive blast tests have been performed by many researchers. However in the current study, in addition to understand the behavior of RC panels, a blast blind simulation was also performed. For this purpose, an experimental study performed by Razaqpur A.G. (2007) was selected and modelling studies were conducted by using commercially available software LS-DYNA (v971, Livermore Software Technology Corporation). LS-DYNA is capable of performing non-linear FE analysis by using explicit time integration method with advanced constitutive models of materials.

## 2. Experimental Program

In total eight RC panels consisting of two groups were tested under blast load at a Canadian armed forces base by Razaqpur et al. (2007). The panel specimens in Group CS (i.e. CS1 to CS4) were the control specimens while those in Group GSS were strengthened by glass-fiber-reinforced polymer (GFRP). A specimen representing each group is illustrated in Figure 1. All panels had 1000x1000x70 mm prismatic geometry and were doubly-reinforced with welded fabric steel mesh of designation MW 25.8/25.8 having 152 mm center-to-center spacing in each direction. Cross-section of a panel is presented in Figure 2. Yield and ultimate strengths

of the rebars were reported to be 480 and 600 MPa, respectively. On the other hand, 42 MPa compressive strength of concrete material was detected at the beginning of panel tests. Throughout the test program two different charge weights, either 22.4 or 33.4 kgf ANFO were used by three-meter standoff distance. Further details are available in the study proposed by Razaqpur et al. (2007).

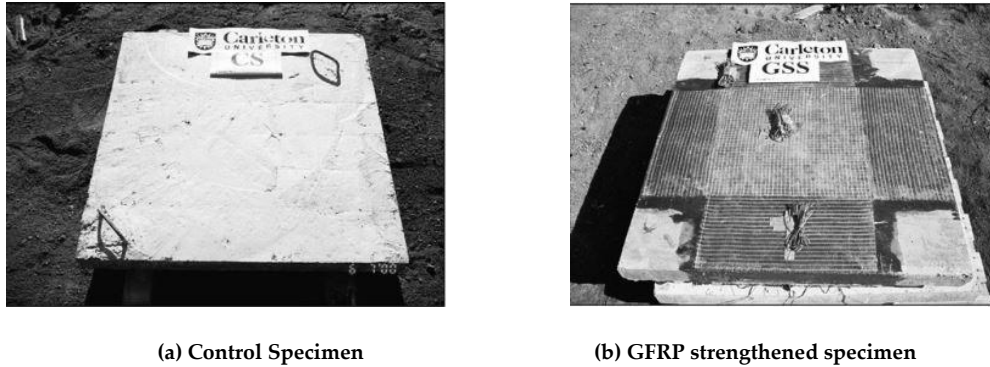


Figure 1. Typical test specimens [Source: (Razaqpur, Tolba, & Contestabile, 2007)]

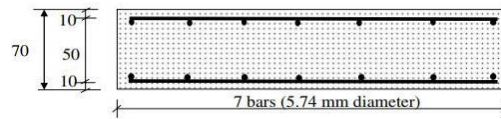


Figure 2. Steel reinforcement detail [Source: (Razaqpur, Tolba, & Contestabile, 2007)]

### 3. Numerical Analysis

Blast test simulation was conducted by LS-DYNA software. In this paper, solely CS3 specimen was investigated. Full-scale models were created and consisted of two main parts as concrete and steel reinforcement as shown in Figure 3 (a and b). Clamped supports of specimens were not modelled explicitly; instead, only translational restraints in X, Y and Z directions were applied for all nodes located along the four sides. Concrete was discretized in space using eight node hexahedron solid elements while beam elements were being used for steel reinforcement. A perfect bond between concrete solid elements and the steel reinforcement beam elements was established by LAGRANGE\_IN\_SOLID keyword in LS-DYNA. In solid elements, stresses and strains are calculated at the integration point. Using one integration point does not yield any strain even though a deformation occurs in the solid element, which results to zero energy modes (hourglass modes). Thus, hourglass control (Flangan-Belytschko type) was utilized to prevent the aforementioned modes. In order to generate the blast load, LOAD\_BLAST\_ENHANCED keyword was used.

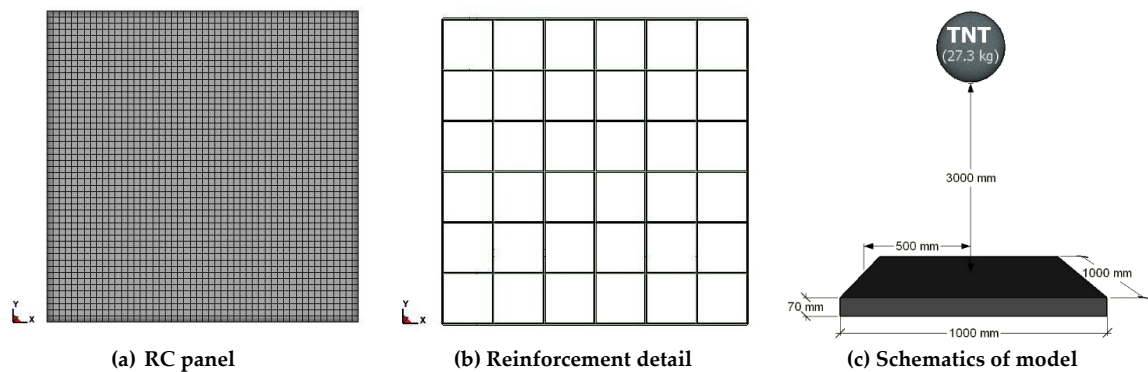


Figure 3. Top view of numerical model with 20 mm mesh size (a and b) and test setup (c)

This input defines an air-blast function for the application of pressure loads caused by the explosives in conventional weapons and requires the amount of TNT equivalency with explosive position regarding the coordinates of target, Figure 3 (c). Next, a segment surface was introduced by BLAST\_SEGMENT\_SET keyword in the top face of the panel to apply the generated blast load. On the other hand, in the analysis, three different mesh sizes were employed to investigate the effects of mesh density on the accuracy of numerical analysis results. For this purpose 5, 10, and 20 mm mesh configurations were studied. All the numerical analyses were carried out to be terminated at three milliseconds (ms) which enabled complete observation of reflected wave. Increment time was selected by software as  $7.70 \times 10^{-4}$ ,  $1.54 \times 10^{-3}$  and  $3.11 \times 10^{-3}$  ms for the analyses having 5, 10 and 20 mm mesh sizes, respectively.

### 3.1 Constitutive Model

WINFRITH\_CONCRETE (MAT 084) was selected as the material model for concrete. The model was developed over many years regarding to the requirements of the nuclear industry. The validity of the model was demonstrated by using a wide range of experimental data that are obtained from impact and blast tests, (Broadhouse, 1995). Accounting the material strain-rate sensitivity and capability of drawing the crack patterns are two outstanding properties of material model with relatively simple input parameters. For this reason, many researchers such as Mousavi and Shafei (2019), Sadraie et al. (2019), Thai and Kim (2018) and Epackachi and Whittaker (2018) have used Winfrith model recently. This model is implemented in 8-node hexahedron continuum element with single integration point and is also appropriate for smeared crack approach of concrete while rebar can be either modelled explicitly or smeared into the concrete. Stress state consists of hydrostatic and deviatoric state components. The hydrostatic stress state is defined by a non-dimensionalised volume compaction curve in default or by a user defined pressure-volumetric strain curve. Ottosen yield surface is used to limit the deviatoric stress which is updated by elastic increments, (Ottosen, 1977), and analytically defined by Equation (1) where  $A$  and  $B$  are meridional shape parameters of failure surface,  $I_1$  is the first invariant of the stress tensor,  $J_2$  is the second invariant of the deviatoric stress tensor,  $\sigma_c$  is the compressive strength of concrete and  $\lambda$  is a function of  $\cos(3\theta)$  and given by Equation (2).

$$A \frac{J_2}{\sigma_c^2} + \lambda \frac{\sqrt{J_2}}{\sigma_c} + B \frac{I_1}{\sigma_c} - 1 = 0 \quad (1)$$

$$\lambda = \begin{cases} K_1 \cos \left[ \frac{1}{3} \cos^{-1}(K_2 \cos(3\theta)) \right] & \text{for } \cos(3\theta) \geq 0 \\ K_1 \cos \left[ \frac{\pi}{3} - \frac{1}{3} \cos^{-1}(-K_2 \cos(3\theta)) \right] & \text{for } \cos(3\theta) \leq 0 \end{cases} \quad (2)$$

In here, it should be noted that WINFRITH\_CONCRETE model does not allow user to detect the parameters  $A$ ,  $B$ ,  $K_1$  and  $K_2$ ; instead, the parameters are internally generated based on a data fit using uniaxial compressive strength and tensile strength gathered from tested material. MAT\_PLASTIC\_KINEMATIC material model was assigned for the steel reinforcement. Material properties are presented in Table 1.

Table 1. Mechanical properties of materials used in LS-DYNA

Material Model	Mass Density (kg/m <sup>3</sup> )	Young's Modulus (MPa)	Tangent Modulus (MPa)	Poisson's Ratio	*UCS (MPa)	*UTS (MPa)
Plastic Kinematic	7850	200000	2000	0.3	-	-
Winfrith Concrete	2400	-	32400	0.2	42	3.629

\*UCS=Uniaxial Compressive Strength \*UTS=Uniaxial Tensile Strength

### 4. Results and Discussion

Peak mid-point deflections of CS3 panel are presented in Table 2. In the numerical analysis, central deflections were acquired when strain experienced by bottom layer steel reinforcement reached to that of maximum measured in test as 2900  $\mu\epsilon$ . According to the obtained central deflection results, analysis having 5 mm mesh size had the highest accuracy ratio compared to remaining two analyses as expected. On the other

hand, 10 mm mesh size also provided a good approximation and quite low computational time. Therefore, numerical analysis with 10 mm mesh size is selected in the current study.

**Table 2. Central displacements obtained from numerical analyses and experimental study**

Mesh Size (mm)	Numerical Analysis			Experiment
	5	10	20	
Central Displacement (mm)	6.42	6.18	5.75	9.53
Accuracy (%)	67.4	64.8	60.4	

Another investigation was performed on the reflected pressure. In the experimental study, reflected pressures were measured by four transducers located at the mid length of specimen supports. Only three pressure gauges provided data for CS3 panel and resulted in 5.50 MPa average reflected pressure with a maximum of 5.71 MPa. Figure 4 presents the reflected pressure history of a selected segment with pressure variation over the top face of panel. As it can be seen from the figure, in the analysis peak reflected pressure was detected to be 4.61 MPa at the central segment (S7492) which is yielding to 80.7% accuracy ratio compared to that of test.

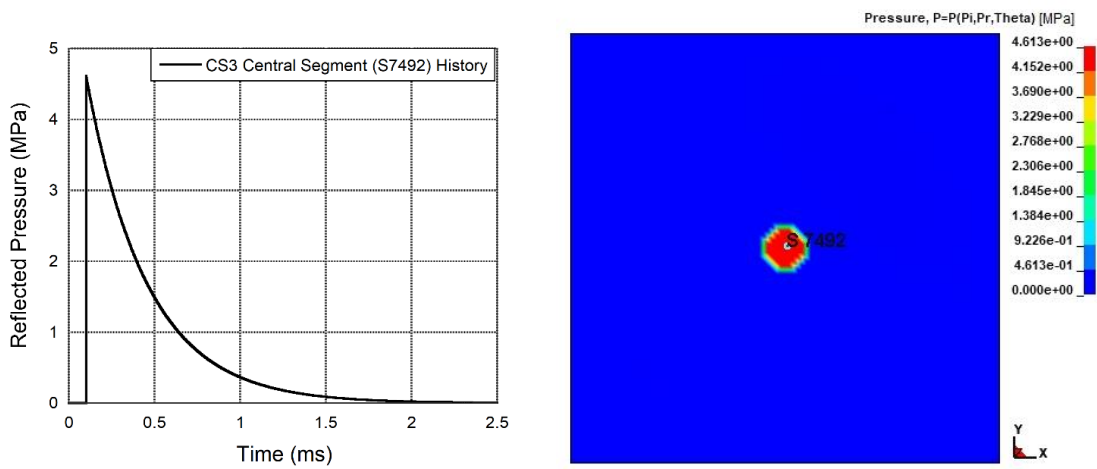
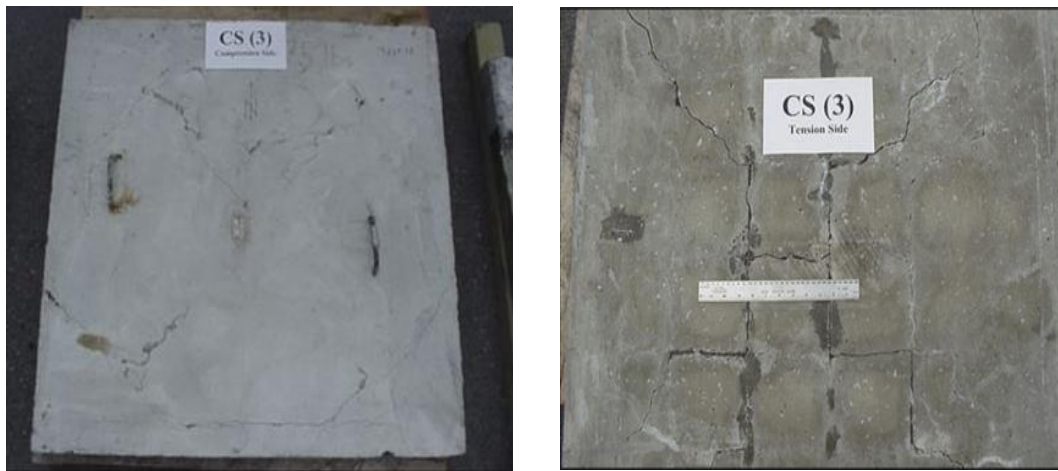


**Figure 4. Reflected pressure history (left) and the variation of pressure over the top face (right)**

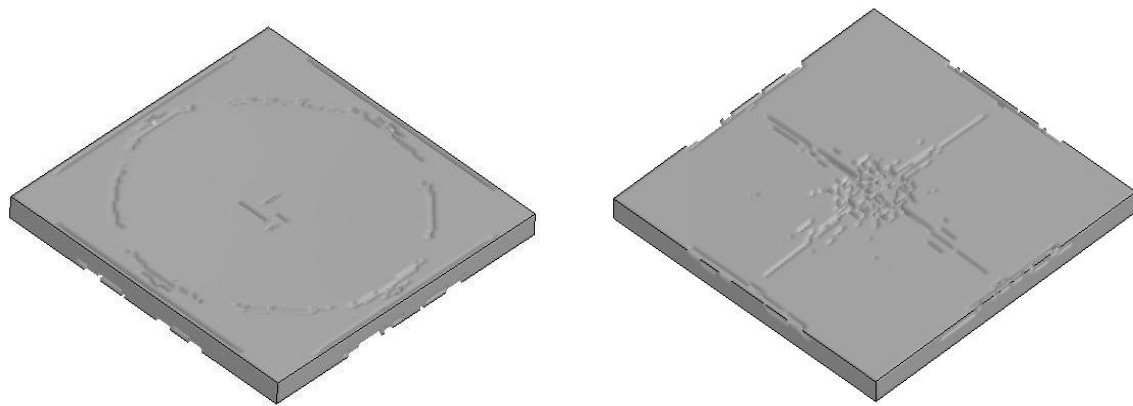
In addition, a comparison between the damage profiles obtained both from the test and numerical analysis is made and presented Figure 5. LS-DYNA predicted a circular damage on the front face of panel similar to that of the test. The specimen was mainly divided into four parts from the bottom face and initiation of diagonal damage was also observed in numerical analysis. A similar damage pattern which reached up to 4 mm crack width was detected on the bottom face of panel in the test.



Top face

Bottom face

a) Experimental study



Top face

Bottom face

b) Numerical analysis

Figure 5. Damage patterns of CS3 panel

## 5. Conclusions

In this report, blind simulation of an RC panel subjected to blast load was performed. Based on the numerical analysis results, maximum pressure was estimated 20% less than that of test. Besides, the central deflection could be detected by 35% error. This error can be attributed to several factors such as error introduced by pressure, by idealization of support conditions and by mesh density. Optimum mesh size was successfully determined by mesh sensitivity analysis. Finally, damage patterns of each face captured well by the numerical model compared to those of the test.

## References

- Broadhouse, B. J. (1995). The Winfrith Concrete Model in LS-DYNA3D. *Structural Performance Department, AEA Technology*.
- Epacakchi, S., & Whittaker, A. S. (2008). A Validated Numerical Model for Predicting the In-Plane Seismic Response of Lightly Reinforced, Low-Aspect Ratio Reinforced Concrete Shear Walls. *Engineering Structures*, 589–611.
- LS-DYNA v971. Nonlinear Finite Element Software. Livermore Software Technology Corporation. (n.d.).
- Mousavi, T., & Shafei, E. (2019). Impact Response of Hybrid FRP-Steel Reinforced Concrete Slabs. *Structures*, 436–448.
- Ottosen, N. S. (1977). A Failure Criterion For Concrete. *Journal of the Engineering Mechanics Division*, 527-535.
- Razaqpur, A., Tolba, A., & Contestabile, E. (2007). Blast Loading Response of Reinforced Concrete Panels Reinforced with Externally Bonded GFRP Laminates. *Composites Part B: Engineering*, 38, 535-546.
- Sadraie, H., Khaloo, A., & Soltani, H. (2019). Dynamic Performance of Concrete Slabs Reinforced with Steel and GFRP Bars. *Engineering Structures*, 62–81.
- Thai, D.-K., & Kim, S.-E. (2018). Numerical Investigation of The Damage of RC Members Subjected to Blast Loading. *Engineering Failure Analysis*, 350–367.

# Comparison of Two Processing Techniques to Characterise the Dynamic Crack Velocity in Armour Ceramic Based on Digital Image Correlation

Yannick Duplan<sup>1\*</sup>, Bratislav Lukić<sup>1</sup>, Pascal Forquin<sup>1</sup>

<sup>1</sup> Univ. Grenoble Alpes, CNRS, Grenoble INP, 3SR, 38000 Grenoble, France,  <https://orcid.org/0000-0002-9276-7457>,  <https://orcid.org/0000-0001-9069-9246>,  <https://orcid.org/0000-0003-0730-5483>

**Keywords:** Dynamic fragmentation, crack velocity, ceramics, rock-spall, DIC, XI-DIC.

**Abstract:** Ceramic materials are being more and more used in bi-layer shielding solutions. When impacted, substantial tensile damage creates within the ceramic tile that manifests as numerous oriented cracks. Understanding the dynamic fracture response under high strain-rates and at the level of a single dynamic crack is of major importance in pushing forward the design of resilient ceramic-based armour solutions. For that purpose, a testing technique called the Rocking-spalling test, using a single Hopkinson bar, is used in this work. This experimental method enables the study of a single quasi-straight dynamic crack which propagates through a double-notched rectangular specimen. A projectile impacts the bar generating a compressive pulse that propagates to the specimen and reflects from its free-end. Upon reflection into a tensile wave, a rocking effect takes place, thanks to the notch positioning, which leads to the inception of a single crack that propagates from the notch tip. The entire crack propagation process is filmed with an ultra-high-speed camera with exposure times down to 200 ns. Digital image correlation (DIC) was used to extract meaningful kinematics at the sample surface. Two post-processing methods for determination of crack velocity in a porous silicon carbide ceramic (Forceram®) are presented.

## 1. Introduction

Depending on the strain-rate  $\dot{\epsilon}$ , single fragmentation in quasi-static ( $10^{-5}$ – $10^{-1}$  s<sup>-1</sup>) or multiple fragmentation in dynamic ( $> 10^1$  s<sup>-1</sup>) takes place. Figure 1a on toughed alumina (Al<sub>2</sub>O<sub>3</sub>) and Figure 1b on silicon carbide (SiC) ceramics illustrate respectively the two regimes of failure. One way to explain the single-multiple transition point is the use of Monte-Carlo simulations [1] of a cubic volume loaded with a randomly-located set of flaws density, as illustrated in Figure 1c for a dense SiC.

The Denoual-Forquin-Hild (DFH) model [2,3] is a micro-mechanical anisotropic tensile damage model based on the crack inception from critical defects activated upon random tensile stress loading (described with a population following the Weibull's law [4,5]) and the obscuration (or relaxation) phenomenon that captures well this transition and that is suitable for modelling the fragmentation in various brittle materials. One of the key parameters within the model is the crack propagation velocity, described by equation (1) [2,3].

$$V_0 \cdot (T - t) = S \cdot [v_{crack} \cdot (T - t)]^n \quad (1)$$

One of the parameters,  $v_{crack}$ , corresponds to the terminal velocity at which crack propagates at “maximum speed”. Consequently, reliable experimental measurement of crack velocity and its characterisation are of crucial importance for improving the accuracy of the numerical simulation of impact events. The theoretical crack speed is often provided either as a function of the elastic 1D-longitudinal (or irrotational) wave velocity  $C_0$  in a bounded medium, which is the speed of the fastest elastic wave that can propagate in solids, or as a function of surface (or Rayleigh) wave speed  $C_R$  in solids, which carries most of

\*Author for correspondence: yannick.duplan@3sr-grenoble.fr.

† Univ. Grenoble Alpes, CNRS, Grenoble INP (Institute of Engineering Univ. Grenoble Alpes), 3SR, 38000 Grenoble, France.

asymptotical limit of  $kC_0$  ( $k$  being a constant equal to 0.38 based on energetic consideration). Yoffé (1951) [9] indicated that a crack tends to branch out or to become curved when travelling faster and faster because there is enough energy to drive two cracks independently. Ravi-Chandar and Knauss (1984) [10] stated that branching may occur for even lower velocities than predicted by Yoffé (1951) [9].

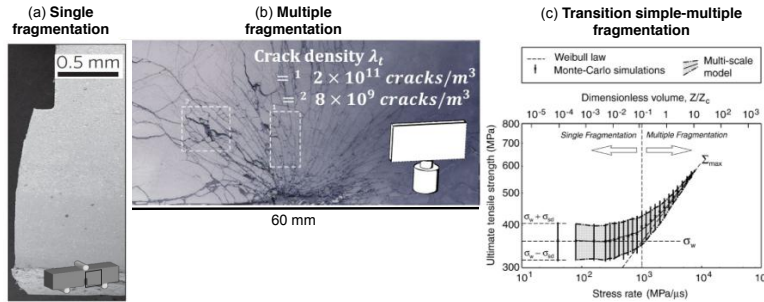


**Figure 1:** Examples of: (a) single and (b) multiple fragmentation tests, with (c) the transition between single and multiple fragmentations (adapted from [11], [12] and [1]).

Experimental works on brittle materials showed that the limiting velocity regarding the Rayleigh wave speed  $C_R$  is material dependant:  $0.45C_R$  in Homalite-100 (polyester resin) [10],  $0.50C_R$  [14] or  $0.60C_R$  [15] in glass, between  $0.53C_R$  and  $0.57C_R$  in concrete (R30A7) [16],  $0.60C_R$  in Plexiglas (Polymethyl methacrylate (PMMA) brittle thermoplastic) [17]. Recently, Anderson Jr., Bigger and Weiss (2014) [18] performed ballistic impacts on borosilicate glass ceramics using a high-speed video camera with interframe time  $\sim 5 \mu\text{s}$ . They observed crack speeds around  $1.92 \text{ km/s}$  ( $\sim 0.59C_R^1$ ) independent from the impact velocity, confirming that crack velocity is an actual material property. However, the effects of the material microstructure were not discussed. Besides, other parameters could influence the crack velocity: when the loading is applied directly at the crack tip [19], presence of void [10,20], change of material behaviour ahead of the crack tip with particular microstructures (increase in fracture toughness  $K_I$  known as the R-curve effect). Under dynamic loading, some main challenges are owing to a large number of micro-cracks generated under impulsive loading which makes the isolated visualisation difficult (crack monitoring) as well as the interpretation of the results due to multiple crack interactions. This leads to a clear need for an experimental method that is able to generate a single dynamic crack under high strain-rate loading.

The current paper presents one such experimental method in conjunction with Digital Image Correlation (DIC) to obtain a crack speed during single fragmentation but in dynamic. The crack tip speed cannot be directly measured by simply looking at the images since the crack opening displacement is far beyond pixel size (1 to 3  $\mu\text{m}$ ). Comparing the first image and last image of the sequence only provides an idea on the crack path; however, the crack kinematics stays out of reach. In this situation, a sophisticated extraction method based on image correlation serves as one of the only method of obtaining such information.

For this reason, two image processing methods are used on a series of ultra-high-speed images obtained with  $0.2 \mu\text{s}$  exposure as to extract the crack velocity of porous Sain-Gobain's armour SiC ceramic commercially named Forceram [21]. The acquisition sequences are obtained by filming a surface of a rectangular sample while being dynamically loaded through the experimental technique called the Rocking by spalling (or "Rockspall") test [16,22]. A single quasi-straight dynamic crack is generated which propagates through a  $60 \times 30 \times 7$ -mm double-notched specimen at high strain-rate. This technique was already employed in [16,22] on concrete material in which the information obtained from DIC was compared to the data of a single velocity-gauge glued on the sample which allowed the evaluation of the crack velocity.

## 2. Methods

### 2.1. Experimental set-up

The entire experimental set-up with corresponding instrumentation is presented in Figure 2. The set-up is used with a single steel Hopkinson bar (about 20 mm diameter, 92 mm length, 225 g mass) to enhance the reproducibility of the tests compared to direct impact, to which a rectangular sample ( $60 \times 30 \times 7 \text{ mm}^3$ ) is glued on one end. The bar is impacted with a steel projectile (Figure 2: about 20 mm diameter and length,

<sup>1</sup>  $C_R$  was calculated using material properties of Borofloat 33 found in [13] ( $C_R \sim 3238 \text{ m/s}$ ).

400 mm slightly-curved surface to provide better contact conditions in case if the impact is not perfectly plan, 48 g mass) accelerated by a gas launcher on the other end. The Kirana® (*Specialised Imaging*) ultra-high-speed camera (5 Mfps capacity, 924×768 px, 180 images) is used to film a zone around the inception notch. Two high-power AD-500 flash lights (*Specialised Imaging*) are used to provide continuous and homogeneous lighting conditions to the imaged scene. The triggering of the flash lights is performed thanks to a signal delay unit (*Specialised Imaging*). The camera, triggered with a laser signal (vibrometer controller OFV-5000® + fiber vibrometer OFV-552 from *Polytec*) pointing on the ceramic rear face which is not impacted, is instrumented with a 180 mm F/3.5 telephoto lens (*Tamron*) coupled with a teleconverter 2× Teleplus Pro 300 DGX (*Kenko*) which allowed reaching an average pixel size of 17  $\mu\text{m}/\text{px}$  ( $\sim 0.059 \text{ px}/\mu\text{m}$ ). Consequently, the samples were prepared with a micrometric speckle.

Numerical work was previously conducted in [23] in order to design and optimise the testing configuration in terms of notch positions and lengths. The resulting sample configuration is used within this work. Impact velocities were also optimised and deduced from numerical simulations using the DFH damage model. It was found that to allow single crack propagation without damaging the ceramic beyond the notch tip, the projectile speed should be around 5 m/s. The velocities of 6.58 m/s (first sample) and 9.04 m/s (second sample) were reached in the actual testing conditions, obtained using three speed barriers positioned at the exit of the barrel (optical fibres).

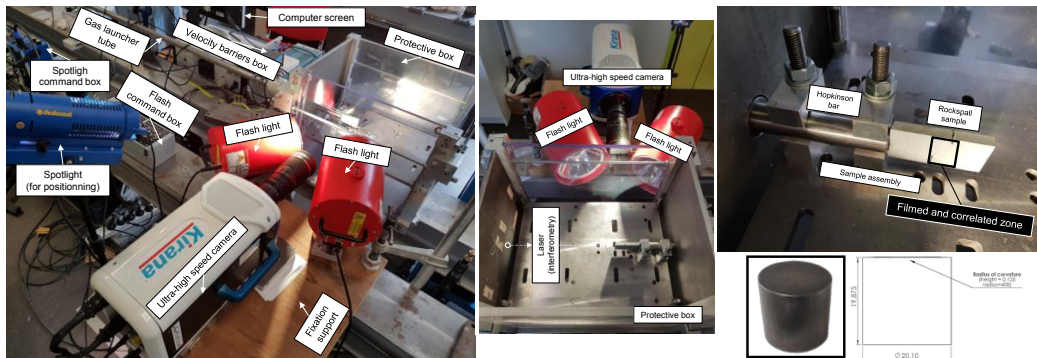


Figure 2: Experimental set-up with a global and two extensive views inside the protective box, along with a projectile view (black box) and its plan (dimensions expressed in millimetres).

## 2.2. Image processing

The DIC technique provides discretised displacement fields on the sample surface by comparing a deformed image with a reference. For that purpose, the visualised part of the sample (or Region Of Interest (ROI)) is sub-divided into Zones Of Interest (ZOI) and the determination of the displacement of each ZOI is obtained by minimising correlation function [24]. In the so-called global approach, the different ZOI constitute a finite-element mesh and the displacements are determined on the element nodes [24].

Presently, two post-processing methods based on global DIC are used to extract the crack velocity:

- **Method 1** - The CORRELI<sup>Q4</sup> software [25], implemented in MATLAB (versions 9.1 (R2016b) and 7.10 (R2010a)), which makes use of Q4(P1)-shape functions (4-noded rectangular elements, linear interpolation) to subdivide the sample surface. This method will serve as a reference.
- **Method 2** - The EIKO-CRACK software (version 1.00, in development), working with a MATLAB standalone set of shared libraries (MATLAB® compiler Runtime), which relies on both a discontinuous enrichment to the finite element approximation (extended approach) and the addition of mechanical constraints to prevent incoherent mechanical displacement regarding material constitutive or propagation law (integrated approach) [26,27].

## 3. Results and discussions

In Figure 3, the ROI with a 16-px or a 64-px resolution *i.e.* ZOI size = 16×16 or 64×64 px, ZOI shift = 16 px, is digitised for a Forceram porous SiC sample, along with the final image in which the corresponding DIC result with a 16-px resolution is superimposed. The 16-px resolution allows to better identifying the path followed by the crack because it provides higher displacement gradients at the expense of both increased uncertainty due to noise and increased calculation time. The noise manifests as the time variation of the image sequence appearing to be characteristic of the Kirana sensor, it presents a variation in grey level around every 20 frames [28].

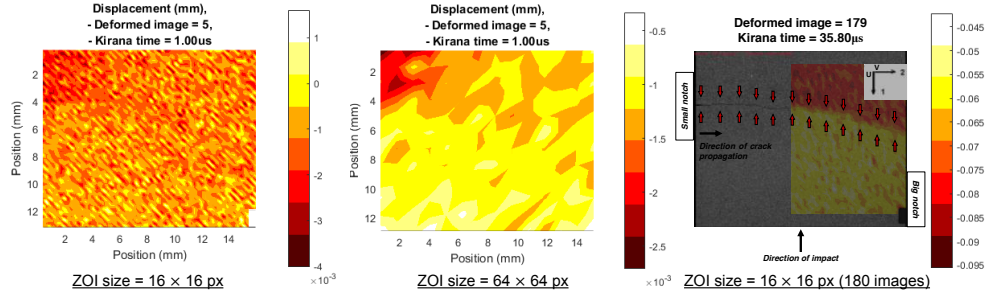


**Figure 3 :** Three DIC results (sample: Force-Rock-1): on the left and in the middle, displacement fields on 1 (reference) + 20 (correlated) images, 1  $\mu$ s regarding the 1<sup>st</sup> image of reference, with two ZOI sizes; on the right, final DIC result on 180 images placed with the corresponding Kirana® experimental image.

At the onset of the crack propagation, the crack opening  $\Delta u$  is approximately 1.5  $\mu$ m ( $\sim$  1/10 px size). Figure 4 quantifies the noise level regarding 16-px and 64-px results obtained from static images taken before the test, as suggested in [28]. The transversal displacement along the direction 1 ( $u_1$ ) is insignificant, however, the standard deviation – which can be considered as measurement uncertainty – is sensible. Especially, for a correlation with a ZOI size of 16×16 px, it reaches 0.63  $\mu$ m of uncertainty (average of the standard deviation of the 180 images) against 0.17  $\mu$ m for a ZOI size of 64×64 px. Nonetheless, the error is inferior to the crack opening of the ceramic.

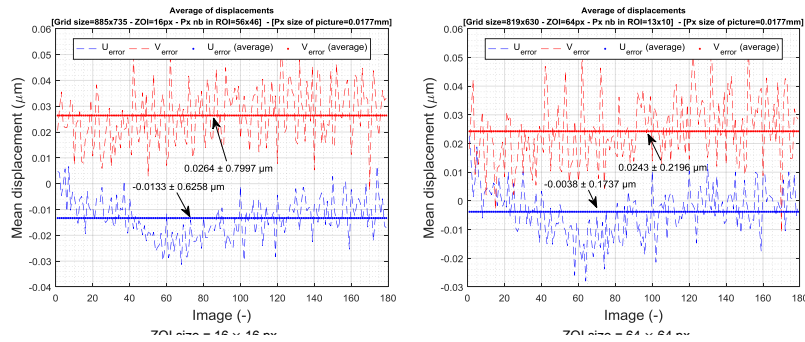


**Figure 4:** Mean displacement per image (sample: Force-Rock-1): for each point (1, 2, 3, ..., 179), the displacement map is averaged in one value (dotted lines), then all the 179 values are averaged into a single one (horizontal lines). For the record, this sample has a pixel-resolution of 17.7  $\mu$ m.

The determination of the crack velocity relies on a known position of the crack tip, frame by frame. Each field of displacement was analysed with a visual method explained in [29,30]. The C(T)OD (Crack (Tip) Opening Displacement:  $\delta = \Delta u$ ) was used as a criterion for setting the range of visualised displacement values. The method consists of estimating the crack tip location using a detection criterion and a contour plot. This criterion relies on the separation of the displacement contours perpendicular to the crack path as shown by numerical works in [30]. Here, in a situation where 5 or more contour lines separate, the observed displacement discontinuity was considered to be due to the presence of the crack tip (or crack opening). The technique requires a hypothesis whereby during crack propagation, the critical mode-I stress intensity factor of the ceramic vary little so is assumed constant:  $K_{Ic} = 3.16 \text{ MPa}\cdot\text{m}^{1/2}$ . Given the small distances considered, even if  $K_I$  varies, the crack will be not far from the estimation. Although this

hypothesis will merit additional investigations, such assumption is justified by the fact that except during inception, the crack velocity in brittle materials is generally constant during propagation [31]. It is decided to look at the separation of the displacement contours with an accuracy of less than half the ceramic thickness (3.2 mm), so the position of the crack tip is obtained considering the distance  $r = 3.2 \text{ mm}$  at which the COD  $\delta$  is measured and supposed to be located. The formula to calculate the resolution of  $\delta$  for monitoring the crack tip is given by the Westergaard's solution [32] (and Irwin theory [33]) in (2) under plane-stress conditions:

$$\delta(r) = 8 \frac{K_{Ic}}{E} \sqrt{\frac{r}{2\pi}} \quad (2)$$

With  $E = 220 \text{ GPa}$  the elastic (or Young's) modulus. One finds  $\delta = 2.59 \text{ }\mu\text{m}$ , since  $1 \text{ px} = 17.7 \text{ }\mu\text{m}$  for the sample Force-Rock-1, then  $\delta = 0.15 \text{ px}$ : this is the minimum input value to set in CORRELI<sup>Q4</sup> as  $\delta_{max}$  (see Figure 5). Besides, to come back to the constant  $K_{Ic}$ , the work is done with low COD to reduce the uncertainty on the crack position; a low COD gives a low distance to the tip. If  $K_{Ic} = 2.84 \text{ MPa}\cdot\text{m}^{1/2}$  (-10%),  $3.16 \text{ MPa}\cdot\text{m}^{1/2}$  or  $3.48 \text{ MPa}\cdot\text{m}^{1/2}$  (+10%), then respectively  $r = 4.0, 3.2$  or  $2.6 \text{ mm}$ ; in other words, a 20%-uncertainty on the  $K_I$  corresponds only to a 1.4 mm of uncertainty on the crack tip, which remains quite low compared to the size of the ZOI window and the distance travelled by the crack. Figure 5 is a screenshot of a DIC result with a 16-px ZOI and a 64-px ZOI. It can be clearly seen that the noise level is too high for proper tracking with ZOI size = 16 px. Still in Figure 5, the MATLAB window is the associate determination of the crack tip position with ZOI size = 64 px. A dotted trend line on the discontinuity is drawn, and the tip of the crack, in the circle, is revealed at a distance  $r$ , where it can be seen a change of angle (displacement discontinuity) for the supposed location.

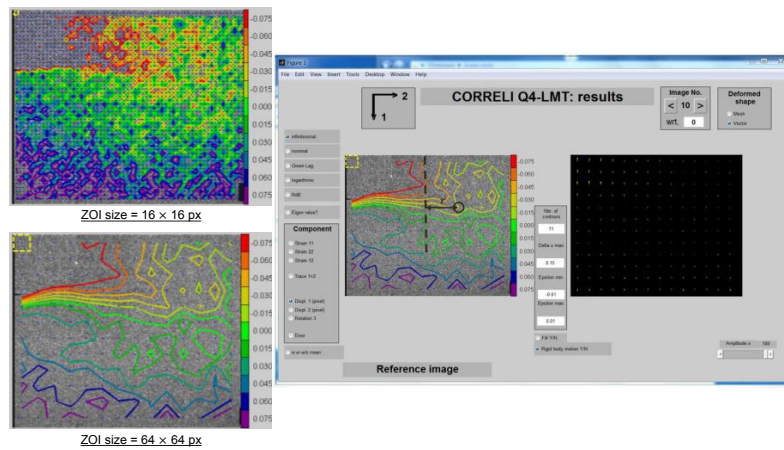
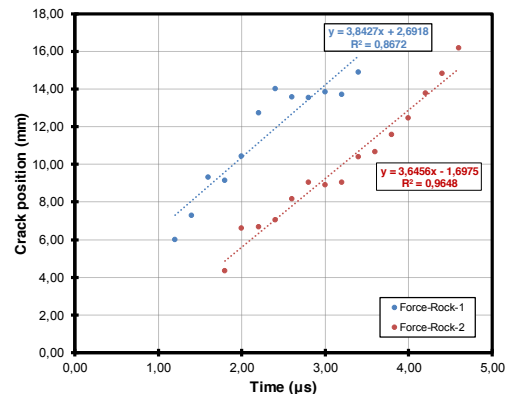


Figure 5: Two DIC results (sample: Force-Rock-1) on the left showing the contours of  $u_1$  for two ZOI sizes which are into evidence by the yellow rectangles in the top left-hand corners. The window on the right (ZOI =  $64 \times 64 \text{ px}$ ) displays: the correlated zone that is annotated, the amplitude of the displacement vectors ( $\times 100$ ), and the user parameters indicating that 11 isocontours are used with  $0.15 \text{ px}$  as max.  $\delta$ .

Figure 6: Crack velocity in the porous SiC ceramic, using CORRELI<sup>Q4</sup>.

This estimation of the crack tip position is repeated for each frame of the DIC pictures. In Figure 6, the trend line (derivative) discloses the crack velocity which is found to be nearly  $3745 \text{ m/s}$ . Given  $C_0 = 8856 \text{ m/s}$  and  $C_R = 5256 \text{ m/s}$  in the considered ceramic, the velocity result is equivalent to  $0.42C_0 = 0.71C_R$ . The formula provided by Broek (1984) [8]



**Method 2:**

On the left of Figure 7, a screenshot of the user interface of the EIKO-CRACK software during processing is shown. Sets of 15 images are correlated (and not 20 like in CORRELI<sup>Q4</sup>, the 5 first images of the selected were deleted to avoid convergence issue). Two key parameters are used to create a mesh (or patch) around the notch in pixels. The eXtended DIC (X-DIC) accounts for the kinematics of a crack specimen, by adding a discontinuous enrichment of the displacement field to the finite elements, to be able to reveal heterogeneous displacement fields in an element [34]. The approach makes it possible to follow the arbitrary crack growth without the need for re-meshing. The main advantage of the technique is to allow coarser mesh (gain in computation time) without any loss of accuracy or even more accuracy since it can feature strong discontinuities that may be poorly captured by standard finite element shape functions [34]. Besides, EIKO-CRACK uses an Integrated DIC (I-DIC) approach, where “integrated” means that the correlation algorithm assumes material behaviour and the balance of momentum thanks to mechanical residual which is introduced [34]. It consists in using displacement fields that are mechanically meaningful [27] (e.g. momentum-balanced stress field obtained through a linear stress-strain relation [34]) calculated using Williams’ series [35] for the determination of the crack tip position.

On the right of Figure 7, self-contained DIC processes are visible with the crack position going negative with a 10-100 patch. With a 50-200 patch, the software is able to generate output data. The distance from the initial crack tip is replotted in Figure 8. The decreasing crack position is due to the background (light) noise. It seems that the software does not allow proper crack monitoring in this situation.

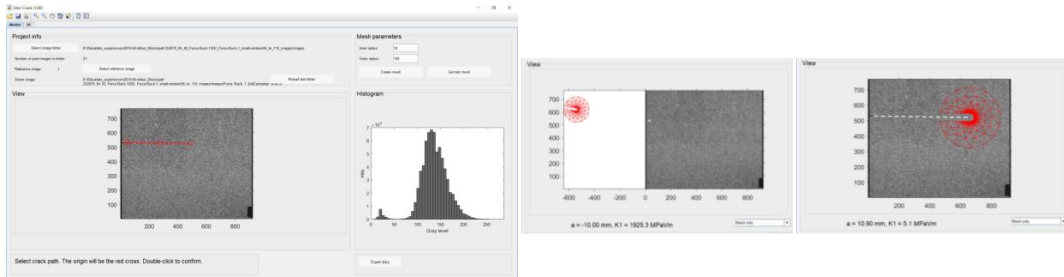
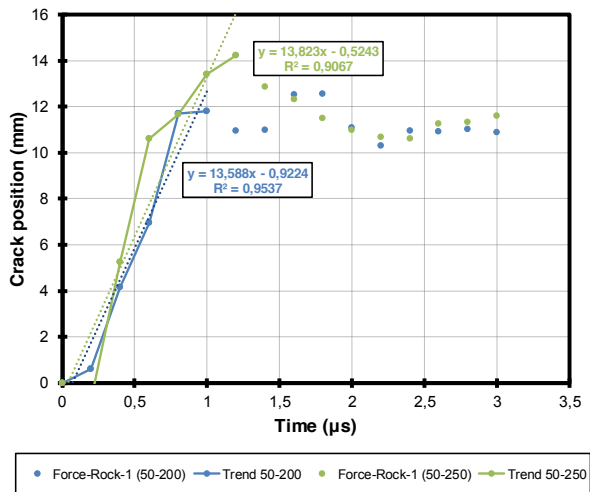


Figure 7: Definition of the approximate crack path during the test in EIKO-CRACK (on the left), two DIC results for crack monitoring using a 10-100 px patch (small in the middle) and 50-200 px patch (small on the right).

Figure 8. Crack velocity in the porous SiC ceramic (sample: Force-Rock-1), using EIKO-CRACK, with two patch sizes.

The crack velocity appears to be 13,588 m/s ( $1.53C_0 = 2.59C_R$ ) or 13,823 m/s ( $1.56C_0 = 2.63C_R$ ), which is unlikely. There are multiple reasons that could explain the difficulty of the post-processing:

- The Young’s modulus of the ceramic (220 – 232 GPa, values provided by Saint-Gobain) may be too high, so  $\delta$  is too small with the current resolution for EIKO-CRACK. In fact, the experimental  $\delta$  is in the order of the micrometre and the resolution reached here is close to  $17 \mu\text{m}/\text{px}$ .



- The signal/noise ratio may be not high enough, the noise of the Kirana® camera (Gaussian blur, variations in luminosity) upsets the Williams' series since the algorithm for the crack tip location is disrupted by parasitic fields.
- The crack path may be sufficiently deviated to upset the Williams' series. In fact, the software is supposed to work only for a straight crack path ( $K_I$  dominance hypothesis). Due to both the high energies involved in ceramics and the complex stress field, the crack is more likely to tilt.

#### 4. Conclusion

An experimental method, the Rockspall test, is used to investigate the cracking velocity of a porous SiC (Forceram®) under dynamic tensile loading. Two DIC software applications are contrasted. CORRELI<sup>Q4</sup> ("classical" global DIC), based on displacement fields, is less dependent on the resolution of the correlated images for the crack monitoring, but more dependent on the user himself since it is optically-based. Though, the software provides reasonable results. Thanks to the CORRELI<sup>Q4</sup> method, the crack velocity on the porous SiC is deduced as equal to 3745 m/s ( $0.42C_0$  or  $0.71C_R$ ). EIKO-CRACK (global XI-DIC) relies on Williams' equations to describe the fields of displacement, so the latter is not directly calculated. Likely due to high noise and small crack opening amplitude, the software is not proficient enough to detect the crack tip and to reproduce a consistent crack path. The unstable results may originate from too low displacement/noise ratio and variation in luminosity. Better results could be obtained with EIKO-CRACK using better conditions (a higher pixel resolution or a less noisy camera). For this reason, quantification of the parameters that can affect crack velocity identification (such as noise levels and image pixel size) is paramount and remains as a future perspective to decrease error and for an optimum use.

#### Acknowledgments

Each author is thankful to Saint-Gobain for providing the tested ceramic samples and to the French MOD (Ministry Of Defence division: *Direction Générale de l'Armement* (DGA)) for co-sponsoring the work. The authors have a thought to Mr. François Bonnel from the CMTC (*Consortium des Moyens Technologiques Communs*) characterisation platform for the optical lens system loan, the LMT-Cachan (*Laboratoire de Mécanique et Technologie – Cachan*) which implemented Correli in a Matlab code; and the authors would also like to thank Dr. Florent Mathieu (from EikoSim company) who developed improved features in Eiko-Crack according to author needs. Some figures (Figure 6 and Figure 8) were exported into vector graphics with aid of Daniel's XL Toolbox add-in (version 7.3.2) for Microsoft Excel.

#### Funding Statement

Source of funding comes from DGA and Saint-Gobain.

#### References:

1. C. Denoual, F. Hild. 2002. Dynamic fragmentation of brittle solids: a multi-scale model. *Eur. J. Mech. – Solids* **21**, 105–120. (10.1016/S0997-7538(01)01187-1)
2. C. Denoual, F. Hild. 2000. A Damage Model for the Dynamic Fragmentation of Brittle Solids. *Comput. Methods Appl. Mech. Eng.* **183**, 247–258. (10.1016/S0045-7825(99)00221-2)
3. P. Forquin, F. Hild. 2000. A probabilistic damage model of the dynamic fragmentation process in brittle materials. *Adv. Appl. Mech.* **44**, 1–72. (10.1016/S0065-2156(10)44001-6)
4. W. Weibull. 1939. A Statistical Theory of the Strength of Materials. *Roy. Swed. Acad. of Eng. Sci.* **151**, 45.
5. W. Weibull. 1951. A Statistical Distribution Function of Wide Applicability. *J. Appl. Mech.* **18**, 293–297.
6. M.A. Meyers. 1994. CHAPTER 2 Elastic Waves (in "Dynamic Behavior of Materials"). 23–65. (ISBN 978-0-471-58262-5)
7. J.W. McCauley, E. Strassburger, P. Patel, B. Paliwal, K.T. Ramesh. 2013. Experimental Observations on Dynamic Response of Selected Transparent Armor Materials. *Exp. Mech.* **53**, 3–29. (10.1007/s11340-012-9658-5)

- 90-247-2580-1)
9. E.H. Yoffé. 1951. The moving Griffith crack. *Phil. Mag.* **42**, 738–750. (10.1080/14786445108561302)
  10. K. Ravi-Chandar, W.G. Knauss. 1984. An experimental investigation into dynamic fracture: I. Crack initiation and arrest. *Int. J. Fract.* **25**, 247–262. (10.1007/BF00963460)
  11. F. Bouville, E. Maire, S. Meille, B. Van de Moortèle, A.J. Stevenson, S. Deville. 2014. Strong, tough and stiff bioinspired ceramics from brittle constituents. *Nat. Mater.* **13**, 508–514. (10.1038/nmat3915)
  12. J.L. Zinszner, P. Forquin, G. Rossiquet. 2015. Experimental and numerical analysis of the dynamic fragmentation in a SiC ceramic under impact. *Int. J. Impact Eng.* **76**, 9–19. (10.1016/j.ijimpeng.2014.07.007)
  13. MakeltFrom.com. “Borosilicate Glass”. Accessed on: <https://www.makeitfrom.com/material-properties/Borosilicate-Glass> (05/12/2019).
  14. H.E. Edgerton, F.E. Barstow. 1941. Further Studies of Glass Fracture with High-Speed Photography. *J. Am. Ceram. Soc.* **24**, 131–137. (10.1111/j.1151-2916.1941.tb14836.x)
  15. G.D. Quinn. 2007. In “Fractography of ceramics and glasses”. (Special Publication 960-16)
  16. P. Forquin. 2012. An optical correlation technique for characterizing the crack velocity in concrete. *Eur. Phys. J. Spec. Top.* **206**, 89–95. (10.1140/epjst/e2012-01590-6)
  17. E.N. Dulaney, W.F. Brace. 1960. Velocity Behavior of a Growing Crack. *J. Appl. Phys.* **31**, 2233. (10.1063/1.1735529)
  18. C.E. Anderson Jr., R.P. Bigger, C.E. Weiss. 2014. Crack and Damage Velocities in Ballistic Experiments. *Int. J. Appl. Glass Sci.* **5**, 374–383. (10.1063/1.1735529)
  19. A.J. Rosakis. 1999. Cracks Faster than the Shear Wave Speed. *Science.* **284**, 1337–1340. (10.1126/science.284.5418.1337)
  20. M.A. Meyers. 1994. CHAPTER 16 Dynamic Fracture (in “Dynamic Behavior of Materials”). 488–566. (ISBN 978-0-471-58262-5)
  21. Saint-Gobain | Performance Ceramics & Refractories. “Law Enforcement Body Armor”. Accessed on: <https://www.ceramicsrefractories.saint-gobain.com/markets/defense-law-enforcement-armor> (27/01/2020).
  22. P. Forquin, R. Cheriguene. 2011. A rocking spalling test to characterize the crack velocity in concrete. *Exp. Appl. Mech.* **26**, 1–2. (10.1007/978-1-4614-0222-0\_1)
  23. Y. Duplan, P. Forquin, B. Lukić, D. Saletti. 2018. Numerical analysis of a testing technique to investigate the dynamic crack propagation in armour ceramic. *EPJ Web Conf.* **183**, 02039. (10.1051/epjconf/201818302039)
  24. G. Besnard, H. Leclerc, F. Hild, S. Roux, N. Swiergiel. 2012. Analysis of image series through global digital image correlation. *J. Strain Anal. Eng. Des.* **47**, 214–228. (10.1177/0309324712441435)
  25. F. Hild, S. Roux. 2008. CORRELI Q4: A Software for “Finite-element” Displacement Field Measurements by Digital Image Correlation. (Internal Report No 269)
  26. F. Mathieu, F. Hild, S. Roux. 2012. Identification of a crack propagation law by digital image correlation. *Int. J. Fatigue.* **36**, 146–154. (10.1016/j.ijfatigue.2011.08.004)
  27. F. Mathieu, F. Hild, S. Roux. 2012. Image-based identification procedure of a crack propagation law. *Eng. Fract. Mech.* **103**, 48–59. (10.1016/j.engfracmech.2012.05.007)
  28. B. Lukić. 2018. Advanced measuring techniques for characterisation of the concrete dynamic tensile response. (PhD Thesis)
  29. F. Forquin. 2003. Endommagement et fissuration de matériaux fragiles sous impact balistique - Rôle de la microstructure. (PhD Thesis)
  30. P. Forquin, L. Rota, Y. Charles, F. Hild. 2004. A method to determine the macroscopic toughness scatter of brittle materials. *Int. J. Fract.* **125**, 171–187. (10.1023/B:FRAC.0000021076.76987.62)
  31. K. Ravi-Chandar, W.G. Knauss. 1984. An experimental investigation into dynamic fracture: III. On steady-state crack propagation and crack branching. *Int. J. Fract.* **26**, 141–154. (10.1007/BF01157550)
  32. H.M. Westergaard. 1939. Bearing Pressures and Cracks. *J. Appl. Mech.* **6**, 49–53.
  33. G.R. Irwin. 1957. Analysis of Stresses and Strains Near the End of a Crack Traversing a Plate. *J. Appl. Mech.* **24**, 351–369.
  34. J. Réthoré, S. Roux, F. Hild. 2009. An extended and integrated digital image correlation technique applied to the analysis of fractured samples. *Eur. J. Comp. Mech.* **18**, 285–306. (doi.org/10.3166/ejcm.18.285-306)
  35. M.L. Williams. 1957. On the stress distribution at the base of a stationary crack. *J. Appl. Mech.* **24**, 109–114.

# Optimization of geometrical parameters under dynamic compression of auxetic re-entrant honeycomb structure

Laura DELCUSE<sup>1\*</sup>, Slim BAH<sup>1</sup>, Paul WOOD<sup>2</sup>, Urvashi GUNPUTH<sup>2</sup>, Alexis RUSINEK<sup>1</sup>

<sup>1</sup>Laboratory of Microstructure Studies and Mechanics of Materials, UMR-CNRS 7239, 7 rue Félix Savart, 57000 Metz, France

<sup>2</sup>Innovation Institute of Sustainable Engineering (IISE), University of Derby, Quaker Way, Derby, United Kingdom

**Keywords** : auxetic re-entrant, dynamic, compression, numerical, taguchi

**Abstract** : The paper describes a computational numerical study of an auxetic re-entrant honeycomb cell architecture in a Ti-6Al-4V alloy, to identify and rank the geometric features that influence the behaviour of the material architecture under dynamic impact compression loading. A 2x2 two-dimensional unit cell architecture was selected for the study. In this study, the radius at the corner of each cell was identified as a new parameter to represent the constraints of a manufacturing process. A new process of optimisation by FEA was found to achieve our goal with an experimental plan. Moreover, the study identified and ranked the geometric features and it was found the cell wall angle had the most influence followed by the radius at the corner in enhancing the mechanical properties. The parameter identified with the least influence was the thickness.

## 1. Introduction

An auxetic structure is a material that has a negative poisson's ratio under compression or tension. Such material has been shown to possess enhanced energy absorption, stiffness and many more mechanical properties, as shown in studies of Scarpa et al (2005) and Bezazi et al (2009). The mechanical properties of an auxetic structure has been associated with the different geometrical parameters previously (Hu et al, 2018). Hence this study was aimed towards the optimisation of the geometry of a re-entrant honeycomb structure with regards to enhanced Effective Elastic Modulus, Poisson's ratio and Specific Energy Absorption. The present work propose a new way to optimize the geometrical parameters to enhance those mechanical properties by the Taguchi's method. Finite element analysis was used for the computational simulation. The Taguchi's design (L9) was employed in order to validate the effects of the different geometries and the respective mechanical properties. The Taguchi's method was also compared to a global parametric study, which is not treated in this paper. The deformation mode under dynamic compression was studied, to understand the behaviour of an auxetic structure.

## 2. Structural design

### 2.1. Auxetic re-entrant honeycomb

Various auxetic structures has been developed over the last few years, based on metamaterial or chiral design (Yuan et al, 2017 ; Fu et al, 2018). In this study, an 2D auxetic re-entrant structure as shown in Fig. 1, was investigated. The structure was extruded with a width of 1 mm. The studied parameters was the following :

\*Author for correspondence (laura.delcuse@univ-lorraine.fr).

† Present address : LEM3, University of Lorraine, 7 rue Félix Savart, Metz, 57000, France

the height  $h$  and the length  $l$  with the length ratio  $\alpha = \frac{h}{l}$ ; the cell wall angle  $\theta$ ; the thickness  $t$ ; and the radius  $R$ . The radius used in this study was selected as such to match that produced during selective laser melting.

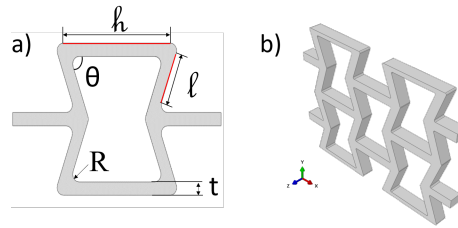


**Figure 1** : Schematic of a) one auxetic cells b) 2x2 auxetic cells

The various geometric parameters can be used to calculate the relative density of the re-entrant honeycomb structure as per Equation 1 (Gibson and Ashby, 1997) :

$$\frac{\rho_*}{\rho_s} = \frac{\frac{t}{l} \left( \frac{h}{l} + 2 \right)}{2 \sin \theta_0 \left( \frac{h}{l} - \cos \theta \right)} \quad (1)$$

when  $\rho_*$  is the density of the honeycomb re-entrant and  $\rho_s$  is the density of bulk material. In order to avoid the influence of the relative density on the final geometry, a fixed value of 0.28 was used.

### 2.2. Taguchi's method

Taguchi method was worked on the basis of statistical tools to highlight and quantify the rank of many factor and the optimal parameters for a given study. With this method, each parameter was investigated individually with an orthogonal arrays and triangular tables.

In the present work, a L9 array was chosen to determine the effect of these geometrical parameters, and so improve the following responses : Effective Elastic Modulus, Poisson's ratio and Specific Energy Absorption. To have a L9 arrays, 3 levels for the 4 studied factors were necessary. With the aim of maintaining the relative density, the 3 levels of the different factors used were as per Table 1.

For each run, a Signal-to-Noise method was employed to evaluate the association between the parameter and resulting properties according to the larger-the-better equation (Equation 2; Tamizharan et al, 2019). :

$$S/N = -10 \log \left( \frac{1}{n} \sum_{i=1}^n \frac{1}{y_i^2} \right) \quad (2)$$

where  $y_i$  is the experimentally value, such as the Effective Elastic Modulus, of the  $i^{th}$  experiment and  $n$  the total number of the experiment.

Level	$\alpha = \frac{h}{l}$	$\theta$	Thickness (mm)	Radius (mm)
1	1.5	84	0.3	0.1
2	2.5	67	0.6	0.7
3	3.5	58	0.9	1.3

**Table 1** : Values of level for each factor for Taguchi's method

### 3. Finite Element Analysis

#### 3.1. Material Model

In this study, Ti-6Al-4V alloy was considered, with the different properties associated using the Johnson-Cook constitutive model as per Equation 3. The latter material properties were selected as per Kay et al (2013) as followed : A, B and n are equal to 1097.76 MPa, 1091.96 MPa and 0.93 respectively. As concerned C, its value was 0.014. The Young Modulus E was set to 120 GPa, the Poisson's Ratio  $\nu = 0.3$  and the density  $\rho = 4520 \text{ kg.m}^{-3}$ . For the heating parameters, the specific heat and the melting temperature were set at 610 J/kg.C and 1670°C respectively. Adiabatic effect with Johnson-cook constitutive law was considered, with m equal to 1.1.

$$\sigma = (A + B\epsilon_p^n) \left[ 1 + C \ln \left( \frac{\dot{\epsilon}}{\dot{\epsilon}_0} \right) \right] \left[ 1 - \left( \frac{T - T_r}{T_m - T_r} \right)^m \right] \quad (3)$$

#### 3.2. Boundary conditions and meshing

Using Abaqus<sup>®</sup>, a 8-node linear brick C3D8T was used for this study. With L9 from Taguchi method, 9 simulations was done for 9 different geometries. Each combination of parameters gave a new length and weight of the 2x2 auxetic cells. As different parameter was used, the size of each structure changed and hence the number of element which was included between 20348 and 350929. The Figure 2 shows an example of the mesh for a 2x2 auxetic cells.

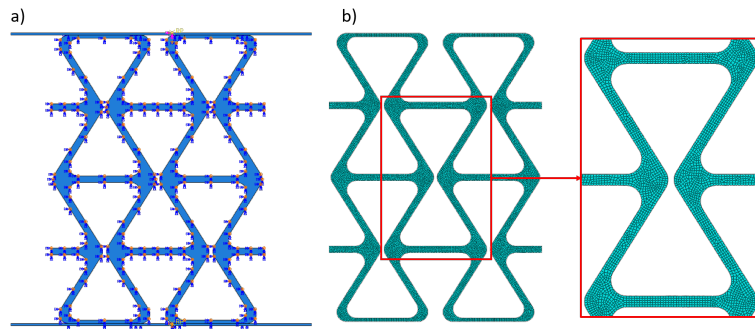


**Figure 2 :** Schematic of a) Boundary conditions and b) Mesh of 2x2 auxetic cells

For the finite element analysis, a dynamic compression was simulated with the auxetic structure in between two horizontal rigid plates. A symmetry was set on one face of the auxetic structure to avoid buckling and sliding of the structure. The bottom plate was encastred and a velocity of  $4 \text{ m.s}^{-1}$  was applied on the top, as shown the Figure 2.

A tangential and normal contact with a coefficient of friction  $\mu = 0.36$  were considered for dynamic as Novak et al (2018). A self-contact on all auxetic structure was also defined with the general contact from Abaqus<sup>®</sup>.

#### 3.3. Calculation method

The geometrical parameters of 2x2 auxetic re-entrant structure was optimized with respect to the Effective Elastic modulus, Poisson's Ratio and Specific Energy Absorption. The Effective Elastic Modulus was

calculated from the Apparent Elastic Modulus divided by the Young Modulus of the bulk material. The Apparent Elastic Modulus corresponds to the slope of the elastic part of the stress-strain curve. The Poisson's ratio was calculated at the final stage of the simulation for  $\epsilon = 0.3$  using the following equation 4 :

$$\nu = - \left( \frac{\epsilon_{Transverse}}{\epsilon_{Longitudinal}} \right) \quad (4)$$

As concerned the Specific Energy Absorption, it was the work done per unit mass in  $J.g^{-1}$ .

## 4. Results and discussion

### 4.1. Optimization of cells

From Taguchi's method, an average of the Signal-to-Noise ratio was made for each factor at each level. By subtracting the minimum from the maximum, the obtained value gives the rank of effect of the factor. The highest value of the average gave the optimize value for the studied parameter.

The value from Taguchi shown that the Effective Elastic modulus was more influenced by the cell wall angle, with much more difference between the lowest and the highest value. This difference means that the cell wall angle  $\theta$  was the most influant parameter for this mechanical properties. Moreover, the highest Signal-to-Noise ratio was reached for  $\theta = 84^\circ$ , which signifies that the best value of  $\theta$  for an optimize Effective Elastic Modulus was  $84^\circ$ . In same way, the radius in the corner was the most influant factor for the Poisson's ratio regarding the difference between the highest and the lowest value of the Signal-To-Noise ratio in function of each level. The highest value of Signal-to-Noise ratio was achieved for 0.1 mm as radius. Then, the Specific Energy Absorption was significantly impacted by the cell wall angle  $\theta$  too, with an optimize value about  $84^\circ$ . Finally, the best parameters to improve Effective Elastic Modulus, Poisson's ratio and Specific Energy Absorption seem to be  $\alpha = 1.5$ ;  $\theta = 84^\circ$ ; Radius = 0.1 mm. The most influant parameters were  $\theta$  for the Effective Elastic Modulus and for the Specific Energy Absorption, while the Radius was the one for the Poisson's ratio. The less important was the thickness of the struct.

In the global parametrical study, the optimised parameters were  $\theta = 85^\circ$ , radius R = 0.1 mm, the length ratio  $\alpha = 1.58$ , thickness = 0.3 mm. In excluding the thickness because his weak influence under this range, the same results was obtained for the both study, with a rank of each feature with Taguchi method.

### 4.2. Deformation mode

Under compression, the auxetic re-entrant structure had different deformation mode in function of parameters. The Fig. 4 shows an example of a stress strain curve of 2x2 auxetic cells. On this graph, four zones were represented. The zone one represents the elastic behaviour of the cells, with the apparent elastic modulus. Then, the shape of the curves shown a reducing force per area due to the buckling of the oblique struct. The engineering stress kept decreasing until the first lock point was reached as shown in Fig. 4, where zone 3 of the stress-strain curve started. This indicate a self contact of the cells during the compression. After this contact, the cells densifies itself and hence the increase in the stress with respect to strain both for zone 3 and 4 as shown in Fig 4. Yang et al (2012) found also the densification of a lattice structure after a collapse under quasi-static compression.

When the structs touch each other, the energy was transfered to other struct, so the force per area increased. This rise of force per area corresponds to the densification of the structure. The repetition of the lock point and so densification were dependant of the geometrical parameter. In function of the geometrical parameters, the lock point happens at different strains. To show this effect, three curves was plotted for different level value

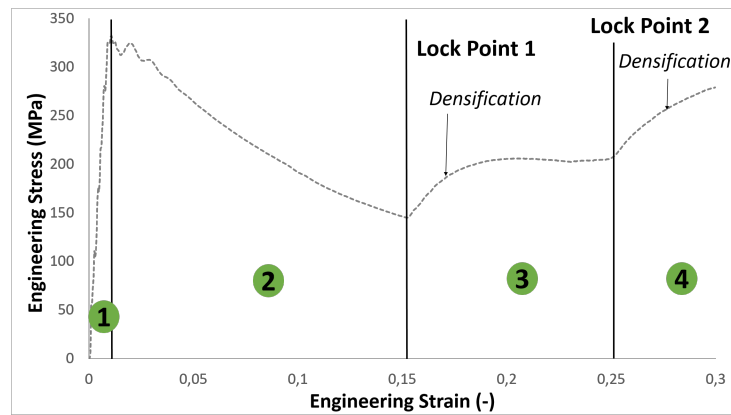


Figure 3 : Example of a stress strain curve of a dynamic compression of 2x2 auxetic re-entrant cells

of  $\theta$ , as this one was the most influant factor. The Figure 4 shown the apparition of the lock point which was delayed in function of the value of  $\theta$ . For a bigger  $\theta$ , the densification comes in earlier because the distance of edges in the middle of the cells. In comparison, a low value like  $55^\circ$  induced a self contact more quickly due to the close length at the centre of the re-entrant cells, as shown pictures on the right hand of the Figure 4. All the other parameters as the length ratio  $\alpha = \frac{h}{l}$ , the thickness, the radius and the relative density were the same for all three geometries displayed.

### 5. Conclusion

This work shown the optimization of the auxetic re-entrant honeycomb structure by the Taguchi method under dynamic compression. This study was conducted in Finite Element Analysis and gave optimum geometrical parameter for the cell wall angle  $\theta$  with  $84^\circ$ , the radius with a value of 0.1 mm and the length ratio  $\alpha$  equal to 1.5. The thickness was considered as the least influence parameters for the studied mecha-

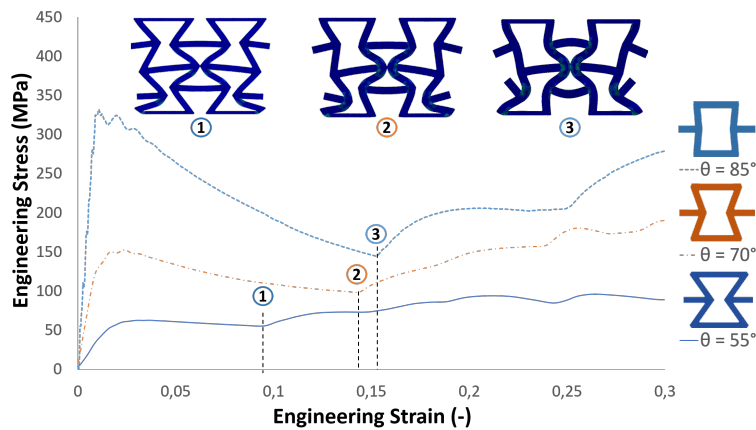


Figure 4 : Three example of stress strain curve for the most influant parameter  $\theta$  with value of  $85^\circ$ ,  $70^\circ$  and  $55^\circ$ . Pictures of lock point was displayed for each curve.

nical properties. Moreover, it was demonstrated the existence of a lock point, which was to the origin of the densification of the cells. This lock point and the densification was dependant of the geometrical parameters.

This deformation mode with the lock point was demonstrated by the geometrical parameter study, which shown the limitation of Taguchi Method. The effect of one important factor like  $\theta$  on this point couldn't find with the Taguchi Method only. To conclude this work, the Taguchi Method is the best way to optimize and obtain the rank of each parameter but remains inconsistent to study the deformation mode of an auxetic re-entrant honeycomb structure.

### Acknowledgments

The authors want to thank the University of Lorraine and the University of Derby for their support.

### Funding Statement

This research was supported by the LEM3 of the University of Lorraine at Metz for the funding of the thesis of Laura Delcuse with Alexis Rusinek and Slim Bahi as supervisors. Pr Paul Wood was supported by the IISE of the University of Derby.

### Références

- [1] Lorna J. Gibson, Michael F. Ashby. *Cellular Solids : Structure and Properties*. Cambridge University Press, Cambridge. 1997.
- [2] F. Scarpa, P. Pastorino, A. Garelli, S. Patsias, M. Ruzzene. Auxetic compliant flexible PU foams : Static and Dynamic properties. *Physica Status Solidi (B)* **242** , 2005, no. 3, p. 681-694. (<https://doi.org/10.1002/pspb.200460386>)
- [3] Bezazi, A., Scarpa, F., 2009. Tensile fatigue of conventional and negative Poisson's ratio open cell PU foams. *International Journal of Fatigue* **31** , 488-494. (<https://doi.org/10.1016/j.ijfatigue.2008.05.005>)
- [4] Novak, N., Vesenjak, M., Krstulović-Opara, L., Ren, Z., 2018. Mechanical characterisation of auxetic cellular structures built from inverted tetrapods. *Composite Structures* **196** , 96-107. (<https://doi.org/10.1016/j.compstruct.2018.05.024>)
- [5] Hu, L.L., Zhou, M.Zh., Deng, H., 2018. Dynamic crushing response of auxetic honeycombs under large deformation : Theoretical analysis and numerical simulation. *Thin-Walled Structures* **131** , 373-384. (<https://doi.org/10.1016/j.tws.2018.04.020>)
- [6] Yang, L., Harrysson, O., West, H., Cormier, D., 2012. Compressive properties of Ti-6Al-4V auxetic mesh structures made by electron beam melting. *Acta Materialia* **60** , 3370-3379. (<https://doi.org/10.1016/j.actamat.2012.03.015>)
- [7] Yuan, S., Shen, F., Bai, J., Chua, C.K., Wei, J., Zhou, K., 2017. 3D soft auxetic lattice structures fabricated by selective laser sintering : TPU powder evaluation and process optimization. *Materials & Design* **120** , 317-327. (<https://doi.org/10.1016/j.matdes.2017.01.098>)
- [8] Fu, Minghui, Fengming Liu, Lingling Hu, 2018. A Novel Category of 3D Chiral Material with Negative Poisson's Ratio. *Composites Science and Technology* **160** , 111-118. (<https://doi.org/10.1016/j.compscitech.2018.03.017>)
- [9] Kay, G., 2003. Failure model of Titanium 6Al-4V and aluminium 2024-T3 with the Johnson-Cook material model.
- [10] Tamizharasan, T., Senthilkumar, N., Selvakumar, V., Dinesh, S., 2019. Taguchi's methodology of optimizing turning parameters over chip thickness ratio in machining P/M AMMC. *SN Appl. Sci.* **1** , 160. (<https://doi.org/10.1007/s42452-019-0170-8>)

## On the energy absorption capability of lattice structures: a numerical study

Alexandre RIOT<sup>1,2\*</sup>, Marco MONTEMURRO<sup>1</sup>, Enrico PANETTIERI<sup>1</sup>,  
Sandra GUERARD<sup>1</sup>, Antonio COSCULLUELA<sup>2</sup>

1: Arts et Métiers ParisTech, I2M CNRS UMR 5295, F-33400 Talence, France

2: CEA-CESTA, 15 Avenue des Sablières, 33114 LE BARP, France

**Keywords:** Energy absorption, optimization, genetic algorithm, lattice structures, lightweight structures

---

**Abstract:** The introduction of additive manufacturing (AM) processes and innovative design methodologies into the manufacturing industry leads to the study and production of original designs. This study focuses on the development of a suitable modelling strategy for polymer lattice structures manufactured by AM technology to be used for design purposes. The objective is the improvement of the lattice energy absorption capability, by considering requirements of different nature (such as mass, stiffness and manufacturing limits). To this end, a suitable numerical mechanical model of the lattice, integrating the non-linear behaviour of the repetitive unit cell (but not taking into account thermal effects), specially conceived to obtain a good balance between accuracy and computational costs, has been developed for design purposes. The proposed strategy relies on a general homogenisation method (based on the strain energy of periodic media) and on a special genetic algorithm (GA) developed at I2M, able to deal with optimisation problems defined over a domain of variable dimension. The effectiveness of the approach is tested on a meaningful benchmark.

### 1. Introduction

Although lightweight solutions manufactured by AM are already available in high technology products (planes, rockets, high speed cars), the struggle to design and produce highly solicited structures by taking into account the AM process-related requirements, since the preliminary design phase, is a true challenge. Optimisation algorithms are often used to deal with the structure design in the framework of linear elasticity, by considering classical requirements such as compliance, mass, or buckling phenomena. However, the integration of highly non-linear phenomena within the optimisation process, e.g. induced by the material behaviour such as hyper-elasticity, or strain rates ranging from 1 to  $1.10^3 \text{ s}^{-1}$ , is anything but trivial. Accordingly, the development of pertinent numerical models able to integrate such non-linear phenomena and offering a good balance between accuracy and computational cost for design/optimisation purposes is of paramount importance. This is especially true when dealing with the design of lightweight structures, like lattices, that must withstand severe solicitations (e.g. in case of impacts) for which the non-linear behaviour of the system cannot be neglected.

High strain rates occur in many real-world engineering applications. For instance, in nuclear transportation, a common practice consists in using containers specifically designed to withstand impacts to transfer hazardous material from one location to another. In this context, the structure design is based on a compromise between lightness, stiffness, and energy absorption capability. To achieve this ambitious goal, the commonly-employed solutions, which make use of a foam core, can be replaced by an optimised lattice structure. In particular, the lattice can be conveniently optimised (at each pertinent scale) to maximise the absorbed energy by meeting, simultaneously, some requirements on mass, stiffness, transportability, as well as technological constraint related to AM technology specificities.

Another application focuses on military infantry equipment: in conflict zones, infantry equipped with personal communications relay is subjected to harsh and stressful environmental conditions. The

\*Author for correspondence (alexandre.riot@ensam.eu).

†Address: Arts et Métiers ParisTech, Esplanade des Arts Et Métiers, 33400 TALENCE, FRANCE

development of lightweight, stiff equipment is, thus, of crucial importance for both the soldier's comfort and the equipment's protection.

## 2. The multi-scale optimisation approach

Hence, the development of a dedicated problem formulation and a suitable modelling strategy for lattice structures integrating a number of manufacturing requirements is a crucial point. Different optimisation algorithms and problem formulations are available in the literature [1-4]. Some authors make use of deterministic algorithms [1-4], whilst in other cases meta-heuristics represent the best choice [5, 6]. As a matter of fact, the use of a specific optimisation algorithm is strictly related to the problem formulation and, therefore, to the nature of the objective function and the constraint functions and of the design variables.

The first challenge focuses on the problem formulation. In this specific context, impact dynamics and polymers are important sources of nonlinearities. Many problem formulations are available in the literature. When dealing with the optimum design of lattices, Pedersen [1] makes use of peak accelerations or compliance (i.e. the work of internal forces), depending on the problem at hand, as an objective function to be minimised by considering a constraint on the volume. Unfortunately, this approach does not take into account for the non-linear material behaviour. Caccese *et al.* [2] make use of the HIC (Head Injury Criteria) as an objective function (for a given impact energy), and look for the optimum value of the geometric parameters of a honeycomb material minimizing the HIC. However, they do not take into account for material nonlinearities. Deng *et al.* [3] use elements distortion energy as an objective function to be maximised by considering a hyper-elastic behaviour of the material, but implemented only a quasi-static hyper-elastic law, thus not suited to high strain rates. Jamil *et al.* [4] make use of elasto-visco-plastic laws in order to model rate-dependant material behaviour and experimental-numerical correlation to enhance the finite element (FE) model accuracy. However, the computational cost of the resulting FE model is not suited for optimisation purposes.

The second challenge is the identification of pertinent mechanical responses in order to give a measure of the absorbed energy. Such information must be retrieved by using a dedicated FE model of the lattice constituting a good compromise between computational effort, in order to be integrated into an optimisation process, and required accuracy, to capture fundamental non-linear phenomena.

The core of the proposed approach is to develop a suitable multi-scale FE model of the lattice, integrating the full set of design variables describing its geometry and mechanical behaviour, at each pertinent scale, by reducing the number of simplifying hypotheses at the basis of the physical model. This model will be then integrated in a multi-scale optimisation methodology developed at the I2M laboratory. In this sense, this study constitutes the generalisation of the multi-scale optimisation approach of cellular structures, initially presented in [5-8]. The effectiveness of the proposed modelling approach is tested on a lattice structure whose representative volume element (RVE) is an octahedron (c.f. Figure 1). The goal is to develop a general multi-scale FE modelling strategy allowing a fast calculation of the lattice energy absorption capability. This multi-scale FE model will be included, in a second time, into an optimisation procedure aiming at maximising the lattice absorption capability subject to constraints on its mass, stiffness and AM process-related requirements as well. The effect of different loading conditions (mono-axial and multi-axial) on the optimised solution is also considered in this numerical study.

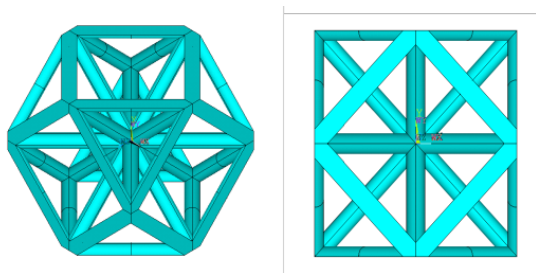


Figure 1 Iso view and side view of an octahedron cell

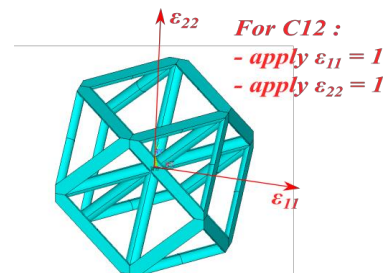


Figure 2 Example of multi-axial loads

- 3.
4. A general homogenization method based on strain energy

The development of a fully-parametrised FE model of the octahedron RVE is of paramount importance for the optimisation procedure. However, since a non-linear FE (quasi-static) analysis must be performed on the lattice RVE, the resulting FE model must constitute a compromise between computational efficiency and good accuracy. Since the FE model is invoked a huge number of times during the iterations of the optimisation process, it is necessary to reduce the computation time without degrading too much the accuracy of the model in terms of the measured responses. To fulfil this requirement, a possible strategy is to develop a hybrid model composed of both high-fidelity elements (HFEs), i.e. solid elements, and low-fidelity elements (LFEs), e.g. beam elements. Of course, the number of HFEs must be kept as low as possible and they should be used in those zones where the strain/stress field is characterised by strong gradient (e.g. at the intersection among the lattice struts). Conversely, LFEs should be used in those regions sufficiently far away from stress concentrations zones, where the displacement field can be accurately described by well-established kinematic models, e.g. the Timoshenko's model. In the following, two FE models are presented: (1) a high-fidelity FE model composed exclusively of solid elements and (2) a hybrid FE model composed of both solid and beam elements. Both models are built in the ANSYS® environment by means of the ANSYS Parametric Design Language (APDL). The RVE topology selected for all the numerical analyses is the octahedron configuration.

### 3.1. The high-fidelity finite element model of the lattice RVE

The high-fidelity model is composed of ANSYS SOLID187 elements, i.e. solid elements with 10 nodes and 3 degrees of freedom (DOFs) per node. As a first methodological approach, a bilinear material law has been duplicated over a mechanical response of elastomeric polyurethane (Carbon3D EPU40), and then used as the constitutive law of the model (c.f. **Table 1**), and thermal effects are not taken into account. In order to evaluate the dissipated energy, one must know the most important energy dissipation mechanisms for the considered material. In the case of bilinear laws, which could be representative of elastic-plastic materials, the plastic component is the only dissipation mechanism. Of course, this is a strong simplification whose aim is to investigate the effect of the material non-linearity on the optimised solutions. The goal of this FE model is twofold. Firstly, a sensitivity of the computational time to the average element size is carried out. Secondly, it is used to compare two homogenisation methods, in order to understand which one should be used during the optimisation process. The sensitivity of the homogenised elastic properties to the average element size are also investigated. The two homogenisation methods compared in this study are: (a) the numerical homogenisation procedure based on average strains and stresses presented in [9], and (b) the homogenisation technique based on the strain energy of periodic media developed at the I2M laboratory [5-8]. For both sensitivity analyses, the worst-case scenario, i.e. maximum value of the strut length  $L$  and minimum value of the radius of the strut cross-section  $R_a$ , has been selected as the reference case. The threshold values for the maximum allowable computational time of the single FE analysis, i.e.  $t_{\text{comp}}$ , and the maximum allowable error on the Cartesian components  $C_{ij}$  of the RVE stiffness tensor at the macroscopic scale, i.e.  $\delta_{\text{max}}$ , are listed in **Table 2**.

**Table 1 Material properties**

Material property	Value
$E_{\text{young}}$ (MPa)	158
$R_e$ (MPa)	11.58
$E_{\text{plas}}$ (MPa)	134.04

**Table 2 Sensitivity parameters**

Sensitivity parameters	Values
$t_{\text{comp}}$ [s]	< 55
$\delta_{\text{max}} = \max_{C_{ij}} \left( \left  \frac{C_{ij} - C_{ij}^{\text{ref}}}{C_{ij}^{\text{ref}}} \right  \right)$	< 0.005

**Table 3 Sensitivity of the computational time to the mesh size**

$k$	$t_{\text{comp}}$ [s]
0.3	351.6
0.4	176.1
0.5	86.3
0.6	<b>54.2</b>
0.7	<b>36.2</b>
0.8	<b>40.0</b>
0.9	<b>33.0</b>

For the first sensitivity analysis the average element size has been related to the strut cross-section radius as follows:

$$e_{mesh} = kR_a, \quad (1)$$

where  $k$  is a parameter varying in the range [0.3, 0.9]. The RVE is submitted to a uniaxial strain field along the  $x_1$  axis, i.e.  $\varepsilon_{11} = 0.1$  and periodic boundary conditions (PBCs), as usual in numerical homogenisation techniques, are applied on the RVE faces, edges and vertices [5-9]. The material behaviour is represented by a simple bi-linear law, representing a reasonable approximation of the true hyper-elastic material behaviour (this simplification is useful for design/optimisation purposes). The computational time vs. the mesh parameter  $k$  is reported in **Table 3**. As it can be easily inferred from these results, a value of  $k \geq 0.7$  satisfies the requirement on the maximum allowable computational time.

As stated above, the aim of the second analysis is to assess the accuracy of the homogenisation method based on the strain energy of periodic media presented in [5-8] by comparing the results with those provided by the homogenisation technique based on volume average stresses and strains [9]. The method proposed in [9] requires only six static analyses to determine the stiffness tensor of the homogenised material at the macroscopic scale, while the method proposed in [5-8] requires a number of static analyses equal to the number of independent components of the homogenised stiffness tensor (which are related to the symmetries of the lattice RVE). On the other hand, the homogenisation technique presented in [9] is based on a strong hypothesis, i.e. the lattice RVE and the corresponding volume of the homogenised material undergo the same average strain field, whilst the method presented in [5-8] is characterised by a less restrictive hypothesis, i.e. the RVE and the homogenised material has the same strain energy. For this second analysis, the bulk material of the RVE has a linear behaviour. For both homogenisation techniques a sensitivity analysis of the maximum error on the components of the homogenised stiffness tensor to the parameter  $k$  has been conducted. For each method the reference value of the homogenised stiffness tensor components has been evaluated for  $k = 0.3$ :

$$C_{ij}^{ref} = C_{ij}^{(k=0.3)}, \quad i, j = 1, \dots, 6. \quad (2)$$

The results of this sensitivity analysis are given in **Table 4**:  $\delta_{\max-B}$  and  $\delta_{\max-E}$  are the maximum relative errors evaluated by using the homogenisation method presented in [9], and in [5-8], respectively, whilst the maximum relative difference between the homogenised stiffness tensor components resulting from the two approaches is denoted as  $\delta_{\max-BE} = \max_{C_{ij}} \left| \frac{C_{ij}^B - C_{ij}^E}{C_{ij}^B} \right|$ .

The results clearly indicate that both approaches provided equivalent results and that the method proposed in [5-8] is less sensitive to the element size. According to the results summarised in **Table 4**, a value of  $k$  equal to 0.7 represents a good compromise between accuracy of results and computational costs.

**Table 4 Numerical results for the stiffness sensitivity analysis**

$k$	$\delta_{\max-B}$	$\delta_{\max-E}$	$\delta_{\max-BE}$
0.7	<b>0.44%</b>	<b>0.39%</b>	0.058%
0.8	0.62%	0.51%	0.1%
0.9	0.60%	0.53%	0.08%

**Table 5 Numerical results for full-beam and hybrid FE models of the RVE**

	<i>Beam</i>	<i>Hybrid</i>
$\delta_{\max}$	39%	18%
$t_{\text{comp}}$ [s]	7	76

### 3.2. The hybrid finite element model of the lattice RVE

In this section, two different simplified FE models are presented. The first one is made of ANSYS BEAM189 elements, i.e. beam elements with 3 nodes and 6 DOFs per node, where the cross-section kinematics is described through the classical Timoshenko's model. The second FE model is composed of a combination of SOLID187 and BEAM188 elements. Of course, solid elements are used to represent the intersection among struts, as shown in **Figure 3**.

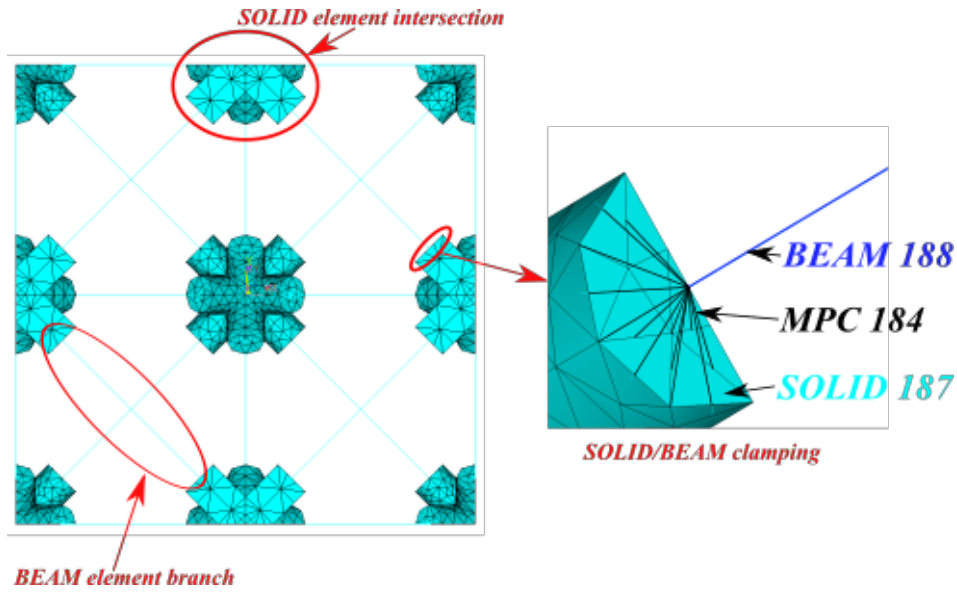


Figure 4 Detailed side view of the hybrid cell and 3D view of the BEAM/SOLID junction

The compatibility of the displacement fields between different elements in the hybrid model is ensured through multi-point constraint elements ANSYS MPC184. The average element size for the solid elements has been chosen by setting  $k = 0.72$ . The material behaviour is described by the bi-linear law used for the high-fidelity FE model described above. The reference value of the homogenised stiffness tensor components, for this case, are those resulting from the high-fidelity FE model for the same value of parameter  $k$ :

$$C_{ij}^{ref} = C(\text{HF} - \text{FEM})_{ij}^{(k=0.72)}, \quad i, j = 1, \dots, 6. \quad (3)$$

As far as the homogenisation method is concerned, the technique presented in [5-8] is used for this case. Of course, the PBCs provided in [5-8] have been reformulated for beam elements due to the additional DOFs (i.e. rotations). As shown in **Table 5**, the hybrid FE model is characterised by a better accuracy than the low-fidelity FE models composed solely of beams elements. Conversely, the latter provides a result in a very short time. Of course, the better accuracy of the hybrid FE model is due to the presence of solid elements able to properly capture the 3D stress field at the intersection between struts. However, despite an increased accuracy when compared to the low-fidelity counterpart, the Hybrid model does not fulfil the requirement of reduced computational costs, surely due to the introduction of MPCs. Inasmuch as both the low-fidelity and the hybrid FE models do not compete with the high-fidelity FE model in terms of accuracy, the later will be used for the optimisation procedure.

## 5. Numerical results

The goal of the parametric optimisation is to determine the optimum lattice configuration maximising the ratio between the dissipated energy  $E_{dis}$  and the total energy  $E_{tot}$  such as  $R_{E-dis} = \frac{E_{dis}}{E_{tot}}$  (which corresponds in this case to the ratio between plastic strain energy and total strain energy) subject to a requirement on the overall volume and to specific load and boundary conditions. The high-fidelity FE model (made of solid elements) has been integrated into the optimisation process, including non-linear behaviour and PBCs. This specific study aims at optimising the cell submitted to a quasi-static compression, thus a periodic uniaxial compressive strain field  $\varepsilon_{xx} = 0.1$  has been imposed to the RVE (as shown in **Figure 4**). The parametric optimisation has been carried out by means of the ERASMUS (Evolutionary Algorithm for optimiSation of ModUlar Systems), developed by Montemurro [12], on two different populations of individuals. For the problem at hand, ERASMUS acts on two design variables, i.e. the cell's length  $L$  and the strut's cross section radius  $R_a$ . The optimisation problem is formulated as a standard constrained non-linear programming problem (CNLPP) as:

$$(P): \begin{cases} \max_{\Omega} R_{E-dis} \\ \frac{V}{V_0} \leq 1 \end{cases} \text{ with } \begin{cases} L \in [3; 6] \\ R_a \in [0.6; 1] \end{cases} \quad (4)$$

Variables  $L$  and  $R_a$  are of discrete nature and have a discretisation step of 0.1 and 0.01, respectively. The upper bound on the lattice volume is  $V_0 = \frac{25}{100} \times V_{REV}$ , with  $V_{REV}$  being the representative elementary volume of the lattice. As shown in **Figure 5**, the two populations converge towards slightly different solutions which are really close in the design space, suggesting in this way that the CNLPP of Eq. (4) is probably convex. The stop criterion used for ERASMUS is based on a maximum number of generations which has been set equal to 200. The dissipated energy ratios of the optimal configurations are **2.0041%** and **2.0053%** for solutions 1 and 2, respectively.

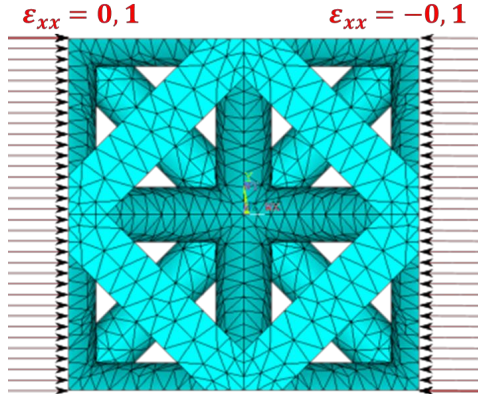


**Figure 4** Side view of the octet cell subject to periodic compressive strain field

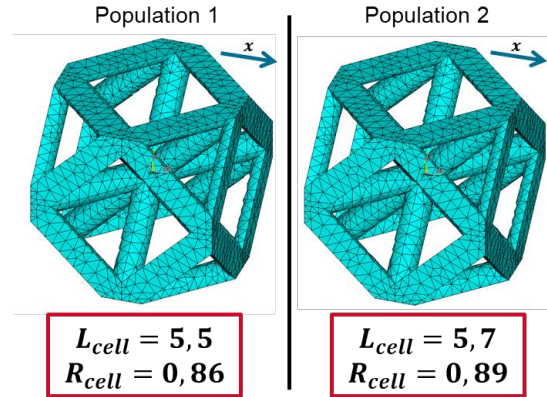


**Figure 5** Result of the optimisation performed with the ERASMUS algorithm

## 6. Conclusions and perspectives

In this study a hybrid FE model of the lattice RVE for design/optimisation purposes has been presented. The model is made of a combination of solid and beam elements and constitutes a good compromise between accuracy and computational costs. Solid elements are used to model the intersection among struts which are characterised by a strong gradient of the stress field, whereas beam elements are used to model the central zone of each strut which behaves in agreement with classical Timoshenko's beam theory. Moreover, an efficient homogenisation method based on the strain energy of periodic media has been validated by comparing the results with those provided by classical homogenisation techniques available in the literature. However, due to the presence of MPC elements the computational costs of the hybrid FE model is still higher than that of the high-fidelity FE model made of solid elements. This results suggests that the hybrid model can be improved by replacing 3D solid elements with higher-order beams elements able of catching the real 3D stress state at the intersection of the struts without increasing too much the overall computational effort. Research is ongoing on this topic.

As a consequence of these results, the high-fidelity FE model has been integrated in the optimisation procedure. The goal is the maximisation of the lattice energy absorption capability (via a quasi-static simplified functional to keep as low as possible the computational time) subject to a requirement on the mass. The optimal configurations found by means of the ERASMUS algorithm are characterised by a dissipated energy ratio of 2%. As far as prospects of this study are concerned, firstly the multi-scale optimisation will be applied to a lattice structure characterised of several arrays which is representative of real applications and the results compared to those that can be obtained with foams having equivalent relative density and material properties. Secondly, the optimisation process will be carried out on further lattice topologies (e.g. cubic, gyroid, etc.) taken from the literature by considering different loading conditions. Thirdly, the problem formulation will be generalised by looking for the optimised topology of the lattice subject to the same set of design requirements. In this case, the topology optimisation will be

carried out in the framework of the NURBS-based SIMP method [10, 11] developed at the I2M laboratory in Bordeaux. In fine, the quasi-static analysis carried out during the optimisation process will be replaced by an explicit dynamic analysis, enabling the introduction of large deflections into the model. This explicit model will make use of strain dependant material properties, typical behaviour for polymers, which will be characterized through the results of ongoing experimental campaigns.

**Funding Statement:** This work is co-funded by the CEA and the Agence Innovation Défense (AID), the R&D department of the French Direction Générale de l'Armement (DGA).

#### References:

- [1] C. B.W. PEDERSEN. 2004. Crashworthiness design of transient frame structures using topology optimization. *Comp. Methods Appl. Mech. Engrg.* **193**, 653-678.
- [2] V. CACCESE, J. R. FERGUSON, M. A. EDGECOMB. 2013. Optimal design of honeycomb material used to mitigate head impact. *Composites Structures* **100**, 404-412.
- [3] H. DENG, L. CHENG, A. C. TO. 2018. Distortion energy-based topology optimization design of hyperelastic materials. *Structural and Multidisciplinary Optimization* **59**, 1895-1913.
- [4] A. JAMIL, Z.W. GUAN, W.J. CANTWELL, X.F. ZHANG, G.S. LANGDON, Q.Y. Wang. 2019. Blast response of aluminium/thermoplastic sandwich panels – experimental work and numerical results. *International Journal of Impact Engineering* **127**, 31-40.
- [5] A. CATAPANO, M. MONTEMURRO. 2014. A multi-scale approach for the optimum design of sandwich plates with honeycomb core. Part I: homogenisation of core properties. *Composite Structures* **118**, 664-676.
- [6] A. CATAPANO, M. MONTEMURRO. 2014. A multi-scale approach for the optimum design of sandwich plates with honeycomb core. Part II: the optimisation strategy. *Composite Structures* **118**, 677-690.
- [7] M. MONTEMURRO, A. CATAPANO, D. DOROSZEWSKI. 2016. A multi-scale approach for the simultaneous shape and material optimisation of sandwich panels with cellular core. *Composites Part B: Engineering* **91**, 458-472.
- [8] G. BERTOLINO, M. MONTEMURRO, G. DE PASQUALE. 2019. Multi-scale shape optimisation of lattice structures: an evolutionary-based approach. *International Journal on Interactive Design and Manufacturing* **13** (4), 1565-1578.
- [9] E.J. BARBERO. 2013. *Finite Element Analysis of Composite Materials using Abaqus (TM)*. Taylor & Francis Inc., London.
- [10] G. COSTA, M. MONTEMURRO, J. PAILHÈS. 2018. A 2D topology optimisation algorithm in NURBS framework with geometric constraints. *International Journal of Mechanics and Materials in Design*, 14(4), 669-696.
- [11] G. COSTA, M. MONTEMURRO, J. PAILHÈS. 2019 (in press). Hypersurfaces for 3D Topology Optimisation Problems. *Mechanics of Advanced Materials and Structures*, URL: <https://doi.org/10.1080/15376494.2019.1582826>
- [12] Montemurro M. A contribution to the development of design strategies for the optimisation of lightweight structures. Bordeaux, France: Université de Bordeaux; 2018. (HDR thesis), <http://hdl.handle.net/10985/15155>.

# Modeling the dynamic strength of tantalum

Roman Kositski, Dan Mordehai

*Department of Mechanical Engineering, Technion – Israel Institute Of Technology, Haifa, Israel*

**Keywords:** Constitutive model, tantalum, dislocation, high strain rate, dynamic strength

---

**Abstract:** Plastic deformation of metals is the result of motion of crystal defects called dislocations. The well-known Orowan's equation connects dislocation density and dislocations mean glide velocity with the plastic strain rate in the deformed material. At sufficiently high deformation rates, the dislocations present in the crystal cannot glide fast enough to relax the shear stresses. The increasing stress causes a stress-driven dislocation nucleation, resulting in a rapid increase in the dislocation density. As a consequence, the high shear stresses can be relaxed by plastic deformation. We have developed a physically, dislocation-based dynamic strength model, using dislocation mobility curves from molecular dynamics simulations coupled with a dislocation nucleation model. Using the proposed model, we are able to study the effect of initial dislocation density on the dynamic strength of tantalum. In particular, we can investigate the effect of deformation rate, study the elastic precursor evolution, and examine the effects of pre-shock on the target as well as the effect of elevated temperature.

## 1. Introduction

Rapid plastic deformation characterizes a variety of dynamic processes in both civil and military applications. Experience shows that most metals react differently to a rapid dynamic load relative to a slow load rates [1]. For the most part, metals exhibit higher strength, with no significant change in the elastic properties, and sometimes without a decrease in ductility. In order to understand, describe and even control the properties of a material under dynamic loading conditions, we require models that describe the strength of metal at the relevant strain rates. The desire and need to model the dynamic strength of metals, of course, is not new. Over the past 50 years, a large number of constitutive laws have been developed, with most of the models that have been implemented in the popular simulation codes are phenomenological. Examples of such models are Johnson-Cook, Steinberg-Guinan, Zerilli-Armstrong, etc. In all of these models, the yield stress (or flow stress) is a function of state variables such as strain, strain rate, pressure, and temperature and material parameters calibrated using experiments. In this study we focus on modeling plate impact experiments performed by Zaretsky and Kanel [2]. In these experiments a target plate is impacted by a flyer at an impact velocity of few hundred meters per second and the free surface velocity on the back surface of the target is measured. Modeling these experiments with the Johnson-Cook [3] or the Zerilli-Armstrong [4] strength models give adequate results only for the thicker targets (i.e thicker than 1 mm) as depicted in Figure 1. In addition, because of the phenomenological nature of these models, they contribute only minimally to the description and understanding of the micromechanical mechanisms governing the plastic deformation of the metal. In this work we present a physically based viscoplastic model that takes into account the rapid nucleation of dislocations at the front of the shock wave.

## 2. Dislocation nucleation-based plasticity model

The dislocation nucleation-based model was recently presented [5] and we will only describe its main feature here. Orowan's equation connects between the plastic strain rate ( $\dot{\epsilon}^p$ ), mobile dislocation density  $\rho_m$ , the mean velocity of dislocations  $v$  and the Burgers vector  $b$ .

\*Author for correspondence (kositski@gmail.com).

†Present address: Department of Mechanical Engineering, Technion – Israel Institute of Technology, Haifa, Israel

$$\dot{\varepsilon}^p = b\rho_m v. \quad (1)$$

The mobility of screw dislocations in Ta was calculated by Barton et al. [6] from molecular dynamics simulations. The effect of temperature on the dislocation mobility can be seen in Figure 2. It is evident that the temperature has a “softening” effect at low stresses at the thermal regime but no effect at the higher stresses and velocities at the athermal regime. This temperature dependence will play a role in explaining results of experiments at elevated temperatures.

Knowing the mobility of dislocations  $v = f(\tau, T)$ , i.e. how stress ( $\tau$ ) and temperature ( $T$ ) affects dislocation velocity, one can in essence, construct a viscoplastic constitutive model [6,7]. But if the stress is sufficiently high the density of mobile dislocations can increase rapidly by a thermally activated process:

$$\dot{\rho}_m = \begin{cases} Ae^{-\beta(E_0 - V_0\tau)}, & \tau < \tau_{sn} \\ A, & \tau \geq \tau_{sn} \end{cases} \quad (2)$$

where  $\beta = 1/K_B T$  has its usual meaning. Here we are postulating a free-energy barrier for dislocation nucleation, which is decreasing linearly with the stress  $E_0 - V_0\tau$ , where  $E_0$  is the stress-free activation, and  $V_0$  is an effective activation volume and  $\tau$  is the resolved shear stress.  $A$  is a rate prefactor and  $\tau_{sn}$  is the stress threshold for spontaneous dislocation nucleation. If the stress exceeds the limit of spontaneous nucleation ( $\tau \geq \tau_{sn} = E_0/V_0$ ), the nucleation rate becomes athermal  $\dot{\rho}_m = A$ .

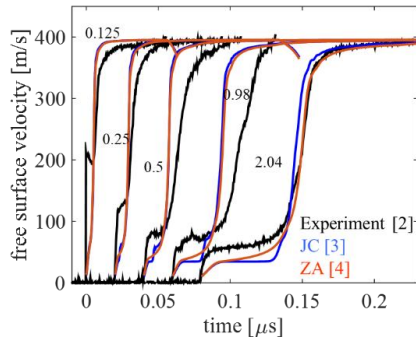


**Figure 1: Free surface velocities from plate impact experiments by Zaretsky and Kanel [2] and simulations with Johnson-Cook and Zerilli-Armstrong models. The numbers next to the graphs are the target thickness.**

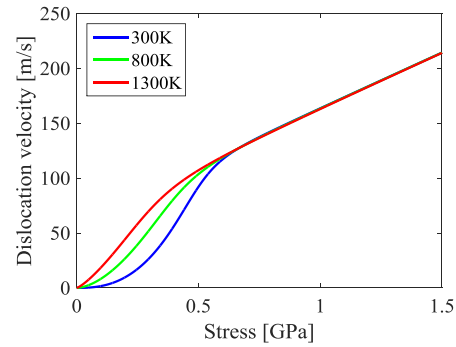


**Figure 2: Screw dislocation velocity as a function of shear stress at room and elevated temperatures. Following Barton et al. [6]**

### 3. Simulation setup

The dislocation nucleation-based model was implemented as a constitutive law into the LsDyna hydrodynamic solver and the simulations were performed with the Gruneisen equation of state (EOS). Full details can be found in [5]. Implementing the strength model in LsDyna enabled us to take advantage of the efficient parallelization of the code as well as prepare the foundation for mode complex 2D and 3D problems in the future.

For the test cases presented here we performed effectively 1D simulations by constructing the target plate as a set of solid elements with element size of 0.01 mm along the shock direction and restraining the motion of all nodes to be only in the shock direction. This results in a pure uniaxial deformation. The nodes on the impact face were prescribed a constant velocity to match the material velocity of the Ta in the experiments and the free surface velocity was monitored during the simulation.

### 4. Results and Discussion

We start our discussion presenting the results of a plate impact simulation of a 1.0 mm Ta target shocked to particle velocity of about 200 m/s and pressure of 12 GPa. We use this type of experiment [2] to calibrate the

parameters of the nucleation model. Figure 3 shows the evolution of the compressive stress wave as it propagates into the target. We model a target, one with low ( $10^7 \text{ cm}^{-2}$ ) and high ( $10^9 \text{ cm}^{-2}$ ) dislocation density. One can clearly see that the rate of the elastic precursor wave decay is more pronounced in the annealed (low density) target and the final precursor stress level, known as HEL (Hugoniot Elastic Limit) stress, ( $\sigma_{HEL}$ ) is lower for the cold-rolled (high dislocation density) target. This was also observed in the experiments [2,8] where the annealed target is stronger than the cold-rolled or “as received” material. This phenomenon can be explained if we recall that to relax the shear stress, plastic deformation must occur. But if there is low number of mobile dislocations, the shear stress will increase, effectively resulting in a higher flow stress at high strain rates.

At low strain rates annealed tantalum is significantly softer (i.e lower yield strength) than work hardened tantalum [9]. Work hardening increases the dislocation density thus increasing the resistance to glide of the present dislocation as described by Taylor hardening law. But at strain rates of the order of  $10^5 \text{ s}^{-1}$  or higher, as in plate impact experiments, it is the phonon drag that is limiting the dislocation motion so the more mobile dislocations are present in the crystal, the lower glide velocities are needed and the “work hardened” material is in fact softer [10].

Another interesting observation was made by Razorenov et al [11] who shock loaded Ta with coarse-grained (CG), and ultrafine-grained (UFG) structure as well as reshock experiments of those targets. They observed that The CG specimens were stronger compared to the UFG and also exhibited a more pronounced elastic precursor decay between 0.5 mm to 2 mm targets. For the case of reshocked targets, both materials exhibited practically the same strength and showed less significant decay of the precursor.

Using our model, we can reproduce the experimental results and claim that the difference between the CG and UFG materials is in the number of nucleation sites and thus a difference in the rate of dislocation nucleation [5]. In the case of the reshocked targets, the nucleation plays a minor role as both targets have high dislocation density which is sufficient to accommodate the plastic strain and relax the stresses. The HEL stresses from our simulations and experiments [7] are plotted in Figure 4. Based on the calibrated parameters of the nucleation model we can claim that the nucleation sites are on the grain boundaries rather than a truly homogenous nucleation inside the grains. This results in an “inverse” Hall-Patch effect where the material with smaller grains has lower dynamic yield stress because the material response is governed by the nucleation of new dislocations rather than their glide.

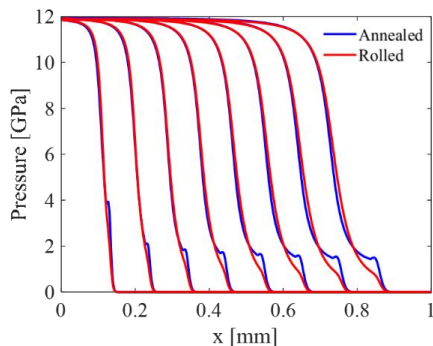


Figure 3: Evolution of the stress wave as it propagates into a target.

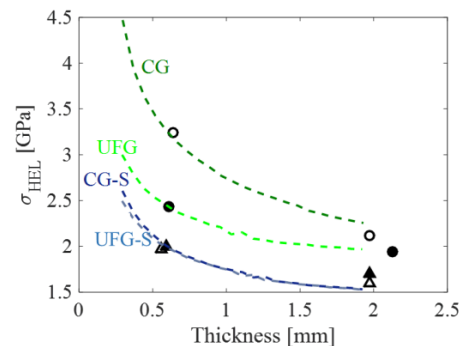


Figure 4: HEL Stress in coarse-grained (CG), ultrafine-grained (UFG) targets and after reshocking (CGS and UFGS, respectively). Dashed lines are from simulation results and the markers are experiments [11].

Finally, we wish to discuss the effect of elevated temperature on the dynamic strength of Ta as it manifests itself in plate impact experiments. At strain rates on the order of  $1000 \text{ s}^{-1}$  the strength of Ta is quite significantly affected by temperature even with its high melting temperature [12,13]. In Split Pressure Hopkinson Bar (SPHB) experiments increasing the temperature to  $800^\circ\text{C}$  resulted in a 50% decrease in yield stress at any given plastic strain. On the other hand, in plate impact experiments increasing the temperature as high as  $1300^\circ\text{C}$  resulted in only small effect on the HEL stress at thin target plates (less than 1 mm). At thicker

targets (i.e 2 mm) the significant drop in yield strength was evident. This effect can be explained if we examine the mobility curve of dislocations in Ta as shown in Figure 2. At a sufficiently high strain rate the motion of dislocations is temperature independent while at the lower velocity range the effect of temperature is pronounced. We should remember that Ta is a BCC metal thus having a high Peierls Barrier stress (unlike FCC metals). This results in relatively high stresses even for low glide velocities making the transition from thermal to athermal glide be evident at strain rates accessible by plate impact experiments rather than SPHB.

## 5. Conclusions and Outlook

The dynamic strength of a material can exhibit non intuitive behaviors if one's intuition is based on low rate experiments. For example, at high strain rates work hardened Ta actually becomes softer compared to an annealed sample. The effect of temperature, which at low rates commonly lowers the yield stress of a metal can have non monotonic effect on the strength [ref-roman] or even increase the strength as in Cu at very high strain rates [14]. Using physically based novel constitutive laws can help model problems over a large range of material and loading states, and help gain better understanding of the complex interplay between the microstructure and loading conditions that both govern the plastic deformation of a metal.

The presented model is only limiter to relatively small plastic strains as it does not account for strain hardening due to an increase in dislocation densities or the evolution of grains during deformation. Future work will incorporate these phenomena. We plan to expand the model to FCC metals (e.g. Cu) which have significantly different dislocation mobility enabling us to further study the interesting field of plasticity at extreme conditions.

## References

- [1] M. A. Meyers. 1994. Dynamic Behavior of Materials. *Dynamic Behavior of Materials* (John Wiley & Sons, Inc., Hoboken, NJ, USA, 1994).
- [2] E. B. Zaretsky and G. I. Kanel. 2014. Tantalum and vanadium response to shock-wave loading at normal and elevated temperatures. Non-monotonous decay of the elastic wave in vanadium. *J. Appl. Phys.* **115**, 243502.
- [3] A. Dorogoy and D. Rittel. 2017. Dynamic large strain characterization of tantalum using shear-compression and shear-tension testing. *Mech. Mater.* **112**, 143–153.
- [4] R. W. Armstrong and F. J. Zerilli. 2010. High rate straining of tantalum and copper. *J. Phys. D: Appl. Phys.* **43**, 492002.
- [5] R. Kositski and D. Mordehai. 2019. On the origin of the stress spike decay in the elastic precursor in shocked metals. *J. Appl. Phys.*
- [6] N. R. Barton, J. V. Bernier, R. Becker, A. Arsenlis, R. Cavallo, J. Marian, M. Rhee, H. S. Park, B. A. Remington, and R. T. Olson. 2011. A multiscale strength model for extreme loading conditions. in *J. Appl. Phys.* (2011).
- [7] H. Lim, C. C. Battaile, J. L. Brown, and C. R. Weinberger. 2016. Physically-based strength model of tantalum incorporating effects of temperature, strain rate and pressure. *Model. Simul. Mater. Sci. Eng.* **24**, 055018.
- [8] J. C. F. Millett, D. L. Higgins, G. Whiteman, B. Pang, Y.-L. Chiu, and I. P. Jones. 2018. Contrasting the effects of cold rolling on the shock response of typical face centred cubic and body centred cubic metals. in *AIP Conf. Proc.* (AIP Publishing LLC, 2018), p. 060004.
- [9] J. House, P. Flater, R. Harris, R. De Angelis, M. Nixon, J. Bingert, and J. O'Brien. 2011. Annealing and mechanical properties of ECAP tantalum. *Annealing and Mechanical Properties of ECAP Tantalum* (2011).
- [10] J. C. F. Millett, G. Whiteman, N. T. Park, S. Case, and N. K. Bourne. 2013. The role of cold work on the shock response of tantalum. *J. Appl. Phys.* **113**.
- [11] S. V. Razorenov, G. I. Kanel, G. V. Garkushin, and O. N. Ignatova. 2012. Resistance to dynamic deformation and fracture of tantalum with different grain and defect structures. *Phys. Solid State* **54**, 790–797.
- [12] G. P. Škoro, J. R. J. Bennett, T. R. Edgecock, and C. N. Booth. 2012. Yield strength of molybdenum, tantalum and tungsten at high strain rates and very high temperatures. *J. Nucl. Mater.* **426**, 45–51.
- [13] S. Nemat-Nasser, J. B. Isaacs, and M. Liu. 1998. Microstructure of high-strain, high-strain-rate deformed tantalum. *Acta Mater.* **46**, 1307–1325.
- [14] E. B. Zaretsky and G. I. Kanel. 2013. Response of copper to shock-wave loading at temperatures up to the melting point. *J. Appl. Phys.* **114**, 083511.

# Mesoscopic Modelling of a Polymeric Foam under Dynamic Loading

P. Pradel<sup>1,\*</sup>, F. Malaise<sup>1</sup>, J.-H. Quessada<sup>1</sup>, C. Delhomme<sup>2</sup>

<sup>1</sup>CEA CESTA, 15 avenue des Sablières CS60001, 33116 Le Barp Cedex, France

<sup>2</sup>CEA LR, BP 16, 37260 Monts, France

**Keywords:** Polymeric foam, plate impact experiment, mesoscopic modelling

---

**Abstract:** Cellular materials are widely used in many industrial fields as shock wave mitigators. Polymeric foams would be valuable candidates to protect structures against intense mechanical stress wave loadings generated by laser irradiation or high velocity impact of very small debris. The search for the optimal size and shape of the porosities are essential data to improve the mitigation ability of foams. Thus, this article presents numerical results obtained to simulate a plate impact experiment on a polyurethane foam, using a mesoscopic model. Three different mesoscopic models were used: Thouvenin model, and mesostructures with square and circular pores. Comparisons between experiment and calculation were made on velocity profiles obtained by PDV at the rear surface of the foam samples. Numerical results show a clear dependence of the modelling of foam on wave propagation velocities. Square pores seem to give better restitutions than circular pores, but these latter have a better physical meaning regarding real voids shape inside the foam.

## 1. Introduction

Polymeric foams are commonly used in aerospace, automotive and military industries for the protection against crashes or high velocity impacts. At CEA CESTA, these loadings are representative of the ones that will be carried out with the Laser MégaJoule (LMJ). Effective protective systems, such as polymeric foams, against laser irradiation or very high velocity impacts of small debris must be developed to protect diagnostics or target holders.

The foam of interest is a rigid closed cell polyurethane foam ( $320 \text{ kg/m}^3$ ), which was characterized extensively under dynamic loadings. In this study, we focus on a plate impact experiment; previous works permitted to identify a macroscopic model, which enables to fairly reproduce experimental results [1,2]. But this model is unable to predict either the influence of porosities size and shape, or matrix nature on the foam mitigation ability.

In order to take these phenomena into account, a numerical mesoscopic approach was developed by using three different mesoscopic models: Thouvenin model, and mesostructures with square and circular pores. The objective of this paper is to present comparisons between experiment and calculation, and to analyze the influence of modelling shape of porosities on the foam dynamic response.

## 2. Experimental results

Plate impact experiments have been performed on a gas gun launcher based at CEA CESTA to apply high loading rates on foam samples. The experimental configuration is represented in Fig. 1.a. The projectile is made of a polyethylene sabot, a low density foam and a 90 mm-diameter, 12 mm-thick PMMA impactor. A 1 mm-thick PMMA driver is put in front of foam samples. It permits the calculation of impact velocity and tilt at impact by free surface velocity measurements (Fig 1.b). A 30 mm-diameter, 2 mm-thick foam sample is inserted between the driver and a 15 mm-thick PMMA window. The diameter of the bore is large enough to test three samples on the same shot. As usual in this kind of experiments, the dynamic response of the foam

\* Author for correspondence (pierre.pradel@cea.fr).

was investigated by measuring velocity profiles at foam/window interface using PDV. In this study, we focus on a single shot at an impact velocity of  $V_{imp} = 282$  m/s.

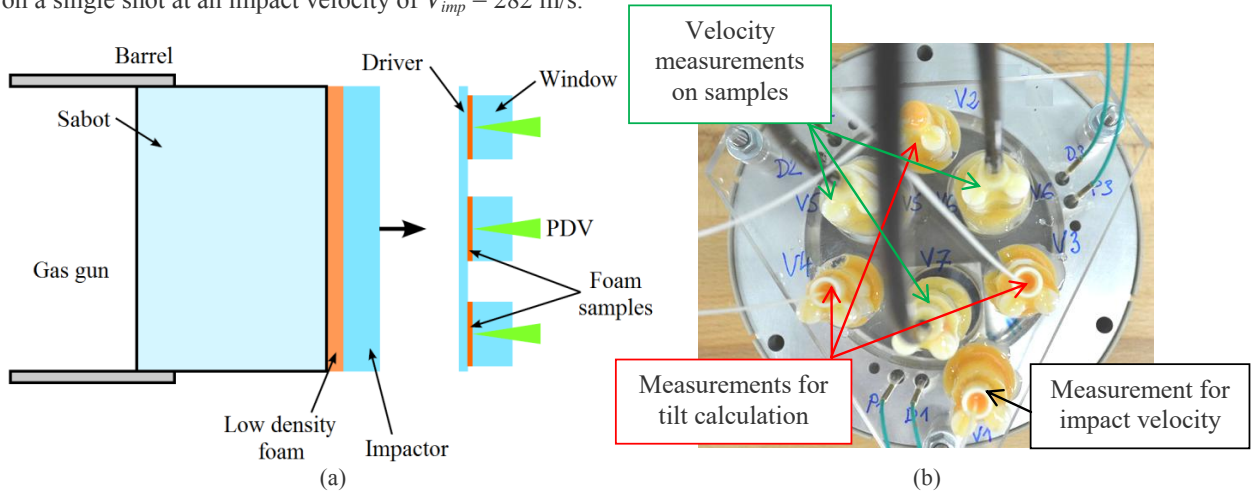


Figure 1: (a) Scheme of plate impact experiment. (b) View of the rear surface.

The experimental velocity profile measured at foam/window interface is shown in Fig. 2. After the PMMA projectile has impacted the PMMA driver, a shock wave propagates into the latter. This wave splits in two into the foam: an elastic wave, called elastic precursor, and a compaction wave. As the propagation velocity of the elastic precursor is higher than the compaction wave one, it is recorded first on the velocity profile. The compaction wave arrives later and, as the impedance of PMMA is higher than the foam one, even compacted, it is reflected in another shock wave into the foam. Thus, the foam compacts progressively due to the propagation of re-shock waves generated at foam/PMMA interfaces. The final velocity level corresponds to the one that could be recorded after the impact of a PMMA projectile on a PMMA target, i.e. approximately  $V_{imp} / 2 = 141$  m/s.

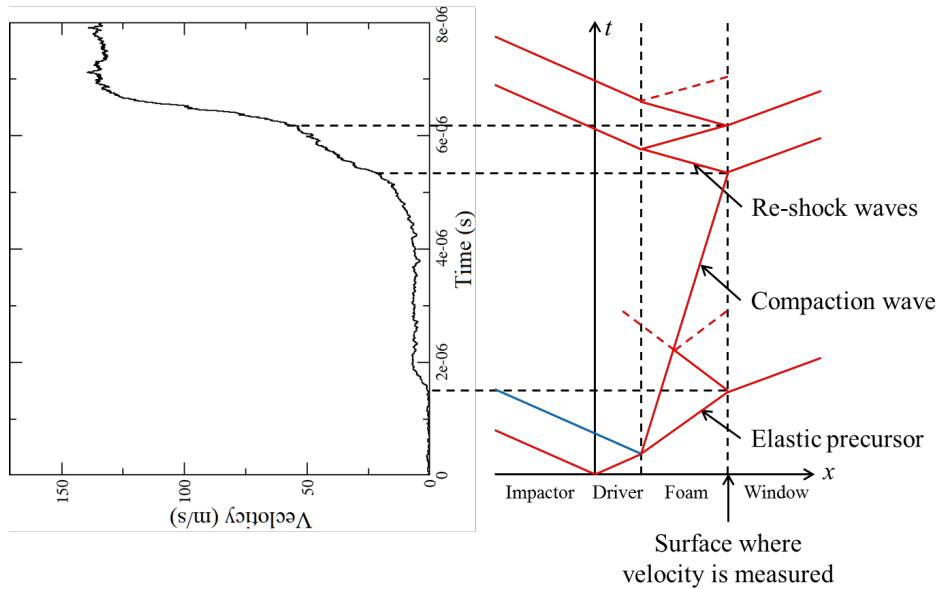


Figure 2: Experimental velocity profile measured at foam/window interface and time-distance diagram.

### 3. Numerical results

2D planar simulations were performed using the hydrocode Hésione from CEA. The foam was modelled at the mesoscopic scale, i.e. at a representative scale of foam porosities ( $\sim 100 \mu\text{m}$ -diameter). Three mesostructures were selected to represent the foam: Thouvenin model [3], and mesostructures with square and circular pores.

The first one considers the material as a succession of layers of dense material separated by  $100 \mu\text{m}$  voids. Layers thicknesses were determined accordingly to initial foam porosity (Fig. 3.a). The second mesostructure describes the foam as a stack of square pores. It is similar to Thouvenin model but interconnecting struts are added to successive layers of dense material (Fig. 3.b). The last mesostructure considers the material as a stack of circular pores, which better represent the real mesostructure (Fig. 3.c).

For these three mesostructures, we modelled dense polyurethane by a Mie-Grüneisen equation of state (EOS) combined with an elastic perfectly plastic (EPP) constitutive law. Model parameters refer to data from literature [4]. They are given in Tab. 1. No damage model was used.

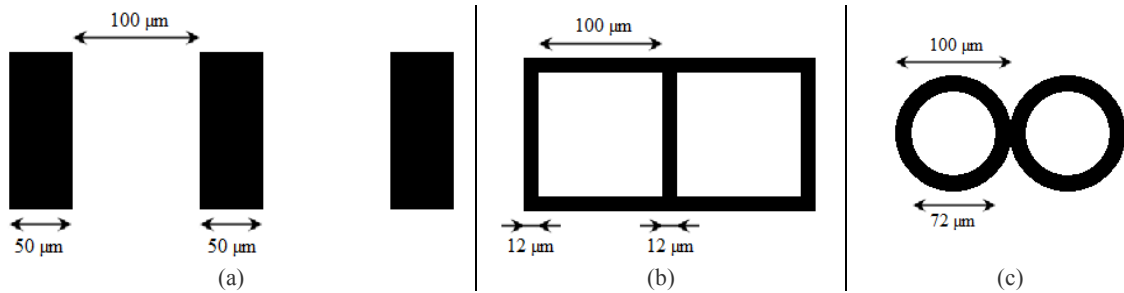


Figure 3: Mesostructures used to model the foam. (a) Thouvenin. (b) Square pores. (c) Circular pores.

Table 1: Model parameters of dense polyurethane.

<b>Mie-Grüneisen EOS</b>	
Initial density $\rho_0$ ( $\text{kg/m}^3$ )	1264
Sound speed $C_0$ (m/s)	2073
Hugoniot slope coefficient $S_1$	2.3896
Hugoniot slope coefficient $S_2$	-0.0532
Hugoniot slope coefficient $S_3$	0.132
Coefficient of the volume dependence of Grüneisen coefficient $b$	0
Initial Grüneisen coefficient $\Gamma_0$	1
<b>EPP constitutive law</b>	
Initial shear modulus $G_0$ (MPa)	2055
Initial yield stress $Y_0$ (MPa)	83

The plate impact experiment was first simulated using Thouvenin model for the foam. Displacements and deformations of layers during the propagation of waves are shown in Fig. 4, and the velocity profile measured at foam/window interface is shown in Fig. 7. In this figure, one can see that the arrival time of the compaction wave and the last velocity level are well reproduced using this mesostructure. This means that the model chosen to simulate dense material and the parameters associated, which refer to literature, are quite consistent. On the contrary, the elastic precursor is not simulated. Indeed, waves can propagate up to the rear surface of the foam only once all layers have come into contact. However, the velocity level and time arrival of the elastic precursor are important data, since this wave is the first to propagate into the material to be protected. One way to overcome this problem is to add connections between each layer, so that waves can propagate into the material before each porosity is closed.

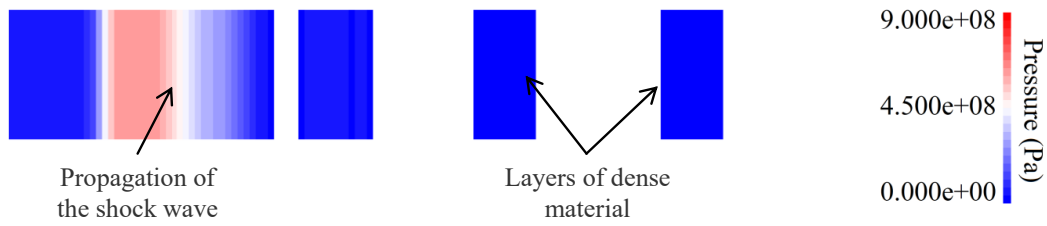


Figure 4: Deformation of layers during the propagation of waves, using Thouvenin model.

Thus, a mesostructure based on square pores was then used to model the foam. The progressive compaction of porosities during the propagation of the waves is shown in Fig. 5. Arrival times and velocity levels of the elastic precursor, compaction and re-shock waves are fairly reproduced. Waves propagating on edges parallel to the direction of propagation are responsible of the presence of the elastic precursor. Since these waves are subjected to multi-reflections on free internal surfaces of porosities, their stress level and then velocity level are reduced. This is a reason why the velocity level of the elastic precursor is lower than the compaction wave one. The shock wave that arrives later and which is responsible of the irreversible closure of the pores constitutes the compaction wave. Again, the model for dense polyurethane is quite satisfactory. One can see the influence of porosities shape on the foam behaviour: just adding interconnections between layers of dense polyurethane can generate waves propagating at different velocities.

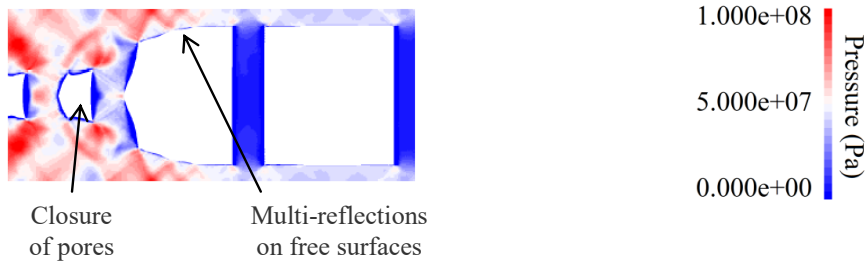


Figure 5: Compaction of porosities during the propagation of waves, using square pores mesostructure.

A mesomodel based on circular pores was also tested, since it better represents the foam mesostructure. Using this model, the compaction wave and re-shock waves are still reproduced. The elastic precursor is also represented, but its velocity level and arrival time are incorrect. As the path travelled by elastic waves is longer, they take longer to propagate. For the same reason, waves are also more subjected to reflections on free surfaces, which contributes to the attenuation of the stress level, causing a diminution of the velocity level too. One can see again the influence of porosities shape on the foam mechanical behaviour.

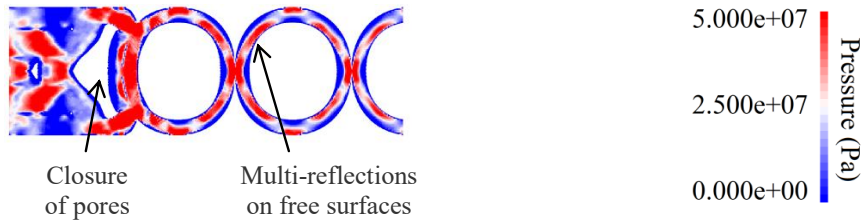


Figure 6: Compaction of porosities during the propagation of waves, using circular pores mesostructure.

Nevertheless, this last mesostructure is closer to the real structure of the foam. As model parameters for dense material refer to literature, further improvements can be expected to modify these parameters, on which the dense material model is based on, in order to better reproduce the experiment. Moreover, the choice of using a Mie-Grüneisen EOS coupled to an EPP constitutive law may not be adapted for the dense material, and other models, such as viscoelastic models, can be tested.

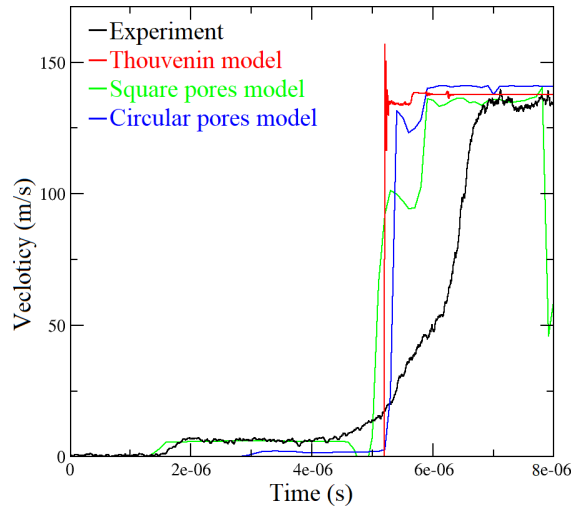


Figure 7: Comparison between experimental and calculated velocity profiles at foam/window interface.

#### 4. Conclusion

Different mesoscopic models were developed to simulate the dynamic behaviour of a polyurethane foam subjected to a plate impact. The influence of porosities shape has clearly been shown: interconnections between porosities are the cause of the propagation of waves, which can be recorded at the rear surface, and considering square or circular pores can modify the foam mechanical behaviour and velocity profiles. Comparing experimental and calculated velocity profiles, square and circular pores mesostructures give interesting results. An optimization of parameters for dense polyurethane will have to be performed to better match the experiment. Further works will consist in conducting experiments on other facilities (laser, electron beam generator...), then confront our modelling with experimental data before optimizing the properties of the mesostructure to improve the mitigation ability of the foam.

#### References:

1. P. Pradel, F. Malaise, T. de Rességuier, et al. 2018. Stress Wave Propagation and Mitigation in Two Polymeric Foams. *AIP Conference Proceedings*. **1979**, 110015 (<https://doi.org/10.1063/1.5044934>).
2. P. Pradel, F. Malaise, T. de Rességuier, et al. 2018. Dynamic Compaction of Polyurethane Foam: Experiments and Modelling. *Eur. Phys. J. Spec. Top.* **227**, 3-16 (<https://doi.org/10.1140/epjst/e2018-00116-7>).
3. J. Thouvenin. 1966. Action d'une onde de choc sur un solide poreux. *J. Phys.* **27**, 183-189 (<https://doi.org/10.1051/jphys:01966002703-4018300>).
4. S.P. Marsh. 1980. LASL Shock Hugoniot Data. *University of California Press*.

# High-speed imaging for ballistic impact damage assessment of composites

Karthik Ram Ramakrishnan<sup>1\*</sup>, Yanhong Chen<sup>1</sup>, Matilde Fiori<sup>1</sup>, Nik Petrinic<sup>1</sup>

<sup>1</sup>*Department of Engineering Science, University of Oxford, Oxford OX1 3PJ, UK*

**Keywords:** CFRP composites, gas gun, high-speed camera, DIC

---

**Abstract:** Impact damage in fibre reinforced composites such as from bird strike is a critical issue. Experimental impact testing using gas gun device has been typically used for assessment of the ballistic limit and energy absorbed in the plate. Recent developments in high speed camera technology have allowed to capture out-of-plane displacements and strains using stereo-Digital image correlation (DIC). An experimental methodology using single stage gas gun to study the oblique impacts of fibre reinforced composites is described in this paper. Two synchronised high speed cameras at frame rate of 40000 fps were used to capture the impact phenomenon on the rear surface of the composite while a third high speed camera was used to measure the initial and rebound velocities. Aramis software was used to conduct DIC analysis and the out-of-plane displacement and strain histories were calculated. These quantitative measurements are not only useful to understand the dynamic behaviour of the composite but also to validate numerical models of the ballistic impact of composites developed using Finite Element Method.

## 1. Introduction

Fibre reinforced polymer (FRP) composite materials have been used in aerospace applications such as engine blades, brackets, interiors, nacelles, propellers/rotors, single aisle wings, etc. It is well recognized that composites are sensitive to impact damage caused by bird strikes, debris or ballistic events during their service life. Impact induced damage can severely reduce the structural integrity of the material and it is therefore important to understand the material response to ballistic velocity impact loading. The behaviour of composite structures including the effects of damage is very complex and is dependent on a range of parameters including the geometry, material, lay-up, loading conditions, load history and failure modes. Several researchers have studied the energy absorption and evolution of damage of composites through experimental impact testing (1–3). Typically, the ballistic experiments are conducted using a gas gun and are evaluated based on the initial and residual velocities of the projectile, and the energy absorbed in the target to determine the ballistic limit or failure threshold (2). High speed cameras, if they were used in ballistic testing were only used to measure the initial and residual velocities of the projectile but not for damage assessment (4). Additionally, the size of damage is also evaluated, for instance with Ultrasonic C-scan imaging of the plate after the impact (3). However, post-mortem damage assessment does not provide information about the deformation and damage modes in the composite in real time. Full field measurement using Digital Image Correlation (DIC) has emerged from quasistatic applications to more dynamic cases with the advent of High-speed and Ultra-high-speed cameras (5). The DIC technique is a full-field, non-contact method for measuring the displacement and strain of a deformed surface. High speed DIC has been used for many experiments including for fracture, and impact testing. Recently high speed imaging and DIC have been applied in the measurement of displacement and strain histories of a composite during impact loading (7). Tiwari et al. (6) used a 2D-DIC method to make full field measurements during high speed impact conducted using the split Hopkinson Pressure Bar (SHPB) setup. The use of two high-speed cameras

\*Author for correspondence (karthik.ramakrishnan@eng.ox.ac.uk).

relatively new topic and there are no accepted standard test methods (8). While stereo-DIC has been used for low (7,9) and medium velocity (10) impacts, the application of high speed imaging for ballistic impacts is very limited. In this paper, an experimental methodology is proposed for the oblique angle impact testing of fibre reinforced composites at ballistic velocities. Some of the challenges and practical considerations for using high speed imaging for ballistic impact testing are discussed.

## 2. Experimental setup

A schematic diagram of the experimental setup used for conducting ballistic impact test using a 70mm gas gun is shown in Figure 1. For a typical ballistic impact test, a carbon fibre-reinforced polymer (CFRP) composite panel with dimensions of 550 mm × 360 mm is impacted by an aluminium projectile with a diameter of 44 mm. The projectile is placed in a nylon sabot with same diameter as the barrel and a ball valve system was used to accelerate the sabot and projectile along the length of the barrel. Helium gas was used at pressures ranging from 10 – 30 bars depending on the desired initial velocity. The composite panel is clamped between two fixtures at an oblique angle to the barrel. The entire fixture is housed in a containment chamber for safety and in order to protect the cameras from debris. The impact event was tracked by using three high-speed cameras. Two Photron Fastcam SA5 cameras (left and right cam) were used to observe the rear of the impacted panel, and the recorded images were used for stereo digital image correlation (DIC). The frame rate of the high speed cameras is determined based on the duration of the impact event and the number of images required. For example, if the impact duration is 1.25 milliseconds and at least 50 images are needed, the frame rate should be no less than  $50 / (1.25 \times 10^{-3})$ , i.e. 40000 fps. This frame rate results in a lower resolution of 448 x 376 pixels. A third camera (Phantom) recording from the top was used for measuring the initial velocity and rebound velocity of the projectile. An additional high-speed camera may be optionally positioned in front of the impact cell to record the front view. Light curtains present at the end of the barrel were used to trigger the image capture and also to measure the initial velocity.

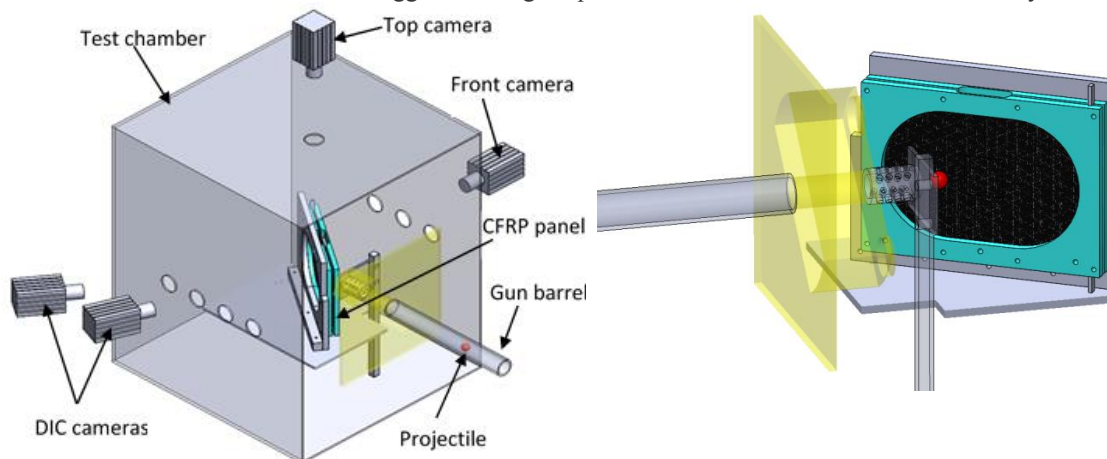
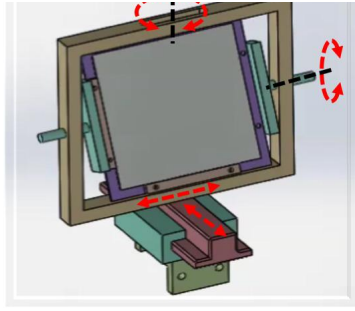
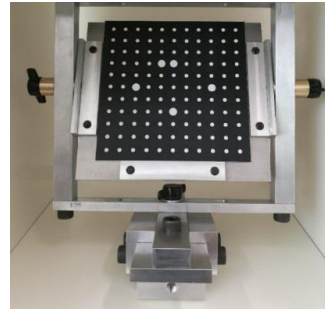


**Figure 1 Schematic of the typical setup for ballistic impact testing of the composite panel on a gas gun**

GOM Aramis software was used for the image correlation of the high-speed image data recorded by the two synchronised cameras. The accuracy of the out-of-plane displacement and strain measurements of the DIC is dependent on a valid Stereo-DIC calibration. However, the calibration process is a time-consuming procedure involving positioning a calibration panel in 13 different orientations. A calibration fixture was designed and built to position the calibration panel in the required orientation quickly and easily. As shown in Fig. 2, this calibration mechanism is capable of achieving four types of basic motions, i.e. in-plane translation, out-of-plane translation, rotation with respect to the horizontal axis, and rotation with respect to the vertical axis. As a result, the calibration panel could be moved to the required orientation efficiently and the time taken for a typical stereo-DIC calibration was significantly reduced.



(a) CAD model



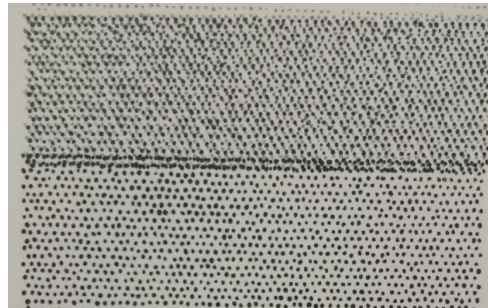
(b) Manufactured fixture

**Figure 2 Stereo-DIC calibration fixture: a) CAD model, b) manufactured fixture**

DIC algorithms require the sample surface to have random intensity variations as a carrier of deformation information. In case the material does not have evident discernible natural texture, a random speckle pattern must be artificially created. Typically, black paint is sprayed on a white background to create a high contrast speckle pattern. The speckle size distribution when a spray bottle or an airbrush is used depends on parameters such as the nozzle diameter, the distance between the substrate and the nozzle, air pressure and viscosity of the solution. In the case of the impact panel, where the Region of Interest (ROI) is an area of 150 mm × 150 mm, spray painting would not provide consistent speckle size big enough to meet the recommendations given by Sutton et. al (11). The initial approach was to use a maker to create speckles, which is time-consuming and labour-intensive as marking speckles with an average diameter of ~ 1 mm in the ROI required generating 5,000 to 10,000 dots on a single specimen. To improve the efficiency of speckling, an Imetrum stamp with a random speckle pattern and the required speckle diameter was used, as shown in Fig. 5. The rear surface of the target is painted with a random speckled pattern using an Imetrum stamp set. The average feature area was 6.6 pixels<sup>2</sup> with standard deviation of 2. By using the stamp, the time taken to speckle an area of 150 mm × 150 mm was significantly reduced from initially 1 ~ 1.5 hours to merely minutes.



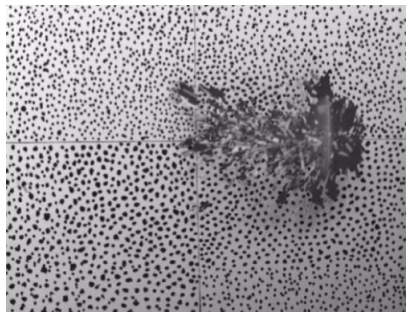
(a) The 1.1 mm Imetrum stamp



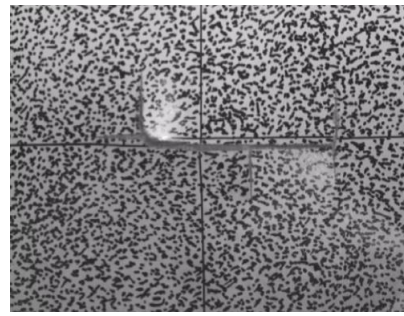
(b) Typical stamp generated patterns

**Figure 3 Utilisation of a) the 0.2 mm Imetrum stamp for fast generation of b) speckle patterns**

The application of a thin layer of primer paint (Ambersil White Satin Finish Galvanised Paint) to form the white background of the DIC area posed another challenge. As this primer is relatively brittle and has a low surface adhesion strength, the paint peeled off early during the impact and resulted in invalid image correlation, as shown in Fig. 4(a). To address this problem, a layer of 3M epoxy adhesive DP460 was applied before spraying the primer paint. As a result of the epoxy adhesive providing a strong surface adhesion, the primer paint did not peel off even after the presence of cracks in the painted area, as shown in Fig. 4(b).



(a) Results of the initial painting method



(b) Results of the improved painting method

**Figure 4 Comparison between a) results of the initial painting method (primer paint only) and b) results of the improved painting method (3M epoxy adhesive + primer paint).**

### 3. Results and discussion

Figure 5 show an example of the recorded high sped camera images to evaluate the impact event. The view from the top camera shows the time progression of the projectile just before impacting the target, to contact, sliding and rebound. The dots on the projectile are tracked to calculate the initial and rebound velocities from the images of the top camera. In this typical case, an initial velocity of the projectile is 130 m/s and the rebound velocity is approximately 100 m/s. Figure 5 also shows the typical images from the DIC cameras in the rear. The speckled pattern of the target ROI is clearly visible. It can be seen that the images show the panel before contact, then at the point of contact, initiation of damage and finally at rebound. Since this is an oblique impact, the initial point of contact is to the right of the centre.

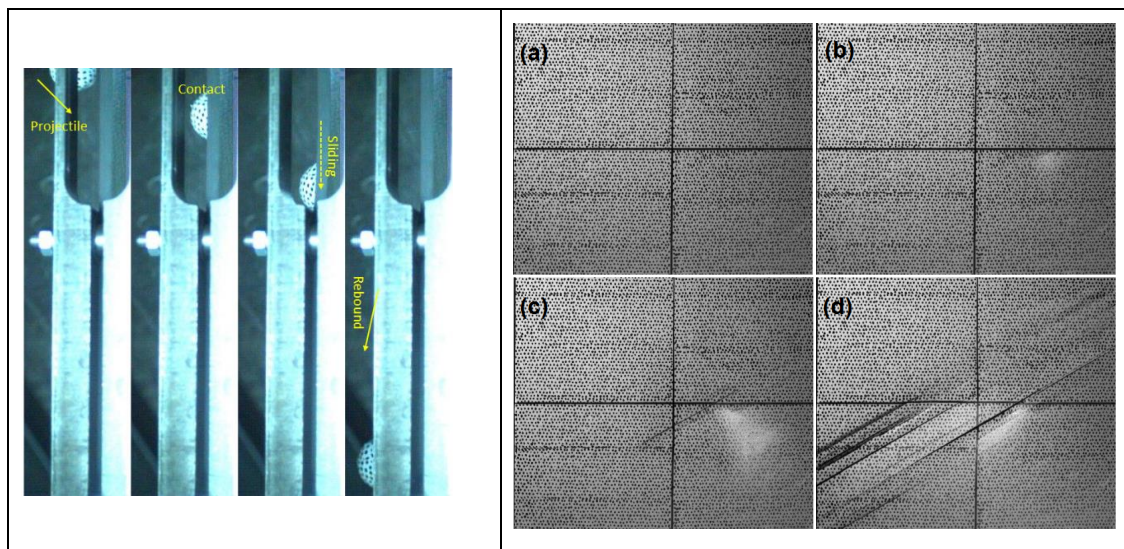


**Figure 5 (Left) View from the top camera showing impact and rebound; (Right) View from rear camera showing contact and damage**

The objective of this work was to qualitatively observe the damage and failure modes and more importantly to obtain image data for quantitatively measuring the displacements and strains of the impacted panel through DIC analysis, which was performed using the commercial DIC software Aramis. Stereo-DIC of the left and right camera images involve correlating subsets of size 19 pixels to reference images and each camera, along with the parameters of the stereo-system calibration to calculate the evolution of displacements in the target. The main benefit of the DIC technique is its capability of reproducing the impact event by means of quantitatively generating full-field strains and displacements for the entire impact duration. It is possible to accurately identify the critical locations of the impact event, such as the primary impact point, the peak strain point before failure initiation, the primary and secondary z-displacement points by comparing the

traditional experimental methods and will be valuable in the development of computational models for the prediction of high velocity impact of composite structures.

Figure 6 shows the contours of the out-of-plane displacement (z-displacement) obtained from the stereo-DIC for different times. It can be seen that the first image shows the initiation of contact. Since the frame rate of the camera is 40000, each image is obtained at 0.025 milliseconds interval. The second image at 0.075 ms shows a maximum displacement of approximately 3 mm. In the third image which corresponds to time of 0.15 ms, we can see the initiation of damage. In this case the damage is a combination of matrix cracking and ply delamination. In the fourth image, corresponding to the time of 0.425 ms, we can see the crack has propagated along the fibre direction of the last ply and there are discontinuities in the displacement contour. The correlation algorithm will fail in the case of large damage or fibre failure. However, it can be seen from the contours that the speckled pattern preparation procedure followed in this study, namely the epoxy primer and stamping, can be used in the high speed imaging of ballistic impacts.

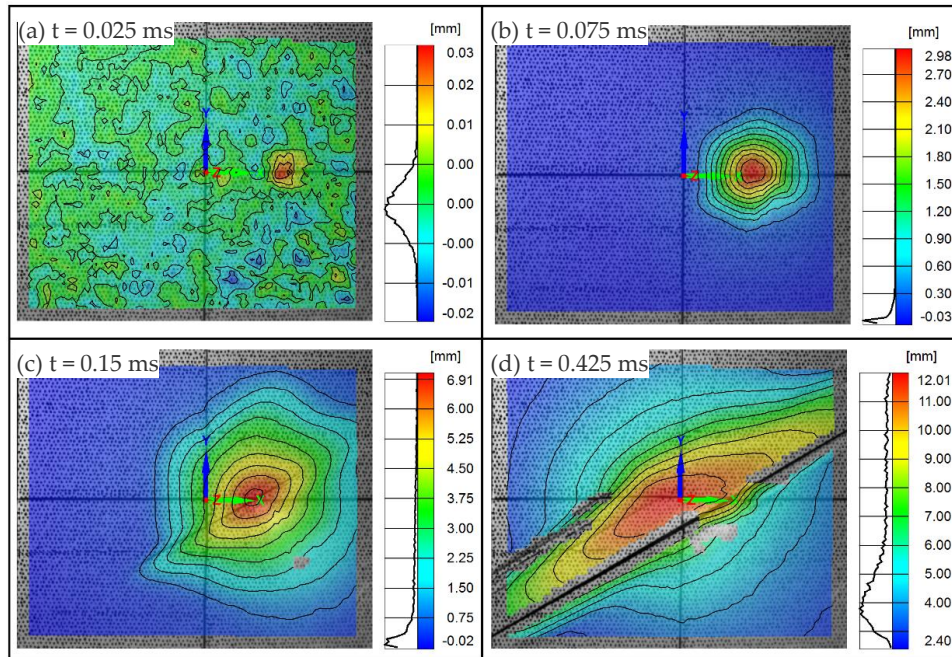


Figure 6 Contour plot of z-displacement obtained from stereo-DIC

Different points of interest were chosen on the surface of the target and the time history of in-plane and out-of-plane displacements of the points were plot (Figure 7). P1 corresponds to the point of impact and P3 corresponds to the location of maximum displacement. Additionally a secondary maximum point P4 was defined for the peak displacement from the reflected wave. It can be seen that the in-plane displacements (x and y) are very small compared the z-displacement. The maximum displacement reached is about 12.2 mm. The figure also shows the advantage of full-field measurements. If the displacement was only measured at the centre of the plate or at point of contact, it will underestimate the peak displacement value.

#### 4. Conclusions

The ballistic impact testing of composites is necessary to ensure the structural reliability of the composites to extreme loading conditions. However, it poses some challenges as they are not instrumented the same way as drop tower experiments where the initiation of damage can be identified from the force-displacement curve. The assessment of creation and propagation of damage requires the use of a local approach such as that presented in this paper. Digital Image Correlation was used to study the displacement and strain history of the composite and to observe the initiation and progression of damage. The paper also deals with some of

designed and manufactured to allow easy calibration of the stereo-DIC system. A speckled stamp was used to create the pattern required for the image correlation. The use of a thin epoxy basecoat for the primer also solved the problem of peeling of the paint from the composite surface. The developed method can be used for the evaluation of impact damage for different composite materials. In future work, the full-field displacement and strain measurements are used to validate the numerical model of impact.

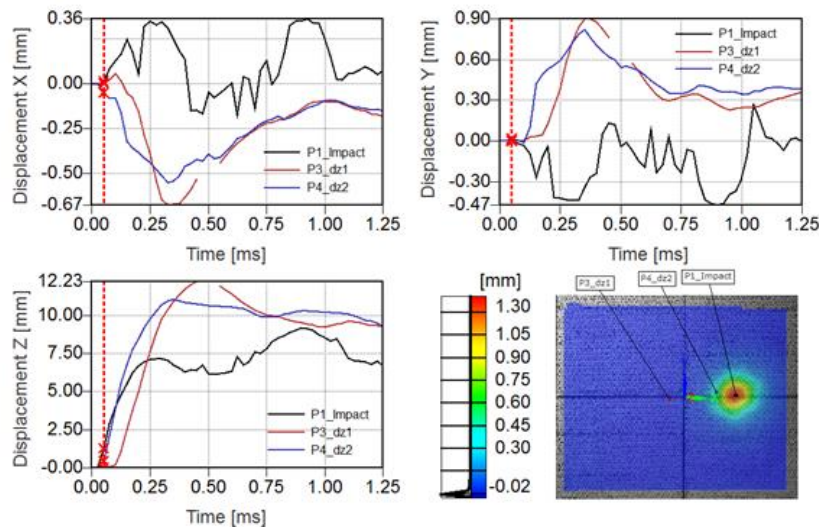


Figure 7 Time history of displacement obtained from stereo-DIC

#### References:

1. VanderKlok A, Stamm A, Dorer J, Eryi H, Auvenshine M, Pereira JM, et al. An experimental investigation into the high velocity impact responses of S2- glass/SC15 epoxy composite panels with a gas gun. *Int J Impact Eng.* 2018;111:244–54.
2. Liu L, Luo G, Chen W, Zhao Z, Huang X. Dynamic behavior and damage mechanism of 3D braided composite fan blade under bird impact. *Int J Aerosp Eng.* 2018;2018.
3. Pernas-Sanchez J, Artero-Guerrero J, Varas D, Lopez-Puente J. Experimental analysis of normal and oblique high velocity impacts on carbon/epoxy tape laminates. *Compos Part A Appl Sci Manuf.* 2014;60:24–31.
4. Ramadhan AA, Abu Talib AR, Mohd Rafie AS, Zahari R. High velocity impact response of Kevlar-29/epoxy and 6061-T6 aluminum laminated panels. *Mater Des.* 2013;43:307–21.
5. Reu PL, Miller TJ. The application of high-speed digital image correlation. *J Strain Anal Eng Des.* 2008;43(8):673–88.
6. Tiwari V, Williams S. Application of digital image correlation in impact testing. *SEM Annu Conf Expo Exp Appl Mech.* 2005;1(Ccd):2–3.
7. Flores M, Mollenhauer D, Runatunga V, Bebernis T, Rapping D, Pankow M. High-speed 3D digital image correlation of low-velocity impacts on composite plates. *Compos Part B Eng.* 2017;131:153–64.
8. Sharma AP, Khan SH. Influence of metal layer distribution on the projectiles impact response of glass fiber reinforced aluminum laminates. *Polym Test.* 2018;70(May):320–47.
9. Cuyenet A, Scida D, Roux É, Toussaint F, Ayad R, Lagache M. Damage characterisation of flax fibre fabric reinforced epoxy composites during low velocity impacts using high-speed imaging and Stereo Image Correlation. *Compos Struct.* 2018;202(May):1186–94.
10. Ramakrishnan KR, Hokka M, Sarlin E, Kanerva M, Kouhia R, Kuokkala VT. Experimental investigation of the impact response of novel steel- biocomposite hybrid materials. In: *EPJ Web of Conferences, Dymat 2018.* 2018.
11. Sutton M. *Digital Image Correlation for Shape and Deformation Measurements.* Springer Handb Exp Solid Mech SE - 20. 2008;565–600.

# In-Situ Flash X-ray Tomography of Low-Strength Mortar Concrete Subjected to Low Velocity Impact

S. C. Paulson<sup>1,\*</sup>, M. Hossain<sup>2</sup>, W. Tsutsui<sup>1</sup>, H. Liao<sup>3</sup>, C. Bouman<sup>4</sup>, W. W. Chen<sup>5</sup>

<sup>1</sup>*School of Aeronautics and Astronautics, Purdue University, 701 W Stadium Ave, West Lafayette, IN 47907, USA, ORCID ID: 0000-0001-8505-1015*

<sup>2</sup>*School of Electrical and Computer Engineering, Purdue University, 465 Northwestern Ave, West Lafayette, IN 47907, USA*

<sup>3</sup>*Lam Research, 4400 Cushion Pkwy, Fremont, CA 94538, USA*

<sup>4</sup>*School of Electrical and Computer Engineering, Purdue University, 465 Northwestern Ave, West Lafayette, IN 47907, USA, ORCID ID: 0000-0001-8504-0383*

<sup>5</sup>*School of Aeronautics and Astronautics, Purdue University, 701 W Stadium Ave, West Lafayette, IN 47907, USA*

**Keywords:** Split Hopkinson bar, Concrete, Dynamic behaviour, Impact, Tomography

---

**Abstract:** This paper details an investigation into the use of flash X-ray imaging to obtain a tomographic reconstruction of concrete during dynamic failure. Similar cylinder specimens were created from a preblended dry mortar mix. These specimens were subjected to axial impact using a modified Split Hopkinson bar fitted with a single loading device to limit load duration in the sample. Strain gauge signals were used to evaluate the dynamic behaviour in the sample in addition to triggering the firing of four flash X-ray heads mounted at specified angles around the specimen. The X-ray heads, combined with phosphor storage plate detectors, created four two-dimensional images of the sample during dynamic failure. The X-ray images collected were successfully implemented into a rough tomographic reconstruction. The images and reconstructions produced by this study provide an early look at the capabilities of flash X-ray imaging to create three-dimensional images of materials at a specified moment during dynamic failure.

## 1. Introduction

Concrete is one of the most widely used structural materials in the world today, being used to form both foundations and framing systems. Further, these concrete components are used in a myriad of applications, including high rise buildings, bridges, tunnels, and military fortifications. In each of these applications, these components are subject to dynamic and high rate loading events, including seismic, blast, and impact events. Previous studies have shown that the applied strain rate has a significant effect on the response of concrete materials [1-7]. Most investigations into this rate-dependent behaviour show agreement regarding an increase in strength; however, even current studies disagree on the cause of this observed increase in strength. Several studies have demonstrated the likelihood of an inertial effect during specimen unloading that likely contributes to the increase in observed failure stress [2-6] while others have been able to isolate an increase in strength to a material property separate from inertial effects [7]. While certain threshold values have been discussed regarding this inertial effect [2,5], it is still unclear to what degree the observed increased failure stresses are affected by specimen geometry or the constituent materials.

In this study, the authors seek to develop an imaging technique that will allow for further characterization of the failure of concrete materials under dynamic load conditions. Traditional computed tomography techniques have demonstrated the capability of producing high-quality images of fracture and failure surfaces in concrete

\*Author for correspondence (scpaulson42@gmail.com).

†Present address: School of Aeronautics and Astronautics, Purdue University, 701 W Stadium Ave, West Lafayette, IN 47907, USA

samples [8,9]. While in-situ tomographic imaging has been successfully used at quasi-static load rates [8], the capability of computed tomography is still limited to post-mortem evaluation for dynamic events [9]. This study seeks to combine tomographic reconstruction techniques with the use of flash X-ray radiography, which has a demonstrated capability of exposure times as short as 10 ns [10], allowing for the capture of high-speed events with greatly reduced motion blur.

## 2. Methods

For this study, a low-strength, small particle concrete was desired to minimize both observed sample stresses and sample size. As a result, a Type S mortar product was selected, supplied as product number 1136 by Quikrete®. Mortar samples were formed in custom moulds to form cylinders 12.7 mm in diameter by 25.4 mm in height. Samples were open-air cured at an average temperature of 23 °C for 28 days before demoulding. The mortar concrete samples were loaded in uniaxial compression by an aluminium split Hopkinson pressure bar detailed in the schematic in Figure 1. The incident and transmission bars were both of a diameter of 19.05 mm and lengths of 10.97 m and 7.32 m, respectively. The striker bar was 19.05 mm in diameter with a length of 1.22 m. A copper pulse shaper of diameter 7.2 mm and 0.5 mm thickness was used for each sample to achieve a near-constant strain rate of 860 s<sup>-1</sup> with an initial impact velocity of 22 m/s.

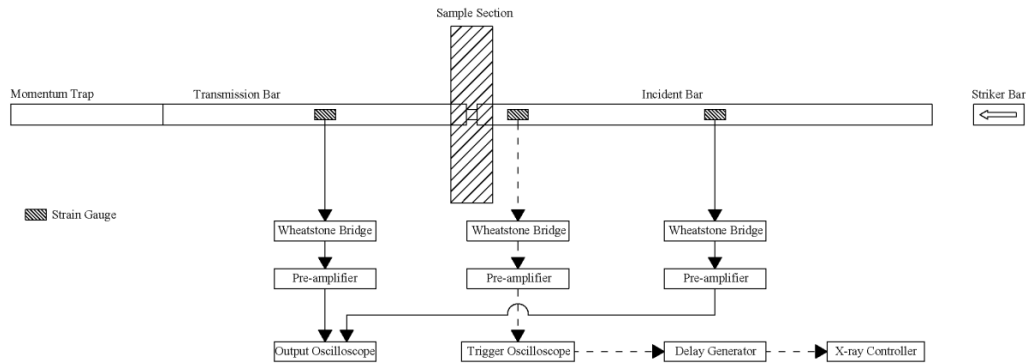


Figure 1: Schematic of Kolsky Bar used in this study

Four X-ray images were obtained for each sample using four flash X-ray heads connected to a series of X-ray controllers. Each X-ray controller was triggered simultaneously using a user-defined delay time and an input signal provided by the strain gauges mounted on the incident bar. In order to obtain a useful reconstruction, the four X-ray heads were mounted at specific angles with respect to each other. In the case of this study, the heads were each mounted at an angle of 72° with respect to the neighbouring channel. Four ScanX phosphor storage plates were used as detectors in this experiment, each aligned to a specific X-ray channel. These phosphor storage plates have a reported resolution of 20 line pairs per millimetre. The detectors were placed within a lead tube with holes machined to allow each X-ray beam to pass to its detector. The arrangement of the detectors and beams is shown in Figure 2. Prior to each experiment, a series of brightfield images were also obtained by firing the X-ray heads without the sample in the field of view. The collected images were reconstructed using model-based iterative reconstruction.

Model-based iterative reconstruction (MBIR) is a framework for solving inverse imaging problems of the form  $Y = AX + W$ , using maximum a posteriori (MAP) estimation. In the case of tomographic reconstruction,  $Y \in \mathbb{R}^M$  is the noisy radiograph, and  $A \in \mathbb{R}^N$  is the stack of images that represents the volume we wish to recover.  $A \in \mathbb{R}^{M \times N}$  is calculated based on the system geometry of the parallel beam tomographic imaging system. Pre-multiplication with  $A$  represents the Radon transform of the optical density data modelled by  $X$ .  $W \in \mathbb{R}^M$  is zero mean white additive Gaussian noise.

The map estimate is the instance  $\hat{x}_{MAP}$  of random variable  $X$  that maximizes the conditional probability of  $X$  given observation  $Y$ . Thus, the problem can be formulated as a cost function with two parts: a likelihood term

to enforce data fidelity and a prior term to act as a regularizer. The alternating direction method of multipliers (ADMM) can split this optimization into its constituent parts [11]. Multi-agent consensus equilibrium (MACE) is a generalization of ADMM, where multiple denoisers can be fused to form a prior model for  $X$  [12]. For this 3D reconstruction, we used three BM3D denoisers along the  $x$ - $y$ ,  $y$ - $z$ , and  $z$ - $x$  axes to form a higher dimension 3D prior [13]. A rotational averaging operation was used as an additional denoising agent in the MACE framework, which exploits the fact that the object is approximately rotationally symmetric in  $x$ - $y$ . For the reconstruction presented here, an initial reconstruction was generated using MBIR with a qGGMRF prior. This initial reconstruction was then used to initialize the MACE routine.

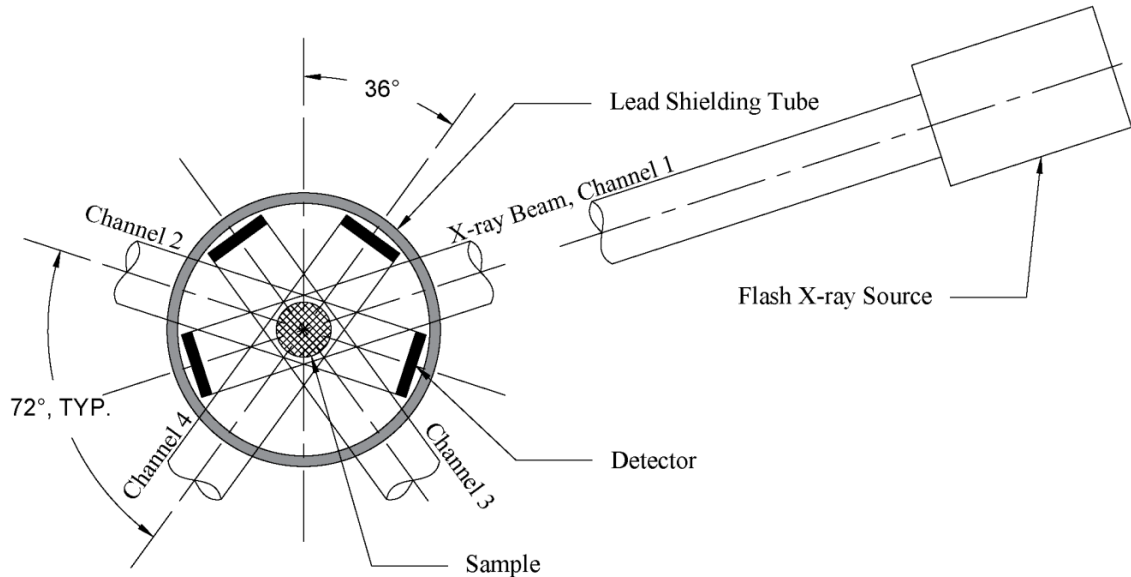


Figure 2: Layout of X-ray source channels and respective detectors, as viewed looking from the transmission bar towards the incident bar

### 3. Results and Discussion

The raw output signals from the strain gauges are presented in Figure 3, along with the input and output stresses for the sample. The strain results indicate a high input stress at the incident end coupled with a low maximum stress at the transmission end. The raw strain gauge data include a very sharp peak at  $t = 3.64 \times 10^{-3}$  s in Figure 3a. This sharp peak is not indicative of actual strain in the bars; rather it is a result of electrical interference from the flash X-ray system at the moment the flash X-ray heads were fired. Using the location of the strain gauges in concurrence with the elastic wave speed of the aluminium bars, the “true” moment of image capture was calculated, noted by the blue dot in Figure 3b.

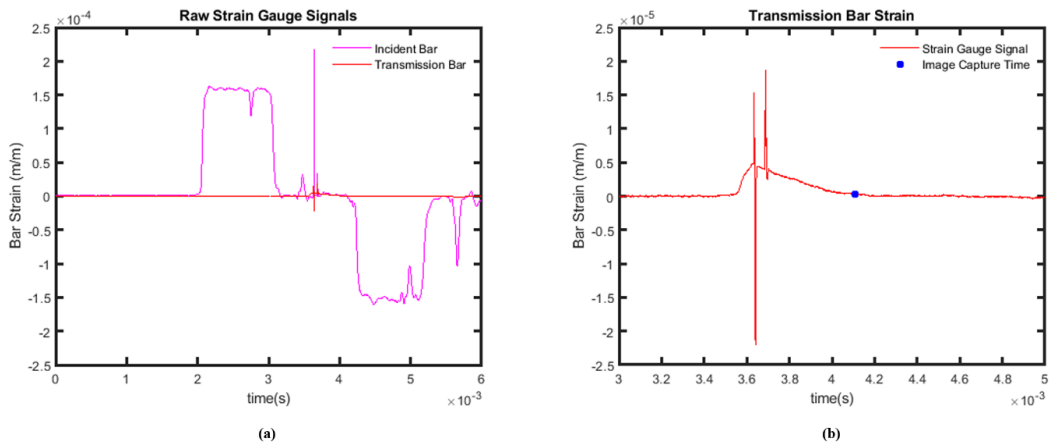


Figure 3: (a) Raw strain gauge data for the incident and transmission bars. (b) Strain gauge data from the transmission bar from the period of interest, that of the initial loading and image capture. The blue dot notes the corrected capture time from the raw data provided by the electrical interference from the system.

At the moment of image capture, a raw image was recorded on each of the four PSP detectors. The raw radiographs obtained are provided in Figure 4a. While the system provides four images, the log of each image must be taken for use in tomographic reconstruction. The normalized log X-ray input from the detector located at  $-36^\circ$  is shown in Figure 4b with slice 21 marked. As shown in Figure 4a, each raw image has some initial tilt resulting from the manual scanning process. These different tilt angles were corrected using the Kolsky bars as an alignment reference. The bars were then cropped, and each view was binned by a factor of  $2 \times 2$  to improve the signal to noise ratio. The resulting dataset is 251 slices of 220 detector channels for each view. The projection of slice 21 at  $-36^\circ$  and its reconstruction using all four tilts are shown in Figures 5 and 4c. As there are only four views, circular objects appear octagonal in the reconstruction with edges parallel to the view angles. The dip in the projection plot at the 104<sup>th</sup> channel corresponds to the crack through the centre of the object at  $-36^\circ$  measured from the vertical. Figure 6a is a 3D render of the entire reconstruction, and it shows the start of the radial crack that also appears in Figure 4c. Figure 6b shows a cross section at slice 238 from the top and is labelled to map fragments between slices and the 3D render in Figure 6a.

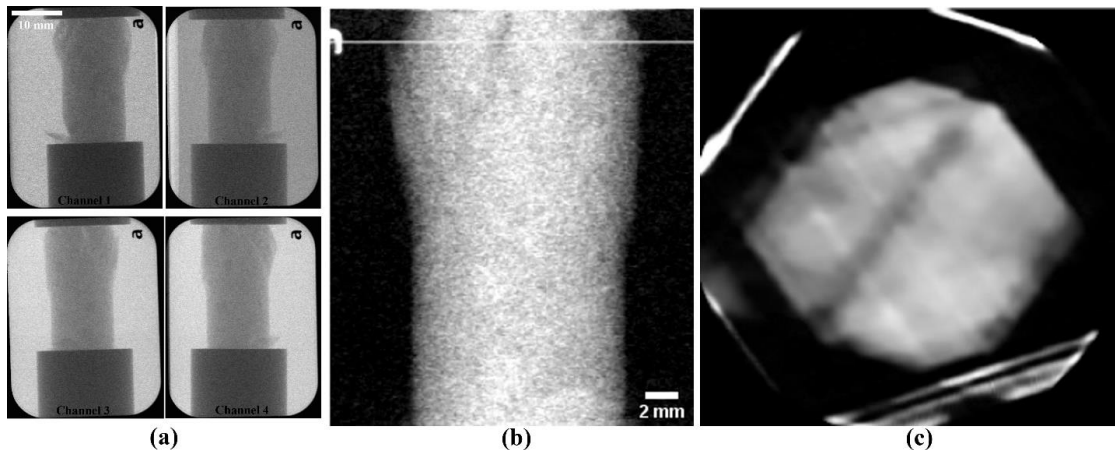


Figure 4: (a) Raw radiograph images for each X-ray channel acquired by the PSPs and digitized by a ScanX digital scanner. (b) Normalized log image from X-ray Channel 3. The white horizontal line notes the location of Slice 21 in (c). The slice shown in (c) shows a clear diagonal crack feature, corresponding to cracking features seen in both the raw radiograph in (a) and normalized log image in (b).

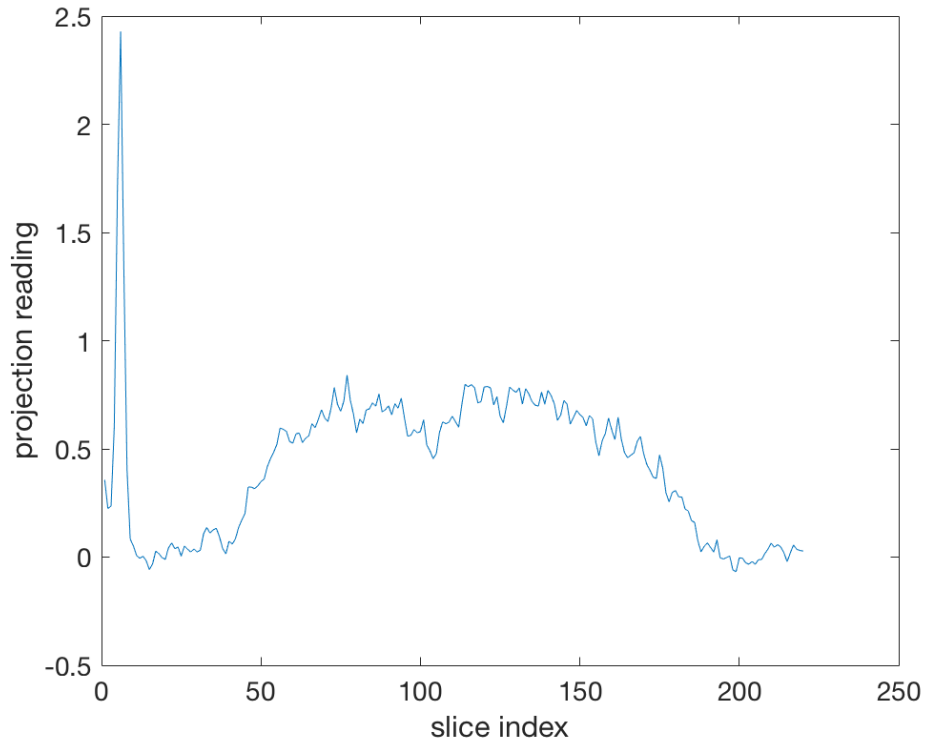


Figure 5: Projection reading data from Channel 3 at Slice 21. The sharp peak at index near zero corresponds to an artefact of the PSP detector. The plot shows increased reading values over the region containing sample material, with a notable drop at index 104 corresponds to the crack feature presented in Figure 4.

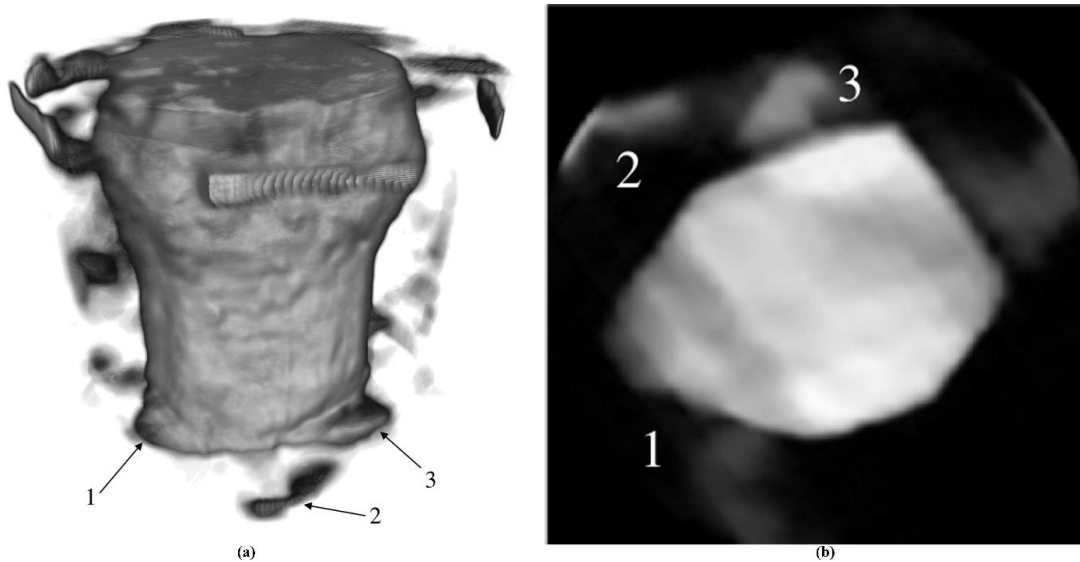


Figure 6: (a) Three-dimensional render produced from the stack of reconstructed slices. Small fragments of sample material are observed at locations 1, 2, and 3. These locations are noted and labelled in Slice 238 in (b). Other features surrounding the sample are artefacts of noise present in the raw images and are not physically significant.

#### 4. Conclusions

This study evaluated the viability of a four-channel X-ray tomography reconstruction for the evaluation of fracture patterns in low-strength mortar concrete under dynamic load conditions. The raw data from each experiment provided four 2-D projected images of a fractured sample in addition to stress and strain histories. Evaluating the strain gauge data allowed for the correlation of the acquired images with an associated state of stress and strain. Further, applying an iterative tomographic reconstruction approach to the four 2-D images produced 3-D images and 2-D cross-sectional slices with clear fracture patterns. This technique allowed us to identify rough fracture patterns as they developed in low-strength mortar concrete. Further improvement of both the detectors and the reconstruction algorithms used will greatly advance the understanding of fracture pattern development and fragmentation in concrete and other geomaterials subjected to impact.

#### Acknowledgments

The authors would like to thank Zherui Guo for his help managing the laboratory space and setting up the necessary safety restrictions for our experiments. We would also like to thank the members of Purdue University's Impact Science Laboratory for their support for this project.

#### Funding Statement

This research was supported by the United States Air Force Research Laboratory through contract number FA8651-18-P-0053 with PM&AM Research.

#### References:

1. P.H. Bischoff and S.H. Perry. 1991. Compressive behaviour of concrete at high strain rates. *Mater Struct* **24**, 425-450. (doi: 10.1007/BF02472016)
2. P.H. Bischoff and S.H. Perry. 1995. Impact Behavior of Plain Concrete Loaded in Uniaxial Compression. *J. Eng. Mech.* **121**, 685-693. (doi: 10.1061/(ASCE)0733-9399(1995)121:6(685))
3. T. Krauthammer, M.M. Elfahal, J. Lim, T. Ohno, M. Beppu, and G. Markeset. 2003. Size effect for high-strength concrete cylinders subjected to axial impact. *Int J Impact Eng* **28**, 1001-1016. (doi: 10.1016/S0734-743X(02)00166-5)
4. M.M. Elfahal, T. Krauthammer, T. Ohno, M. Beppu, and S. Mindess. 2005. Size effect for normal strength concrete cylinders subjected to axial impact. *Int J Impact Eng* **31**, 461-481. (doi: 10.1016/j.ijimpeng.2004.01.003)
5. G. Cusatis. 2011. Strain-rate effects on concrete behavior. *Int J Impact Eng* **38**, 162-170. (doi: 10.1016/j.ijimpeng.2010.10.030)
6. Z.C. Mu, A.N. Dancygier, W. Zhang, and D.Z. Yankelevsky. 2012. Revisiting the dynamic compressive behaviour of concrete-like materials. *Int J Impact Eng* **49**, 91-102. (doi: 10.1016/j.ijimpeng.2012.05.002)
7. Y.B. Guo, G.F. Gao, L. Jing, and V.P.W. Shim. 2017. Response of high-strength concrete to dynamic compressive loading. *Int J Impact Eng* **108**, 114-135. (doi: 10.1016/j.ijimpeng.2017.04.015)
8. S.C. de Wolski, J.E. Bolander, and E.N. Landis. 2014. An *In-Situ* Microtomography Study of Split Cylinder Fracture in Cement-Based Materials. *Exp Mech* **54**, 1227-1235. (doi: 10.1007/s11340-014-9875-1)
9. M.C. Blasone, D. Saletti, E. Andò, J. Baroth, and P. Forquin. 2018. Investigation of Spalling Damage in Ultra-High Performance Concrete Through X-ray Computed Tomography. *EPJ Web of Conferences* **183**, 03024. (doi: 10.1051/epjconf/201818303024)
10. R. Germer. 1979. X-ray flash techniques. *J. Phys. E: Sci. Instrum.* **12**, 336-350. (doi: 10.1088/0022-3735/12/5/001)
11. S. Sreehari, S.V. Venkatakrishnan, B. Wohlberg, G.T. Buzzard, L.F. Drummy, J.P. Simmons, and C.A. Bouman. 2016. Plug-and-Play Priors for Bright Field Electron Tomography and Sparse Interpolation. *IEEE Trans. Comput. Imaging.* **2**, 408-423. (doi: 10.1109/TCI.2016.2599778)
12. S. Majee, T. Balke, C.A.J. Kemp, G.T. Buzzard, and C.A. Bouman. 2019. 4D X-Ray CT Reconstruction using Multi-Slice Fusion. arXiv: 1906.06601
13. M. Lebrun. 2012. An Analysis and Implementation of the BM3D Image Denoising Method. *Image Processing On Line.* **2**, 175-213. (doi: 10.5201/ipol.2012.l-bm3d)

# Dynamic Stress Evaluation due to Hypervelocity Impact using Time Gated Raman Spectroscopy

Abhijeet Dhiman, Ayush Rai, Hao Wang, Chandra Prakash, Vikas Tomar\*<sup>†</sup>

*School of Aeronautics and Astronautics, Purdue University, West Lafayette, IN, 47907, USA*

**Keywords:** Micro-particle impact Raman microscope, Time gated Raman spectroscopy, Hydroxyl-terminated polybutadiene

---

**Abstract:** In this work, an experimental setup based on time-gated Raman spectroscopy for impact-induced local stress evolution measurements is presented. The setup is used to obtain local Raman shift variation as a function of time at strain rates approaching  $10^6 \text{ s}^{-1}$ . Based on an empirical expression, stress evolution as a function of time under dynamic impact loading is presented. The setup is shown to be able to measure the local in-situ evolution of dynamic stress in a Hydroxyl-terminated polybutadiene (HTPB) sample induced by an impact from 250 micron-sized microsphere using a laser induced particle launch system.

## 1. Introduction

Application such as Armor design and meteor impact resistant structure design require high-performance composite materials resistant to impact failure. Under impact, stress-wave interacts with the material interfaces and defects that play an important role in determining the material performance. Material behavior under shock is entirely different from materials behavior under static loading. Understanding of material behavior in-situ under shock can lead to important new advances in material development not currently possible. It is, therefore, important to investigate the dynamic behavior of materials under shock at fundamental microscale level in an in-situ manner. One aspect of such an understanding is stress-strain behavior at a local microscale material length scale under hypervelocity ( $> 1 \text{ km/sec}$ ) impact-induced shock. This work presents real-time measurements of stress evolution under impact shock loading at micron length scale.

There are several experimental tests that have been used to characterize a material's response to an impact or shock loading. Drop weight test, light gas gun-based Taylor Impact test, Split Hopkinson Bar test are some of the specialized experimental techniques that are primarily used. The outcome of such tests are the deformation and strain as well as strain rates which can be used to obtain strain rate dependent material constitutive behavior [1]. The measurement techniques used in these experiments involve strain gauges, digital image correlation, X-ray diffraction (XRD), Photonic Doppler Velocimetry (PDV) or the electron diffraction based methods. These methods are either of insufficient time and length resolution (strain gauge etc.) or are based on large-scale facilities (XRD, phase contrast imaging, etc.) [2]. Also, these methods can only measure strains directly and stress is a derived quantity [3] using the constitutive models of the respective materials. Currently the only laboratory method available, which can directly measure stresses in the material without using a constitutive model, is mechanical Raman spectroscopy (MRS) developed by Tomar and co-workers [4, 5]. Several previous works [4, 5] have established the robustness and repeatability of MRS for stress measurement without constitutive models under quasi-static loading conditions in different materials by comparing the results with constitutive model based predictions. However, when it comes to the direct stress measurement at microscale under hyper-velocity impact conditions, there are no established experimental techniques available. In this work, time gated Raman spectroscopy is extended for direct in-situ measurement of stress evolution at microscale under hyper-velocity particle impact loading using a MRS setup developed earlier [6]. Figure 1 shows the experimental setup developed to perform dynamic stress evolution under shock loading.

\*Author for correspondence (tomar@purdue.edu).

<sup>†</sup>Present address: School of Aeronautics and Astronautics, Purdue University, West Lafayette, IN, 47907, USA

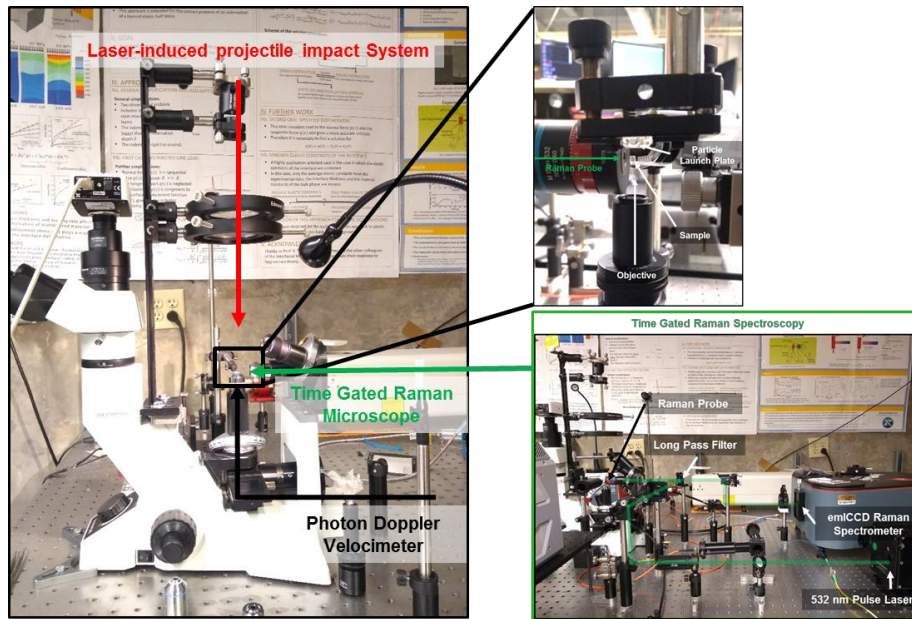


Figure 1: Micro-particle impact Raman microscope

## 2. Experiment Method

Figure 2(a) shows the schematic of the Micro-particle impact Raman spectroscopy system designed to perform time-gated Raman spectroscopy to evaluate local stress evolution due to microsphere impacts. The apparatus for this system consists of a 1064nm YAG-laser from Continuum Lasers with pulse width of 7 ns and 900 mJ pulse energy. The optical path of this laser consists of an optical isolator, beam expander, and aspheric lens to focus the pulse energy on a particle launch system designed to launch microspheres of size between 10-500 $\mu$ m. The particle launch system is designed as shown in Figure 2(b) with Ytria-stabilized zirconia microspheres purchased from Cospheric LLC backed with an aluminum flyer disk. The yttria-stabilized zirconia microspheres were selected because of their high impact resistance and high operating temperature. The aluminum flyer disk was glued to a 3 mm borosilicate backglass using two-part epoxy and cured at 80 °C for 4 hrs. The aluminum flyer disk absorbs the pulse energy from YAG laser and accelerates the microsphere due to plasma expansion between back glass and disk as shown in Figure 2(c).

This state of the art particle launch system is combined with an emCCD Raman spectrometer from Princeton Instruments to perform time-gated Raman spectroscopy synchronized with a 532 nm pulsed laser (Quantel Lasers). The flash lamp charging cycle of the two pulsed lasers were synchronized with a delay generator. The delay between the charging cycle two lasers can be varied to perform time-resolved Raman spectroscopy with respect to the Q-switch of 1064nm pulsed laser. A part of pulse energy from 532 nm pulse laser was diverted and expended to capture a snapshot of particle location on the high-speed camera. This in-situ imaging technique provides the delay time required between the two lasers and sample deformations under the shock loading. Since the dynamic stresses due to shock last for few nanoseconds, the nanosecond time resolution is crucial to evaluate stress during the high strain rate developed at the time of impact. In this work, nanosecond resolved mechanical Raman spectroscopy was performed using a pulse laser with the gate width of 50 ns and delay of 100 ns between successive time histories.

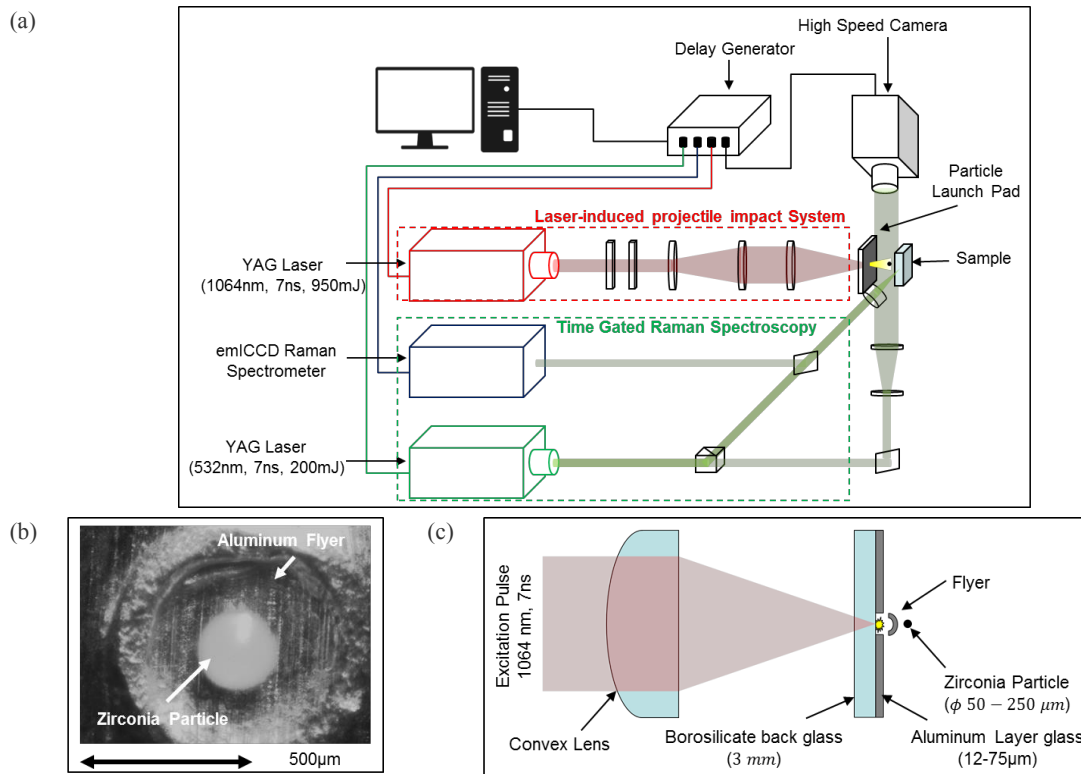


Figure 2: (a) Schematic of micro-particle impact Raman microscope (b) Particle launch pad (c) Particle launch system.

### 3. Results and Discussion

The acceleration of microspheres to hypersonic velocities requires special design of launch pads based on the sphere size. For smaller microspheres of size 50 µm, the particle launch pad is designed using a 75 µm aluminum layer. The laser pulse is focused on the spot size of 300 µm and particle is precisely placed at the focus point under the microscope. The ablation of aluminium layer behind the microsphere provides the momentum to the microsphere where the velocity of the microsphere was quantified using shadowgraph imaging at 480 kHz. Figure 3 shows the image captured for 50µm microsphere moving at approximate speed of 1.6 km/s.

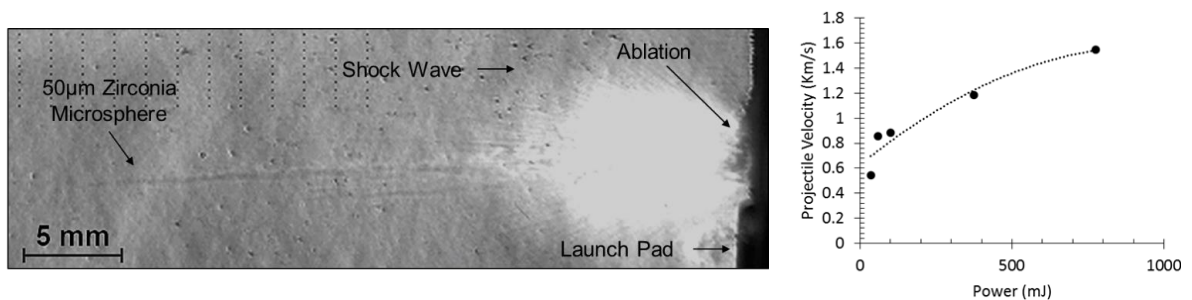


Figure 3: Shadowgraph for 50µm microsphere moving at 1.6km/s and velocity-power calibration for system with 50µm particle and 75µm aluminum layer.

To launch 250 µm microspheres a special design of launchpad was used with a pre-cut flyer disk of size 500 µm. Figure 4 (a) and (b) show a comparison between 50 µm and 75 µm thickness of aluminum flyer disk with

ablation of 680 mJ. The 75 μm aluminum flyer provides enough stiffness and increase in projectile velocities are observed until 680 mJ ablation as shown in Figure 4(c).

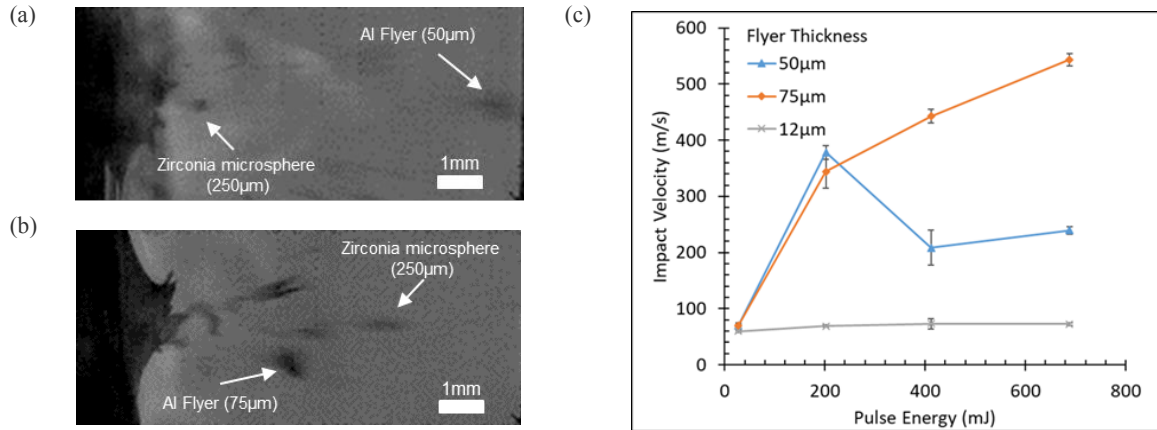


Figure 4: 250 μm Zirconia microsphere launch at 680mJ using (a) 50 μm and (b) 75 μm flyer thickness. (c) Velocity – Power calibration for different thicknesses of flyer disk.

The particle launch system with 250 μm zirconia microspheres and 75 μm aluminum layer was used to induce shock in Hydroxyl-terminated polybutadiene (HTPB) samples with impact velocities of  $543.52 \pm 6.74$  m/s. The impact behavior of HTPB due to impact was recorded using high speed camera with frame rate of 900 kHz. Figure 5 shows the impact history where microsphere completely goes inside the sample during the impact. The strain rate due to impact is given by [4]

$$\dot{\epsilon} = \frac{V}{h} \quad (1)$$

Where V is the impact velocity and h is the depth during the impact. It can be inferred that the strain rate during the impact is of the order  $10^6$  s<sup>-1</sup>.

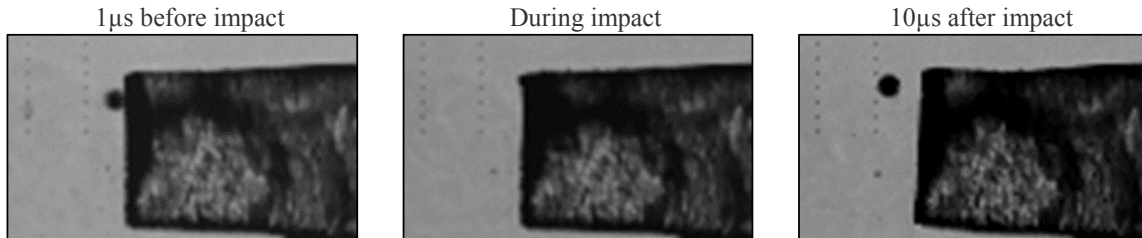


Figure 5: Micro-particle impact on HTPB at 543m/s.

The Raman spectrum were collected at different time delays between 1064 nm ablation laser and 532 nm Raman spectroscopy laser in succession of 100ns. The Raman spectrum was acquired over gate width on 50 ns and cumulative spectra were obtained from 40 impacts at every time delay. Figure 6(a) shows Raman spectra of HTPB for CH<sub>2</sub> stretching and peak fitting using Gaussian curve for 2915.45 cm<sup>-1</sup> peaks corresponding to CH<sub>2</sub> stretching accumulated over 40 impacts. The change in the Raman shift due to stress follows the linear correlation given by [7]:

$$\sigma = C \Delta w \quad (1)$$

where  $\Delta w$  is the shift in wavenumber due to loading and C is a correlation factor at a particular strain rate and gate width.

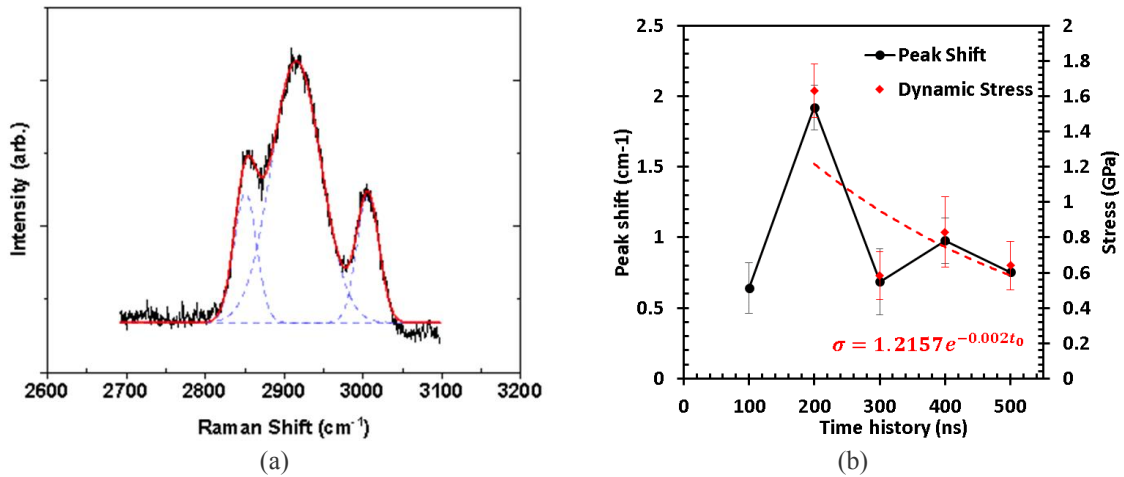


Figure 6: (a) Raman spectra of HTPB collected over 40 accumulations and fitted with Gaussian peaks (b) Raman peak shift and dynamic stress evolution over impact time history.

The analytical solution for 1D longitudinal stress propagation in a rod due to spherical ball impact is given by [8, 9]:

$$\sigma_{\max} = \rho U_s u_{p_{\max}} \quad (2)$$

Using equations (1) and (2), the Raman shift due to  $543.52 \pm 6.74$  m/s impact using 250  $\mu\text{m}$  microsphere can be calibrated as

$$\sigma = 0.85 \Delta w [\text{GPa}] \quad (3)$$

Figure 6(b) shows the change in Raman peak due to shock loading which lasts for microseconds. Similar results have been observed by [10-12]. Based on the Raman shift at different impact time history, the stress evolution after the impact is given by exponential fitting as where  $t_0$  is the time after impact:

$$\sigma(t) = 1.257 e^{-0.002t_0} [\text{GPa}] \quad (4)$$

The future work will include calibration of dynamic stress and Raman shift to particle velocity using photon Doppler velocimetry (PDV). The use of PDV will facilitate the more accurate calibration of dynamic stress based on the particle velocity history during and after the impact. This state of the art technique will be used to evaluate interaction of stress wave in composite materials where interface behaviour has significant role in failure mechanism.

#### 4. Conclusion

In this work, the stress evolution due to shock-induced by microparticle impact on Hydroxyl-terminated polybutadiene was characterized using time-gated Raman spectroscopy. The current works provide further opportunities to evaluate stress using Raman shift under different loading scenarios. Future work will involve increasing the impact velocities for bigger size microspheres and integrating Photon Doppler Velocimetry system to obtain time-resolved deformation on the sample.

#### Funding Statement

The authors gratefully acknowledge the financial support from the Air Force Office of Scientific Research, Dynamic Materials and Interactions program (Grant No.: FA9550-19-1-0318, Program Manager: Dr. Martin Schmidt).

**References:**

1. Ruan, D., M.A. Kariem, and I.G. Crouch 2017. "High strain rate and specialised testing." Woodhead Publ Mater: 581-637 (10.1016/B978-0-08-100704-4.00010-4).
2. Dieing, T., O. Hollricher, and J. Toporski, *Confocal Raman microscopy*. Springer series in optical sciences, 2010, Heidelberg Germany ; New York: Springer. xv, 289 p.
3. Johnson, Q., L. Evans, and A.C. Mitchell 1972. "X-Ray-Diffraction Study of Single-Crystals Undergoing Shock-Wave Compression." Appl Phys Lett **21**(1): 29-& (Doi 10.1063/1.1654205).
4. Prakash, C., I.E. Gunduz, and V. Tomar 2019. "Simulation guided experimental interface shock viscosity measurement in an energetic material." Model Simul Mater Sc **27**(8) (Artn 08500310.1088/1361-651x/Ab4148).
5. Gan, M., V. Samvedi, and V. Tomar 2015. "Raman Spectroscopy-Based Investigation of Thermal Conductivity of Stressed Silicon Microcantilevers." J Thermophys Heat Tr **29**(4): 845-857 (10.2514/1.T4491).
6. Gan, M. and V. Tomar 2014. "An in situ platform for the investigation of Raman shift in micro-scale silicon structures as a function of mechanical stress and temperature increase." Review of scientific Instruments **85**(1) (Artn 01390210.1063/1.4861201).
7. Prakash, C., et al. 2018. "Effect of interface chemistry and strain rate on particle-matrix delamination in an energetic material." Eng Fract Mech **191**: 46-64 (10.1016/j.engfracmech.2018.01.010).
8. Millett, J.C.F., N.K. Bourne, and J. Akhavan 2004. "The response of hydroxy-terminated polybutadiene to one-dimensional shock loading." J Appl Phys **95**(9): 4722-4727 (10.1063/1.1689758).
9. Akhondizadeh, M. 2018. "Analytical solution of the longitudinal wave propagation due to the single impact." J Low Freq Noise V A **37**(4): 849-858 (10.1177/1461348418793122).
10. Hebert, P., et al. 2012. "Raman Spectroscopy Study of Laser-Shocked Tatb-Based Explosives." Shock Compression of Condensed Matter - 2011, Pts 1 and 2 **1426** (10.1063/1.3686587).
11. Rastogi, V., et al. 2017. "Time-resolved Raman spectroscopy of polystyrene under laser driven shock compression." Journal of Raman spectroscopy **48**(7): 1007-1012 (10.1002/jrs.5166).
12. Tang, C., et al. 2019. "Characterization of laser-driven shock compression by time-resolved Raman spectroscopy." Phys Scripta **94**(1) (Artn 01540110.1088/1402-4806.Aae1e).

# Modelling of behavior of aluminum 7020-T651 under dynamic loadings

Teresa Fras

*French-German Research Institute of Saint-Louis (ISL), 5 rue du General Cassagnou, 68301 Saint-Louis, France*

**Abstract:** The stress–strain behavior of the rolled AA7020 aluminum tempered in T651 conditions is studied at various strain rates and temperatures. Basing on tensile, shear and compression tests, the effects of strain and strain-rate hardening, thermal softening and plastic anisotropy are discussed. The parameters of the thermo-viscoplastic flow and fracture models proposed by Johnson and Cook are identified and validated basing on the numerical modeling. The obtained constitutive relations may be applied to model more complex states of stresses resulted from different loading conditions, like in particular impact events.

**Keywords:** AA7020-T651, ballistic impacts, perforation modelling, flow and fracture models, metals under dynamic loadings, numerical simulation of metal deformation

---

## Introduction

Metals, in particular aluminum alloys, are important components in the automotive, avionic and civil industry. The weight optimization leads to applications of lighter components of reduced volumes which may increase probability of their fracture. As virtual prototyping allows for the optimization of used materials, time and costs; design process is often based on numerical modeling. A proper numerical prototype requires material models based on careful identification of involved coefficients. To obtain highly accurate modeling, there is a need for experimental data concerning the quasi-static and dynamic behavior of materials and for their mathematical models.

Thermo-mechanical behavior of metals can be described by different constitutive models, which can be generally divided into three groups: physically-based, semi-physical and empirical. Physically-based constitutive models allow for describing not only the macroscopic behavior of the material but also the changes in the microstructure during the process of plastic deformation. In such constitutive relations, certain internal variables related to the microstructure are involved to describe a deformation of FCC, BCC or HC microstructures. The most popular example of the physically based approach is the model proposed by Zerilli and Armstrong (1987). Other exemplary propositions can be attributed to Voyiadjis and Abed (2005) or to Rusinek and Klepaczko (2001). These models are based on the theory of dislocation; they account for the coupling between the temperature and strain rate and a modest number of parameters is required for their determination. Another approach is based on phenomenological observations of material deformation. The most popular flow and fracture model was proposed by Johnson and Cook (1983), (1985). This relation is a particular type of the von Mises plasticity with analytical forms of the hardening law and rate dependence. The functions accounts for the strain and strain rate hardening, as well as for thermal softening of the described metal. Despite several criticisms, as the parameters of the JC models cannot be physically proven, the models are implemented in most computer codes and numbers of successful applications stay in their favor.

The study is based on results discussed in details in Fras et al. (2015 and b) and presents the behavior of the rolled AA7020-T651 aluminum at a various range of strain rates and temperatures. In order to understand the mechanisms occurring in a material subjected to complex loadings, it is necessary to know its mechanical properties and conditions leading to failure. The determined models constants may be useful for an evaluation and development of lightweight and cost-effective structures.

## Material description

The AA7020-T651 belongs to a group of Aluminum Zinc Magnesium ternary alloys. The major alloying element in 7xxx series is Zinc, Magnesium and a reduced percentage of other elements are added to obtain a higher strength. Higher strength 7xxx aluminum alloys exhibit reduced resistance to stress corrosion (due to a Zink addition) and are often utilized in a slightly overage temper to provide better combinations of strength and fracture toughness (Cobden and Banbury 1994; Hatch 2000; Kumar and Nambodhiri 2011; Embury and Nicholson 1965). 7xxx series alloys are

\* Teresa Fras (teresa.fras@isl.eu).

† French-German Research Institute of Saint-Louis (ISL) France

used in airframe structures, mobile equipment, aerospace applications, railway coach bodies, containers and building constructions, and other highly-stressed parts. The investigated aluminum alloy was delivered as rolled plates, tempered and aged in T651 conditions (defined in European Standard NF EN 515). Due to the thermo-mechanical treatment of the AA7020-T651, the microstructure of the alloy consists of grains with a high density of fine hardening precipitates formed during artificial aging and grains with a lower density of larger particles not affected by the thermal treatment, which are characterized by much lower strength. The hardness and mechanical resistance of the Al-Zn-Mg alloys depend mainly on precipitates formed during quenching of the material or due to the aging treatment. The inhomogeneous microstructure results in local variations of the properties. In the areas of lower, precipitation-free density, strain localization occurs causing fracture initiation, crack growth, intergranular cracking, delamination, etc. (Kumar and Nambodhiri 2011; Embury and Nicholson 1965).

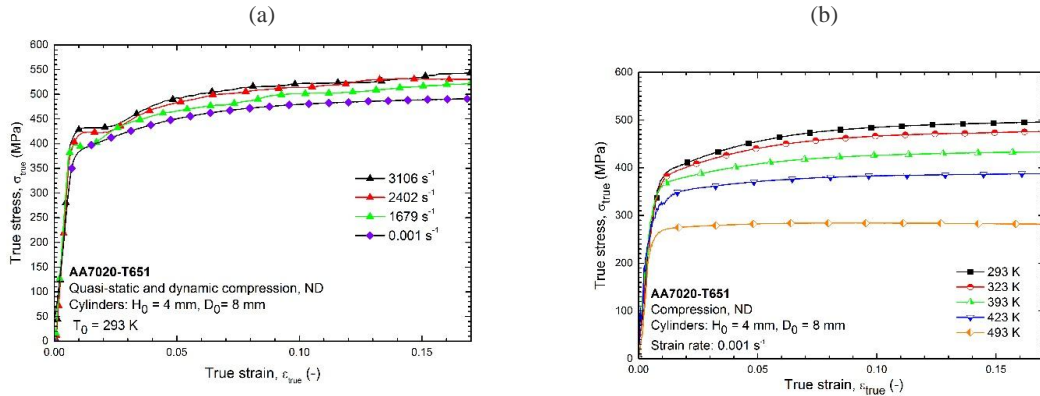


Figure 1: (a) True stress vs. true strain curves resulting from quasi-static and SHPB compression tests. (b) True stress vs. true strain curves at various temperatures.

The number of different tests and types of loading modes that are required for material model calibration is dependent on the required accuracy of the chosen material model. In the present study, the parameters of the Johnson Cook models are determined. To investigate the behavior of AA7020-T651, several tests were performed under various loading conditions in a quasi-static and dynamic range of strain rates. To eliminate the effect of sample geometry, the material response is given by the true strain – true stress relations. For all curves resulted from compression and tension, the Young modulus is found to be 70 GPa.

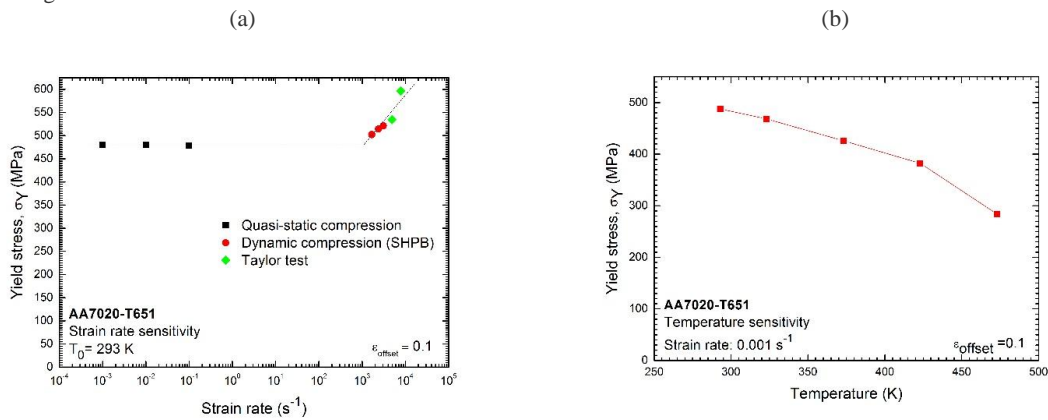


Figure 2: (a) Strain rate sensitivity and (b) temperature sensitivity of AA7020-T651.

To perform compressive tests, cylindrical specimens of 4 mm height and 8 mm diameter are used. The specimens are compressed in the direction normal to the rolling direction (i.e. the ‘through-thickness’ direction). Samples are placed between two hardened steel plates; a graphite lubricant is used at the interfaces to minimize the effect of friction (Fras et al. 2014). The results of the compression test performed at various strain rates are given in Fig. 1(a). The results of a dynamic compression test are obtained using the technique of the split-Hopkinson pressure bar. Each curve is an average curve resulting from 3 tests for an imposed strain rate and temperature. Comparison between curves, resulting from quasi-static and dynamic compression tests, indicates that the investigated Al alloy is moderately rate-sensitive. This observation is common for most of 7xxx Al alloys, e.g. AA7003 or AA7108 (Chen et al. 2009). Fig. 1(b) shows the stress-strain curves of AA7020-T651 compressed at the strain rate of  $0.001 \text{ s}^{-1}$  for different temperatures. A decreasing trend of the yield stress versus increasing temperature is observed. Such a property has been also noticed for other 7xxx

Al alloys, e.g. AA7075-T651, AA7075-T6 (Brar and Joshi 2009). In Fig. 2, the effect of the strain rate for AA7020-T651 is shown as a function of the yield stresses, determined for an offset strain equal to 0.1 and for the strain rate given in a logarithmic scale.

Basing on the summarized results, it can be noticed that the material is not much sensitive to the rate of compressive loading. Additionally, the data presented in Fig. 2(a) are completed by the results of the Taylor impact test. The results of the Taylor impact test allow us to observe the behavior of AA7020-T651 for strain rates greater than  $10^4 \text{ s}^{-1}$ . Low strain rates have a minor influence on the flow stress and the stress is a linear function of strain rates. After the point of transition, which in the case of the discussed material occurs for a strain rate close to  $1500 \text{ s}^{-1}$ , the strain rate sensitivity increases rapidly and the slope change becomes positive and much more pronounced. Such a property is characteristic also for other Al alloys, e.g. AA7075-T651, AA7075-T6 (Brar and Joshi 2009), AA2024-T3 (Rusinek and Rodriguez-Martinez 2009). Fig. 2(b) presents the yield strengths for a fixed offset strain,  $\epsilon_{\text{offset}} = 0.1$ , determined at different temperatures.

Increasing the temperature leads to a decrease of stress values when the loading is quasi-static. This effect is stronger at higher temperatures. A reduction in the flow stress is more distinct when the temperature increases from 373 K to 473 K; while, for lower temperatures, the flow stress decrease is less significant.

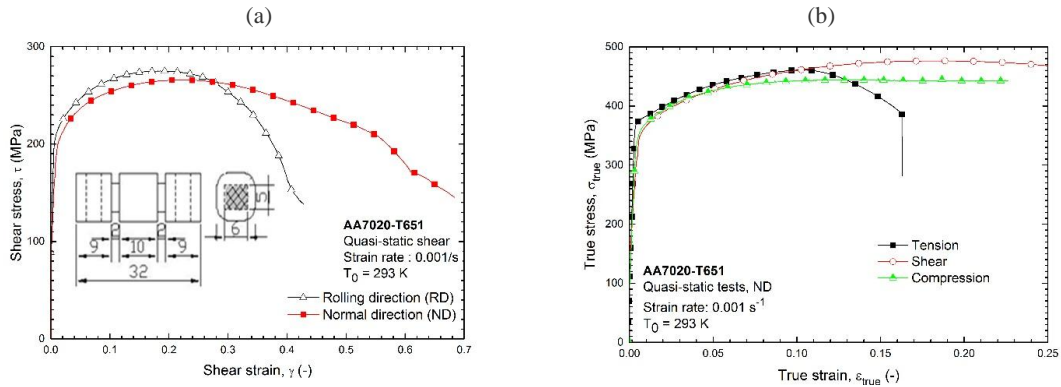


**Figure 3: (a) Results of the double shear tests carried out in the directions parallel and normal to the rolling direction. (b) Comparison of curves obtained from the quasi-static compression, tension and shear tests when loading is applied in the normal direction.**

As shear deformation is often a result of material failure, for the tested alloy shear tests have been performed. The tests are carried out using modified double shear specimens (MDS). The dimensions of the shear zones are  $6 \times 5 \text{ mm}$ , Fig. 3(a). Shear tests are performed in the rolling direction and the direction normal to it, in a quasi-static strain rate. Regarding the values of yield strength in shear, they do not vary much depending on the direction of loading. However, for the tests performed in the rolling direction, shear fracture occurs when the shear strain is equal to 0.4. Whereas, for the tests performed in the normal direction, a more ductile fracture mode takes place, shear strain is larger than in the case of loading in the normal direction and it is equal to 0.7. The ductility of AA7020-T651 is dependent on the direction of loading, which is a property also reported for other rolled Al alloys, e.g. AA7030 (Pedersen et al. 2004). The ductility depends on the material orientation resulting from a rolled texture, as the void shapes (which nucleation results in a crack occurrence) vary with a material orientation.

A comparison of the curves obtained from the quasi-static compression, tension and shear (multiplied, according to the Huber–Mises theory, by the square root of 3) is given in Fig. 3(b). One can observe that the strength differential effect is not characteristic for AA7020-T651, neither a deviation of yield strength in shear from a value anticipated due to the Huber–Mises theory.

Deformation of a ductile material involves an increase of the dislocation density, arrangement in pile-ups, then, the nucleation and growth of internal voids until the final failure. Initiation of a damage results from micro-defects or micro-stress concentrations provoking decohesion and subsequently nucleation, growth and coalescence of micro-cracks and micro-voids. According to the Bridgman (1952) theory, the damage evolution is strongly influenced by the hydrostatic stress state. The plastic flow is driven by the deviatoric stress state in the material (Bridgman 1952). The triaxiality shows the influences of an amount of plastic strain which a material may undergo before a ductile failure occurs. As the stress triaxiality is a ratio of the hydrostatic stress,  $\sigma_m$ , and the effective stress,  $\sigma_{\text{eq}}$ , defined as  $\sigma^* = \sigma_m / \sigma_{\text{eq}}$ , it is used to describe a material deformation (Rice and Tracey 1969, O’Dowd and Fong Shih 1991).

The dependence between the triaxiality and fracture strain is investigated for AA7020-T651. Experimental data are collected from quasi-static tensile tests performed by using the notched specimens as adding a notch in the geometry of a tensile specimen increases the stress level and reduces the strain to fracture. The induced stress triaxiality increases with decreasing notch radius; it leads to a reduced ductility of tested specimens and to fracture.

(a) (b) (c)

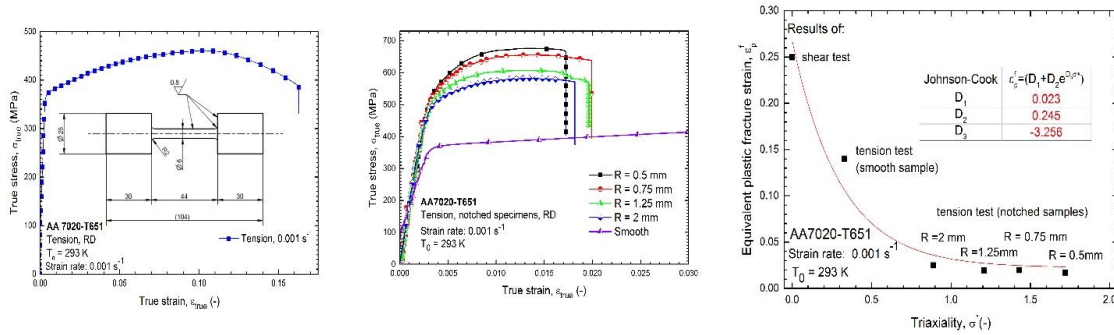


**Figure 4: True stress – true strain curves resulting from the quasi-static, uniaxial tension test performed in the rolling direction using (a) smooth and (b) notched specimens. (c) Fracture strain versus stress triaxiality for the quasi-static tensile tests at room temperature.**

In Fig. 4(a), a representative curve shows the result of the tension test performed in the rolling direction with a quasi-static strain rate equal to  $0.001 \text{ s}^{-1}$ . The specimens have a classical bulk ‘dog-bone’ shape (a sample diameter equal to 6 mm and a ‘reduced’ section of 40 mm) as defined in ASTM E8/E8M-11 ‘Standard test methods for tension testing of metallic materials’. The yield stress and tensile strength are equal to 385 MPa and 460 MPa, respectively. To obtain different values of the triaxiality factor, the notched samples have been used with a notch radius equal to 2 mm, 1.25 mm, 0.75 mm and 0.5 mm, cut in the central part of a smooth sample, Fig. 4(b). Each of presented tensile curves is an average of 5 tests. They are compared with the tension of a smooth specimen. Tensile loading is applied in the rolling direction of the plate. Fig. 4(c) presents the average fracture strain as a function of the initial stress triaxiality at room temperature. The equivalent plastic fracture strain is calculated as  $\ln(A_0/A_f)$ , where  $A_0$  is the initial cross-section area of a sample in the notched zone and  $A_f$  is the cross-section area after fracture. In Fig. 4(c), it is noticed that the fracture strain depends considerably on the stress triaxiality; it is reduced for increasing stress triaxiality. As it was observed by Bao and Wierzbicki (2004), at high stress triaxiality, the final rupture is caused by the internal void nucleation mechanism. The high plastic strain level promotes a nucleation of voids, inclusions by particle cracking or interface decohesion. If the specimen is subjected to a shear-dominated stress state, then the failure mode is characterized by shallow, small and elongated shear dimples, which are oriented along the shear direction. This rupture mode involves internal shearing between voids and is favored at the lower stress triaxiality values.

### Flow and fracture models

The Johnson and Cook flow model is relatively easy to calibrate – the individual expressions in the three sets of brackets represent the strain hardening, strain rate hardening and thermal softening, and can be calibrated separately using experimental data presented as stress-strain curves at different strain rates and temperatures. It should be remembered, however, that despite its success and simplicity, the JC model does not present a good understanding of the materials’ mechanical behavior as the model parameters cannot be physically proven. The strain rate effect on material strength is not a linear function (of the natural logarithmic function) but rather an exponential function – which is not taken into account in the JC model. Coupling between strain rate and temperature is not included, either.

To describe the various phenomena taking place during dynamic loadings, it is necessary to account for the material stress-strain response at large strains but also for the accumulation of damage and the mode of failure in the structure, Eq. (1).

$$\sigma_{eq}(\varepsilon, \dot{\varepsilon}, T) = (1 - D)\sigma(\varepsilon, \dot{\varepsilon}, T) \quad (1)$$

where  $D$  is the damage variable and if  $D = 0$ , there is no coupling between damage and the constitutive equation. The discussed model is the modified formulation of the classical JC model (Johnson and Cook 1983, 1985) which was implemented in Ls-Dyna by Borvik et al. (2001) to avoid numerical instabilities when strain rates are lower than 1.

$$\sigma(\varepsilon, \dot{\varepsilon}, T) = \left[ A + B\varepsilon^n \right] \left[ 1 + \frac{\dot{\varepsilon}}{\dot{\varepsilon}_{ref}} \right]^C \left[ 1 - \left( \frac{T - T_0}{T_m - T_0} \right)^m \right] \quad (2)$$

where  $A$ ,  $B$ ,  $C$ ,  $m$ ,  $n$  are material constants and  $T_0$ ,  $T_m$  are the initial and melting temperature and  $\dot{\varepsilon}_{ref}$  is a user-defined reference strain rate.

The damage evolution is described by the damage variable  $D$ , representing the surface density of intersections of micro-cracks and micro-cavities for any plane in the body,  $D = 0$ , for a material in an initial state of loading and for a material which is fully broken,  $D = 1$ , (Berstad et al. 1994). The evolution of damage is related to irreversible strains;

therefore, it may be taken as a function of the accumulated plastic strains. The damage starts to evolve at a threshold of the accumulated plastic strain. In the Johnson and Cook (1985) fracture model the damage evolution is defined as:

$$\mathcal{D} = \frac{\mathcal{E}}{\varepsilon_f} \quad (3)$$

where  $\varepsilon_f = \varepsilon_f(\sigma^*, \mathcal{E}, T)$  is the actual value of the fracture strain depending on stress triaxiality, strain-rate and temperature.

(a)				(b)	
A [MPa]	300	D <sub>1</sub>	0.011	$\rho$ [kg/m <sup>3</sup> ]	2770
B [MPa]	260	D <sub>2</sub>	0.42	E [GPa]	71
n	1.65	D <sub>3</sub>	-3.26	$\nu$ [-]	0.3
C	0.0009	D <sub>4</sub>	Literature	C <sub>p</sub> [J/kg.K]	910
m	1.26	D <sub>5</sub>	Literature	Hardness	133 HV $\pm$ 2

**Table 1: (a) The parameters of the JC models, Eqs. (2, 5), for AA7020-T651, and (b) some its physical properties.**

The modified expression of the Johnson and Cook fracture strain is given in Eq. (5). The damage evolution during plastic straining is given by Eq. (4), (Bammann et al. (1993)), and  $D_C$  is the critical damage,  $p_d$  is the damage threshold (in the discussed case, it is assumed that  $p_d = 0$  and  $D_C = 1$ ).

$$\mathcal{D} = \begin{cases} 0 & \text{when } \varepsilon \leq p_d \\ \frac{D_c}{\varepsilon_f - p_d} \mathcal{E} & \text{when } \varepsilon > p_d \end{cases} \quad (4)$$

and

$$\varepsilon_f(\sigma^*, \mathcal{E}, T) = [D_1 + D_2 e^{D_3 \sigma^*}] \left[ 1 + \frac{\mathcal{E}}{\mathcal{E}_{ref}} \right]^{D_4} \left[ 1 + D_5 \frac{T - T_0}{T_m - T_0} \right] \quad (5)$$

where  $D_1 - D_5$  are fracture model constants.

The constitutive relation and function describing the fracture Eqs. (1-5) are implemented in LS-DYNA as \*MAT\_107, i.e. \*MAT\_MODIFIED\_JOHNSON\_COOK. The detailed, theoretical considerations regarding this formulation are described by Borvik et al. (2001).

In Table 1, there is given a set of parameters of the JC model, Eq. (2), describing AA7020-T651. It is determined on the basis of the compression tests in the ‘through-thickness’ direction performed with various strain rates and temperatures. The parameters are determined by best fits to the experimental data using the method of least squares.  $D_4$  and  $D_5$  of Eq. (5) must be taken from literature, e.g. from a study of Brar and Joshi (2009) describing AA7075-T651. The physical constants of material AA7020-T651, also necessary in the numerical simulation, are based on data provided by literature, Table 2(b).

### Model validation

To verify the material model - i.e. \*MAT\_MODIFIED\_JOHNSON\_COOK, the uniaxial tensile and compression tests are simulated using the LS-DYNA explicit formulation (with a scaled mass to avoid a prolonged time of calculations). Such a model validation based on simple loading cases proves that the material model is able to reproduce a more complex material behavior. Calculations of tension tests have been performed using the axisymmetric models of ‘reduced’ sections (length of 40 mm and diameter of 6 mm) of the smooth sample (meshed by 4200 elements of size 0.3 x 0.3 mm) and of the notched samples – a finer mesh (nodes each 0.1 mm) is applied in the notched zone. The cylindrical specimen used during the uniaxial compression test, has height of 4 mm and diameter of 8 mm which is modeled by 1600 axisymmetric elements (3600 nodes located each 0.1 mm). It must be remembered also that the accuracy of FE calculations are based on the element size, the dependency between mesh size and results must be checked. If the mesh density has a minor effect on numerical results, they element size may be considered as optimal. Calculations of the compression are performed in the frictionless conditions.

The numerical model describes linear elasticity, the von Mises plasticity and initial yielding, strain hardening, strain-rate hardening, damage evolution and fracture. It is developed for an isotropic material and it includes linear thermo-elasticity, viscoplasticity and ductile damage. The material anisotropy and the material texture are not taken into account in the numerical calculations. The elastic and viscoplastic properties of the material depend on the temperature

generated by adiabatic heating under high strain-rate loading conditions, while any thermo-mechanical coupling with the surroundings is not included in the formulation. Strain hardening is described in terms of the damage accumulated plastic strains. In order to allow a crack growth during a penetration process, the model is coupled with an element-kill algorithm. As the damage variable  $D$  reaches its critical value  $D_C$ , a damaged element is removed from the mesh.

The classical metal plasticity based on the von Mises theory assumes that the pressure effect and the effect of the third deviatoric stress are not included in the yield criterion. Introduction of a geometric notch to a smooth round bar increases the hydrostatic pressure inside the neck zone during the uniaxial tensile test, like it is showed by Wilson (2002). Consequently, the numerical simulation of the tension of notched specimens may reveal a discrepancy between the flow stress curves resulted from the experiment and from the calculations if the von Mises yield criterion is used and the material is sensitive to the hydrostatic pressure. The effect of hydrostatic pressure is quantitatively described by the strength differential effect, i.e. inequality of the tensile and compressive yield strengths. However, for the described AA7020-T651, the strength differential effect is negligible which can be seen in Fig. 3(b). Consequently, the calculations with an assumption of the classical von Mises plasticity allow for the verification of the material model by means of the tensile test of a round, notched specimen.

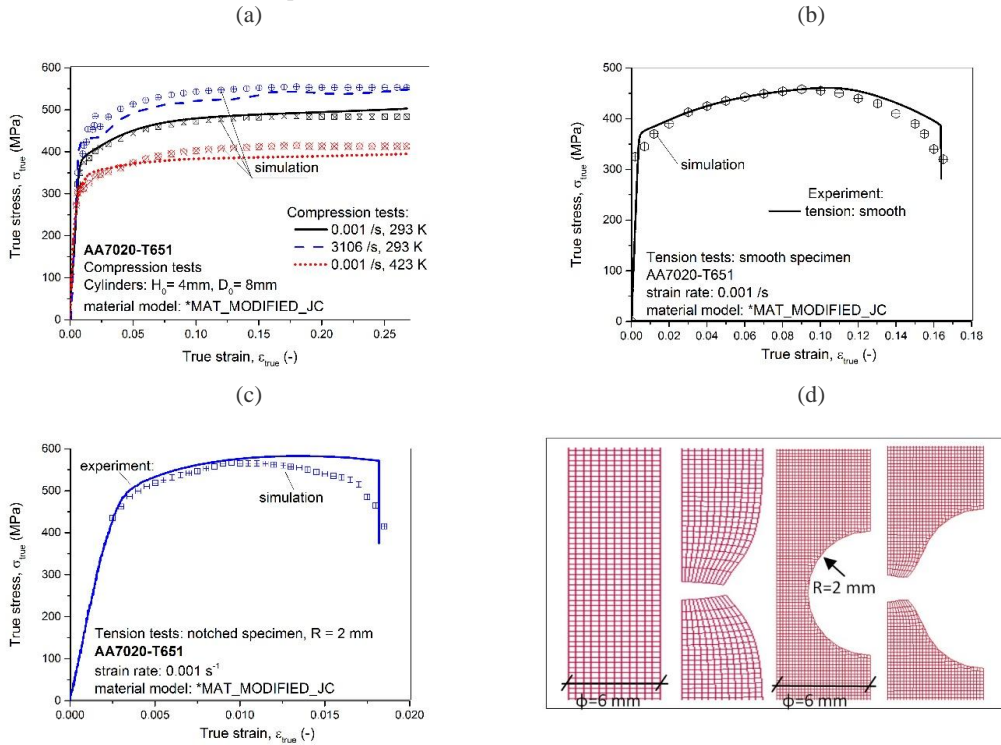


**Figure 5: Comparison between experimental and numerical curves for (a) the compression tests and the tension test for (b) the smooth sample and (c) for notched sample. (d) Details of an initial and deformed mesh of the smooth and notched specimens.**

A comparison between numerical and experimental results is presented in Fig. 5(a-d). It can be concluded that the numerical results are within the accepted accuracy when compared to the experimental curves. The material model calibration is a final step before the model parameters are input into calculations of more complex load cases, e.g. in Fras et al. (2015a, 2015b).

### Impact test

The impact tests were performed on 40mm thick plates impacted by the 20 mm-diameter fragment simulating projectiles (FSPs). A FSP of 20 mm diameter and weight of 53.8 grams represents a 155 mm artillery shell fragment. The ballistic impact test, in which these projectiles are used, is mandatory for an evaluation of protection levels 4 and 5 in the component acceptance tests, Stanag 4569. The FPSs, embedded in sabots before the launch, were accelerated up to 1500 m/s by means of a powder gun. It is observed that failure modes caused by the impacts of fragment simulating projectile depend on the projectile impact velocity, Fig. 6 The global deformation mode of a target changes from a ductile hole enlargement, through a mechanism of highly localized shear around the projectile nose, to a combination of plugging and discing (scabbing) mode. A plug is a part of a metallic material which is sheared out from a target plate by a deformed projectile. Discing leads to a material separation within same horizontal planes, parts of such planes are thrown away from a target. Such failure modes are characteristic for a ductile, anisotropic material, when texture influences a fracture

direction. The structure of rolled material is prone to be stretched and bended forward more easily over series of thin layers at the remained plate thickness resting below the projectile nose.

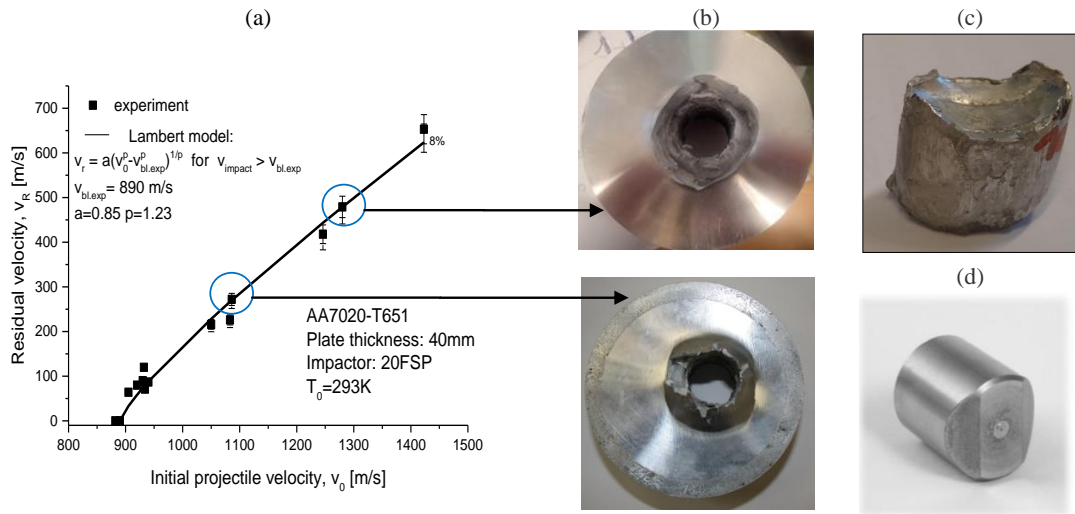


**Figure 6: (a) Ballistic curve for 40 mm thick AA7020-T651 plates impacted by 20 mm FSPs. (b) Depending on the impact velocity the plates failed due to plugging (impact velocities lower than 1100 m/s) and discing (impact velocities higher than 1200 m/s). (c) Plug. (d) Fragment-simulating projectile (FSP).**

Due to the manufacturing processes of the AA7020-T651 target plates, the microstructure of the alloy consists of grains with a high density of fine hardening precipitates formed during artificial aging and grains with a lower density of larger particles not affected by the thermal treatment, which are characterized by much lower strength. The inhomogeneous microstructure results in local variations of the properties of the Al-Zn-Mg alloys. In such areas, strain localization occurs, causing fracture initiation, intergranular cracking and delamination, Fig. 7. The materials microstructure and its rolled texture have an influence on protective properties of the material, as the discing failure mode may be observed.

The deformation of the microstructure was caused by severe shearing and extensive bending. Microstructural observations revealed that impact conditions leading to shear plugging did not cause the adiabatic transformation in the material. Adiabatic shear bands are easily recognizable under the microscope and no observations proved occurrence of this kind of distinct, etching areas. The material structure consists of heavily sheared initial microstructure but it seems that strain rates occurred in the aluminum due to the impacts were not high enough to cause a local temperature increase resulting in the adiabatic transformation.

#### Numerical simulation of the impact test

Having the material verified basing on the simpler, uniaxial cases of loading, a more complex case of the perforation and penetration processes may be simulated. A fine mesh using linear hexahedral elements of a size  $0.6 \times 0.6 \times 0.6$  mm is applied, Fig. 8. The projectile deformation is determined by the JC model \*MAT\_JOHNSON\_COOK (\*MAT\_015). The elements are eroded when the effective plastic strain at failure reaches an assumed value, in this case  $p_{fail} = 1.5$ . To reduce a number of elements, only a quarter of the configuration, Fig. 3, is modeled. The simulation is performed using 3D solid elements. Since FSPs have a non-axi-symmetrical shape, 2D modeling of a plate perforation – efficient in other cases of the impact tests, is not suitable. The 8-node constant-stress solid elements with one integration point and stiffness-based hourglass control are applied. The frame is fully clamped, the plate is in contact (\*AUTOMATIC\_SURFACE\_TO\_SURFACE) with the frame and an initial velocity is applied to the projectile. Contact between the target and projectile is modeled using an eroding surface-to surface algorithm (\*ERODING\_SURFACE\_TO\_SURFACE). Friction between parts is not accounted for. The target mesh is gradually finer to the centre of a plate – as it is an expected perforation zone. The target model results in about 300000 elements, the mesh of a projectile contains of 28000 elements, whereas the frame consists of 2500 elements of size  $1.5 \times 1.5 \times 1.5$  mm. To minimize the mesh dependency of the results, the function \*MAT\_NONLOCAL, implemented in LS-DYNA, is used with the parameter values suggested by User Manual,  $p=8$  and  $q=2$ .

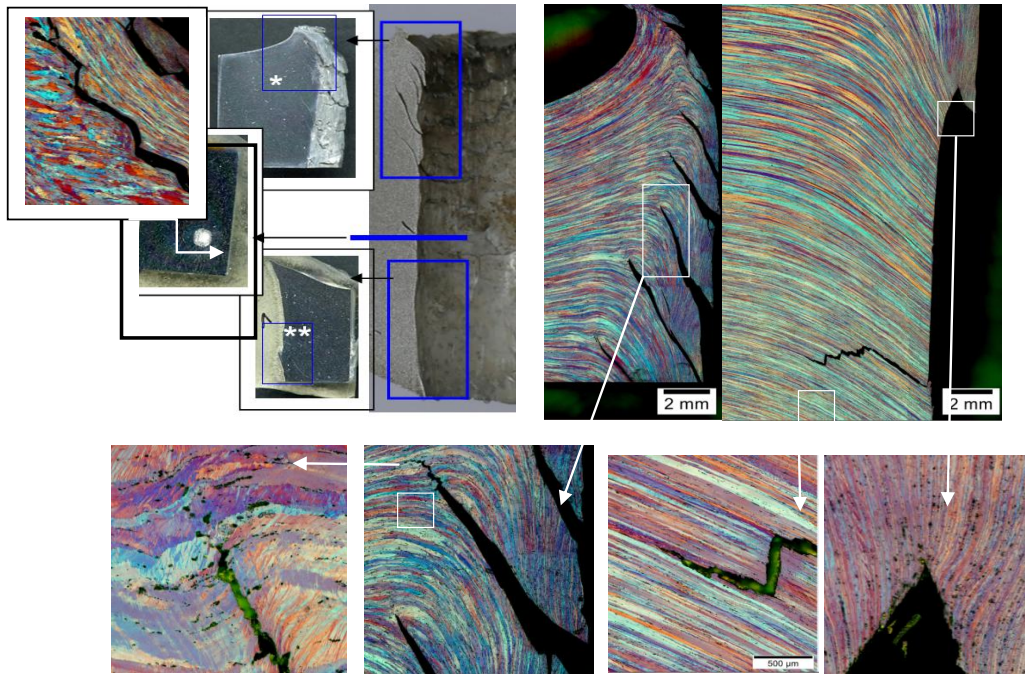


Figure 7: Optical micrographs of AA7020-T651 impacted by a FSP at the impact velocity 1100 m/s.

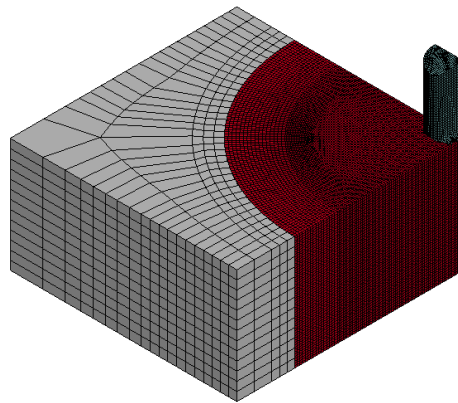


Figure 8: Numerical configuration.

The parameters of the plasticity and fracture model are given in Table 1.  $D_1$ - $D_3$  are obtained from our own experimental results described above; whereas, the values  $D_4$  -  $D_5$  are chosen from a set of parameters describing the fracture of an alloy AA7075- T651, belonging to the same series of Al alloys, i.e. 7xxx, (Brar and Joshi (2009)), in that case  $D_4$  equals 0.016. The set of parameters used in simulations allows the result which model the discing failure at impact velocity of 1300 m/s. Although, a discing failure mode is described correctly, the used set of the material parameters does not allow the plugging failure mode to be obtained, its shape is incorrect. Consequently, the parameter  $D_4$  value is taken from Clausen et al. (2004). That paper discusses the properties of an alloy AA5083-H116 under impacts showing the plugging modelling. By using the fracture model, in which the  $D_4$  is equal to 0.15, it is possible to obtain a plug of a shape and mass close to the experimental one also in the case of the 40 mm thick AA7020-T651 plates, Fig. 9a.

Two different failure modes observed experimentally are obtained by varying one parameter  $D_4$  (influence of the strain rate) of the function describing the fracture strain, Eq. (5). In the first case, when  $D_4 = 0.016$ , the discing failure mode is obtained; in the second case, when  $D_4 = 0.15$ , the complete plug separation is observed.

(a)

(b)

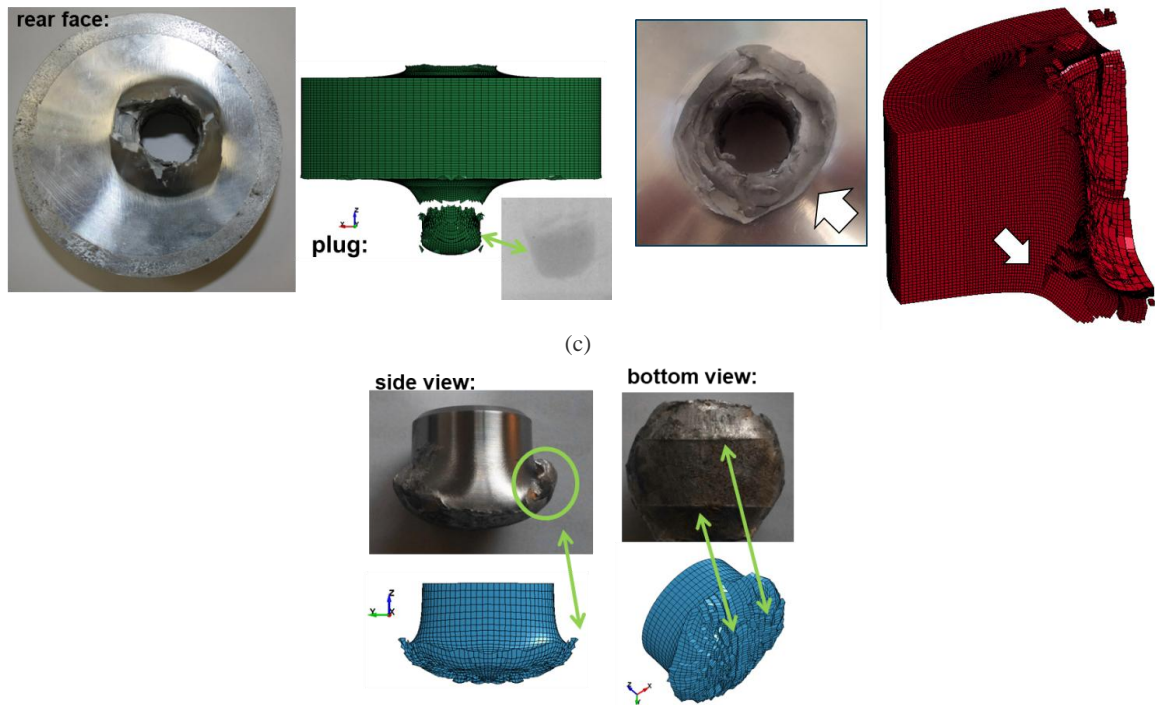


**Figure 9: Modelling of: (a) plugging, (b) discing target failure modes and (c) FSP deformation.**

In the case of AA7020-T651, the parameter  $D_4$  has a large influence on the calculated fracture strain. Changes of the  $D_4$  parameter result in distinctly different values of fracture strain. Consequently, the way of the damage accumulation differs (via a direct dependency between  $D_c$  and  $\epsilon_f$ ) which leads to changes in the calculation of the resulting failure mode. The strain evolution leading to a final failure of a target plate depends on many factors (like geometry, strain accumulation, mesh erosion, etc.). A change of one parameter influences the whole way of a fracture initiation and its propagation in the calculations.

### Conclusions

The mechanical and micro-structural properties of AA7020-T651 have been identified and described. Based on the material tests, the constitutive relation and the fracture criterion – the Johnson and Cook models have been determined. The flow and fracture models are implemented in \*MAT\_107 of the Ls-Dyna explicit Lagrangian code. The models describe the material flow and fracture behavior as a function of the strain rate and temperature and it accounts for the damage accumulation in a deforming material. The models have been validated basing on the uniaxial stress modes with a sufficient agreement with the experiment results. Such prepared constitutive relations may be applied in calculations of complex loading modes. Properly determined, calibrated and validated material models are a basis for reliable predictions of materials behavior.

The observed failure modes during the impact tests of 40 mm thick AA7020-T651 plates varies between plugging and discing, which occur in the material due to a combination of shear and bending stresses. In the case of the impact velocities lower than 1100 m/s, the targets fail due to shear plugging. With the increasing impact velocity, a discing failure is observed, in which the structure of rolled material is prone to be stretched and bended forward more easily over series of thin layers at the remained plate thickness resting below the projectile nose. Large target material parts are thrown away from the rear surface of targets.

Based on the performed ballistic tests, a numerical model using the Lagrangian approach implemented in LS-DYNA is introduced, which results in the acceptable modeling of the target response. The transformation of the material failure from discing to plugging is realized however by using different parameters  $D_4$  and  $D_5$  for the Johnson – Cook fracture model. Linking a killing-element algorithm to the fracture strain function, results in a strong sensitivity to changes of the function's parameters, which allows for a numerical modelling of two different target failure modes.

## References

- Bammann, D.J., Chiesa, M.L., Horstemeyer, M.F., and Weingarten, L.I. (1993) Failure in ductile materials using finite-element simulations, in: Jones N, Wierzbicki T, editors. *Structural crashworthiness and failure*. Amsterdam: Elsevier, pp. 1-54
- Bao, Y., and Wierzbicki, T. (2004) On fracture locus in the equivalent strain and stress triaxiality space, *Int J Mech Sci*, Vol. 46, No. 1, pp. 81-98.
- Berstad, T., Hopperstad, O.S., and Langseth, M. (1994) Elasto-viscoplastic constitutive models in the explicit finite-element code LS-DYNA 3D, in: *Proceed 2nd Int LS-DYNA 3D Conf*. San Francisco.
- Borvik, T., Hopperstad, O.S., Berstad, T., and Langseth, M. (2001) A computational model of viscoplasticity and ductile damage for impact and penetration, *Eur J Mech A/Solids*, Vol. 20, No. 5, pp. 685-712.
- Brar, N.S., Joshi, V.S., and Harris, B.W. (2009) Constitutive model constants for Al7075-T651 and Al7075-T6, In: *Shock Compression of Condensed Matter. AIP Conf Proc*, Vol. 1195, No.1, pp.945-948.
- Bridgman, P.W. (1952) *Studies in large plastic flow and fracture with special emphasis on the effects of hydrostatic pressure* 1st ed., New York: McGraw-Hill.
- Clausen, A.H., Børvik, T., Hopperstad, O.S., Benallal, A. (2004) Flow and fracture characteristics of aluminium alloy AA5083-H116 as function of strain rate, temperature and triaxiality. *Mat Sci Eng A*, Vol. 364, No. 1, pp. 260-272.
- Chen, Y., Clausen, A.H., Hopperstad, O.S., and Langseth, M. (2009) Stress-strain behaviour of aluminium alloys at a wide range of strain rates, *Int J Solids Struct*, Vol. 46, No. 21, pp. 3825-3835.
- Cobden, R., and Banbury, A. (1994) Aluminium: physical properties, characteristics and alloys, *Talat lectures*, pp. 19-26
- Fras, T., Rusinek, A., Pecherski, R.B., Bernier, R., and Jankowiak, T. (2014) Analysis of friction influence on material deformation under biaxial compression state, *Tribol Int*, No. 80, pp. 14-24.
- Fras, T., Colard, L., Lach, E., Rusinek, A., and Reck, B. (2015) Thick AA7020-T651 plates under ballistic impact of fragment-simulating projectiles, *Int J Impact Eng*, No. 86, pp. 336-353.
- Fras, T., L. Colard, and Pawlowski, P. (2015) Perforation of aluminum plates by fragment simulating projectiles (FSP), *Int J Multiphysics*, Vol.9, No. 3, pp. 267-286.
- Hatch, J.E. (2000) Aluminum: properties and physical metallurgy, *Metals Park, OH: American Society for Metals*.
- Johnson, G.R., and Cook, W.H. (1983) A constitutive model and data for metals subjected to large strains, high strain rates and high temperatures., in: *Proceed 7th Int Symp on Ballistics IBS*. The Hague, pp. 541-547.
- Johnson, G.R., and Cook, W.H. (1985) Fracture characteristics of three metals subjected to various strains, strain rates, temperatures and pressures, *Eng Fract Mech*, Vol. 21, No. 1, pp. 31-48.
- Kumar, S., and Nambodhiri, T.K.G. (2011) Precipitation hardening and hydrogen embrittlement of aluminum alloy AA7020, *Bull Mater Sci*, Vol. 34, No. 2, pp. 311-321.
- Rusinek, A., and Klepaczko, J.R. (2001) Shear testing of a sheet steel at wide range of strain rates and a constitutive relation with strain-rate and temperature dependence of the flow stress, *Int J Plast*, Vol. 17, No. 1, pp. 87-115.
- Rusinek, A., and Rodriguez-Martinez, J.M. (2009) Thermo-viscoplastic constitutive relation for aluminium alloys, modeling of negative strain rate sensitivity and viscous drag effects, *Mater Des*, Vol. 30, No. 10, pp. 4377-4390.
- Pedersen, K.O., Roven, H.J., Lademo, O.G., and Hopperstad, O.S. (2004) Strength and ductility of aluminum alloy AA7030, *Mat Sci Eng A*, Vol. 473, No. 1, pp. 81-89.
- Rice, J.R., and Tracey, D.M. (1969) On the ductile enlargement of voids in triaxial stress fields, *J Mech Phys Solids*, No. 17, pp. 201-217.
- O'Dowd, N.P. and Fong Shih, C. (1991) Family of crack-tip fields characterized by a triaxiality parameter – I. Structure of fields, *J Mech Phys Solids*, Vol. 39, No. 8, pp. 989-1015.
- Wilson, C.D. (2002) A critical reexamination of classical metal plasticity, *J Appl Mech – T ASME*, Vol. 69, No. 1, pp.63-68.
- Voyiadjis, G.Z., and Abed, F.H. (2005) Microstructural based models for BCC and FCC metals with temperature and strain rate dependency, *Mech Mater*, Vol.37, No. 2, pp. 355-378.
- Zerilli, F.J., and Armstrong, R.W. (1987) Dislocation-mechanics-based constitutive relations for material dynamics calculations, *J Appl Phys*, Vol. 61, No. 5, pp. 1816-1825.

# Polycrystal plasticity approach of the sheet necking problem

Dequiedt J.L.<sup>1,\*</sup>, Denoual, C.<sup>1</sup>

<sup>1</sup> CEA, DAM, DIF, F-91297 Arpajon France

**Keywords:** crystal plasticity, polycrystals, necking, instability

**Abstract:** The development of plastic strain localization in a stretching metal sheet is simulated with integration of the sheet microstructure in the form of a polycrystalline aggregate: the elasto-plastic behaviour in each grain is ruled by a Teodosiu type crystal plasticity formulation. The evolution from strain heterogeneity at the grain scale to the emergence of larger strain patterns and at last the concentration of deformation in a few necks is displayed. Correlation with lattice orientation in grains is analysed by computing an extended Schmid factor. The incidence of the number of grains on the one hand and of an initial texture on the other hand is investigated.

## 1. Introduction

In ductile metals, the localization of plastic deformation is usually explained by the instability of the homogeneous deformation loading paths. In the case of structures under dynamic expansion, the localization pattern is assumed to be driven by unstable necking modes at the macroscopic scale linked with the saturation of the applied force and triggered by random perturbations such as geometrical or loading defects (Mercier and Molinari [1], Jouve [2]). However, these approaches ignore strain heterogeneity at the mesoscale (the one of the polycrystalline aggregate) and cannot evaluate its influence as an initiator for macroscopic localization.

For this reason, polycrystal plasticity modelling appears as a relevant tool to investigate localization of plastic deformation. In this work, the case of tantalum sheets loaded in biaxial stretching is addressed and the microstructure is incorporated by the generation of a polycrystalline aggregate. Plasticity inside grains is ruled by a crystal plasticity model, the constitutive relations being presented in Section 2 as well as the simulated geometry. The simulation of a sheet with isotropic texture is analysed in Section 3 and the question of the number of grains in the sheet thickness is investigated. Section 4 is devoted to the incidence of a pronounced cross-rolling texture on the localization process.

## 2. Cristal plasticity model and simulated geometry

The deformation of grains is formulated in a finite deformation framework and plasticity is ruled by a Teodosiu type model taking dislocation densities as internal state variables [3]; the deformation gradient tensor is decomposed into an elastic and a plastic part:

$$\mathbf{F} = \mathbf{F}^e \cdot \mathbf{F}^p \quad (1)$$

The elastic transformation  $\mathbf{F}^e$  encompasses all lattice deformations and rotations (the relaxed configuration is said “isoclinic”) and the plastic transformation rate expresses as a sum of slip rates on the different slip systems of the crystal lattice:

$$\mathbf{L}^p = \dot{\mathbf{F}}^p \cdot \mathbf{F}^{p-1} = \sum_{\alpha} \dot{\gamma}^{\alpha} \mathbf{m}_0^{\alpha} \otimes \mathbf{n}_0^{\alpha} \quad (2)$$

In the case of BCC structures, there are 24 slip systems, 12 with  $\{110\}$  slip planes and 12 with  $\{112\}$  slip planes. Slip rates are governed by a thermal activation law:

\* jean-lin.dequiedt@cea.fr.

$$\dot{\gamma}^\alpha = \dot{\gamma}_0 \exp\left(-\frac{\Delta G}{k_B T}\right) \quad \text{with} \quad \Delta G = \Delta F \left(1 - \left(\frac{\tau^\alpha - \tau_c^\alpha}{s}\right)^p\right)^q \quad (3)$$

The resolved shear stress  $\tau^\alpha$  is the projection of the stress tensor on the slip system and expresses in finite deformations ( $\boldsymbol{\pi}$  is the second Piola-Kirchhoff stress tensor, cf Balasubramanian and Anand [4]):

$$\tau^\alpha = (\mathbf{F}^{eT} \cdot \mathbf{F}^e \cdot \boldsymbol{\pi}) : (\mathbf{m}_0^\alpha \otimes \mathbf{n}_0^\alpha) \quad (4)$$

Strain hardening is quantified by the evolution of the critical shear stress with dislocation densities per system:

$$\tau_c^\alpha = \tau_0 + \mu b \sqrt{\sum_\beta a^{\alpha\beta} \rho^\beta} \quad (5)$$

The hardening matrix  $a^{\alpha\beta}$  is derived from dislocation dynamics simulations and coefficients for tantalum are given in Madec and Kubin [5]. The evolution of dislocation densities is driven by the competition between dislocation multiplication and annihilation by dynamic recovery:

$$\dot{\rho}^\alpha = \frac{1}{b} \left( \sqrt{\sum_\beta d^{\alpha\beta} \rho^\beta} - 2\gamma_c \rho^\alpha \right) \dot{\gamma}^\alpha \quad (6)$$

Sheet simulations (cf. figure 1) are performed with the crystal plasticity code Coddex using an Element Free Galerkin numerical scheme. A polycrystalline structure is generated by a Voronoï tessellation algorithm and both 4000 and 50000 grain aggregates are considered: a set of 100 crystal orientations is distributed among these grains. Periodic boundary conditions and an average equi-biaxial deformation gradient  $\mathbf{F}$  are imposed:

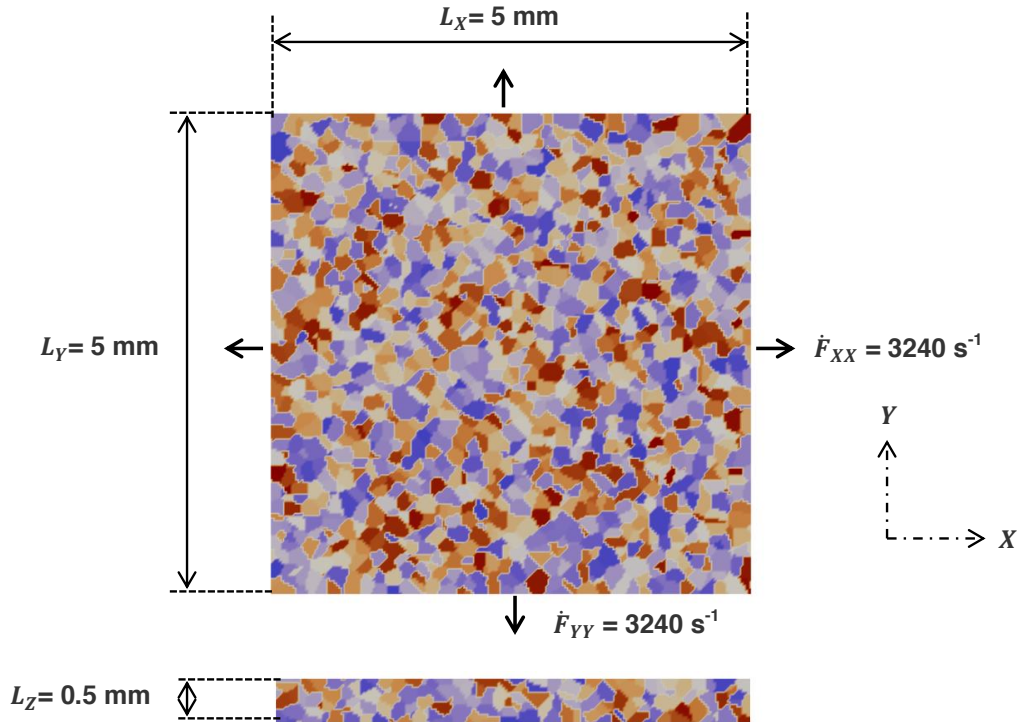


Figure 1: Simulated stretching sheet in the case of a 4000 grain aggregate.

### 3. Sheet with isotropic texture

This section is devoted to localization in an isotropic sheet (crystal orientations are randomly selected in all directions). In the early stages, a heterogeneous deformation develops with fluctuations at the scale of the

crystal structure, but this pattern progressively evolves towards a few high deformation zones forming macroscopic localization. In the sheet thickness, strain first organizes along bands oriented approximately 45° but necking appears in the later stages.

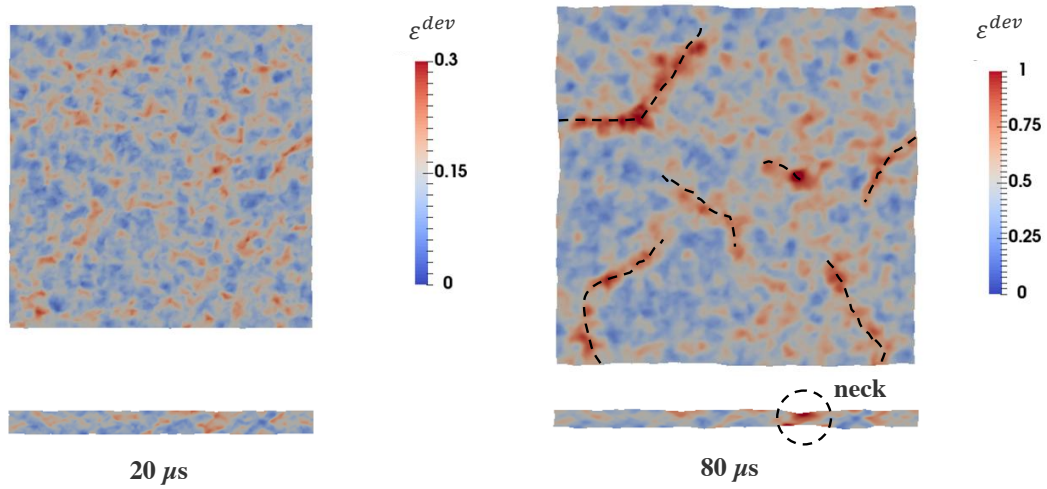


Figure 2: Maps of deviatoric (Hencky) strain  $\varepsilon^{dev}$  at times  $t = 20 \mu s$  and  $80 \mu s$  in average plane and sheet thickness.

The link between in-grain strain intensity and local constitutive properties is investigated in the following way. At the onset of plastic straining, local slip resistance is controlled by the more or less favourable orientation of the different slip systems towards the stress state. A measure of this effect is given by the Schmid factors  $\eta^\alpha$  the definition of which could be extended to triaxial stress conditions as the ratio between  $\tau^\alpha$  and the Von Mises norm of tensor  $(\mathbf{F}^{eT} \cdot \mathbf{F}^e \cdot \boldsymbol{\pi})$ . Correlation graphs between deviatoric strain and maximum Schmid factor are provided on figure 3 for the early and late loading stages: strain is on average higher in grains with higher Schmid factor but, when macroscopic localization arises, it encompasses both favourably and unfavourably oriented grains (points on the right side of the graph).

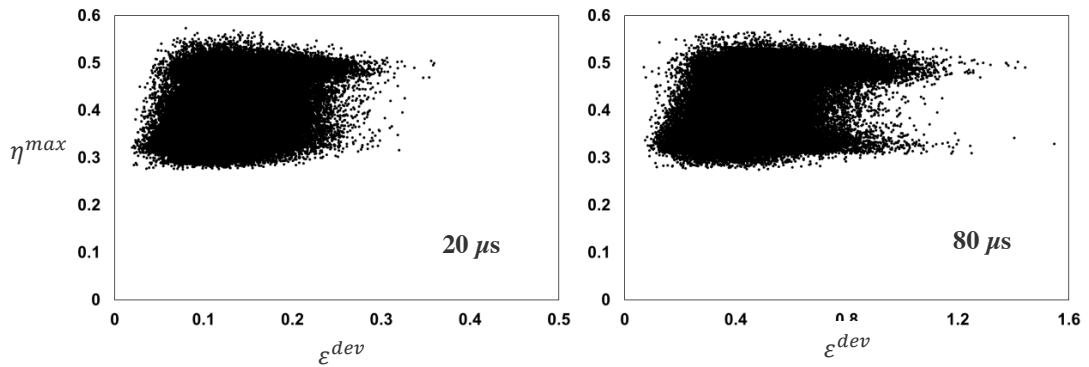


Figure 3: Correlation graphs between deviatoric strain  $\varepsilon^{dev}$  and maximum Schmid factor  $\eta^{max} = \max_\alpha(\eta^\alpha)$  at times  $t = 20 \mu s$  and  $80 \mu s$ .

When the number of grains is increased up to 50000, the formation of macroscopic localization is delayed and preceded by the emergence of patterns larger than the crystal structure (figure 4).

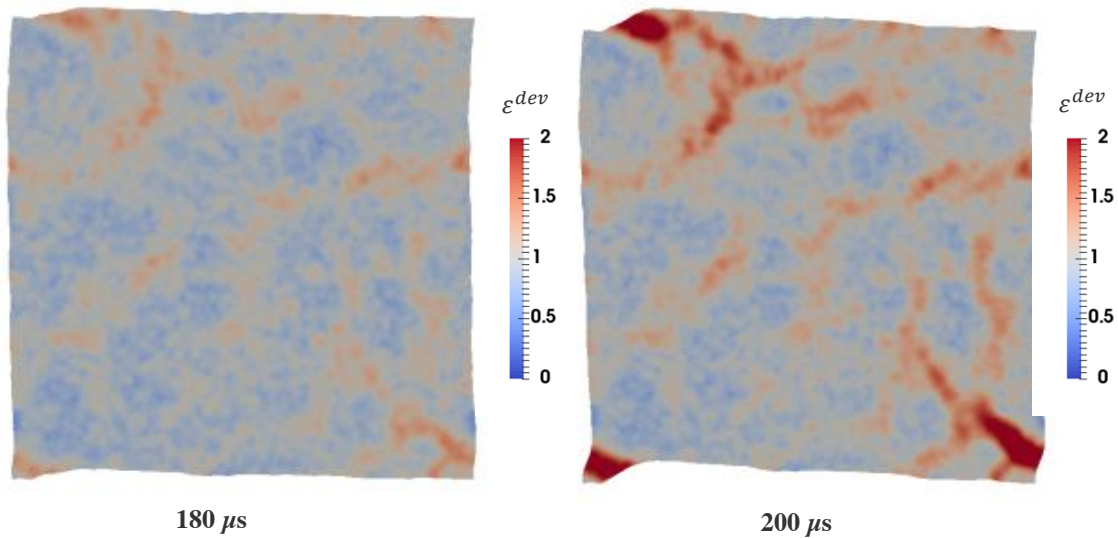


Figure 4: Maps of deviatoric strain for the 50000 grains aggregate at times  $t = 180 \mu s$  and  $200 \mu s$  in average plane.

#### 4. Texture influence

A cross-rolling texture is introduced in the simulation of the 4000 grain aggregate by computing the effect of an equi-biaxial pre-deformation on each of the initial crystal orientation. In a pole figure, these orientations then concentrate around two families of orientations (“fibers”), the first one corresponding to the z-axis aligned with one of the lattice axis ( $z \parallel (100)$ ) and the second one corresponding to the z-axis aligned with the diagonal of the lattice cell ( $z \parallel (111)$ ). In the early loading stage, the heterogeneity of deformation is stronger than in the isotropic case and strain concentrates in the grains of the first fiber (figure 5-a). Macroscopic localization next develops for shorter times than in the non-textured sheet (Figure 5-b).

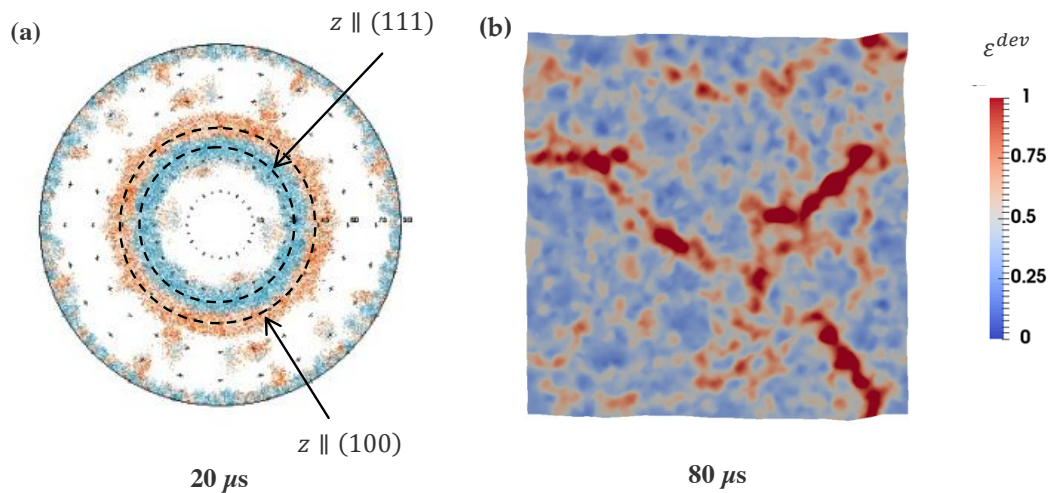


Figure 5: (a) Deviatoric strain versus crystal orientation at time  $t = 20 \mu s$  in the textured sheet and (b) localization in average plane at time  $t = 80 \mu s$ .

## 5. Conclusion

In a stretching sheet, strain heterogeneity at the mesoscale (the one of grains) can be the initial perturbation which triggers macroscopic localization. When it is of sufficient amplitude, the necking zones seem to take paths of initially high strain. However, when the number of grains in the sheet thickness is raised, the process seems to be controlled by perturbation modes of wavelengths larger than grain orientation fluctuations, which enforces the idea of a structural instability process.

### References :

1. Mercier, S., Molinari, A., 2003. Prediction of bifurcation and instabilities during dynamic extension. *Int J. Struct. Solids* **40**, 1995-2016 (doi: 10.1016/S0020-7683(03)00020-9).
2. Jouve, D., 2013. Analytic study of plastic necking instabilities during plane tension tests. *Eur. J. Mech. A/ Solids* **39**, 180-196. (doi: 10.1016/j.euromechsol.2012.09.008)
3. Teodosiu, C., Raphanel, J.L., Tabourot, L., 1991. Finite element simulation of the large elastoplastic deformation. In: *Large Plastic Deformations* edited by Teodosiu, C., Raphanel, J.L., Sidoroff, F., Rotterdam, A.A. Balmkema, pp. 153-168.
4. Balasubramanian, S., Anand, L., 2002. Elasto-viscoplastic constitutive equations for polycrystalline FCC materials at low homologous temperatures. *J. Mech. Phys. Solids*, **50**, 101-126. (doi: 10.1016/S0022-5096(01)00022-9)
5. Madec, R., Kubin, L., 2017. Dislocation strengthening in FCC metals and in BCC metals at high temperatures. *Acta Mater.* **126**, 166-173. (doi:10.1016/j.actamat.2016.12.040)

# Effect of porosity on the failure mechanisms induced in SiC brittle materials upon dynamic impact

M. Dargaud\*<sup>1</sup> and P. Forquin\*<sup>1</sup>

<sup>1</sup>Laboratoire Sols, Solids, Structures – Risks (3SR)  
University of Grenoble Alpes, Grenoble F-38041 Cedex 9, FRANCE

**Keywords:** Ceramics, Silicon carbide, Microstructure, Porosity, Dynamic fragmentation, High strain rates

---

## Abstract

The present work investigates the behaviour of two SiC-based ceramics with different level of porosity (2% and 11%) when subject to high strain-rate loading conditions. Under impact, dynamic tensile stresses spread in ceramic plate due to the propagation of numerous oriented cracks, leading to its fragmentation. This dynamic fragmentation is supposed to be highly related to the ceramic performance for armour protection. Therefore, the main motivation for this study is to understand the fragmentation process occurring in SiC-based ceramics under impact loading, and identify the link between the level of porosity and the induced failure mechanisms. Specific experiments, such as edge-on-impact, normal and tandem impact tests, were performed on these two materials. Thanks to the damage growth observation via ultra-high speed camera and post-mortem tomography analysis, a better understanding of the failure mechanisms induced in the dense and porous SiC-based ceramics under impact is provided.

Edge-on impact and normal impact tests showed that the presence of porosity significantly change the failure behaviour of the ceramic upon impact. While the dense ceramic undergoes a high fragmentation, typical of brittle materials under dynamic tensile loading, the crack density of the porous ceramic remains moderated. Complementary tandem tests highlighted that the pre-fragmented porous ceramic presents a greater resistance to the penetration of a projectile. This change of dynamic behaviour and damage modes for porous ceramics is attributed to the dissipation of energy through the collapse of porosity under prior compression stress. These results are of paramount importance to better understand the effect of the ceramic microstructure on its performance for bulletproof applications and to figure out how armour ceramics need to be designed to reach improved level of protection for multiple hits.

## 1. Introduction

Systems made of a hard ceramic front face and a composite backing present suitable properties for personal and vehicle lightweight protections. Silicon carbide (SiC) is widely used for ceramic armour due to its high hardness and low density. Moreover, the microstructure of SiC-based ceramic armour is found to highly influence its dynamic fragmentation [1]. However, so far, the failure mechanisms induced in such brittle materials under impact are still not well understood. Therefore, the link between the ceramic microstructure and its dynamic performance remains not clear.

Upon impact, the propagation of a spherical compressive wave generates hoop tensile stresses. Once this compressive wave reaches the specimen edges and backside, its reflection creates a tensile state as it crossed the initial compressive wave [2]. Many microstructure heterogeneities, such as sintering defects, pores or micro-cracks are inherent to ceramic material. When the tensile state exceed any of these flaws activation stress, multiple cracks oriented perpendicular to the tensile loading direction are nucleated on these microstructural defects [3]. It has been found that the porosity level influence the dynamic properties of alumina ceramics, as the Hugoniot Elastic Limit (HEL) was demonstrated to decrease with an increase of

\* marielle.dargaud@3sr-grenoble.fr and pascal.forquin@3sr-grenoble.fr  
† University of Grenoble Alpes, Grenoble Cedex 9, France

porosity [4]. Martin showed that, although a small change of porosity distribution (3.50 and 3.15%) modified the quasi-static properties of SiC materials, it had no clear effect on HEL and spalling strength, when tested via plate impact tests [5]. In the present study, the two studied SiC-based materials differ greatly by their level of porosity (2 and 11%).

The goal is to identify the failure mechanisms induced under impact loading in these two materials. To this end, three impact configurations were tested: edge-on-impact (EOI), normal and tandem impact tests. Riou et al. first developed EOI test in 1997. This experiment consists in impacting a ceramic tile on its edge with a rigid projectile. In such configuration, it becomes possible to visualize the fragmentation process, usually inaccessible as it occurs in a cone localized in the bulk of the material [6]. Normal impacts were performed to see the fragmentation patterns obtained when the ceramic is impacted in a configuration closer to a ballistic impact. As initiated by Forquin and Ando, micro-tomography was used to quantify the fragmentation intensity in the entire post-mortem specimens [7]. Then, both materials were tested in tandem impact configuration, similarly to Zinszner et al., in order to evaluate each microstructure potential to withstand multiple hits [8].

## 2. Materials and methods

Two SiC-based materials presenting clear difference of porosity distribution are studied. The dense ceramic is made from the uniaxial pressing and natural sintering of small alpha-SiC grains at high temperature. The obtained material has a theoretical porosity lower than 2%, mainly due to sintering defects at the SiC grain boundaries (~ 1-2µm). The second material is made of a matrix of SiC grains, 70% by volume, densified by a ceramic binder phase. The generated phase during the sintering process leads to the part densification but with around 10-11% of remaining open porosity, including some coarse pores (~ 50µm). Moreover, a specificity of this material is its heterogeneity of porosity across a tile thickness, which is due to the green part shaping process. A 1mm-thick median plan presents a higher porous volume. Both material have a high hardness and relatively low density, making them ideally suited to application involving dynamic solicitations.

The fragmentation behaviour of both materials under impact loading was first studied via an Edge-On-Impact (EOI) test [6]. The ceramic tiles dimensions are 60\*30\*7mm<sup>3</sup>. Cylindrical projectiles (Ø10mm and 15mm-height) made of a high elastic limit steel (1300MPa) were used as impactors. The projectile speed was set to 175 m/s in order to simply generate an intense fragmentation of the ceramic, which can be observed via a high-speed recording device. In this work, a Kirana camera was used with a recording speed of 2 million frames per second. Such high-speed imaging required the use of a flashlight to reach a substantial lighting level. Three speed gates, made of optical fibres spaced by 25mm and placed in the launcher tube to record the projectile velocity, were used to trigger the flashlight. In parallel, a laser pointing at the rear face of the target recorded the material velocity and allowed the camera triggering. In order to reach a clear contrast visualization of the fragmentation process, the observed ceramic face was mirror polished and the camera was placed along the reflexion axis of the light, as shown in Figure 1.

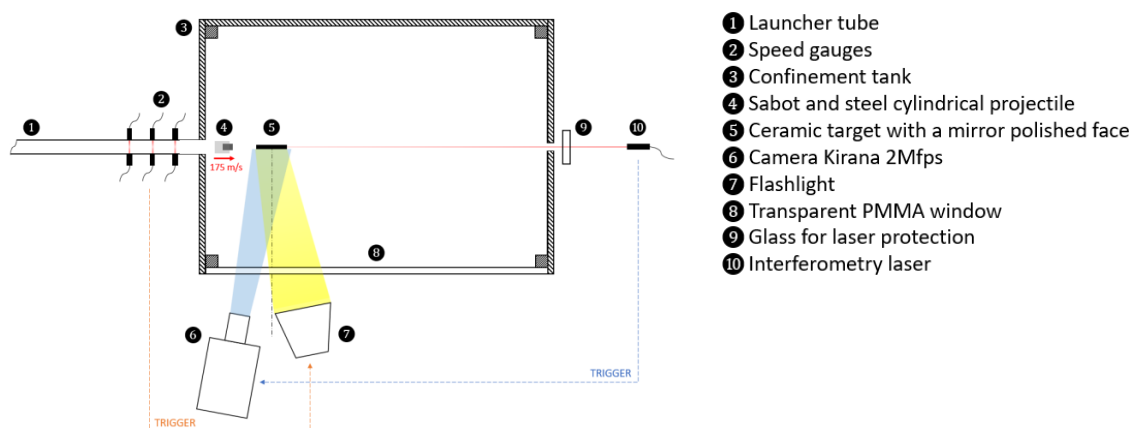


Figure 1: Top view of edge-on impact test configuration

Additional tests were made on ceramics placed in a polycarbonate sarcophagus, such casing combining the transparency and resistance required to capture the fragmentation growth and perform post-mortem analysis on the fragmented tile via tomography examination. Applying a confinement to the ceramic did not show any change in term of dynamic fragmentation as a space of 0.1mm was fixed between the specimen and the sarcophagus. An impacted ceramic in a sarcophagus is presented in Figure 2 a). A pixel size of 20  $\mu\text{m}/\text{pixel}$  was yield while keeping the entire target in the camera field of view.

The second test consisted in performing an impact normal to the ceramic surface with the same projectile in a confined configuration. The ceramic sample ( $50*50*7\text{mm}^3$ ) was placed between a 1mm-thick steel front layer having a high elastic strength of 1300MPa and a 6mm-thick aluminum alloy backing. The configuration details were reproduced similarly to the experiments performed in [8]. A schematic of the normal impact configuration is given in Figure 3. The confinement of the ceramic sample in a metallic casing ensured its intense fragmentation while keeping all the fragments in place. It was demonstrated in previous works that the same failure mechanisms are activated for both, EOI and normal, impact configurations [8]. Once impacted at 175 m/s with the cylindrical projectile, the front face of the sarcophagus was removed, keeping the fragmented ceramic in the sarcophagus. The confinement system is presented on Figure 2 b), after removing the front metallic casing. The fragmented media was infiltrated with a hyper-fluid resin under vacuum and removed from the casing for further analysis via micro-tomography. The scans resolution was  $30\mu\text{m}/\text{pixel}$ . Tomography scans of the post-mortem ceramics after EOI and normal impacts were analysed by using a 3D-segmentation algorithm. Based on the local measurement of a hessian gradient, this post-processing allowed a clear detection of the cracks.

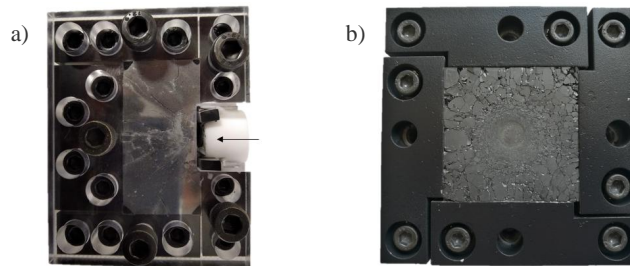


Figure 2: Fragmented ceramics in sarcophagus for a) EOI impact and b) normal impact (removed front casing)

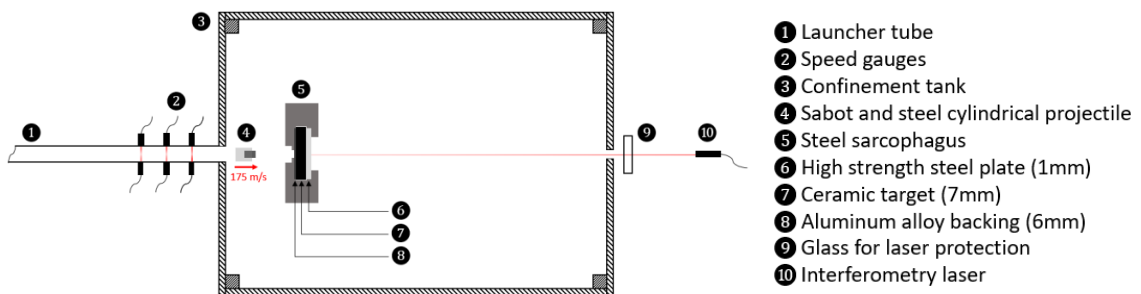


Figure 3: Top view of normal impact configuration

In order to properly predict the interaction between a projectile and a ceramic target, it is necessary to take into account the behaviour of the fragmented media and its residual resistance to perforation. This residual strength was evaluated using a test often called tandem test [8]. This test consists in performing a second shot with a perforating conical projectile on the pre-fragmented tile, resulting from normal impact. The interaction between the fragmented media and the projectile was recorded via the ultra-high-speed camera. The free surface velocity at the rear face of the aluminum alloy backing was recorded via interferometry during the perforating shoot. In order to prevent the sabot from passing in front of the camera field of view and hitting the pre-fragmented ceramic, it was removed from the projectile by placing a perforated plate at the exit of the launcher tube. A schematic of the tandem test configuration is given in Figure 4. The reproducibility of the results was demonstrated by Zinszner in [8], so for this study, only one test was performed on each material.

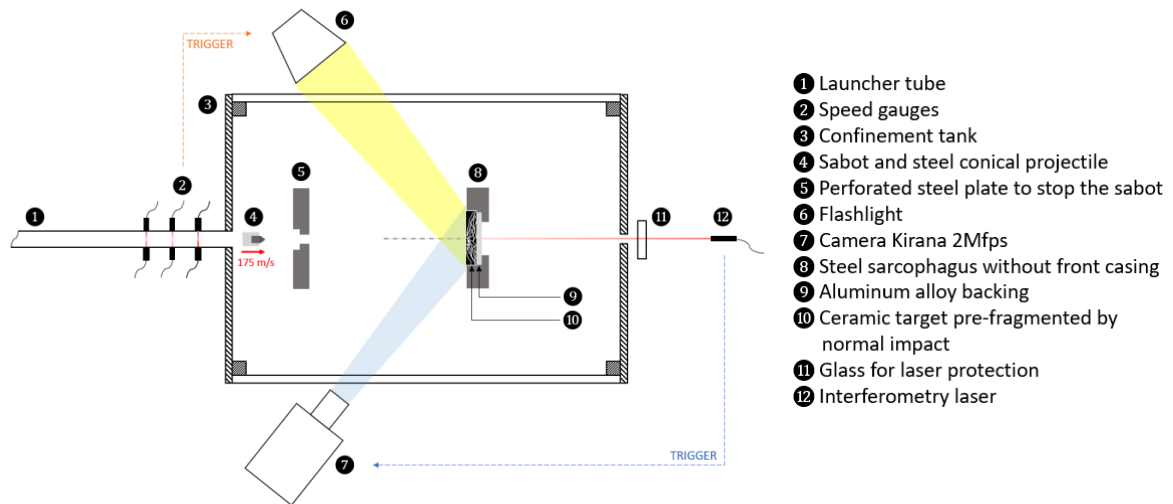


Figure 4: Top view of tandem impact configuration

### 3. Results and discussion

The EOI test combined to ultra-fast imaging allowed observing the damage evolution in the ceramic tiles. A comparison of the fragmentation chronology between the dense and porous ceramics is presented in Figure 5. Pictures were selected between  $2\mu\text{s}$  and  $12\mu\text{s}$  after the contact between the impactor and the ceramic edge. This time range covers the fragmentation initiation until cack propagation end. A clear difference of failure behaviours can be observed thanks to the use of an ultra-high-speed camera. The high strain-rate loading lead to the development a conical zone with a high crack density only  $3\mu\text{s}$  after impact for the dense ceramic. Whereas, the fragmentation observed in the porous ceramic was delayed ( $10\mu\text{s}$ ) and attenuated. The ejection of fragments under the projectile was found to be more pronouce for the dense ceramic than for the porous one.

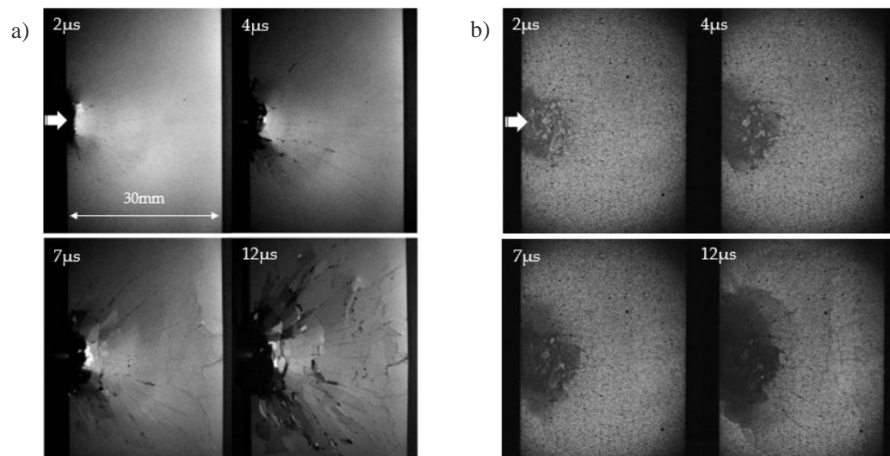
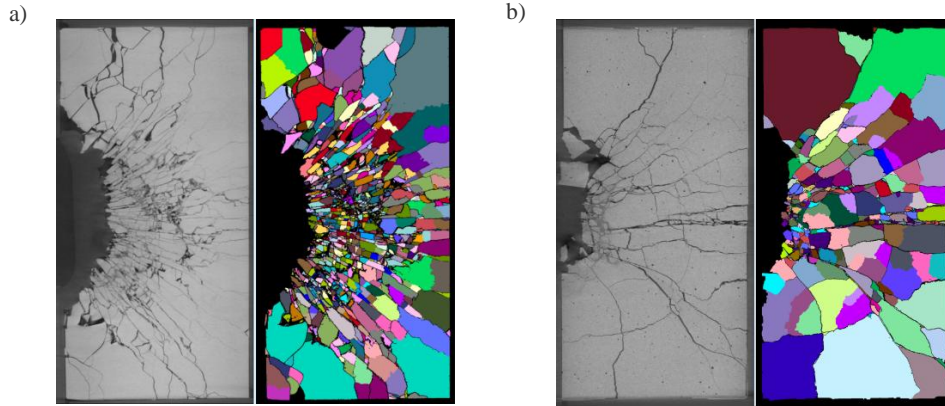


Figure 5: Fragmentation process of a) a dense (180 m/s, 1 Mfps) [8] and b) porous (178 m/s, 2 Mfps) SiC-based ceramic tile upon edge-on impact test

For both materials radial and orthoradial cracks, respectively coming from the initial tensile hoop stress and the reflection of the incident wave on the sample backside, are visible. The dense ceramic was subject to a high fragmentation upon the impulsive load, whereas very large fragments remained intact for the impacted porous ceramic. This observation can be explained by the pore volume collapse under the compression wave, thus responsible for energy dissipation. This crush of porosity was found to be even more pronounced in the

median sections of the tile, where the initial level of porosity was higher. For EOI test, two samples of the porous microstructure were impacted in the same experimental configuration to assess the reproducibility of the test and post-tomography analysis for fragment size determination. Tomography scans of the post-mortem ceramics confined in polycarbonate sarcophagus and the corresponding fragment identification is presented on Figure 6 for one selected slice of the 3D images. From the segmentation, each fragment size could be approximated by considering an equivalent radius of a sphere of the same volume.



**Figure 6: Slices of 3D tomography scans of the a) dense and b) porous SiC ceramics after EOI impact and identification of the fragments**

The patterns of fragmentation after normal impact are visible on the 3D micro-tomography scans of the infiltrated ceramics. Slices corresponding to front and rear faces are presented in Figure 7, and confirm observations made with EOI tests on the relative intensity of the fragmentation between both materials. The cross section images display a conical zone under the projectile contact patch with highly comminuted ceramic. This conical zone is formed by cracks propagating at 15-65° into the surface, which are characteristic of Hertzian cracks [9]. The fragment size distribution (FSD) of each microstructures in both configurations are compared in Figure 8. The fragment distributions between dense and porous materials are consistent with the ability of porosity to prevent the ceramic from intense fragmentation. It can be noticed from the FSD that the dense ceramic is more intense for the normal impact configuration, with no remaining fragments larger than 6mm, than the EOI configuration. Whereas, fragmentation of the porous microstructure was found to be deterministic as it was similar for both porous samples tested and even relatively similar between both experimental configurations. The cylindrical projectile indentation in the steel front layer was found to be more consequent for the dense ceramic than the porous one, with respective maximal deformation of 723 and 344 μm. Moreover, unlike the dense ceramic, the steel face in direct contact with the ceramic media under the projectile nose was found to be highly eroded for the porous ceramic.

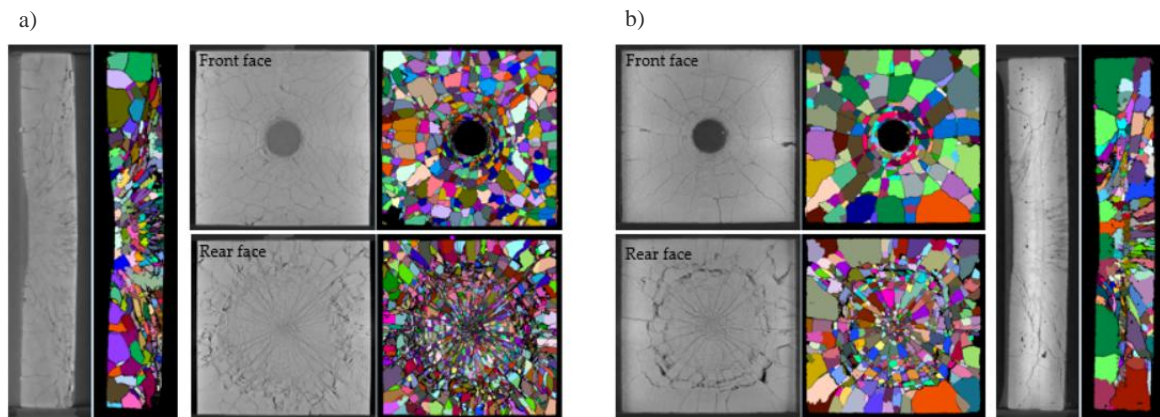


**Figure 7: Slices of 3D tomography scans corresponding to the tiles front and rear faces and the cross section under the impact zone of the projectile for the a) dense and b) porous SiC-based ceramics and identification of the fragments**

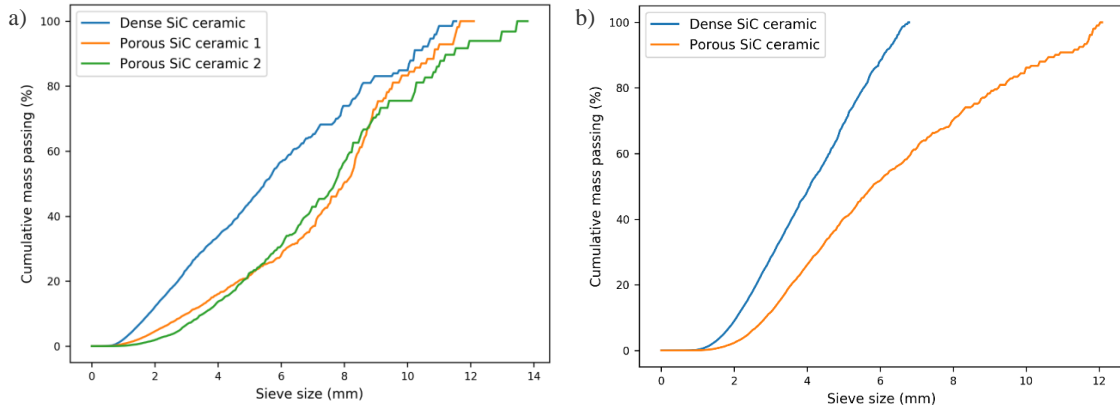


Figure 8: Fragment size distributions of dense and porous ceramics after a) EOI and b) normal impact

The ability of an armour system to defeat an incoming projectile is mainly related to the ceramic ability to spread energy over a large area of the backing via the Hertzian conoid, to erode the projectile and, less significantly, to dissipate some of the projectile kinetic energy via its fragmentation [9]. Tandem tests allowed comparing the kinetic energy dissipated by both pre-fragmented ceramics, by evaluating the load transfer to the backing plate during the perforation impact. The aluminum plates used as backing for the dense and porous ceramics respectively presented a maximal deformation of 658 and 420  $\mu\text{m}$ . This result suggests a better resistance of the porous ceramic to multiple impacts. Furthermore, the velocity of the aluminum backing, recorded via interferometry, is presented in Figure 9 for both materials. The clear jump of speed for the porous ceramic, pre-fragmented via normal impact, compared to the dense one, traduces the direct transfer of energy to its backing. This rapid transfer can be explained by the presence of relatively coarse fragments under the impactor nose. Indeed, the shape of the fragments under the projectile nose is linked to the resistance of the fragmented to perforation, as it involves particles flows and friction interactions [10]. Therefore, for an impact velocity around 175 m/s, the pre-fragmented porous ceramic displayed greater resistance to perforation than the highly fragmented dense material. The appropriate level of porosity required in the initial ceramic to accurately withstand a second perforating impact could be linked to the dynamic loading rate.

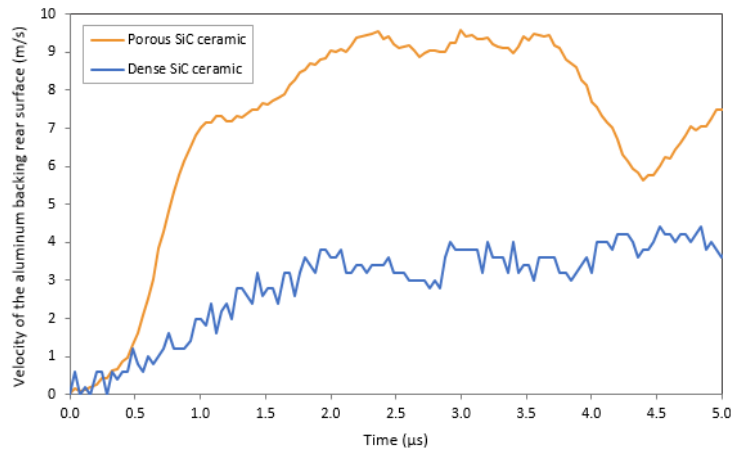


Figure 9: Velocity profile of the aluminum backing rear surface for both ceramics, captured via laser interferometry

#### 4. Conclusion

Two SiC-based materials presenting different microstructures, mainly in terms of porosity level, were tested in three configuration in order to identify the effect of this microstructural feature on their behaviour when subject to high strain-rate loadings. In the present study, the damage modes were induced at strain-rates

and pressure levels representative to those of ballistic impacts. The edge-on impact test allowed visualising the kinetic of failure in each ceramic target and therefore comparing the chronology of their damage initiation and propagation. The dense ceramic was subject to an intense fragmentation only 1-2 $\mu$ s after impact. On the contrary, the porous material was found to undergo a collapse of porosity under the compression wave initiated in the material upon impact. This compaction delayed the fragmentation process and limited the crack density. Tomography scans of confined ceramics in EOI and normal impact configurations confirmed the same distinction of fragmentation behaviour for both materials. This collapse of pores under compression led to the conservation of large fragments after impact. This presence of remaining coarse fragments in the damaged ceramic was found to improve the resistance of the pre-fragmented ceramic to the penetration of a projectile during a second impact. Therefore, this work suggests that the intensity of fragmentation is linked to the porosity distribution in the loaded ceramic, and has an influence on its resistance toward successive impacts.

The phenomenon of porosity compaction in highly porous brittle materials has to be taken into account for the description of the failure mechanisms occurring in ceramic materials under impact loadings. Indeed, it is essential to implement such damage modes into existing models, such as the Denoual–Forquin–Hild (DFH) model, to properly predict the dynamic behaviour in armour ceramics under high-strain rates loading [11]. Quantitative analysis were achieved in the present work by using a ultra-high speed camera to record the damage kinetic and the tomography technic to evaluate the fragmentation intensity. These results are essential tools to assess the suitability of a damage model to faithfully predict the failure behaviour of ceramic materials under high strain-rate loadings via numerical simulations.

### Acknowledgments

This work was sponsored by Saint-Gobain Research Provence, who provided the ceramic materials. The support of this company is gratefully acknowledged.

### References

1. P. Forquin, G. Rossiquet, J. L. Zinszner and B. Erzar. 2018. Microstructural influence on the fragmentation properties of dense silicon carbides under impact. *Mechanics of Materials* 123, 59-76.
2. J.S. Rinehart. 1975. *Stress transients in solids*. Hyper Dynamics, Santa Fe, NM.
3. H. Senf, E. Strassburger and H. Rothenhäusler. 1994. Stress wave induced damage and fracture in impacted glasses. *J. Phys. IV France*, 04, C8-741-C8-746.
4. F. Longy and J. Cagnoux. 1989. Plasticity and Microcracking in Shock-Loaded Alumina. *Journal of the American Ceramic Society*, 72(6), 971-979.
5. S. R. Martin. 2008. *Effects of Porosity Distribution on the Dynamic Behavior of SiC*. PhD manuscript.
6. P. Riou, C. Denoual and C.E. Cottenot. 1997. Visualization of the damage evolution in impacted silicon carbide ceramics. *Int. J. Impact Eng.* 21(4), 225-235.
7. P. Forquin and E. Ando. 2017. Application of microtomography and image analysis to the quantification of fragmentation in ceramics after impact loading. *Philosophical Transactions of the Royal Society*. 2016. 375(2085), 20160166.
8. J.L. Zinszner, P. Forquin and G. Rossiquet. 2014. Experimental and numerical analysis of the dynamic fragmentation in a SiC ceramic under impact. *Int. J. Impact Eng.* 76, 9-19.
9. I. Horsfall and D. Buckley. 1996. The effect of through-thickness cracks on the ballistic performance of ceramic armour systems. *Int. J. of Impact Eng.*, 18(3), 309 – 318.
10. A. Hameed, G. J. Appleby-Thomas, D. C. Wood, P. J. Hazell and K. M. Jaansalu. 2014. On the ballistic response of comminuted ceramics. *J. Phys. Conf. Ser.* 500 112005.
11. P. Forquin, F. Hild. 2010. A probabilistic damage model of the dynamic fragmentation process in brittle materials. *Adv. Appl. Mech.* 44, 1–72.

## Porosity influence on the dynamic tensile strength of polycrystalline ice

\*David GEORGES<sup>1, 2</sup>, Dominique SALETTI<sup>1</sup>, Pascal FORQUIN<sup>1</sup> and Maurine MONTAGNAT<sup>2</sup>

<sup>1</sup>Univ. Grenoble Alpes, CNRS, Grenoble INP 1, 3SR, F-38000 Grenoble, France

<sup>2</sup>Univ. Grenoble Alpes, CNRS, Grenoble INP 1, IGE, F-38000 Grenoble, France

**Keywords:** Ice, Dynamic, Microstructure, Tensile strength, High strain rates.

### Abstract

Polycrystalline ice has been extensively investigated during the last decades regarding its mechanical behaviour for quasi-static loadings. Conversely, only few studies can be found on its dynamic behaviour and scientists suffer from a lack of experimental observation to develop relevant modelling at high strain rate ranges. Dynamic experiments have already been conducted in compression mode using Hopkinson bar set-up. Regarding tension, the literature gives only approximated strength values and experimental observations and measurements are scarce. This knowledge is essential to design structures that may experience ice impact. The present study aims at providing complementary results to the first reproducible experimental data of the tensile strength of polycrystalline ice subjected to dynamic tensile loading presented in [4]. In addition to this previous work a particular focus has been made on porosity influence. To do so, a spalling test technique has been used on two different ice microstructures with a different porosity, to apply tensile loading at strain rates from  $24 \text{ s}^{-1}$  to  $120 \text{ s}^{-1}$ . The experimental results show that the tensile strength is sensitive to the applied strain rate, and seems to be weakened by an increase of the porosity.

### 1 Introduction

Isotropic polycrystalline ice, also known as granular ice, is one form of the only stable phase of ice at atmospheric pressure on Earth. Its mechanical behavior has been extensively studied and is now relatively well known under creep and quasi-static conditions [5]. Dynamic loading is also of concern in situation of ice impacts on structures. Hailstones or frost for instance can severely damage buildings, aircrafts or trains. An accurate understanding of the ice dynamic response is of interest to provide relevant dimensioning of the structures sollicitated. The experimental studies conducted so far were focused on the validation and/or the development of impact numerical models, through dynamic compression on Hopkinson bars or ice impacts on rigid target. Most of these studies took very little care of the ice microstructure, which is problematic as the microstructural properties are involved in the different damage mechanisms observed at high loading rates in quasi-brittle materials. Regarding tension only [4] studied the strain rate sensitivity of the ice dynamic tensile strength with a spalling configuration on Hopkinson bar, where they observed a clear strain-rate hardening. Though, the tensile strength is at the forefront among all the mechanical parameters that should be investigated and identified in order to get satisfying modelling.

This study aims to fill this gap by providing complementary datas to the first reproducible and robust set of experiments to measure the dynamic tensile strength of polycrystalline ice and to assess its sensibility to the strain rate presented in [4]. Two different microstructures, with different porosity but similar grain size and shape, are considered in order to investigate the effect of the porosity on the dynamic ice response, the bubbles being expected to act as critical defects during crack initiation. The studied material and the method used are presented in details in a first section. Then the results are analyzed and discussed before concluding on the strain rate sensitivity at high strain rate and the effect of microstructure.

\*Author for correspondence (david.georges@univ-grenoble-alpes.fr).

† Present address: Univ. Grenoble Alpes, CNRS, Grenoble INP 1, 3SR, F-38000 Grenoble, France

## 2 Material and method

### 2.1 Specimen description

The material studied is artificial polycrystalline ice grown in the laboratory. Two microstructures were designed : a microstructure with a low porosity ( $\approx 1 - 2\%$ , named **LP** for "Low-Porosity" in the following) and a microstructure with an higher porosity ( $\approx 7 - 10\%$ , named **HP** for "High-Porosity" in the following). Both microstructures are obtained using two growth technique inspired by the one described in [1]. Specimens are grown out of isotropic seeds made of crushed ice (with a maximum particle diameter of 2 mm) surrounded by water at  $0^\circ\text{C}$ . The slurry is placed on a Peltier element ( $-15^\circ\text{C}$ ), in a  $0^\circ\text{C}$  room, to grow gently from bottom to top, and avoid internal stresses during freezing. To obtained the **LP** microstructure, the isotropic seed is pumped before adding the water. The air trapped between the snow grains is maintained in order to produce the **HP** microstructure.

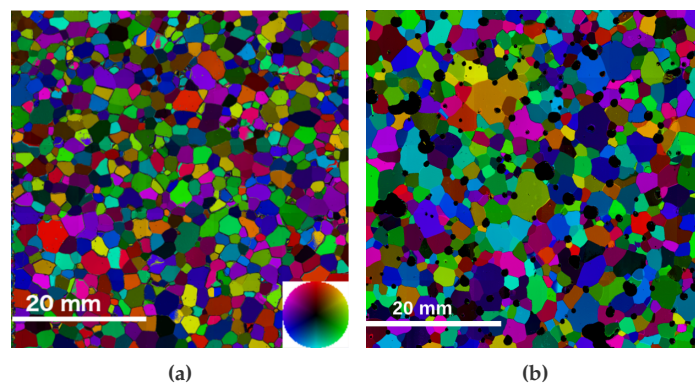


**Figure 1:** (Microstructure colour-coded with the [0001] crystallographic axis orientation of **LP** (a) and **HP** (b) microstructures, as measured with an Automatic Ice Texture Analyzer [6])

Both microstructures have equi-axed grains and an isotropic crystallographic texture, the mean grain size being about 1 to 2 mm (see Figure 1a and 1b). A detailed description of the bubble size distribution is obtained via  $\mu\text{CT}$  analysis (see Figure 2). The main difference between these two distributions is the presence in the **HP** microstructure of a large amount of bubbles whose the equivalent diameter exceeds 0.8 mm (population A). This feature is not observed in the **LP** bubble size distribution where only few bubbles are larger than 0.8 mm. The distributions are relatively similar below this threshold (population B). Bubbles belonging to population A have spherical shapes whereas the bubble geometry of bubbles in population B is random.

### 2.2 The spalling technique

To measure the dynamic tensile strength of these microstructures the so-called spalling technique on Hopkinson bar has been used. The originality of this method is that the specimen equilibrium is never reached. A projectile impacting one side of the incident bar generates a compressive pulse that propagates through the bar and the specimen. The perturbation is reflected as a tensile pulse when reaching the free surface of the specimen. The interactions of both signals generates a dynamic tensile loading in the core of the specimen. This method allows to reach strain rate up to  $200 \text{ s}^{-1}$ . The experimental device and the equipment used are detailed in [2], minor modifications have been made to adapt the experience to ice specimens especially concerning the temperature issue [4]. The ultimate spalling strength  $\sigma_u$  is deduced from the pullback velocity  $\Delta V_{pb}$  measured on the specimen free-surface by applying the linear acoustic approximation :

$$\sigma_u = \frac{1}{2} \rho_{ice} C_{ice} \Delta V_{pb} \quad (1)$$

\*Author for correspondence (david.georges@univ-grenoble-alpes.fr).

† Present address: Univ. Grenoble Alpes, CNRS, Grenoble INP 1, 3SR, F-38000 Grenoble, France

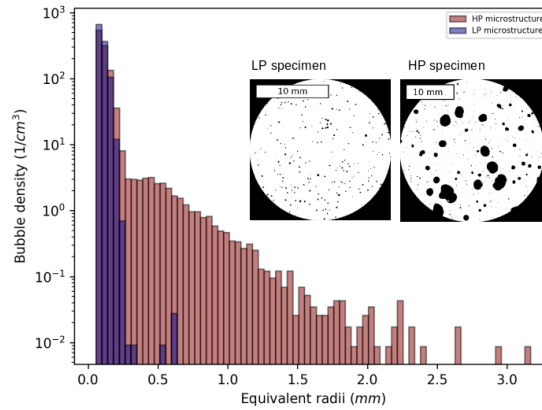


**Figure 2:** Bubble size distribution of **LP** (blue) and **HP** (red) microstructures according to the equivalent radii. Typical binary images from  $\mu$ CT analysis are also shown for both microstructures.

Gluing strain-gauges on an ice surface is challenging, especially in these experimental conditions where each second matters. To estimate the strain-rate applied during spalling tests elastic numerical simulations are then performed with the software ABAQUS-explicit. For each test the profile of material velocity is artificially converted into an elastic profile. After this point, this curve is virtually prolonged keeping the slope of the tensile phase before spalling fracture occurred. The stress corresponding to the material velocity  $V(t)$  according to the equation 2 is used as a loading pulse in the numerical simulations. We invite the reader to refer to [4] for further details on the procedure.

$$\sigma_T(t - \Delta t) = \frac{1}{2} \rho_{ice} C_{ice} V(t) \quad (2)$$

Several indicators assessing the quality of each test have been established: the use of an Ultra High Speed camera (1 *Mfs*) allows one to detect any compressive damage during the compression stage. Also the computation of the amount of transmitted energy into the specimen informs about the interface quality between the ice and the bar.

## 3 Results

### 3.1 Dynamic tensile strength

The results of 11 tests with **HP** specimens and 10 tests with **LP** specimens, obtained on several experimental campaigns, are considered here. Most of the **LP** specimens are already introduced in [4]. The strain-rates applied range between 24 and 112  $s^{-1}$  and between 41 and 120  $s^{-1}$  for **HP** and **LP** specimens respectively. The spalling stresses measured, i.e. tensile strengths, increase from 0.8 to 3.0 *MPa* and from 1.9 to 5.3 *MPa* over these ranges for **HP** and **LP** specimens respectively.

The results presented in Figure 3 highlight a variation of the spalling strength, i.e. tensile strength, with the strain rate applied. Since temperature conditions were repeatable, and since we expect reproducible microstructures in term of grain size and orientations within each specimen population (**LP** and **HP**), this result evidences a strain-rate sensitivity of the dynamic tensile strength of ice. A significant strength weakening with an increasing porosity is also observable. In brittle materials, the final fragmentation is the result of a competition between the activation of critical flaws and the obscuration phenomenon [3]. In the microstructures considered in this study, the critical flaws are assimilated to bubbles. Consequently for a similar failure stress, **LP** and **HP** specimens are expected to present different crack densities due to different bubble distributions. At the loading rates applied during the spalling tests only the bubbles belonging to the population

\*Author for correspondence (david.georges@univ-grenoble-alpes.fr).

† Present address: Univ. Grenoble Alpes, CNRS, Grenoble INP 1, 3SR, F-38000 Grenoble, France

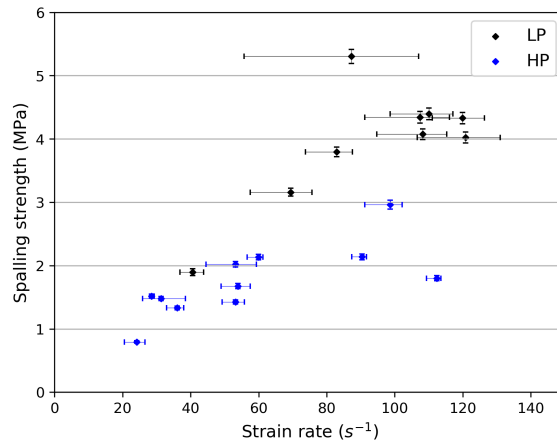


**Figure 3:** Tensile strength results with strain-rate. The displayed intervals on the curve correspond to the minimum and maximum values of strain rate measured during the tensile phase of the elastic simulations. The markers in between the intervals corresponds to the mean values of determined strain rates.

**A** (i.e. bubbles larger than 0.8 mm in diameter) are activated in the **HP** specimens. This is not the case in the **LP** microstructure as the density of bubbles larger than 0.8 mm is too low to relax efficiently the inner stress. The population **B** is thus activated, requiring higher energy to achieve the complete fragmentation observed. This result confirms the role of bubbles as a key parameter controlling the ice fragmentation at high loading rates.

### 3.2 Fragmentation analysis from UHS camera

The UHS camera allowed to observe the crack propagation in the volume of the specimen during each test. Even if the latter is a qualitative piece of information, it enables to distinguish two main different scenarios as a function of strain rate. At low solicitation rates the ice experiences a single fragmentation occurring randomly in the volume loaded in tension as it can be observed in Figures 4a and 4c. At higher strain-rates the specimens undergo intense multiple fragmentation. In Figures 4b and 4d one can see several cracks oriented perpendicularly to the specimen axis developing in a small volume (white dashed-line rectangle). In the next steps of the tests, this zone of damage spreads out toward the bar side of the specimens as observed on the last images. Finally, the higher the loading rate, the higher the crack density, which is consistent with the behaviour expected for brittle materials [3]. However the quality of the images did not allow one to find significant variations between the fragmentation pattern of each microstructure.

\*Author for correspondence (david.georges@univ-grenoble-alpes.fr).

† Present address: Univ. Grenoble Alpes, CNRS, Grenoble INP 1, 3SR, F-38000 Grenoble, France

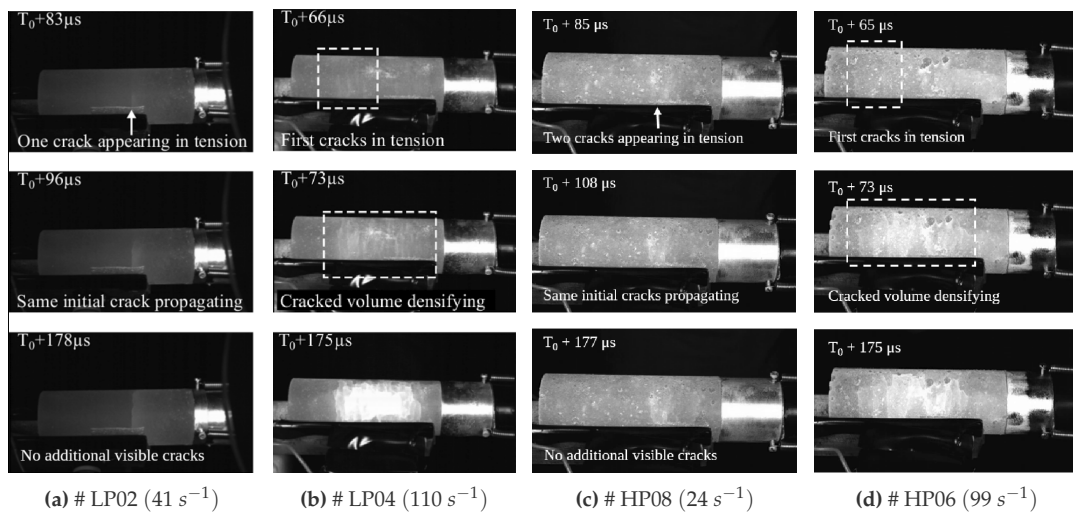


**Figure 4:** Fracture in LP and HP specimens for different strain rates. The projectile velocity applied during these tests was (a) 3.28 m/s, (b) 5.32 m/s, (c) 2.37 m/s and (d) 3.86 m/s respectively.

## 4 Conclusion

This paper presents a complementary study to [4] by investigating the dynamic tensile behavior of two different reproducible microstructures of ice, subjected to strain rate ranging from 24 to  $120 s^{-1}$ . 50 specimens were prepared and 20 tests considered to present the final results based on the Novikov approximation. The results show that tensile strength is clearly influenced by the strain rate and the porosity. The analysis of the fracture patterns occurring in the specimen during the test confirms also the elastic brittle behaviour in tension of ice at this range of strain rates.

### Acknowledgments

The present work was developed in the framework of the Brittle's Codex chair (Fondation UGA) and thanks to the support from the CEA-CESTA (France). The provided support and fundings are gratefully acknowledged by the authors.

\*Author for correspondence (david.georges@univ-grenoble-alpes.fr).

† Present address: Univ. Grenoble Alpes, CNRS, Grenoble INP 1, 3SR, F-38000 Grenoble, France

## References

- [1] P Barnes, David Tabor, and JCF Walker. The friction and creep of polycrystalline ice. *Proc. R. Soc. Lond. A*, 324(1557):127–155, 1971.
- [2] Benjamin Erzar and Pascal Forquin. An experimental method to determine the tensile strength of concrete at high rates of strain. *Experimental Mechanics*, 50(7):941–955, 2010.
- [3] Pascal Forquin and François Hild. A probabilistic damage model of the dynamic fragmentation process in brittle materials. In *Advances in applied mechanics*, volume 44, pages 1–72. Elsevier, 2010.
- [4] Dominique Saletti, David Georges, Victor Gouy, Maurine Montagnat, and Pascal Forquin. A study of the mechanical response of polycrystalline ice subjected to dynamic tension loading using the spalling test technique. *International Journal of Impact Engineering*, page 103315, 2019.
- [5] Erland M Schulson and Paul Duval. *Creep and fracture of ice*. Cambridge University Press, 2009.
- [6] Christopher JL Wilson, David S Russell-Head, and Hadi M Sim. The application of an automated fabric analyzer system to the textural evolution of folded ice layers in shear zones. *Annals of Glaciology*, 37:7–17, 2003.

\*Author for correspondence (david.georges@univ-grenoble-alpes.fr).

† Present address: Univ. Grenoble Alpes, CNRS, Grenoble INP 1, 3SR, F-38000 Grenoble, France

## Split Hopkinson bar testing at non-ambient temperatures

Stephen M. Walley\*

*SMF Fracture and Shock Physics Group, Cavendish Laboratory, J.J. Thomson Avenue, Cambridge CB3 0HE,  
United Kingdom ORCID ID 0000-0002-5399-6185*

**Keywords:** split Hopkinson pressure bar, non-ambient temperature, elastic wave propagation

**Abstract:** Some materials such as water ice only exist at cryogenic temperatures. Other materials may be subjected to a heat pulse at the same time as a shock in, for example, blast loading. If such events are going to be accurately modelled, a full constitutive relation for the material of interest is needed and this in turn requires mechanical data to be obtained for that material over a wide range of temperature and strain rate. Thus it is necessary to be able to perform high rate split Hopkinson bar tests at both high and low temperatures. Heating and cooling techniques for achieving this have been recently reviewed. So the emphasis of this paper will not be on the experimental methods but on the effect of temperature gradients on elastic wave propagation in the bars themselves.

### 1. Introduction

Some materials such as water ice only exist at cryogenic temperatures. Other materials may be subjected to a heat pulse at the same time as a shock in, for example, blast loading of concrete [1] or rock [2]. In any event, if such events are going to be accurately modelled, a full constitutive relation for the material of interest is needed and this in turn requires mechanical data to be obtained for that material over a wide range of temperature and strain rate [3-6]. Thus it is necessary to be able to perform high rate split Hopkinson bar tests at both high and low temperatures. Heating and cooling techniques for achieving this have been reviewed by Chen & Song [7]. So the emphasis of this document will not be on the experimental methods but on the effect of temperature gradients on elastic wave propagation in the bars themselves.

If the specimen (and hence the Hopkinson bar ends) are at a different temperature to ambient, there are several problems that have to be addressed.

**First:** the elasticity of the Hopkinson bar rods (and hence their mechanical impedance) changes with temperature. As this document shows, this is a problem even for elastic metallic bars, but it would be much worse for Hopkinson bars made from viscoelastic polymeric materials as their mechanical properties depend on frequency (and hence also temperature) [8-11].

The change of elasticity has three effects:

- (i) the particle velocity at the end of the bar for a given force will change (figure 1; [12, 13]);
- (ii) some of the input pulse will be reflected from the temperature gradient (figure 2; [14, 15]); and
- (iii) elastic waves propagating through the temperature gradient will be distorted differently by dispersion compared to a uniform rod [15-22].

\*Author for correspondence (smw14@cam.ac.uk).

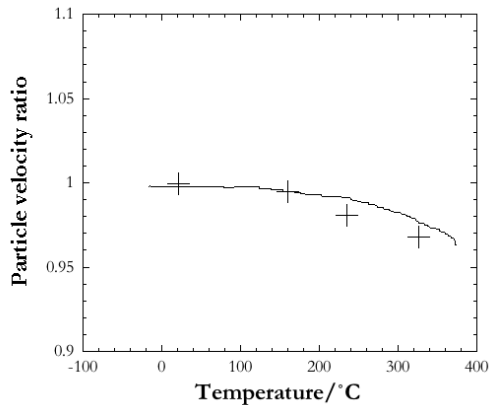


**Figure 1.** Ratio of particle velocity at the strain gauge to the particle velocity at the end of the bar as a function of temperature of heated end. Solid line, theory; + experiment. From [12].

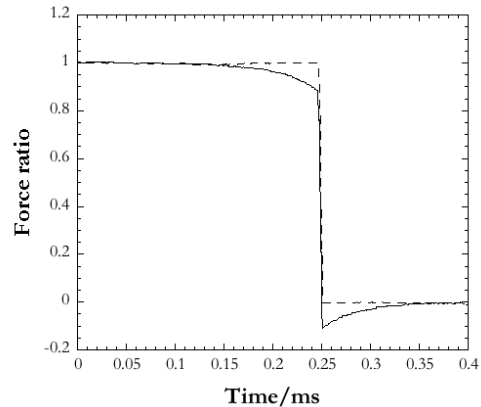


**Figure 2.** Computed effect of reflection from a temperature gradient on the force measured at a strain gauge station 'upstream' of the gradient (input pulse was a Heavyside function). Solid line: heated rod. Dotted line: unheated rod. From [14].

**Second:** the strain gauges must be kept at the temperature they were calibrated at (usually ambient), particularly if they are semiconductor gauges, or their response will be changed [7, 23, 24].

**Third:** if tests are to be carried out above ambient temperature, the heating rates should ideally be rapid to avoid annealing the specimen and hence changing its structure [7, 25-27] (unless, of course, the specimen is initially in a fully annealed state). Cooling rates for cryogenic studies are not normally so critical as lowering the temperature usually does not alter the microstructure. Most authors have, however, used conventional resistance furnaces rather than induction or radiant heaters for high temperature studies e.g. [7, 12, 28-32].

Figure 2 shows the error that results in the calculation of the force on a specimen at 1000°C if it is assumed that the temperature gradient has no effect. This error rises from 1.5% for  $T_F=125^\circ\text{C}$  to 12% for  $T_F=1000^\circ\text{C}$ . The calculation was performed using a simple form for the temperature distribution ( $T(x) = T_F e^{-\mu x}$ ) and dividing the rod into 80 equal segments [14].

## 2. The solutions

There have been several approaches to these problems listed above.

**The first** is either to ignore it [33, 34] or to say that thermal gradients in the bars have only a small effect on the measured stress pulses so that their effects are less than the experimental error (unless the temperature excursion is large; [35-38]). This is usually the case for metallic bars from liquid helium temperatures [38] up to around +300°C. For temperatures between 300 and 600 °C, Inconel Alloy 718 can be used. This alloy has a Young's modulus (and hence mechanical impedance) which is a weak function of temperature over the temperature range -200 to +600 °C [39].

**The second** is to seek to heat only the specimen and not the bar. This is essential if it is desired to test above 600 °C.

Several ways of doing this have been devised:

(i) construct an automatic mechanical device to bring the (cold) bars into contact with the heated specimen a fraction of a second before it is loaded [30]. Lindholm & Yeakley [12] had previously reported that this cannot be done manually fast enough to avoid cooling the specimen substantially (see also [7]). This technique has been used successfully up to 1200°C [40]. High temperature tension and torsion experiments cannot be performed this way as the specimen in these cases has to be in mechanical (and hence thermal) contact with the bars at all times [41];

- (ii) load the specimen through a thermal insulator (such as alumina) which has an impedance nearly equal to steel (at room temperature) [42, 43];
- (iii) keep the impedance constant along the length of the bar by shaping it to compensate for the temperature gradient [29]. So far this has only been implemented for torsion testing and dynamic fracture testing of ceramics in an SHPB; [44]). This method has the disadvantage that a bar of a particular profile can only be used for one temperature gradient;
- (iv) calculate the effect of the temperature gradient on the wave propagation [12, 28, 45]. One way of doing this is to determine the impedance as a function of position [13, 14, 44] using the two-point measurement technique pioneered by Lundberg and colleagues for waves propagating down rods of changing cross-section [46, 47].
- (v) perform an experimental check on whether stress pulses really do propagate from the input to the output bar through both a negative and a positive temperature gradient without significant distortion [48].

One way of calculating the impedance as a function of position and the amount of energy reflected from the temperature gradient is to determine the functional form of the temperature distribution along the bar  $T(x)$ . As most researchers use resistance furnaces (which can take up to 30 minutes to heat the specimen; [28]), the bar can be assumed to be in a steady state thermally [13, 28]. Bacon *et al.* [13] checked the temperature distribution using thermocouples (see figure 3). Then to turn this into an impedance versus position graph, the relationship between Young's modulus and temperature must also be known for the bar material (the effect of temperature on the density of the bar is ignored as being a relatively small effect; [13, 14]). This relationship has usually been taken to be linear [12, 13]:

$$E(T) = E_0[1 - \beta(T - T_0)] \tag{1}$$

where  $E_0$  is Young's modulus at ambient temperature,  $\beta$  is the measure of the dependence of modulus on temperature (*ca.*  $4 \times 10^{-4} \text{ K}^{-1}$  for steel; [14]), and  $T_0$  is the ambient temperature.

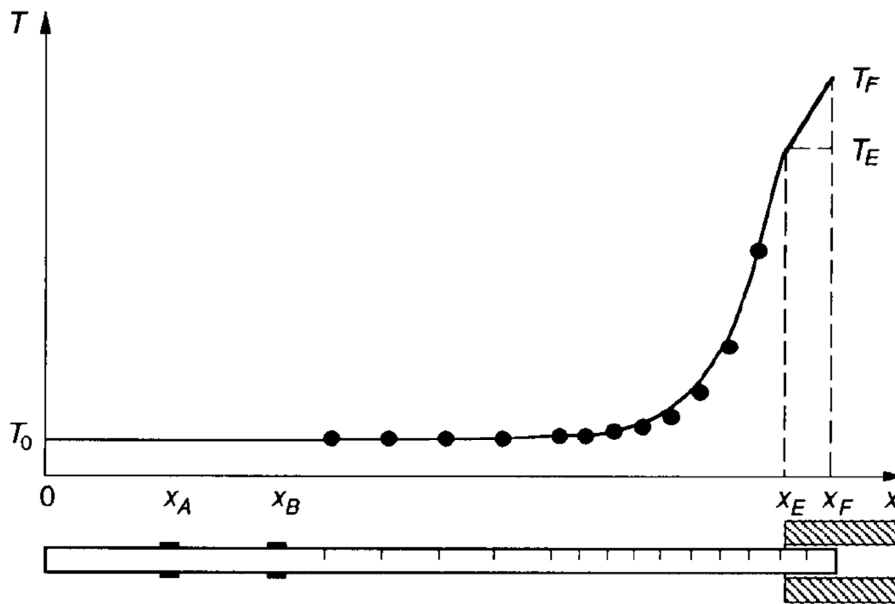


Figure 3. Temperature distribution in a Hopkinson pressure bar where the end temperature is 950 °C. Solid circles are measured values, the solid line was calculated. From [13].

Chiddister & Malvern [28] found that approximating the temperature distribution along a bar by a set of five discrete temperature steps allowed them to calculate the strain in the specimen to within 1% of the value measured by a gauge attached directly to the specimen at temperatures up to 480°C and to within 3% at 650°C. The reason for their procedure is that the reflection of a stress wave from a set of step changes in

modulus can be calculated analytically. They made a further check on this procedure by comparing their predictions with the measured stress pulse reflected back down the input bar.

Bacon *et al.* [13] found that solving the one-dimensional heat equation gave almost the same answer as solving the two-dimensional heat equation (assuming that the heat flux down the bar is constant down the bar and that the temperature gradient inside the furnace is linear). Both solutions lay close to the measured temperature values (see figure 3). They quote the 1D solution for  $T(x)$  as follows:

$$T(x) = \begin{cases} T_0, & x \leq x_B, \\ (T_E - T_0) \frac{\sinh \mu(x-x_B)}{\sinh \mu(x_E-x_B)} + T_0, & x_B \leq x \leq x_E, \\ \frac{T_F(x-x_E) + T_E(x_F-x)}{x_F-x_E}, & x \geq x_E, \end{cases} \quad (2)$$

where the variables are defined in figure 3. The definition of  $Z$ , the mechanical impedance, is  $Z = \sqrt{\rho E}$ , where  $\rho$  is the bar density (taken to be constant), and so

$$Z(x) = Z_0 [1 - \beta(T(x) - T_0)]^{0.5} \quad (3)$$

where  $Z_0$  is the impedance at room temperature.

A method that can be used to determine  $Z(x)$  directly is the two-point measurement technique developed by Lundberg *et al.* [46, 47, 49] for use originally with bars having a cross-section that varies with position. The technique involves measuring the strain pulses at two points  $x_A$  and  $x_B$  remote from the furnace (see figure 3). Then dividing up the bar between  $x_B$  and the end into equal segments (Bacon *et al.* [13] used 40 in their calculation), expressions can be derived for the force and particle velocity at the entrance to each segment (making the assumption that the functional form of  $Z(x)$  is as given in equations (2) and (3)) until the end of the bar is reached. If the end of the bar is free, the force there must be zero. This boundary condition was then applied in a minimization routine to determine  $Z(x)$ , and this is plotted in figure 4.

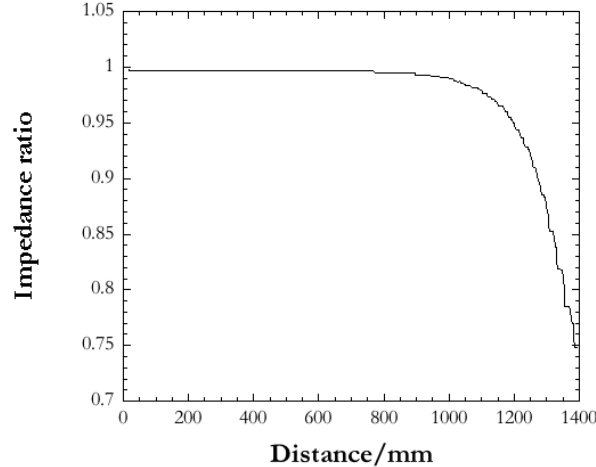


Figure 4. Mechanical impedance as a function of position for an austenitic steel rod heated to 950 °C at the right-hand end. From [13].

Bacon *et al.* [13] also performed an experimental check to see whether their theory correctly predicts the force pulse measured on an extension rod brought into contact with the main rod just before a force pulse was launched down it. The agreement was found to be much better than assuming the impedance did not vary with position, though there was a small residual error in calculating the time at which the particle velocity began to rise (the time at which the force pulse began to rise was correctly predicted). They attributed this discrepancy (equivalent to a displacement of 10 μm) to imperfect contact between the two bars.

### 3. Conclusions

The most sophisticated method developed so far for calculating the effect of a temperature gradient on an elastic wave pulse was developed by Bacon *et al.* [13]. Their method can be applied to any temperature distribution expressible in polynomial form. The main problem with applying their technique to cases where the specimen is heated (or cooled) very rapidly is that the heat flux in the bar is not in a steady state. Thus the functional form of the temperature distribution may not be calculable from the heat diffusion equation: indeed it may vary from shot to shot. Whether a good enough approximation can be arrived at is a matter for future investigators.

#### References :

1. Kristoflensen M, Hauge KO, Valsamos G, Børvik T. 2018. *EPJ Web Conferences* **183** 01057
2. Roy PP, Sawmliana C, Singh RK, Chakunde VK. 2012. *Mining Technol* **121** 46-51
3. Zerilli FJ, Armstrong RW. 1987. *J Appl Phys* **61** 1816-1825
4. Follansbee PS, Kocks UF. 1988 *Acta metall* **36** 81-93
5. Church PD, Andrews T, Goldthorpe B. 1999. A review of constitutive model development within DERA. In: Jerome DM (ed) Structures under Extreme Loading Conditions PVP **394**. New York: American Society of Mechanical Engineers, pp. 113-120
6. Lea LJ, Jardine AP. 2018. *Int J Plast* **102** 41-52
7. Chen W, Song B. 2011. Kolsky compression bar experiments at high/low temperatures. In: Split Hopkinson (Kolsky) Bar: Design, Testing and Applications. New York: Springer, pp. 233-260
8. Williams ML, Landel RF, Ferry JD. 1955. *J Amer Chem Soc* **77** 3701-3707
9. Yunoshev AS, Silvestrov VV. 2001. *J Appl Mech Tech Phys* **42** 558-564
10. Tamaogi T, Sogabe T. 2015. Viscoelastic properties for PMMA bar over a wide range of frequencies. In: Qi HJ, Antoun B, Hall R, Lu H, Arzounanidis A, Silberstein M, Furmanski J, Amirkhizi A, Gonzalez-Gutierrez J (eds) Challenges in Mechanics of Time-Dependent Materials. New York: Springer, pp. 95-100
11. Kendall MJ, Siviour CR. 2014. *Phil Trans R Soc A* **372** 20130202
12. Lindholm US, Yeakley LM. 1968. *Exper Mech* **8** 1-9
13. Bacon C, Carlsson J, Lataillade J-L. 1991. *J Phys IV France Colloq* **1(C3)** 395-402
14. Bacon C. 1993. *Int J Impact Engng* **13** 527-539
15. Loshmanov LP, Nechaeva OA, Rudnev VD. 1996. *Indust Lab* **62** 311-313
16. Stanford EG. 1950. *Nuovo Cimento Suppl (Ser 9)* **7** 332-340
17. Datta AN. 1956. *Indian J Theor Phys* **4** 43-50
18. Sur SP. 1961. *Indian J Theor Phys* **9** 61-67
19. Lindholm US, Doshi KD. 1965. *Trans ASME: J Appl Mech* **32** 135-142
20. Whittier JS. 1965. *Trans ASME: J Appl Mech* **32** 947-949
21. Francis PH. 1966. *Trans ASME: J Appl Mech* **33** 702-704
22. Francis PH. 1967. *Trans ASME: J Appl Mech* **34** 226-227
23. Gorham DA, Pope PH, Cox O. 1984. *Inst Phys Conf Ser* **70** 151-158
24. Dally JW, Riley WF. 1987. Strain gages. In: Kobayashi AS (ed) Handbook on Experimental Mechanics. Eaglewood Cliffs, NJ: Prentice-Hall, pp. 41-78
25. Rosenberg Z, Dawicke D, Bless SJ. 1986. A new technique for heating specimens in split Hopkinson bar experiments using induction coil heaters. In: Murr LE, Staudhammer KP, Meyers MA (eds) Metallurgical Applications of Shock Wave and High Strain Rate Phenomena. New York: Marcel Dekker, pp. 543-552
26. Rosenberg Z, Dawicke D, Strader E, Bless SJ. 1986. *Exper Mech* **26** 275-278

28. Chiddister JL, Malvern LE. 1963. *Exper Mech* **3** 81-90
29. Eleiche AM, Duffy J. 1975. *Int J Mech Sci* **17** 85-95
30. Frantz CE, Follansbee PS, Wright WT. 1984. Experimental techniques with the SHPB. In: Berman I, Schroeder JW (eds) High Energy Rate Fabrication – 1984. New York: American Society of Mechanical Engineers, pp. 229-236
31. Gálvez F, Cendón D, Sánchez-Gálvez V. 2005. *Anales Mecánica Fractura* **22** 508-513
32. Gálvez F, Cendón D, Enfedaque A, Sánchez-Gálvez V. 2006. *J Phys IV France* **134** 269-274
33. Krafft JM, Sullivan AM, Tipper CF. 1954. *Proc R Soc Lond A* **221** 114-127
34. Samanta SK. 1971. *J Mech Phys Solids* **19** 117-135
35. Campbell JD, Dowling AR. 1970. *J Mech Phys Solids* **18** 43-63
36. Campbell JD, Ferguson WG. 1970. *Philos Mag* **21** 63-82
37. Senseny PE, Duffy J, Hawley RH. 1978. *Trans ASME: J Appl Mech* **45** 60-66
38. Kishida K, Kataoka T, Yokoyama T, Nakano M. 1987. Behaviour of materials at high strain rates and cryogenic temperature. In: Kawata K, Shioiri J (eds) Macro- and Micro-Mechanics of High Velocity Deformation and Fracture. Berlin: Springer-Verlag, pp. 75-84
39. Kandasamy R, Brar NS. 1994. Flow stress and material model study at high strain rate and low temperature. In: Schmidt SC, Shaner JW, Samara GA, Ross M (eds) High Pressure Science and Technology 1993. New York: American Institute of Physics, pp.1031-1034
40. Sizek HW, Gray III GT. 1993. *Acta metall mater* **41** 1855-1860
41. Gray III GT. 2000. Classic split-Hopkinson pressure bar testing. In: Kuhn H, Medlin D (eds) ASM Handbook Vol 8: Mechanical Testing and Evaluation. Materials Park, OH: ASM International, pp.462-476
42. Lankford J. 1977. *J Mater Sci* **12** 791-796
43. Lankford J, 1981. *J Mater Sci* **16** 1567-1578
44. Bacon C. 1993. Mesure de la tenacité dynamique de matériaux fragiles en flexion-trois-points à haute température – Utilisation des barres de Hopkinson. PhD thesis, Univ. of Bordeaux I
45. Bacon C, Brun A. 2000. *Int J Impact Engng* **24** 219-230
46. Lundberg B, Henchoz A. 1977. *Exper Mech* **17** 213-218
47. Lundberg B, Carlsson J, Sundin KG. 1990. *J Sound Vibration* **137** 483-493
48. Potter RS, Cammack JM, Braithwaite CH, Walley SM. 2019. *J Dyn Behav Mater* **5** 198-211
49. Lundberg B, Blanc RH. 1988. *J Sound Vibration* **126** 97-108

## The Brittle's CODEX chair

**P. Forquin<sup>\*</sup>, M. Blasone, D. Georges, M. Dargaud, D. Saletti, E. Andò**

*Univ. Grenoble Alpes, CNRS, Grenoble INP, Laboratoire 3SR, BP53, 38041 Grenoble Cedex 9*

**Keywords:** Brittle materials, Microstructure, Plate-impact, Damage mechanisms, Mesoscale modelling, Micro-tomography

---

**Abstract:** Brittle materials are subjected to impact or blast loadings when used as protective structures, in the mining industry or in various industrial processes. Under these shock or very high strain-rate conditions, brittle materials experience extreme damage mechanisms such as plasticity, microcracking, fragmentation or pore collapse, which until now remain poorly understood. The Brittle's CODEX chair aims to gain insight into the link between the microstructural parameters of brittle materials and their response under extreme conditions (shock, impact, high pressure, high-strain-rate loading, spalling), mainly through analysis of the damage mechanisms involved. To do so, the microstructure of various brittle materials is being analysed by using x-ray micro-tomography and new dynamic testing methods based on shockless plate-impact experiments are being developed. These experimental approaches allow the improvement of the modelling and the numerical simulation of damage processes induced in such materials under high-strain-rates.

### 1. Introduction: Brittle materials at high strain-rates, numerous applications

Brittle materials such as ceramics, rocks, glass and concrete, are widely used in many civil and military applications involving dynamic loading, impulse loading, shock or impact. For instance, in the introduction of Meyers's book [Meyers, 1994], it is worth noting that among the examples of “applications where high-strain-rate phenomena are important” given to illustrate the need to investigate materials under dynamic loading, many concern brittle materials: “Explosive compaction of powders”, “explosive breakage (blasting)” of rocks, “oil well perforation” by shaped charge, “seismological studies”, “ballistic impact” against ceramic armour, “plastic explosive” against concrete structures. In most of these applications, the brittle material is subjected to **intense loading** characterised by high or very high strain-rates (a few hundred to several tens of thousands  $s^{-1}$ ), high pressure (hundreds to thousands of MPa) leading to **extreme damage modes** such as dynamic fragmentation and fracturing, pore collapse, shear and plasticity mechanisms, *etc.*

The experimental techniques currently used in research laboratories to test materials at high-strain rates, such as the Split Hopkinson Bar (SHB) (apparatus to perform dynamic compression, shear, torsion or tensile tests) or Taylor tests (for direct impact experiments), are better suited to the characterisation of ductile materials. Moreover, because of their use for involving high-strain-rate loadings specific applications, brittle materials are not investigated to the same extent in research labs. For these reasons, a lack of understanding of the brittle materials behaviour and their damage mechanisms under strain-rates greater than a few hundred of  $s^{-1}$  remain. Therefore, through this project, the goal is to develop innovative experimental approaches dedicated to the study of brittle materials and develop micromechanics-based models in order to improve the understanding and the predictive modelling of induced damage mechanisms.

### 2. Understanding the link between microstructure, damage mechanisms and dynamic behaviour of brittle materials: a major challenge in materials science

Paradoxically, whereas brittle materials remain relatively under-researched compared to ductile materials they present **complex and fascinating features** that justify greater efforts to develop research works. For instance, brittle materials are characterised by their random failure stresses under static tension or unconfined

<sup>\*</sup>Pascal Forquin ([pascal.forquin@3sr-grenoble.fr](mailto:pascal.forquin@3sr-grenoble.fr)).

<sup>†</sup>Present address: Laboratoire 3SR, BP53, 38041 Grenoble Cedex 9

sample size leads to a decrease of its mean strength. Above a given transition strain-rate, the strength of brittle materials increases with the strain-rate and the material tends towards deterministic behaviour.

All of these features are related to the triggering of cracks from defects. At low strain-rates, a single crack is initiated from “worse defect” (the weakest point) in the sample bulk, leading to scattered failure stresses measurements and size effects. On the contrary, at high strain-rates, a large number of cracks are triggered throughout the sample bulk. Indeed, due to the limited cracking velocity, only a small part of the volume is affected by the first crack formation, so the stress keeps increasing and new cracks are spreading throughout the volume [Denoual and Hild, 2000; Forquin and Hild, 2010].

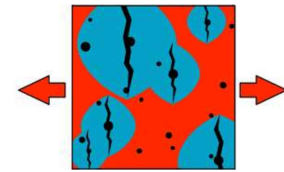


Figure 1: Multiple fragmentation process at high-strain-rates. The Denoual-Forquin-Hild model [Forquin and Hild, 2010].

The failure process becomes a dynamic system that stabilises only when the whole volume is “obscured” by cracks (blue zones in Fig. 1). In conclusion, brittle materials are characterised by:

- Dynamic failure modes (deterministic and strain-rate sensitive in tension) that differ from static failure mode (probabilistic and influenced by the sample size),
- Cracking density which is strongly influenced by the flaw population and microstructure,
- Dynamic strength which is strongly strain-rate sensitive.

Therefore, in order to improve the accuracy of models used for numerical simulations, knowledge and understanding of the **damage mechanisms** controlling brittle materials behaviour at high strain-rates is required. First, it includes a careful study of the material **microstructure** (flaws, existing micro-cracks, pores, aggregates, *etc.*), as it has been shown to play a major role in the material failure behaviour. Then, it also requires the development of innovative experimental techniques allowing investigating the damage and dynamic response of brittle materials while controlling the applied loading-rate.

### 3. Limitations and drawbacks of plate-impact and compact pulsed power generator techniques

Very few techniques are available to investigate the behaviour of brittle materials at strain-rates higher than  $200 \text{ s}^{-1}$ . Essentially, the two following experimental techniques are used: the plate-impact technique and the compact pulsed power generator. However, both testing methods present some strong limitations.

Even though the first technique has been extensively used to study the HEL (the Hugoniot Elastic Limit corresponding to the point on the shock Hugoniot at which a material transitions from a purely elastic state to an elastic-plastic state takes place) and the spall strength of ceramics [Bourne et al, 1997; Feng et al, 1998; Murray et al, 1998; Vogler et al, 2006] and rocks or mortar [Grote et al, 2001] (the spall strength corresponding to the ultimate strength supported by the material in uniaxial strain state), some drawbacks makes it not optimal for the characterisation of brittle materials. The first limitation is that plate-impact produces a shock response corresponding to a discontinuity of pressure. Moreover, below the HEL, the strain-rate is very high (about  $10^7\text{-}10^8 \text{ s}^{-1}$  in [LaLone and Gupta, 2009]) and therefore difficult to measure. In addition, by using a “standard flyer plate” there is no way of **controlling and adjusting the loading-rate**. Then, by using this technique, it is impossible to investigate the mechanical response and damage mechanisms of the material as a function of the strain-rate. Finally, due to the high kinetic energy of the flyer plate, the brittle target is usually pulverized into debris, therefore “post-mortem” studies can hardly be performed.

Until now, two compact pulsed power generator testing facilities have been built in the world by the French company “ITHPP”. The running principle is as follows, a short and intense electrical current of about 3.5 MA in 500 nanoseconds is used to accelerate an electrode by the Laplace effect (Fig. 2b). The electrode in contact with the concrete or ceramic sample plays a role similar to the flyer plate one in a plate-impact experiment. The major difference being that in this case the applied pressure loading is a **ramp** (shockless compression) instead of a sharp pulse (Fig. 2c). Therefore, a “**limited strain-rate**” can be obtained in the tested sample (about  $10^3\text{-}10^6 \text{ s}^{-1}$  according to [LaLone and Gupta, 2009] and [Zinszner et al, 2017]), avoiding the plate-impact method drawbacks.

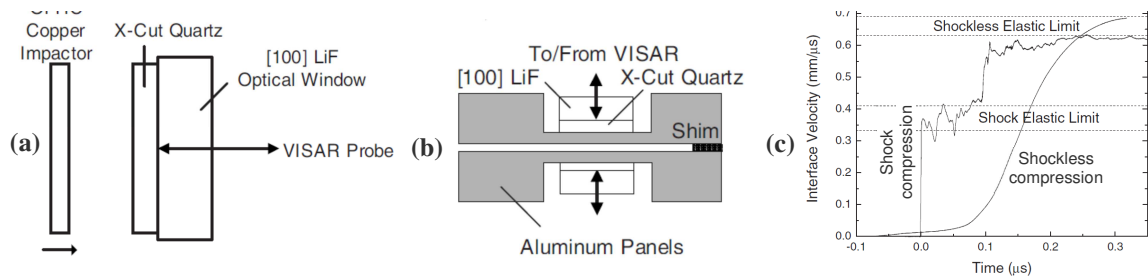


Figure 2: Experiments performed by [LaLone and Gupta, 2009] to characterize the elastic limit of x-cut quartz. (a) Scheme of “classical” plate-impact test. (b) Scheme of shockless compression test by compact pulsed power generator. (c) Interface velocity histories of samples subjected to shock wave (strain-rate about:  $4 \times 10^7 \text{ s}^{-1}$ ) or shockless compression (strain-rate about:  $3 \times 10^5 \text{ s}^{-1}$ ).

However, strong limitations are also observed with the compact pulsed power generator device. First, experiments are costly, very difficult to set up and limited to small-sized samples. Then, the rise time of a given device is fixed and cannot be easily changed. In addition, due to the strong induced electrical perturbations, the use of electronic measuring instruments, such as pressure gauges or ultra-high speed camera, might not be possible. For these reasons, this second experimental method remains largely unused in university research laboratories. Therefore, finding an alternative to compact pulsed power generator and classical plate-impact experiments is necessary to investigate the behaviour and damage mechanisms occurring in brittle materials at high strain-rates.

For this purpose, an innovative testing method was designed by using a “**shockless plate-impact technique**” based on the use of “**wavy**” machined flyer-plate or **buffer-plate**, which allow the applied strain-rate level on the sample to be controlled. This experimental method is detailed below.

#### 4. Experimental method developed in the project

In the present project, a new plate-impact technique that produces a shockless compression of the sample is developed. This method relies on the use of optimized “wavy” machined flyer-plate or buffer-plate (Fig. 3). The concept of “wavy” machined flyer-plate or buffer-plate was examined by [Forquin and Zinszner, 2017]. In this publication, a series of numerical calculations were performed based on the use of the explicit transient dynamic FE (Finite Element) code Abaqus/Explicit. The proposed testing configuration consists of a target made of two different thicknesses half-ceramics-discs sandwiched in-between a steel buffer disc and a LiF window backing, the whole system impacted by a steel flyer plate. This assembly was simulated in 2D plane strain and 2D axisymmetric FE configurations (Fig. 3a).

Numerical simulations on this system have highlighted the following points:

- The “wavy-shape” leads to a pulse-shaping effect resulting in a smooth loading pulse applied to the sample,
- The buffer plate provide an homogenised stress field along the sample transverse (radial) direction,
- The “wavy” pattern on both, the buffer or impactor plate, have the same favourable effect on the loading, which is smoothed, and leads to an isentropic compression loading,
- There appears to be a possibility to play on the wavy period and height to adjust the level of loading rate and rise time in the sample,
- Similar sample responses are observed between both 2D plane strain (half-period’s model) and axisymmetric calculations if the radius is large enough compared to the wave period ( $2a$ ) and small enough compared to the outer radius of the sample,
- The use of Lagrangian data analysis (applied to derive the stress-strain relationship) on the particle velocity measured on the rear face of each half-sample in contact with the window backing can provide the sample fairly accurate axial stress-axial strain response,
- Only a small influence of the measurement points, related to the impactor wavy-shape, can be observed in the Lagrangian data analysis results.

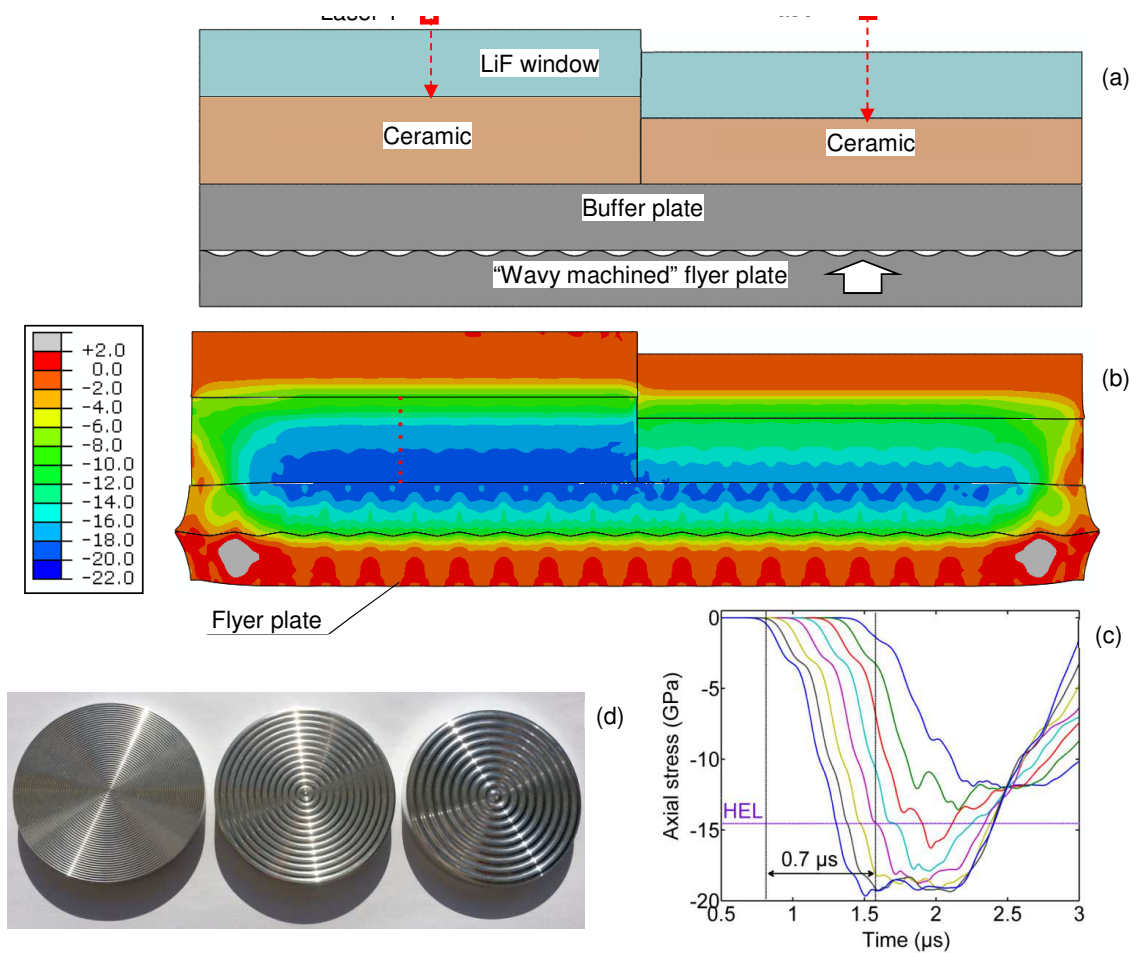


Figure 3: (a) Principle of shockless plate-impact experiment based on the use of a wavy machined flyer plate, (b), (c) Numerical simulation of shockless plate-impact considering the following geometry: ( $a = 2 \text{ mm}$ ,  $h = 0.5 \text{ mm}$ ). (b) Axial stress field (GPa) at  $T = 2 \mu\text{s}$ . (c) Axial stress vs time in elements regularly spaced along the axis of the sample. (d) Three geometries of "wavy machined" flyer plates, 80 mm in diameter, of period 1 mm, 3 mm and 4 mm [Forquin and Zinszner, 2017].

This type of shockless plate-impact experimental method resulted in a patent deposit [Forquin, 2016], in a publication [Forquin and Zinszner, 2017] and is currently further developed in Laboratoire 3SR for different types of brittle material (ceramics, polycrystalline ice and UHPC concrete). Indeed, complementary numerical simulations with the finite-element code Abaqus-explicit are performed in order to determine the most appropriate sample design and experimental configurations (size and shape of "wavy" machined flyer plate or intermediate plate) to obtain a shockless impact.

## 5. Dynamic testing facility used in Laboratoire 3SR

The equipment (Fig. 4) installed in Laboratoire 3SR offers outstanding performance as it provides the possibility to use 4 different calibres (25, 80, 100, 120 mm calibres) dedicated to plate-impact experiments. It allows reaching impact-speeds up to 1000 m/s to be reached with a striker mass of about 400 g. Moreover, it has specifically been designed with large windows allowing the combined use of high-speed camera, lightning, x-ray radiography and laser interferometer.



Figure 4: Testing facility built in Laboratoire 3SR. Main characteristics: 12 meters long device, maximum impact velocity about 1000 m/s, experiments performed under vacuum, exchangeable tubes of calibres  $D = 25, 80, 100, 120$  mm, large windows for ultra-high speed camera, x-ray radiography and lightning.

## 6. Development of mesoscopic modelling based on numerical samples

At high strain-rates, the effect of limited cracking velocity is supposed to play a major role on the tensile response of ceramics (up to  $10^4 \text{ s}^{-1}$ ) [Zinszner et al, 2017] and concrete (up to  $100 \text{ s}^{-1}$ ) [Erzar and Forquin, 2014]. The obscuration model put forward by Denoual-Forquin-Hild [Forquin and Hild, 2010] proposes a description of this mechanism. However, this damage model is based on the strong assumption that the density of critical defects varies as a power law of the applied stress.

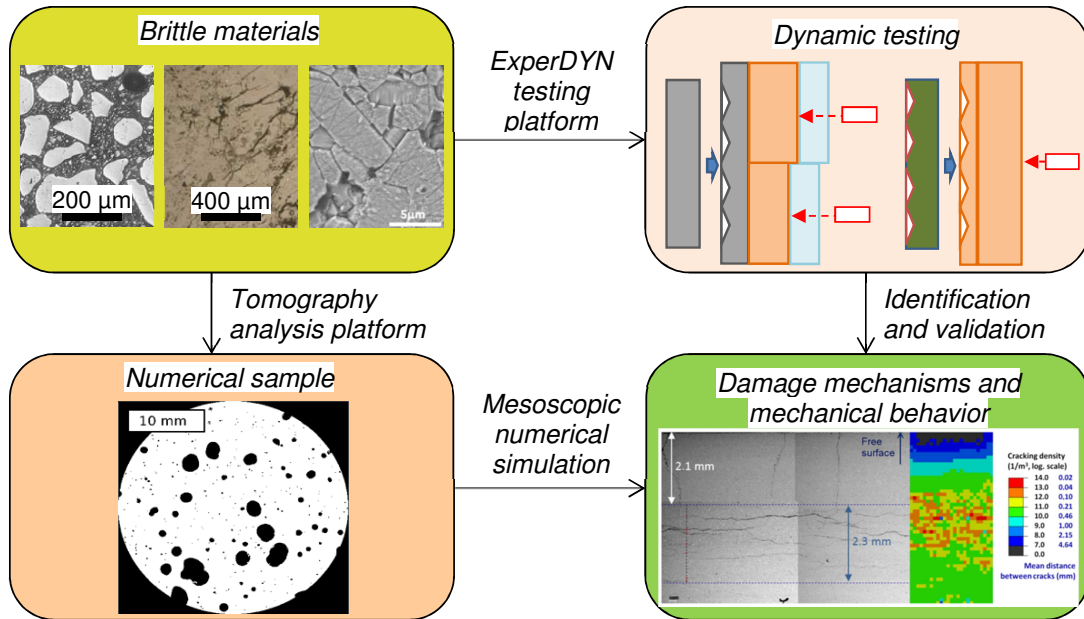


Figure 5: Mesoscopic modelling of shockless plate-impact experiment. (1) The virgin sample is scanned by X-ray tomography analysis. (2) The sample is subjected to shockless plate-impact experiment. (3) A mesoscopic numerical simulation of damage is conducted on the numerical sample. (4) A comparison of damage pattern is performed between experimental data (tomography analysis) and numerical predictions.

As described in [Forquin et al, 2019], a mesoscopic model is developed based on the flaws distribution provided by a micro-tomography analysis. The real samples are tested in shockless plate-impact experiments. Next, the numerical samples are mechanically loaded with the loading identified during the experimental test. Finally, the tested samples are scanned via micro-tomography and the observed fracturing patterns are compared to the state of damage obtained by the numerical simulations (Fig. 5).

Research activities in the field of body armour, protective solutions or related to the use of “extreme loadings” in civil engineering and materials science have been developed very quickly in the last few years. However, due to a lack of experimental methods providing a controlled strain-rate, the understanding and modelling of damage in brittle materials at very high-strain rates remain out of reach.

Based on the design of novel testing techniques (impact experiments, confined compression, shear testing, spalling techniques, “rocking spalling” tests, *etc.*), combined to an advanced instrumentation (gas-guns, ultra-high speed cameras, grid methods and digital image correlation at very high strain-rates, *etc.*) and the DFH obscuration model, new mesoscale modelling are being developed. This methodology should improve the understanding of the link between microstructural parameters of brittle materials and their response under high strain-rate loading conditions.

### Acknowledgments

This work has been performed in the framework of the Brittle’s CODEX chair supported by the UGA (Univ. Grenoble Alpes) Foundation and sponsored by the Saint-Gobain and Lafarge-Holcim companies. These sponsors are gratefully acknowledged by the authors.

### References

- Bourne N., Millet J., Pickup I. (1997). Delayed failure in shocked silicon carbide. *J. Appl. Phys.*, **81**, 6019–2023.
- Denoual C., Hild F. (2000). A damage model for the dynamic fragmentation of brittle solids, *Computer Methods in Applied Mechanics and Engineering*, **183**, 247–258.
- Erzar B., Forquin P. (2014) Analysis and modeling of the cohesion strength of concrete at high strain-rates. *Int. J. Solids Struct.* **51**(14): 2559-2574.
- Feng R., Raiser G.R., Gupta Y.M. (1998). Material strength and inelastic deformation of silicon carbide under shock wave compression. *J. Appl. Phys.* **83**, 79–86.
- Fonseca J., Bésuelle P., Viggiani G. (2013). Micromechanisms of inelastic deformation in sandstones: an insight using x-ray microtomography. *Géotechnique Letters*. **3**(2), 78-83.
- Forquin, P., Hild, F. (2010). A probabilistic damage model of the dynamic fragmentation process in brittle materials. In: Aref, H., van der Giessen, E. (Eds.), *Advances in Applied Mech.* Vol. **44**. Academic Press, San Diego, CA, 1–72.
- Forquin P., Andò E. (2017). Application of micro-tomography and image analysis to the quantification of fragmentation in ceramics after impact loading. *Phil. Trans. R. Soc. A*, **375**: 20160166.
- Forquin P. (2016) « PROCÉDE ET DISPOSITIF POUR MESURER LA RESISTANCE DES MATERIAUX SOLIDES PAR IMPACT DE PLAQUES SANS CHOC » October 11, 2016, INPI, N°1000369617.
- Forquin P, Zinszner J-L. (2017). A pulse-shaping technique to investigate the behaviour of brittle materials subjected to plate-impact tests. *Phil. Trans. R. Soc. A*, **375**: 20160333.
- Forquin P. (2017). Brittle materials at high-loading rates: an open area of research. *Phil. Trans. R. Soc. A*, **375**: 20160436.
- Forquin P, Blasone M. Georges D., Dargaud M., Ando E. (2019). Modelling of the fragmentation process in brittle solids based on x-ray micro-tomography analysis. *24<sup>ème</sup> Congrès Français de Mécanique*, Brest, 26-30 Août 2019, France
- Grote D. L., Park S.W., Zhou M. (2001). Experimental characterization of the dynamic failure behavior of mortar under impact loading. *J. Applied Physics*, **89**(4), 2115-2123.
- LaLone B.M., Gupta Y.M. (2009) Elastic limit of x-cut quartz under shockless and shock wave compression: Loading rate dependence *J. Appl. Phys.*, **106**, 053526.
- Meyers M.A. (1994). Dynamic behavior of materials. John Wiley & Sons, Inc.
- Murray N.H., Bourne N.K., Rosenberg Z., Field J.E. (1998). The spall strength of alumina ceramics. *J. Appl. Phys.*, **84** (2), 734–738.
- Vogler T.J., Reinhart W.D., Chhabildas L.C., Dandekar D.P. (2006). Hugoniot and strength behavior of silicon carbide. *J. Appl. Phys.*, **99**, 1–15.
- Zinszner J-L, Erzar B, Forquin P. (2017) Strain rate sensitivity of the tensile strength of two silicon carbides: experimental evidence and micromechanical modelling. *Phil. Trans. R. Soc. A*, **375**: 20160167.

# Crashworthiness assessment considering the dynamic damage and failure of a dual phase automotive steel

Sarath Chandran<sup>1\*</sup>, Patricia Verleysen<sup>1</sup>

<sup>1</sup>*MST-DyMa Lab, Department of Electromechanical, Systems and Metal Engineering, Ghent University, Technologiepark 46, Zwijnaarde, 9052, Gent, Belgium*

**Keywords:** Crashworthiness, high strain rate deformation, damage and failure

---

**Abstract :** Analyzing crash worthiness of the automotive parts has been posing a great challenge in the sheet metal and automotive industry since several decades. The present contribution will focus on one of the most urging challenges of the crash worthiness simulations, namely, an enhanced constitutive formulation to predict the failure and cracking of structural parts made from high strength steel sheets under impact. A hybrid extended Modified Bai Wierzbicki damage plasticity model is devised to this end. The material model calibrated using the experimental data covering high strain rate deformation, damage and failure successfully predicted the instability and subsequent response of the crash box under impact. Simulation results provide the deformation shape and deformation energy in order to predict and evaluate the vehicle crashworthiness. The simulations further helped in discovering the irrefutable impact of strain rate and stress state on the impact response of the auto-body structure. The strain rate is found to adequately affect the energy absorption capacity of the crash box structure both in terms of impact load and fold formation whereas the complex stress state has a direct association to the development of instability within the structure and early damage appearance within the folds.

## 1. Introduction

In automotive industry, crashworthiness connotes a measure of vehicle's structural ability to plastically deform and yet maintain a sufficient survival space for its occupants in crashes involving reasonable deceleration loads. Crashworthiness has been a major criterion in making vehicles safe to be used and manufactured. There are many factors contributing in determining the level of crashworthiness, one is in identifying the right type of material to be used and the other is in the consideration of the process that can change the properties and characteristic of the material and design. The recent megatrend of both automobile users and industries is to demand better vehicle safety and crashworthiness although the light-weight design for the reduction of fuel consumption becomes a very challenging issue. Confronting these contradictory requirements, steel industry has been reinventing steel over time and pioneering a whole new class of materials that are over 50% stronger than a decade ago. At the core of this innovation lies the advanced high strength steels (AHSS) family [1], which embraces safety in all possible ways. Vehicle body structures are generally constructed from deep-drawn parts of sheet metals. Since the strength of steel sheets depends on the rate of deformation, the dynamic behavior of sheet metals is a key to investigate the impact characteristics of the structure. Initial material failure and subsequent crack propagation should be accurately represented in order to evaluate its effects on structural integrity and crashworthiness. When the structures are exposed to dynamic loads, mechanical behavior becomes increasingly complex and phenomena such as failure and fracture by ductile and shear mechanisms are prevalent. Failure criteria incorporating various failure mechanism representation such as necking instability, ductile and shear fracture was developed to predict failure and establish crashworthiness of aluminum extrusions [2].

\*Sarath Chandran (Sarath.Chandran@UGent.be).

†Present address: MST-DyMa Lab, Department of Electromechanical, Systems and Metal Engineering, Technologiepark 46, Zwijnaarde 9052, Gent, Belgium

However, this strategy is insufficient for modern AHSS due to its complex failure modes and superior strain rate performance [3]. Crash performance has been vastly studied under room temperature and high strain rates [4-9]. In order to manage the energy dissipation in a vehicle structure and to design the individual components to either absorb and/or transmit energy, knowledge and understanding of the impact-dynamic material properties are essential. However, most of the crash resistance prediction strategies either take into account high strain rate material properties with limited stress state influence or failure phenomena only at quasi static loading rates thereby lacking the complex interaction between these two key terminologies. Material plasticity and damage/fracture properties of sheet metals at dynamic loading rates are thus paramount in providing the appropriate constitutive relation and to accurately model a vehicle crash event using finite element methods.

## 2. Material and Methods

A commercial DP-K1000 dual phase automotive steel is used in this study for its crashworthiness analysis. The material is supplied in the form of rolled sheet with a thickness of 1.5 mm. An extensive experimental series encompassing strain rates ranging from 0.0001 to 1100 s<sup>-1</sup> as experienced in crash boxes under impact are conducted to determine the strain hardening and strain rate hardening effects on the material strength and deformation capacity. Quasi-static reference and static tests are performed on an Instron material testing machine whereas high strain rate experiments are executed on a Split-Hopkinson tensile bar setup. Furthermore, tests performed at wide temperature ranges (-40 to 300 °C) as estimated under crash scenarios are taken into account to establish the thermal effects on material flow strength and plastic deformation. The compilation of experimental data thus consists of material flow stress as a function of strain, strain rate and temperature. Of equal importance is the fracture behavior and damage development under high rates of deformation. The instability mechanism within a crash box structure under impact loading is heavily dependent on the state of stress within the material in addition to strain path and strain rate. To account for this undeniable influence, experiments are performed on specially designed specimen geometries (dogbone, central hole, notched dogbone, plane strain and shear) to replicate the wide range of stress states that could be experienced under impact loading situations. Figure 1 displays the fracture specimens which are carefully designed so as to provide locally proportional loading histories (particularly for central hole, plane strain and shear specimens) until fracture initiation at the assumed location of the damage initiation. The readers are directed to [10] to gain more insight into the specimen design procedure. These fracture tensile tests are then used to assess the material damage and fracture behavior under various strain rates and temperatures. Digital image correlation is employed with high speed photography to acquire the full-field deformation measurements and to improve the accuracy of the test data gathered from the experiments. The method also provides insight into damage mechanisms prevalent under various stress states and localization phenomena especially at high strain rates.

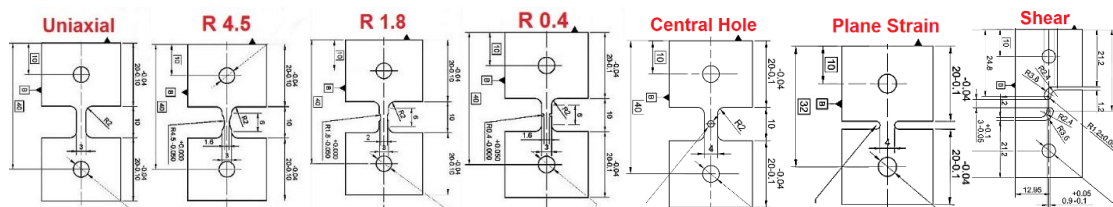


Fig.1. Specially designed specimens for plasticity and damage characterization of DP1000 steel under high strain rates

A hybrid extended modified Bai-Wierzbicki (eMBW) damage plasticity model is implemented to properly describe the non-negligible impact of damage on strength and ductility and the dependence of stress state on damage accumulation. The material model constitutes a plasticity formulation to characterize the material behavior before the initiation of damage followed by a phenomenological criterion to indicate the damage initiation. A phenomenological formulation of ductile damage is used for user friendly and simplified input of material parameters. Finally, a damage induced softening part incorporating a damage mechanics approach, is adopted to characterize the post damage material behavior. The detailed formulation of the eMBW material model can be found in [11]. The performed experimental campaign provide a reliable data set to derive the material parameters of the adopted damage plasticity model which is then used to investigate the crash response of this dual phase automotive steel both qualitatively and quantitatively.

The constitutive model obtained from the experimental series is imposed on the analysis for the dynamic response of auto-body crash box utilizing the explicit finite element scheme Abaqus. The proposed eMBW material model is implemented into Abaqus Explicit via a user material subroutine VUMAT. A full scale model with 3D solid elements and enough mesh refinement is implemented to accurately predict the localization and damage phenomena within the crash box. Detailed description of the model development is given in the subsequent section.

### 3. Results and discussion

To determine the material intrinsic mechanical properties, a comprehensive experimental program considering the material plasticity and fracture behavior under variable loading conditions including static and dynamic loading rates are designed and carried out by the author in a separate study [11].

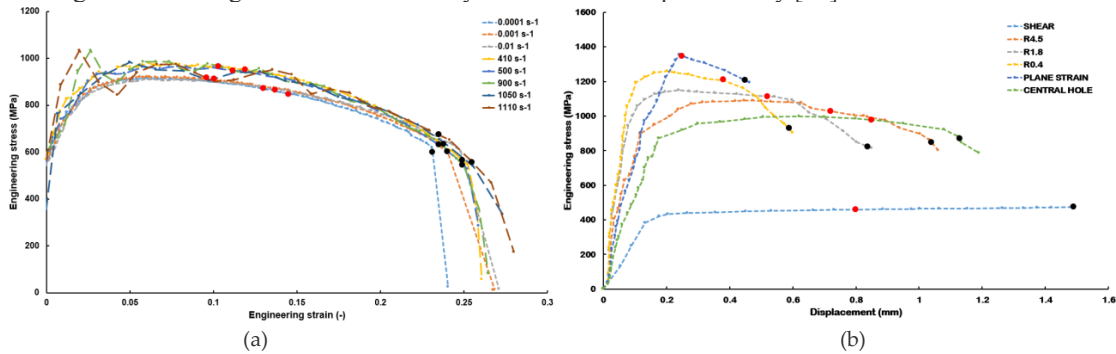


Fig.2. a) Engineering stress-strain curves of uniaxial tensile tests on DP 1000 steel across various strain rates. b) Engineering stress – displacement curves of tensile tests on various damage and fracture specimens at  $500 \text{ s}^{-1}$ . Red solid dots in the figure denotes the instant of damage initiation for the corresponding test and black solid dots specifies the fracture point.

Figure 2 a exemplifies one of the main observations from the analysis. A positive effect of strain rate on the material strength is primarily observed in the transition from static to dynamic loading rates. Moreover, the instant of damage initiation in the material (red dots in Figure 2 a) is found to decrease gradually with increase in the loading rate thereby establishing an undeniable influence of strain rate on the material response and its absorption performance. A specific trend is not observed for fracture point (black dots) from the uniaxial tensile test with respect to change in the strain rate however, post mortem final strain measurements from the fracture surface revealed a declining trend in material ductility with strain rate. Fracture tensile test results from [11] are supplemented with material response from central hole, plane strain and shear experiments to identify the influence of damage on material properties and reveal wide variety of damage mechanisms that could be present during a crash event. Effect of stress state on the material behavior is clearly evident from Figure 2b. It should be noticed that due to deviation on specimen's cross-sections, the stress-displacement values of different fracture specimens are only roughly compared. Higher non-axial stresses leads to increased strength however with a detrimental effect on ductility of the material. Plane strain state and higher stress state induced by the notches result in earlier onset of damage (red dots in Figure 2b) as opposed to uniaxial stress state scenario. Damage initiation is thus clearly influenced by the stress state within the material and this effect is translated to the damage propagation phase until failure (black dots). Delayed onset of damage and rapid damage evolution to fracture is observed for DP1000 steel under most conditions apart from the shear stress state wherein early damage appearance is succeeded by a prolonged damage evolution phase. With the lowest stress triaxiality and Lode angle parameter, shear state exhibits the lowest strength and an extended uniform plastic deformation range. The postponed damage and fracture appearance in the shear stress state is caused by the limited diffuse and localized necking in the thickness direction. Thus, the strain rate has a positive response on the material absorption capacity and thereby the crash performance of DP1000 steel whereas presence of complex multiaxial stress state could lead to earlier damage appearance and limit the subsequent folding in a crash impact event.

The author also studied the thermal effect on the plasticity, damage and fracture performance of DP1000 steel [12]. Dynamic strain aging (DSA) effect is prevalent in both uniaxial and fracture tensile tests and shows similar strain rate and temperature dependencies in both the scenarios. Therefore, the temperature and strain rate effects on the damage and fracture are estimated to succeed mainly from their influence on plastic deformation. Moreover, DSA in this DP steel displays a strong interaction with both strain rate and stress state and negatively affects the absorption capability

Hybrid approach of the MBW model takes into account the linear-elastic deformation, irreversible plastic deformation, ductile damage initiation, damage evolution and ductile fracture theory for the material mechanical mechanism. The deformation of steel before damage initiation obeys the elastoplastic principle following the Hooks law and von-Mises plasticity. During the plastic deformation, isotropic hardening taking account of the strain rate, temperature and stress state effects is introduced to update the plastic flow stress. The flow curve of the plastic characterization is the derivate of the smooth tensile test at room temperature and quasi static loading condition in the formulation of the combined Swift and Voce law. The corresponding temperature and strain rate dependency parameters are calibrated based on the smooth tensile tests across various temperatures and strain rates. The temperature and strain rate correction function in the plasticity formulation of eMBW model is graphically represented in Figure 3 a and b respectively. Ductile damage initiation is controlled by the equivalent plastic strain based locus, i.e. the damage initiation locus which is determined by coupling finite element simulations and experimental results, see Figure 3 c. The instant and location of the ductile damage initiation are determined by an inverse modelling approach involving a finite element (FE) model update procedure integrated with digital image correlation (DIC). The integration process is achieved by mapping the periphery and boundary conditions of both experiments and simulation on top of each other via certain transformation and interpolation function thus resulting in a similar reference coordinate frame. Here, the experimental strains (from DIC) are compared with the computed strains from the finite element simulations based on an initial set of parameters to be optimized. This comparison or difference in strains is defined by a cost function which is iteratively minimized by Gauss-Newton and Levenberg-Marquardt algorithm. Minimum value of the cost function leads to optimized set of parameters congruent with the experiments and thus aid in identifying the damage initiation instant. For all the investigated samples, damage initiation happens after the attainment of maximum force. Based on the local variables, including the equivalent plastic strain, stress triaxiality and Lode angle parameters, accessed from the simulation at the previously determined ductile fracture instant and location, the parameters of the damage initiation locus of DP1000 steel are calibrated. Obtained parameters are eventually validated based on the comparison of the global force-displacement responses and minimum thickness prediction between experiment and simulation until final fracture.

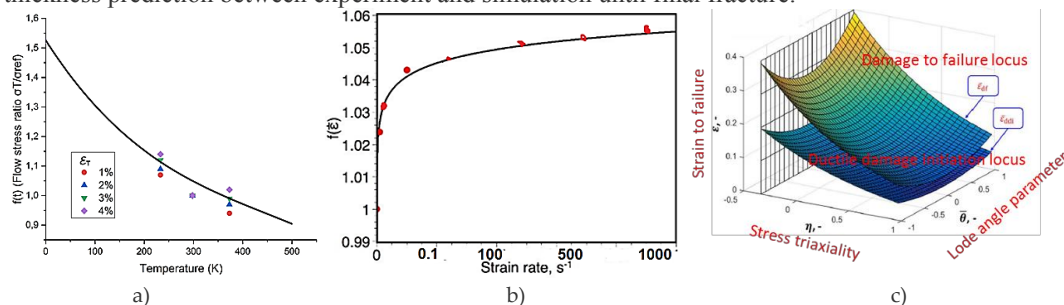


Fig.3. a) Temperature sensitive function b) Strain rate sensitive function c) Ductile damage initiation locus

After the eMBW material model parameter calibration, the determined data set is applied to the component level test. Crash test of the crash boxes are performed on the drop weight tower. Besides the measurement of the temporal evolution of force and displacement of the impactor, each crash test is recorded with a high speed camera system to monitor the evolution of the folds. Crash tests are performed with a constant drop mass of 129.5 kg and a height of 8 m which corresponds to a nominal input crash energy of 10 KJ. These crash parameters leads to a deformation length of 168 mm. All the parts crashed with these parameters show regular folding with small cracks in the fold which is illustrated in Figure 5b exemplarily for one of the crashed profile.

FE model for the crash box test is built up and modified according to the experimental profile geometry and test conditions. Full scale 3D FE model is set up containing C3D8R elements. Figure 4 displays the developed model of the crash box prototype and it's meshed configuration. The mesh type is modified for better prediction performance on the fracture behavior. Global mechanical properties such as force-displacement curves and

absorption values do not experience large deviations due to the mesh types especially in the plastic deformation range. However, variable mesh size will lead to distinctly different strain localization response which will result in the apparent deviation on the damage and fracture behavior. Normally, with the increase in the fineness of the mesh, the local material responses, like the local plastic deformation, are more efficiently captured. Therefore, the optimum mesh type should be balanced based on the combination of finite element calculation time and simulation model prediction performance. The critical zone is chosen to have a minimum mesh size of 0.3 mm x 0.3 mm x 0.5 mm after a mesh convergence analysis. The rest of the part has a coarsely homogenized mesh of 1 mm x 1 mm x 0.5 mm. The top rigid plate represents the impactor in the experiment setting with the drop mass. The original impact energy calculated from the drop height is transformed into initial impact velocity, which is then added as a predefined condition on the center of the top rigid plate. In addition, specimen bottom surface is constrained with the full constraint boundary condition.

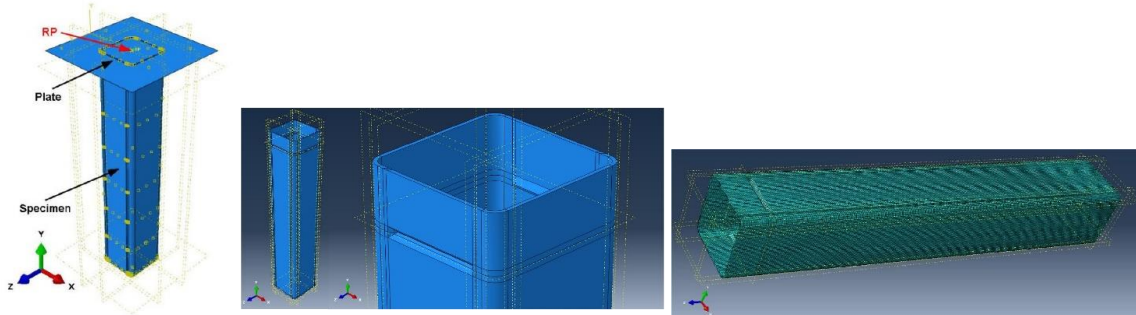


Fig.4. Crash box model development

The recurrence of the crash box material behavior including the force-displacement response, total impact energy absorption and global deformed shape is accurately captured, see Figure 5. Comparing the force-displacement response and deformed profile in the figure 5, it can be noticed that every peak force can be associated with every fold pair formation, except the first peak force which is caused by the impact interaction at the beginning. In both experiment and simulation, there are six fold-pairs in total, as marked by the numbers 1-6 in the Figure 5a and b. The process stops before the seventh fold formation as the total impact energy has already been absorbed. In terms of deviation on the energy/force-displacement curves, the current material parameter set results in a slightly harder material behavior in the simulation in comparison with the experiments, see Figure 5a. With reference to the contours of the numerical and experimental specimen deformation, both crack initiation and propagation on the top part and in the deformed specimen folds of the crash box specimen is well captured by the eMBW model supplemented with dynamic material parameters determined from this analysis. The solution dependent variables (output from the eMBW model) SDV1 reveals the distribution of the equivalent plastic strain in and around the folds whereas SDV2 represent the damage development within the material as shown in Figure 5b. As previously mentioned, damage is mainly observed at the contact between the crash box and top plate and inside the folds of the structure. It can be speculated that severe plastic deformation within the folds paves the way for the crack formation and subsequent damage development.

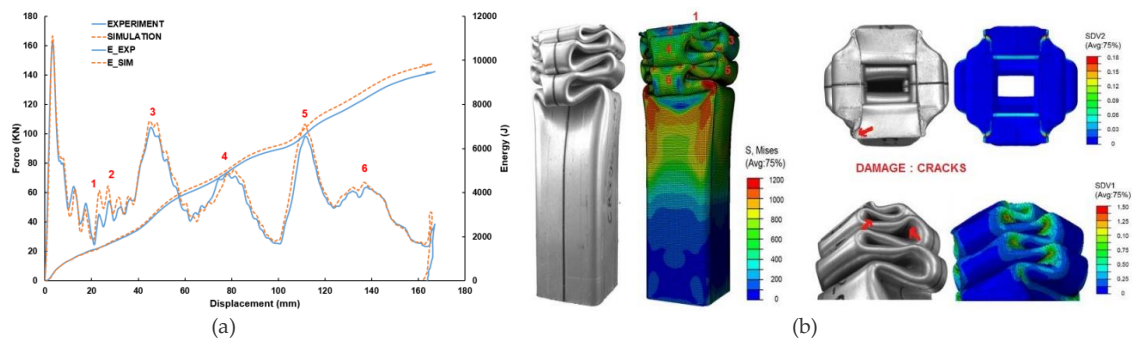


Fig.5. Numerical prediction of the DP1000 crash box test. Numbers (1-6) displays the subsequent folds formed. Damage is indicated by red arrows in the figure. SDV1 represents the equivalent plastic strain and SDV2 gives information on damage.

The good prediction of the crash box deformation behavior establishes the foundation to identify the required mechanical property profile for crashworthiness assessment of DP1000 steel.

#### 4. Conclusions

The extended Modified Bai Wierzbicki material model calibrated using the experimental data covering dynamic deformation, damage and failure successfully predicted the instability and subsequent response of the crash box under impact. The recurrence of the crash box material behavior including the force-displacement response, total impact energy absorption and global deformed shape is accurately captured. The simulations further helped in discovering the irrefutable impact of strain rate and stress state on the impact response of the auto-body structure. The strain rate is found to adequately affect the energy absorption capacity of the crash box structure both in terms of impact load and fold formation whereas the complex stress state has a direct association to the development of instability within the structure and early damage appearance within the folds and limit the subsequent folding in a crash impact event.

#### Acknowledgments

The author acknowledges the partners of the ‘Toolkit’ project for their technical support and fruitful discussions towards the fulfilment of this research. The author also expresses his gratitude towards ThyssenKrupp Steel for supplying steel sheets for the study.

#### Funding Statement

The author gratefully acknowledges the European Commission Research Fund for Coal and Steel (RFCS) [grant number : 709711] for the financial funding of the project “ Toolkit for the design of damage tolerant microstructures”, which supports the investigations.

#### References

1. H. Safari, H. Nahvi, M. Esfahanian. 2017. Improving automotive crash worthiness using advanced high strength steels. *Int. J. Crashworthiness*. **Vol.23**, pp. 645-659. (10.1080/13588265.2017.1389624)
2. H Hooputra, H Gese, H Dell and H Werner. 2004. A comprehensive failure model for crashworthiness simulation of aluminum extrusions. *Int. J. Crashworthiness*. **Vol.9**, pp.449-463. (10.1533/ijcr.2004.0289)
3. J. V Slycken, P. Verleysen, J. Degrieck, J. Bouquerel, B.C. De Cooman.2006. Crashworthiness characterization and modelling of high strength steel for automotive applications. *Proc. Of Inst. Mech. Eng. Part D: J. Auto. Eng*, **Vol. 220**, pp.391-400. (10.1243/09544070JAUTO26)
4. H. Huh, S. B. Kim, J. H. Song, J. H. Lim.2008. Dynamic tensile characteristics of TRIP type and DP type steel sheets for an auto body. *Int.J.Mech.Sci.* **Vol.50**, pp. 918-931. (10.1016/j.ijmecsci.2007.09.004)
5. N.D.Beynon,S.Oliver,B.T.Jones,G.Fourlaris. 2005. Tensile and work hardening properties of low carbon dual phase strip steels at high strain rates. *Mater.Sci.Technol.* **Vol.21**,pp.771-778.(10.1179/174328405X41038)
6. A.Das,M.Ghosh,S.Tarafder,S.Sivaprasad,D.Chakrabarti. 2017. Micro mechanisms of deformation in dual phase steels at high strain rates. *Mater.Sci.Eng.A*.**Vol.680**, pp.259-268. (10.1016/j.msea.2016.10.101)
7. H.Takechi,M.Takahashi,K.Ito,T.Endo,Y.Tomota. 2002. High strain rate deformation behavior of steels for auto body. *J.Iron Steel Inst.Jpn*.**Vol.88**, pp.703-714. (10.2355/tetsutohagane1955.88.11\_703)
8. H.Yu,Y.Guo,K.Zhang,X.Lai. 2009. Constitutive model on the description of plastic behaviour of DP600 steel at strain rates from  $10^{-4}$  to  $10^3$  s $^{-1}$ . *Comput.Mater.Sci.* **Vol.45**, pp. 36-41.
9. S.Curtze,V.T.Kuokkala,M.Hokka,P.Peura. 2009. Deformation behaviour of TRIP and DP steels in tension at different temperatures over a wide range of strain rates. *Mater.Sci.Eng.A.* **Vol. 507**, pp.124-13.
10. S. Chandran , P. Verleysen, J. Lian, W. Liu and S. Münstermann. 2017.Design of an experimental program to assess the dynamic fracture properties of a dual phase automotive steel. *J.Pro. Eng.* **Vol. 197**, pp. 204-213. (10.1016/j.proeng.2017.08.097)
11. S. Chandran , P. Verleysen, J. Lian, W. Liu and S. Münstermann. 2018. Dynamic fracture of a dual phase automotive steel. *EPJ Web Conf.* **Vol. 183**, no. 02047. (10.1051/epjconf/201818302047)
12. S. Chandran, W. Liu, J. Lian, S. Münstermann, P. Verleysen. 2019. Thermal effects on the dynamic damage and fracture of a dual phase automotive steel. *Proc. 24<sup>th</sup> DYMAT Technical Meeting: Temperature of material behaviour at high strain rates*, DYMAT 2019 P04.

## List of participants

LAST NAME	First name	Institution	City	Country	email
ARLERY	Magali	CEA/DAM	Gramat	France	magali.arlery@cea.fr
BAHI	Slim	University of Lorraine	Metz	France	mohamed-slim.bahi@univ-lorraine.fr
BEERLI	Thomas	ETH	Zürich	Switzerland	beerlit@student.ethz.ch
BLASONE	Maria Celeste	Univ. Grenoble Alpes	Grenoble	France	maria.blasone@3sr-grenoble.fr
BOLIS	Cyril	CEA/DAM Ile de France	Arpajon Cedex	France	cyril.bolis@cea.fr
BUZAUD	Eric	CEA/DAM	Le Barp	France	eric.buzaud@cea.fr
ÇANKAYA	Mehmet Alper	Izmir Katip Çelebi University	Izmir	Turkey	m.alper.cankaya@gmail.com
CARASSUS	Hugo	Université Polytechnique des Hauts de France	Valenciennes	France	hugo.carassus@etu.uphf.fr
CASTRES	Magali	Ensta bretagne	Brest	France	magcastres@gmail.com
CHANDRAN	Sarath	Ghent University	Gent	Belgium	Sarath.Chandran@UGent.be
CHEN	Wayne	Purdue University	West Lafayette	United States	wchen@purdue.edu
CORALLO	Luca	Ghent University	Gent	Belgium	luca.corallo@UGent.be
CORRÊA SOARES	Guilherme	Tampere University	Tampere	Finland	guilherme.correasoares@tuni.fi
COSCULLUELA	Antonio	CEA	Le Barp	France	antonio.cosculluela@cea.fr
DARGAUD	Marielle	Univ. Grenoble Alpes	Grenoble	France	marielle.dargaud@3sr-grenoble.fr
DAUDEVILLE	Laurent	Univ. Grenoble Alpes	Grenoble	France	laurent.daudeville@univ-grenoble-alpes.fr
DE GROOF	Vincent	HILTI AG	Schaan	Liechtenstein	vincent.degroof@hilti.com
DEQUIEDT	Jean-Lin	CEA	Arpajon	France	jean-lin.dequiedt@cea.fr
DUPLAN	Yannick	RV team	Gières	France	yannick.duplan@3sr-grenoble.fr
EAKINS	Daniel	University of Oxford	Begbroke	United Kingdom	daniel.eakins@eng.ox.ac.uk
FAGERHOLT	Egil	NTNU, Dep. Structural Engineering	Trondheim	Norway	egil.fagerholt@ntnu.no
FORQUIN	Pascal	Univ. Grenoble Alpes	Saint-Martin D'hères	France	pascal.forquin@3sr-grenoble.fr
FRAS	Teresa	ISL	Saint-Louis	France	teresa.fras@isl.eu
GALVEZ	Francisco	Universidad Politecnica de Madrid	Madrid	Spain	f.galvez@upm.es
GANZENMUELLER	Georg	Fraunhofer Institute for High-Speed Dynamics, EMI	Freiburg	Germany	georg.ganzenmueller@inatech.uni-freiburg.de
GEORGES	David	CNRS	Grenoble	France	david.georges@univ-grenoble-alpes.fr
GIRARDOT	Jérémie	Arts et Metiers Institute of Technology	Talence	France	jeremie.girardot@ensam.eu
GODFROID	Jean Alexandre	Centrale Nantes	Nantes	France	jean-alexandre.godfroid@ec-nantes.fr
GOUR	Govind	University of Oxford	Oxford	United Kingdom	govind.gour@eng.ox.ac.uk
GREIN	Clément	CEA Gramat	Gramat	France	clement.grein@cea.fr
GUSTAFSSON	Pär	Scandiflash	Uppsala	Sweden	Par.gustafsson@scandiflash.se
HANUS	Jean-Luc	INSA Centre val de loire	Bourges	France	jean-luc.hanus@insa-cvl.fr
HAUGOU	Gregory	Université Polytechnique des Hauts de France	Valenciennes	France	gregory.haugou@uphf.fr
HESPER	Johannes	Shimadzu Europa GmbH	Duisburg	Germany	jhe@shimadzu.eu
HESPER	Johannes	Shimadzu Europa GmbH	Duisburg	Germany	jhe@shimadzu.eu
HOKKA	Mikko	Tampere University	Tampere	Finland	mikko.hokka@tuni.fi

JAKKULA	Sivakumar Puneeth Kumar	Albert-Ludwigs-Universität Freiburg, INATECH	Freiburg Im Breisgau	Germany	puneeth.jakkula@inatech.uni-freiburg.de
KAUFMANN	Rene	NTNU	Trondheim	Norway	rene.kaufmann@ntnu.no
KOSITSKI	Roman	Technion - Faculty of Mechanical Eng.	Haifa	Israel	kositski@gmail.com
LEFEBVRE	Martin	INSA Strasbourg - ICUBE	Strasbourg	France	martin.lefebvre@insa-strasbourg.fr
LI	Xueyang	ETH	Zurich	Switzerland	lixue@ethz.ch
LÖRCHER	Lena	Fraunhofer	Freiburg	Germany	reisestelle@emi.fraunhofer.de
LUKIC	Bratislav	Univ. Grenoble Alpes	Grenoble	France	bratislav.lukic@3sr-grenoble.fr
MEYLAND	Martin Jensen	Technical University of Denmark	Kgs. Lyngby	Denmark	majeme@byg.dtu.dk
MOHR	Dirk	ETH	Zurich	Switzerland	dmohr@ethz.ch
MORVAN	Herve	Université Polytechnique Hauts de France	Valenciennes Cede 9	France	herve.morvan@uphf.fr
PACCOU	Thibaut	CEA Gramat	Gramat	France	thibaut.paccou@cea.fr
PALMA DE BARROS	David	CEA Gramat	Gramat	France	david.palmadebarros@gmail.com
PAULSON	Shane	Purdue University	West Lafayette	United States	paulsons@purdue.edu
PEREZ	Ignacio Vidal	Technical Univesity of Denmark	Kongens Lyngby	Denmark	igvipe@mek.dtu.dk
POURNOORI	Nazanin	Tampere University	Tampere	Finland	nazanin.pournoori@tuni.fi
PRADEL	Pierre	CEA CESTA	Le Barp	France	pierre.pradel@cea.fr
RAMAGIRI	Bhaskar	IIT Bombay	Mumbai	India	bhaskar.r@aero.iitb.ac.in
RAMAKRISHNAN	Karthik Ram	University of Oxford	Oxford	United Kingdom	karthik.ramakrishnan@eng.ox.ac.uk
RIOT	Alexandre	CEA/I2M	Talence	France	alexandre.riot@outlook.fr
RUMBAUGH	Todd	Hadland	Santa Cruz	USA	trumbaugh@hadlandimaging.com
SALETTI	Dominique	Univ. Grenoble Alpes	Saint-Martin-D'hères	France	dominique.saletti@3sr-grenoble.fr
SEIDL	Marina	ISL	Saint-Louis	France	marina.seidl@isl.eu
SIU	Derek	Imperial College London	London	United Kingdom	derek.siu11@imperial.ac.uk
STANCZAK	Magda	French-German Research Institut of Saint-Louis	Saint-Louis	France	Magda.STANCZAK@isl.eu
TARTIÈRE	Jérémie	IRDL ENSTA Bretagne	Brest Cedex9	France	jeremie.tartiere@ensta-bretagne.org
TOMAR	Vikas	Purdue University	West Lafayette	United States	tomar@purdue.edu
TRIPPEL	Antonina	Albert-Ludwigs-Universität Freiburg, INATECH	Freiburg Im Breisgau	Germany	a.trippel@inatech.uni-freiburg.de
VAYIG	Yaniv	Rafael	Haifa	Israel	YANIVVAY@rafael.co.il
VIOT	Philippe	Arts et Métiers	Talence	France	philippe.viot@ensam.eu
WALLEY	Stephen	University of Cambridge	Cambridge	United Kingdom	smw14@cam.ac.uk
WANG	Huachuan	Monash University	Melbourne	Australia	whch1000@gmail.com
XAVIER	Mathieu	CEA/DAM Ile de France	Arpajon Cedex	France	mathieu.xavier@cea.fr
XIA	Peikang	IMDEA Materials Institute	Madrid	Spain	xia.peikang@imdea.org
YOO	Sanghyun	Deutsches Zentrum für Luft- und Raumfahrt e.V. (DLR)	Stuttgart	Germany	Sanghyun.Yoo@dlr.de
ZINSZNER	Jean-Luc	CEA/DAM	Gramat	France	jean-luc.zinszner@cea.fr